Low-thrust satellite-aided planetary capture

Thesis report

Jorn Vanwesenbeeck

January 5, 2021

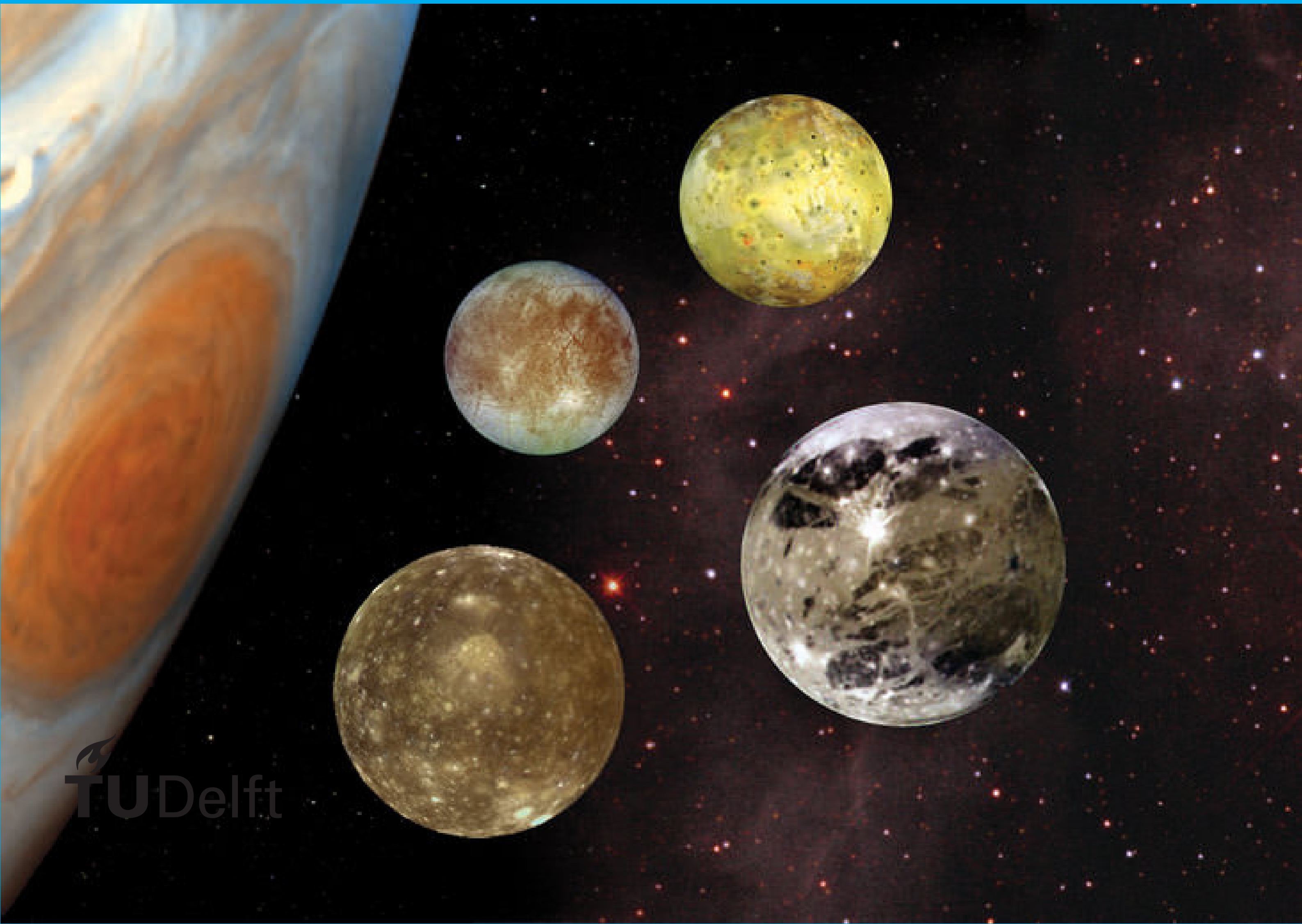

Low-thrust satellite-aided planetary capture

Thesis report

by

Jorn Vanwesenbeeck

to obtain the degree of Master of Science
at Delft University of Technology,
to be defended publicly on January 20th 2021

Student number:	4189299	
Project duration:	January 1, 2020 –	
Thesis committee:	Ir. R. Noomen,	TU Delft, supervisor
	Ir. E. Mooi ,	TU Delft, chair
	Ir. A. Cervone,	TU Delft, external

Cover image credits: Universe Today
(https://www.universetoday.com/44796/galilean-moons/)

TU Delft

Preface

This report serves as a conclusion of my Master of Science study at the Faculty of Aerospace Engineering at Delft University of Technology.

I researched the possible gains of using the Galilean moons to aid a spacecraft arriving at the Jovian system. During this study I was never alone and therefore I like to take some time to say thanks to a few people.

At first, my supervisor Ron Noomen. I would like to thank him for his encouraging conversations and positive criticism. The weekly meetings I had with him helped me stay on track and were very delightful and inspiring for me.

I would like to thank my friends I mostly know from ”The4ce” for enjoying both the good and bad moments with me.

Lastly, I would very much like to thank my family. Especially my mother and father for their encouragement, patience, love and financial support. Without them, I would have never been able to chase and fulfill my dream of becoming an aerospace engineer.

Jorn Vanwesenbeeck
Delft, November 2020

Abstract

The orbit insertion maneuver is, besides the launch, the most intensive maneuver in terms of propellant mass. In 1995 the Galileo spacecraft arrived at the Jovian system and when it did, it performed a first flyby with Io to decrease the required ΔV for orbit insertion with 175 m/s (i.e. down to 644 m/s). This technique is generally known as ”satellite-aided planetary capture”. The Galileo spacecraft proved that this technique could be beneficial. Much research has been conducted on it. In most of it, Io was used as a flyby moon. Although Io is a perfect candidate for employing satellite-aided planetary capture, it lies within Jupiter’s harsh radiation zone. This thesis report aims to investigate the capabilities of low-radiation satellite-aided capture trajectories. These would exclude the use of Io and are therefor left with Europa, Ganymede and Callisto as flyby candidates. These orbit Jupiter at a much higher orbital radius. The orbit insertion that follows would then be executed at a much higher perijove and become less efficient. Therefore, this report will combine these low-radiation capture trajectories with low-thrust propulsion and see what performance improvements can be achieved, compared with direct impulsive orbit insertion and ”conventional” satellite-aided capture.

First, insights into the Tisserand parameter was gained by deriving it from the circular restricted three-body problem. Then Tisserand graphs were constructed for the Solar System and the Jovian system. The Tisserand graph theory was employed in optimizations to find the most optimal sequences for satellite-aided planetary capture in the Jovian system. A brief but thorough investigation was performed on the best tuning settings for the optimization algorithm, that is, Differential Evolution.

Then, to include low-thrust legs in the capture trajectories, a fast and robust method was developed. A second-order Taylor expansion method for the Modified Equinoctial Elements appeared to be the best option considering the transition from high to low orbital energy. This second-order Taylor series expansion was combined in the satellite-aided planetary capture optimizations to investigate low-thrust satellite-aided planetary capture capabilities.

Results from both optimizations were compared and the first conclusions could be taken on the capabilities of these low-thrust capture sequences. In addition, this thesis research also focused on what promising sequences are for mission planning. For this, the phasing problem that treated the locations of the moons under consideration was solved. An ephemerides search supplied both a date and initial perijove distribution for each possible sequence. With this combined, conclusions could be taken with respect to mission planning.

The result was that the addition of low-thrust propulsion along a capture trajectory could be beneficial, but, not for all sequences. For these, it was concluded that it is better to employ a conventional satellite-aided capture trajectory. The minimum ΔV for conventional satellite-aided planetary capture was 255 m/s. This minimum was achieved with a Ganymede-JOI-Europa-Callisto capture sequence. The addition of low-thrust to this further lowered the impulsive ΔV towards 157 m/s.

Contents

Nomenclature

Abbreviations

AOL	Argument of latitude
AU	Astronomical Unit
CR3BP	Circular Restricted Three-Body Problem
DE	Differential Evolution
EVEEJ	Earth-Venus-Earth-Earth-Jupiter gravity assist trajectory
GA	Genetic Algorithm
IC	Initial Condition
JOI	Jupiter Orbit Insertion
JUICE	Jupiter Icy Moon Explorer
LT	Low thrust
MEE	Modified Equinoctial Element
NEP	Nuclear Electric Propulsion
NP	Number of populations
P	Population
PaGMO	Parallel Global Multi-objective Optimizer
PSO	Particle Swarm Optimization
RAAN	Right ascension of the ascending node
RK4	Runge-Kutta 4
SA	Simulated Annaling
SEP	Solar Electric Propulsion
SOI	Sphere Of Influence
TCM	Trajectory Correction Maneuver
Tudat	Technical University Delft Astrodynamic Toolbox
UT	Universal Time

Greek symbols

α^+	Pump angle after flyby [rad]
α^-	Pump angle before flyby [rad]

δ	Turning or Bending angle [rad]
γ	Flight path angle [rad]
μ_i	Gravitational parameter of body i [$\mathrm{m}^3/\mathrm{s}^2$]
μ_J	Gravitational parameter of Jupiter [$\mathrm{m}^3/\mathrm{s}^2$]
μ_S	Gravitational parameter of the Sun [$\mathrm{m}^3/\mathrm{s}^2$]
Ω	Right ascension of the ascending node [rad
Ω_0	RAAN on moment of first flyby [rad]
ω_0	argument of perijove on moment of first flyby [rad]
Ω_1	RAAN on moment directly after first flyby [rad]
ω_1	argument of perijove directly after first flyby [rad]
ω_p	Argument of pericenter [rad]
θ	True anomaly [rad]
θ_0	True anomaly of first flyby [rad]
θ_1	True anomaly directly after first flyby [rad]
θ_2	True anomaly directly before second flyby [rad]
θ_3	True anomaly right after second flyby [rad]
θ_4	True anomaly right before third flyby [rad]

Latin symbols

$\bar{a}_T$	Thrust acceleration vector [m/s^2]
$\bar{r_{Sun}}$	Position vector of Sun [m]
$\bar{X}_p$	Parameter vector [various]
$U_{i,G}$	notation of the trial vector [-]
ΔL_{21}	Phase angle between first and second flyby moon [rad]
ΔL_{41}	Phase angle between first and third flyby moon [rad]
$\Delta L_{Ga,Ca,ephem}$	Ephemerides angle between Callisto and Ganymede [rad]
$\Delta L_{Ga,Sun,ephem}$	Ephemerides angle between Callisto and Sun [rad]
ΔV_{GA}	Velocity increment as a result of gravity assist [m/s]
ΔV_{JOI}	Velocity increment for Jupiter Orbit Insertion [m/s]
ΔV_{LT}	Low-thrust velocity increment [m/s]
$\hat{n}$	Orbital normal vector [m]
a	Semi-major axis [m]
a_0	Initial semi-major axis [m]
a_c	Semi-major axis of captured orbit [m]
a_m	Semi-major axis of second body around first [m]

C_1	first constant of Gaus equations in MEE
C_2	Second constant of Gaus equation in MEE
C_J	Jacobi constant [-]
C_r	Crossover rate [-]
E	(specific) Orbital energy [$\mathrm{m^2/s^2}$]
e	Eccentricity [-]
e_0	Initial eccentricity [-]
$E_{moon,1}$	Eccentric anomaly of first moon [rad]
$E_{moon,2}$	Eccentric anomaly of second moon [rad]
F	Mutation scale factor [-]
f	Second modified equinoctial element [-]
f	True anomaly in 4BP [rad]
F_R	Thrust acceleration in radial direction [$\mathrm{m/s^2}$]
$F_\perp$	Thrust acceleration perpendicular to orbital plane [$\mathrm{m/s^2}$]
F_θ	Thrust acceleration in direction of spacecraft's motion [$\mathrm{m/s^2}$]
G	Universal gravitational constant [$\mathrm{m^3/kgs^2}$]
g	Third modified equinoctial element [-]
g_0	Gravitational acceleration on surface of Earth [$\mathrm{m/s^2}$]
G_i	Number of generation [-]
H	Specific angular momentum [$\mathrm{m^2/s}$]
h	Fourth modified equinoctial element [-]
H_z	z-component of angular momentum [$\mathrm{m^2/s}$]
$H_{moon,1}$	Hyperbolic anomaly of first moon [rad]
$H_{moon,2}$	Hyperbolic anomaly of second moon [rad]
i	Inclination [rad]
i_0	Initial inclination [rad]
$I_{sp,HT}$	Specific impulse of high-thrust engine [s]
$I_{sp,LT}$	Specific impulse of low-thrust engine [s]
J	Fitness [various]
k	Fifth modified equinoctial element [-]
L	Sixth modified equinoctial element or true longitude [rad]
L_0	True longitude of first flyby [rad]
L_1	True longitude directly after first flyby [rad]
L_2	True longitude of directly before second flyby [rad]

L_{12}	Difference in true longitude between first two flybys [rad]
L_{limit}	Hyperbolic limit angle [rad]
m_i	mass of body i [kg]
M_{Ca-Eu}	Mismatch between Callisto and Europa [rad/day]
M_{Ca-Ga}	Mismatch between Callisto and Ganymede [rad/resonanceperiod]
M_{Ga-Eu}	Mismatch between Ganymede and Europa [rad/resonanceperiod]
$M_{initial}$	Initial mass of spacecraft [kg]
$M_{prop,min}$	Minimum propellant mass [kg]
M_{prop}	Propellant mass [kg]
M_{Sun}	Mismatch due to Jupiter’s orbit around the Sun [rad/resonanceperiod]
M_{tot}	Total mismatch [rad/day]
n	Angular velocity or mean angular motion [rad/s]
n_{moon}	Mean angular velocity of moon under consideration [rad/s]
p	Semi-latus rectum/first modified equinoctial element [m]
P_{fb}	Flyby penalty [-]
P_{rad}	Radiation penalty [-]
r	Radial distance [m]
r_1	Distance between third and first body in the CR3BP [m]
r_f	Orbital radius of flyby planet [rad]
R_J	Equatorial radius of Jupiter [m]
r_p	Pericenter- or perijove radius [m]
R_2	Orbital radius of secondary body around primary [m]
r_{Ca}	Position vector of Callisto [m]
r_{Ga}	Position vector of Ganymede [m]
$R_{p_{opt}}$	Optimal initial perijove [$\mathrm{R_J}$] or [m]
R_{SOI}	Radius of SOI [m]
$S_{a,b}$	Synodic period between body a and b [s]
T_a	Orbital period of body a [s]
T_p	Tisserand parameter [-]
t_{12}	Time of flight between first two flybys [s]
t_{34}	Time of flight from second to third moon [s]
$T_{pattern,Ca-Eu}$	Pattern repeat period between Ganymede and Europa [s]
$T_{window,Ca-Ga}$	Flyby-window repeat period between Callisto and Ganymede [s]
$T_{window,Ga-Eu}$	Flyby-window repeat period between Ganymede and Europa [s]

u	Argument of latitude [rad]
V	Velocity [m/s]
V'	Velocity of third body in CR3BP [m/s]
V^+	Spacecraft velocity with respect to central body after flyby [m/s]
V^-	Spacecraft velocity with respect to central body before flyby [m/s]
V_p	Velocity at pericenter/perijove [m/s]
V_∞	Hyperbolic excess velocity [m/s]
$V_{exhaust}$	Exhaust velocity [m/s]
$V_{i,G}$	Mutation method notation [-]
V_{planet}	Velocity of planet [m/s]
W	Weight factor [-]
X	Decision vector [-]
x	x-coordinate in non-rotating reference frame [m]
x'	x-coordinate in rotating reference frame [m]
x_a	x-coordinate in asymptotic frame [m]
y	y-coordinate in non-rotating reference frame [m]
y'	y-coordinate in rotating reference frame [m]
y_a	y-coordinate in asymptotic frame [m]
Z	z-coordinate [m]

Chapter 1

Introduction

This first chapter serves as an introduction to the subject of this master thesis research: ”low-thrust satellite-aided planetary capture”. Section 1.1 elaborates on the relevance of the problem. Section 1.2 presents a short outline of the report.

1.1 Background

Inserting a spacecraft in orbit around another planet requires a significant amount of ΔV. Because of this, rather than flying a direct transfer, a (sequence of) gravity assist(s) can be used to lower mission requirements in terms of ΔV and propellant mass that the spacecraft itself should deliver. These propellant savings could lower the spacecraft’s overall mass or provide extra mass for the spacecraft’s payload. Historical missions such as Cassini [6], Voyager 1 and 2 [4] and Galileo [8] have already reached the outer planets and beyond (Voyager) through sequences of planetary gravity assists. Besides the launch of the spacecraft, the orbit insertion maneuver is the most intensive part of the mission in terms of propellant mass. From this, the idea came of using one or more gravity assists to lower the ΔV requirements on the orbit insertion maneuver. This is to be achieved by performing close flybys (gravity assists) with the target planet’s natural satellites. This is often referred to as ”satellite-aided planetary capture” [18] and much research has already been conducted on this subject. It could lead to significant propellant savings and/or extending the planned mission duration. Obviously, this can only be the case when performed successfully. As an example, the Galileo mission used this technique to insert itself in orbit around Jupiter. This was done through a gravity assist with Io. Because of the relatively massive Galilean moons, the Jovian system is very attractive for employing satellite-aided planetary capture trajectories. That is why most of the research on the subject is conducted for the Jovian system. The challenges of designing satellite-aided capture trajectories lie in finding good sequences with natural satellites and see if they are in line with a foregoing interplanetary trajectory. Also, in recent years numerous missions have used low-thrust electric propulsion. For example, the BepiColombo spacecraft [1] is currently on its way to Mercury. On its heliocentric trajectory, the spacecraft has used and will use multiple low-thrust propulsive trajectory legs. This is done in combination with several planetary gravity assists to reach Mercury. When it reaches Mercury, it will again use low-thrust propulsion to lower its relative velocity with respect to the planet such that it could even be captured in orbit around Mercury without the use of any impulsive orbit insertion maneuver. This master thesis report aims to use the technique of satellite-aided planetary capture in combination with low-thrust propulsion to capture a spacecraft in orbit around Jupiter. Moreover, it aims to finding the best sequences for mission planning. When considering mission planning, clearly the phasing of the moons is of great importance. A certain sequence could look very promising for mass savings, but if the Galilean moons almost never align properly, this sequence could possibly never be flown.

The thesis research was conducted by means of answering the following research question:

> *What are the performance improvements of using low-radiation satellite-aided planetary capture trajectories in the Jovian system compared to a purely impulsive capture maneuver and how could these further be improved by incorporating low-thrust electric propulsion?*

This research question can be split up into three sub-questions:

- What are the potential propellant mass savings for low-radiation satellite-aided planetary capture trajectories compared to purely impulsive capture trajectories?
- What are the potential propellant mass savings for low-radiation satellite-aided planetary capture trajectories when low-thrust propulsion along the trajectory is added?
- Which of the promising trajectories could be considered most useful with respect to mission panning?

1.2 Structure of the report

This master thesis is divided into ten chapters. The first one is this introduction. Chapter 2 presents the heritage of a past mission and earlier research. This chapter also presents the problem statement that outlines the motivation for the thesis topic with the actual research problem, research question and research procedure. The next chapter starts with the basics of investigating multiple gravity assist trajectories. This is done through the Tisserand parameter and constructing a Tisserand graph for the Jovian system. In Chapter 4 this technique is used in optimizations for finding the most optimal conditions for particular capture sequences in the Tisserand graph. Results from these optimizations will give the first insights into what particular sequences are good candidates for planetary capture. Chapter 5 will present a fast method for including low-thrust legs on the Tisserand graph. The importance of this fast technique becomes clear in Chapter 6 where it is combined with the optimizations from Chapter 4 to find optimal low-thrust satellite-aided capture trajectories in the Tisserand graph. Results from this chapter will present the capabilities of low-thrust satellite-aided planetary capture trajectories. Up to this point all calculations and optimizations have been performed without taking into account the locations of the moons. In other words the phasing of the moons was not yet considered. The methodology of solving the phasing problem for both the low-thrust and ballistic satellite-aided capture trajectories is presented in Chapter 7. The results obtained in Chapters 4 and 6 are then fed to this phasing problem and results are presented and summarized in Chapter 8. The verification and validation efforts are outlined in Chapter 9. Finally Chapter 10 presents the conclusions that are based on the results of Chapter 8.

Chapter 2

Heritage

Satellite-aided planetary capture is a unique technique of capturing a spacecraft around a target planet and is the research topic in this Master of Science thesis. This chapter starts with a brief outline of the heritage on this subject. This includes a mission that already employed this technique and has proven its benefits. This is further expanded with earlier research on this topic with the purpose of indicating a knowledge gap for this thesis research. The problem statement in Section 2.2 then outlines this knowledge gap. The actual research problem on which this thesis research is centered is presented in Subsection 2.2.1, this also includes the research questions and research procedure.

2.1 Heritage

This section serves as a more elaborate introduction into the topic of this thesis research. It starts with the Galileo mission that already used the technique of satellite-aided planetary capture. Then an outline of earlier research on the topic will explain on how the author directed his research.

2.1.1 Galileo

The Galileo spacecraft was launched in October 1989 and after a sequence of planetary gravity assists by Venus and Earth it arrived at the Jovian system in December 1995. The spacecraft consisted of an orbiter and an entry probe, which was first released into Jupiter's atmosphere upon arrival at the Jovian system. The most important mission objectives were to investigate the structure of Jupiter's magnetosphere and the chemical composition of the atmospheres of Jupiter and its moons. It made multiple close encounters (flyby's) with the Galilean moons (e.g., Io, Europa, Ganymede and Callisto). The mission was initially planned to last for 24 months. However, the mission was extended twice (once to 1999 and later to 2003) [8].

When it arrived at the Jovian system, the spacecraft performed its first flyby with Io at an intended altitude of 1000 km (actually 892 km). When doing so, it reduced the amount of ΔV required for Jupiter orbit insertion (JOI) by 175 m/s (satellite-aided planetary capture) [8]. Due to the harsh radiation environment, this was the closest flyby that the spacecraft performed with Io. Right after the flyby, the orbiter relayed the data from the probe back to Earth before the actual orbit insertion manoeuvre was initiated. An illustration of the Io flyby, the probe entry and JOI is presented in Figure 2.1a.

Apart from the gravity assist manoeuvre with Io, the transfers from one moon to another within the Jovian system also happened by means of gravity assists in order to save propellant. The initially planned tour (up to 1997) for the Galileo orbiter through the Jovian system is shown in Figure 2.1b. As mentioned earlier in this section, the mission was extended twice up to 2003 when it dived into Jupiter's atmosphere, in order to prevent it to contaminate the

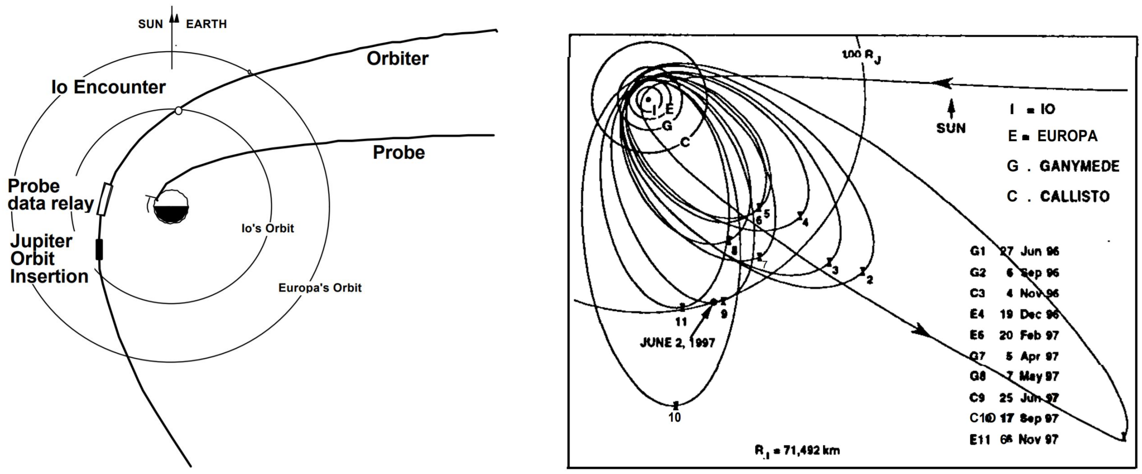

(a) Galileo orbit insertion manoeuvre using gravity assist of Io and probe entry into Jupiter's atmosphere[9].

(b) Complete (initially planned) tour of the Galileo orbiter up to 1997 [8].

Figure 2.1: Illustration of Galileo orbit ensertion and intended tour through the Jovian system.

Jovian moons with terrestrial bacteria.

2.1.2 Earlier research

This subsection expands the earlier research conducted on satellite-aided planetary capture. The purpose of this section is finding a knowledge gap that can be filled by this thesis research.

Jerry K. Cline performed the first research on single satellite-aided capture trajectories [5]. He used a patched-conics approach on which one of the planet's natural satellite aided in the planetary capture. Furthermore, he applied it to multiple planet-satellite systems: Earth-Moon, Jupiter-Ganymede, Jupiter-Callisto, Saturn-Titan and Neptune-Triton. His first assumption was coplanar circular planetary orbits around the Sun. From this, he investigated three sources of bodies to be captured, namely: spacecraft launched from Earth, bodies entering the Solar System from interstellar space, and bodies already in orbit around the Sun such as asteroids or space dust. From his analysis it followed that the Neptune-Triton system had the best capabilities for both capturing an interstellar object and capturing a spacecraft from Earth. All other planet-moon systems could only capture an object that was already in orbit around the Sun (considering appropriate conditions). Cline's investigation was limited to purely ballistic capture only, so no orbit insertion maneuvers were incorporated.

Cline showed what the capabilities were for employing satellite-aided capture. Due to the raising interest in exploring the Jovian system and the presence of the massive Galilean moons, most of the future work around satellite-aided capture was restricted for a mission to the Jovian system.

The Galileo mission proved that employing a Jupiter orbit insertion maneuver in combination with a flyby saved a significant amount of propellant mass that could be used for mission extension or even extra scientific payload. With this in mind, numerous research expanded the idea towards double- [24],[28], triple-[18] [16] and even (although limited) quadruple-aided capture sequences [17]. [27] investigated the capabilities of solar electric propulsion along the interplanetary trajectory to lower the relative velocity when arriving at the Jovian system. In combination with one, two or three flybys with the Galilean moons this would not require any impulsive orbit insertion.

Most of the research mentioned above used an Io flyby in the capture sequence. However as was mentioned in Subsection 2.1.1 during its Io flyby, the Galileo spacecraft experienced

Jupiter's harsh radiation environment. Therefor it never came closer to Io as that first flyby.

2.2 Problem statement

The Galileo mission and the earlier research mentioned in the previous section proved that satellite-aided planetary capture sequences could be very beneficial for missions to the Jovian system. Not only to lower the impulsive orbit insertion maneuver but also for low-thrust interplanetary trajectories.

Keeping in mind that most of the research used flybys with Io because of it's significant orbital velocity, which generally is beneficial for performing flybys. However, the author argues that all Io-aided (single or multiple) capture sequences would imply that they would pass through Jupiter's harsh radiation environment. Therefor either the spacecraft should be equiped with severe radiation shielding material or after the capture sequences a perijove raise maneuver would be required. Both of these diminish the positive effects of an Io flyby upon entry. So from this came the motivation to investigate the possibilities of low-radiation capture trajectories.

[27] proved solar electric propulsion along an interplanetary trajectory combined with satellite-aided capture trajectories would not require an impulsive maneuver for planetary capture. The author further argued that missions to the Jovian system are generally equiped with low-thrust propulsion. Choosing low-thrust propulsion over high-thrust propulsion can significantly extend the lifetime of a mission. Or as an alternative, due to the mass savings that come along with low-thrust propulsion, the spacecraft's payload mass could be increased.

The preceding findings triggered the idea of combining low radiation satellite-aided capture trajectories with low-thrust propulsion. This would imply flybys with one, two or three of the Galilean moons (excluding Io), an impulsive orbit insertion maneuver at the perijove and low-thrust propulsion along the capture trajectory.
From the discussion presented in this section, the author created the following research problem, explained in the next section.

2.2.1 Research problem

The research problem of this thesis research is illustrated in Figure 2.2. A spacecraft coming from a heliocentric trajectory arrives at the Sphere Of Influence (SOI) of Jupiter when it is at its apocenter of the heliocentric Hohmann transfer trajectory. Therefore it arrives with $V_{apocenter} < V_{Jup}$. Thus the spacecraft enters Jupiter's SOI with a certain excess velocity. Assuming proper interplanetary trajectory optimization, the angle of the hyperbolic approach velocity upon entering the SOI of Jupiter, and the velocity vector of Jupiter is assumed to be close to 180°. The magnitude of the hyperbolic excess velocity corresponds to a heliocentric Hohmann transfer from Earth to Jupiter. The desired final conditions for the capture trajectory are taken as a highly eccentric long-period (200 days) orbit, avoiding the harsh radiation environment of Jupiter (Figure 2.2). A long period is desired because long-periodic orbits have significant orbital energy. This orbital energy can then be conserved during the scientific tour through the Jovian system.
The challenge now is to look for possible optimal flyby sequences with the Galilean moons, incorporating low-thrust, that match (or come in the vicinity of) both the initial and final conditions.

2.2.2 Research question

The research problem stated in the previous section will be investigated by answering the general research question:

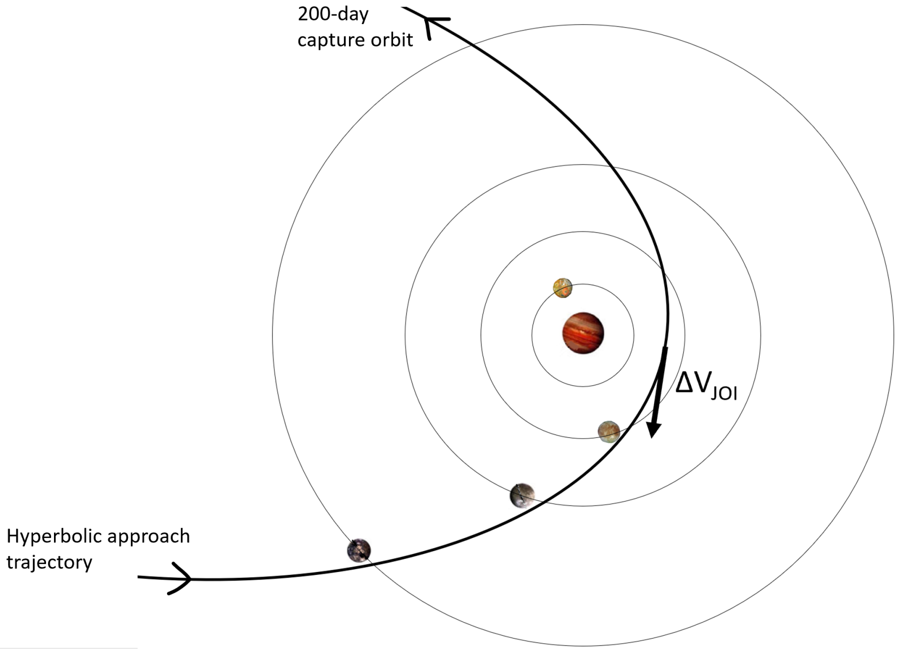

Figure 2.2: Illustration of a satellite-aided planetary capture trajectory in the Jovian system on a Jupiter-fixed reference frame. The schematic shows the approach hyperbolic trajectory as a result of a interplanetary Hohmann transfer from Earth, gravity assist with three of the Galilean moons, the Jupiter orbit insertion (JOI) and the 200 day periodic capture orbit.

What are the performance improvements of using low-radiation satellite-aided planetary capture trajectories in the Jovian system compared to a purely impulsive capture maneuver and how could these further be improved by incorporating low-thrust electric propulsion?

This research question can be split up into three sub-questions:

- What are the potential propellant mass savings for low-radiation satellite-aided planetary capture trajectories compared to purely impulsive capture trajectories?
- What are the potential propellant mass savings for low-radiation satellite-aided planetary capture trajectories when low-thrust propulsion along the trajectory is added?
- Which of the promising trajectories could be considered most useful with respect to mission panning?

The investigation of the first two sub-question will be done by searching for optimal trajectories in terms of ΔV and/or propellant mass without considering the required locations of the moons. This implies an investigation on a purely energetic basis.
The third sub-question takes the positions of the moons into account. By means of an ephemerides search valid dates of arriving in the Jovian system (or performing the first flyby) are to be identified. With these the author can reflect upon which sequences are most attractive, if possible at all.

2.2.3 Research procedure

To answer the research questions from the previous section the following research procedure was used. The author used this procedure to ensure that scientific knowledge would build up steadily towards the last step.

1. Construct the Tisserand graph for the Jovian system that both incorporates hyperbolic and elliptic planetocentric orbits. Validate this methodology by constructing the Tisserand graph for the Solar System and compare it with literature [26].

2. Identify optimal satellite-aided capture trajectories in the Tisserand graph for the Jovian system. Validate optima by reproducing results from literature [24].
3. Create an efficient method for including low-thrust legs in the Tisserand graph. Verification of the method is done by comparing the orbital radius with a reference trajectory.
4. Identify optimal low-thrust satellite-aided capture trajectories in the Tisserand graph for the Jovian system.
5. Create a robust method to solve the phasing problem by incorporating time-of-fight of the spacecraft.
6. Feed results from the phasing problem to an ephemerides search between 2023 and 2065 using a database [24].
7. Evaluate on findings with respect to the research questions.

Chapter 3

Tisserand graph

This chapter discusses the Tisserand parameter and Tisserand graph. It starts with a brief explanation of the origins of the Tisserand parameter. Section 3.2 explains the derivation of the Tisserand parameter from the Jacobi energy integral. The following section discusses the physics of gravity assists. Section 3.4 presents alternative techniques on how to obtain the Tisserand parameter. These will become useful in Subsection 3.5.1, on how to construct a so-called Tisserand graph and how it can be useful for designing multiple gravity assist trajectories. The chapter closes with a discussion on the limitations of a Tisserand graph and parameter in Subsection 3.5.3.

3.1 Tisserand parameter

The French astronomer Félix Tisserand first derived the Tisserand parameter in 1889 [29, p478]. Its purpose was to verify whether a comet observed from Earth is the same comet observed earlier but perturbed due to a close approach with one of the outer planets. By determining the Tisserand parameter for both observations and checking if the quantity was the same, he could conclude that both observations were the same comet. Nowadays, the Tisserand graph provides physical insights into the characteristics of possible flyby trajectories. Due to the fact that the Tisserand parameter is conserved in the three-body problem, it serves as an excellent tool to determine the effect of a close approach (e.g., gravity assist) on the orbit of a spacecraft. The following section presents the derivation of this Tisserand parameter.

3.2 Derivation

The Tisserand parameter derivation starts from the Jacobi energy integral. This is defined in the Circular-Restricted Three-body Problem (CR3BP) [29]. The CR3BP holds the following assumptions:

- The CR3BP consists out of three bodies with masses m_1, m_2 and m_3.
- Two of the masses (m_1 and m_2) are comparable and one (m_3) is considered negligible. This arranges the three masses in the following way: $m_1 \geq m_2 \gg m_3$.
- The only forces acting on the bodies are the mutual gravitational forces between the bodies.
- The two massive bodies (with masses m_1 and m_2) are moving in a circular orbit about their common barycenter with constant angular velocity n.

Following these assumptions, the Jacobi energy of the third body (with mass m_3) is derived as [29]:

$$C_J = 2G\left(\frac{m_1}{r_1} + \frac{m_2}{r_2}\right) + n^2\left(x'^2 + y'^2\right) - V'^2 \tag{3.1}$$

The usage of the prime in Equation 3.1 indicates that the (Cartesian) coordinates in x' and y' direction are defined in a rotating reference frame, with its origin at the barycenter. This rotating frame has the same angular velocity as the two massive bodies (with masses m_1 and m_2) around their mutual center of gravity. Due to this, they appear stationary in this rotating frame. The distances between the third and the first and the third and the second body are r_1 and r_2, respectively. V' is the third body's velocity, again, in this rotating frame. G is the universal gravitational constant. The Jacobi constant is derived in terms of inertial coordinates. This latter demands the above equation also to be expressed in inertial coordinates. For brevity, this process is not repeated here. Equation 3.2 presents the final result. For more information, the reader is referred to [20].

$$C_J = 2\frac{\mu_1}{r_1} + 2\frac{\mu_2}{r_2} + 2n(\dot{y}x - \dot{x}y) - V^2 \tag{3.2}$$

For convenience, the bodies' gravitational parameter, μ_i replaces the product of the universal gravitational constant with each of the masses of the bodies (e.g., $\mu_i = G * m_i$). Also, notice the dot above the coordinates, which indicates the first derivative with respect to time. As all coordinates are now inertial coordinates, the primes are omitted in Equation 3.2. One can also define the Jacobi constant in terms of Kepler elements. From the definition of Kepler elements, this essentially assumes that two-body dynamics can express the third body's motion. In other words, bodies m_2 and m_3 both move in a Kepler orbits around body m_1. Assuming the preceding makes the force exerted by body m_2 on body m_3 essentially a perturbation. Therefore, we change the assumption that the masses m_1 and m_2 are of comparable magnitude even if the mass of the second body m_2 is also negligible compared to the first body's mass m_1. When the distance between the second and third bodies is small enough, the second body's gravitational force acting on the third body will become bigger than that of the first body. So, as long as the distance between the second and third bodies is large, both the second and third bodies can be assumed to have a Kepler orbit around the first body. Kepler orbits are expressed in terms of Kepler elements. For more explanation on these elements, the reader is referred to [12]. The following equations substitute these Kepler elements in Equation 3.2. Note that Equation 3.3 up to Equation 3.6 represent orbital elements of the third body. Equation 3.7 represents the angular velocity of the second body around the first body when the mass m_2 is assumed to be negligible (which is also equal to the rotational rate of the rotating reference frame considered in Equation 3.1).

$$V^2 = \mu_1\left(\frac{2}{r_1} - \frac{1}{a}\right) \tag{3.3}$$

$$H_z = (\dot{y}x - \dot{x}y) \tag{3.4}$$

$$H_z = H\cos i \tag{3.5}$$

$$H = \sqrt{(1 - e^2)\, a\mu_1} \tag{3.6}$$

$$n = \sqrt{\frac{\mu_1}{r^3}} \tag{3.7}$$

The vis-viva equation (Equation 3.3) relates the velocity of the third body to its position r_1 and semi-major axis a. All with respect to the first body. The specific angular momentum H is given by Equations 3.4, 3.5 and 3.6. The subscript z corresponds to the z-component of this quantity. Other orbital elements used are the inclination i of the third body (measured with respect to the second body's orbital plane), e is the eccentricity and r refers to the second body's orbital radius. After substituting the above equations in Equation 3.2 the result is the following:

$$C_J = \frac{\mu_1}{a} + 2n\sqrt{(1 - e^2)\, a\mu_1}\cos i + 2\frac{\mu_2}{r_2} \tag{3.8}$$

As mentioned before, considering a significant distance (r_2) between the third and second body, the last term on the right-hand side becomes negligible. From literature [29], it is known that a distance equal to the radius of the SOI [12] is large enough to make this assumption valid. The equation for determining this sphere of influence is given by:

$$R_{SOI} = a\left(\frac{m_2}{m_1}\right)^{2/5} \tag{3.9}$$

where a is the semi-major axis of the second body around the first. Applying the foregoing to Equation 3.8, the equation reduces to Equation 3.10. Here, the notation T_p is introduced as the Tisserand parameter. Because the Tisserand parameter is derived from the Jacobi energy integral, it in general is a measure of the three-body energy of the third body. From [12] it is known that three-body orbital energy is conserved in one three-body system. So even a close approach with the second body would not change this quantity (determined when the third body is out of the SOI of the second body).

$$T_p = \frac{\mu_1}{a} + 2n\sqrt{(1-e^2)\,a\mu_1}\cos i \tag{3.10}$$

3.3 Gravity assist

The previous section shows that the Tisserand parameter is conserved within the CR3BP after a close encounter with a secondary body. Such a close encounter is often referred to in this thesis report as a gravity assist or flyby. This section will discuss the physical characteristics of an unpowered (purely ballistic) gravity-assist trajectory. A ballistic gravity assist only considers gravitational attraction, thus ruling out all other forces such as atmospheric effects or rocket thrusting. This latter essentially means that a Kepler orbit can describe such a trajectory. A gravity-assist trajectory is a hyperbolic trajectory around the flyby body. A schematic of such an orbit is presented in Figure 3.1 considering a planet as a flyby body.

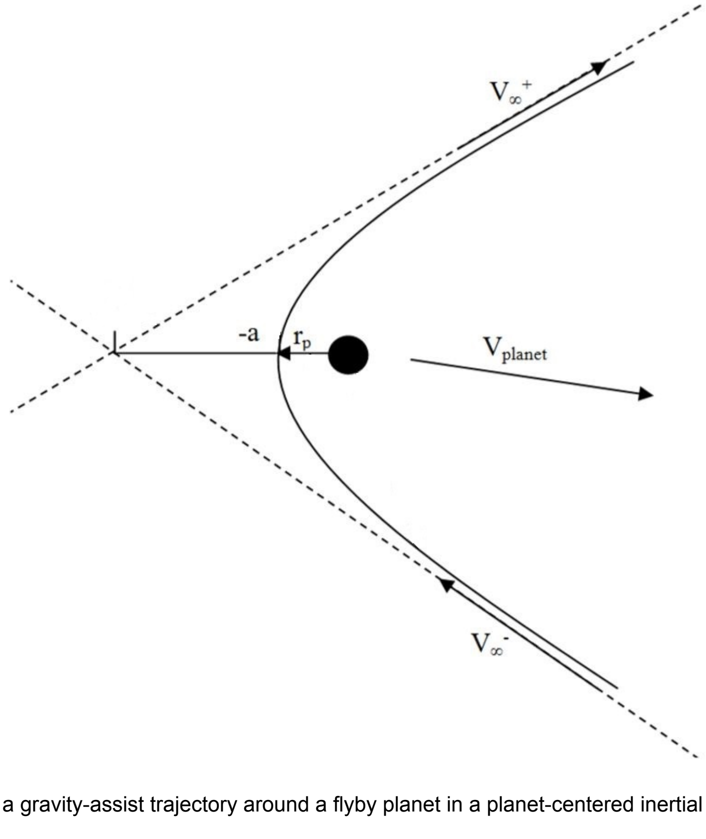

Figure 3.1: Schematic of a gravity-assist trajectory around a flyby planet in a planet-centered inertial reference frame [10].

In this thesis report, the flyby body will mostly be a moon (natural satellite). Still, a planet orbiting the Sun is used here to explain the physics of gravity-assist trajectories. In literature, one often refers it to as the secondary orbiting the primary or central body in the CR3BP. For the gravity-assist trajectory to be a hyperbola, the planet should move in a straight linear motion. Considering the time that the spacecraft is within the SOI of the flyby planet and comparing it with the orbital period of the planet's heliocentric orbit, this is considered a valid assumption. Due to this latter, one can assume a gravity assist as an instantaneous velocity change applied to the heliocentric trajectory. From Figure 3.1, one can create a vector diagram that further illustrates the effects of gravity assists on the velocity. Figure 3.2 shows this vector diagram.

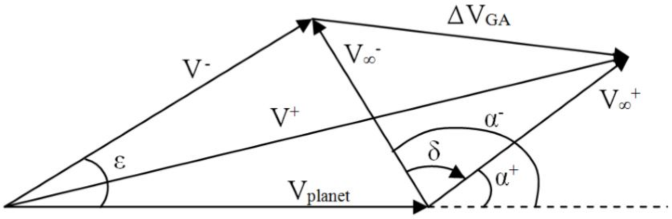

Figure 3.2: Vector diagram of the velocity vectors to be considered for gravity assist trajectories [10].

In this figure, the quantities V^- and V^+ represent the spacecraft's velocities with respect to the Sun, respectively before and after the flyby. In both Figure 3.1 and Figure 3.2, V_{planet} is the velocity vector of the planet with respect to the Sun, V_∞^- and V_∞^+ the hyperbolic excess velocity vectors of the spacecraft before and after the flyby (infinity far away from the planet, i.e., effectively at the sphere of influence of the planet). These are defined with respect to the flyby planet. The pump angles $\alpha^{+/-}$ are measured between the velocity of the planet and the velocities $V_\infty^{+/-}$.

Now considering this pump angle, when $\alpha^+ = 0$, the velocity of the spacecraft w.r.t. the Sun (e.g. V^+) is maximal and visa versa when $\alpha^+ = \pi$, V^+ is minimal. Therefore, both angles $\alpha^{+/-}$ indicate the orbital energy with respect to the Sun. The effect of a gravity assist is generally a change in the pump angle from α^- to α^+ by a quantity δ, which is the turning/bending angle ($\alpha^+ = \alpha^- - \delta$). The turning angle often expresses the ΔV as a result of the gravity assist (ΔV_{GA} in Figure 3.2). Combining this with the property of a hyperbolic trajectory that the velocities $V_\infty^{+/-}$ are the same, one can calculate ΔV_{GA} using the following relation.

$$\Delta V_{GA} = 2\sin(\delta/2)V_\infty \tag{3.11}$$

The vis-viva equation (Equation 3.3) determines the velocity with respect to the Sun before the flyby. The planet's orbital radius gives the position vector r. The velocity of the spacecraft after the gravity assists is calculated using the cosine rule:

$$\left(V^+\right)^2 = V_{\text{planet}}^2 + V_\infty^2 + 2V_{\text{planet}}V_\infty \cos\left(\alpha^+\right) \tag{3.12}$$

Note that Equation 3.12 also holds for the situation before the gravity assist (V_∞^-), by substituting the pump angle before the flyby (α^-). Now to know the pump angle after the flyby, the turning angle needs to be determined. This turning angle is related to the pericenter radius, the velocities(s) $V_\infty^{+/-}$, and the gravitational parameter of the flyby planet μ_p.

$$\sin\delta/2 = \frac{1}{1+\frac{V_\infty^2}{\frac{\mu}{r_p}}} \tag{3.13}$$

Then the hyperbolic excess velocity V_∞ is determined. Up to this point, no assumptions on three-dimensional or two-dimensional geometry were taken. Throughout this thesis report, only two-dimensional flybys (no relative inclination) are considered. The three-dimensional case further complicates the problem geometrically and is left for future recommendations. For the two-dimensional case, the velocity V_∞ is calculated using the following relation:

$$V_\infty^2 = V_{planet}^2 + (V^-)^2 - 2V_{planet}V^- \cos\gamma \tag{3.14}$$

Equation 3.14 introduces the flight path angle γ (ϵ in Figure 3.2). This angle is determined before the gravity assist with the angular momentum H, the orbital radius of the flyby planet r_f and the heliocentric velocity V^-:

$$\cos\gamma = \frac{H}{r_f V^-} \tag{3.15}$$

This concludes that the entire (two-dimensional) hyperbolic flyby trajectory can be expressed by Equations 3.12 up to 3.15.

3.4 Variations of the Tisserand parameter

This section introduces three different ways to calculate the Tisserand parameter (apart from the original one given by Equation 3.10). These will become useful when constructing the so-called Tisserand graph in Section 3.5.

3.4.1 Orbital energy and pericenter radius

A handy set of parameters to calculate the Tisserand parameter is the orbital energy and pericenter radius. When using the semi-major axis and eccentricity, the resulting Tisserand graph shows asymptotic behavior (semi-major axis goes to infinity) around $e = 1$, which is challenging to interpret. The advantage of using orbital energy and pericenter radius is that they are both defined for every Kepler orbit type. Note that the pericenter radius is given by Equation 3.16 and the orbital energy by Equation 3.17. After substitution of these two equations in Equation 3.10 the Tisserand parameter is expressed in terms of orbital energy and pericenter radius:

$$r_p = a(1-e) \tag{3.16}$$

$$E = \frac{-\mu}{2a} \tag{3.17}$$

$$T_p = -2E + 2n\sqrt{2r_p^2 E + 2r_p\mu}\cos i \tag{3.18}$$

Note that Equation 3.18 still considers the inclination. For the purely two-dimensional case, this would be equal to zero and the resulting cosine would be equal to one.

3.4.2 Orbital energy and angular momentum

From the derivation of the Tisserand parameter, it is known that the second term on the right-hand side is the z-component of the angular momentum (Equations 3.4 and 3.5). Therefore one can express the Tisserand parameter in terms of energy and angular momentum as shown in Equation 3.19. Again, note the presence of the inclination in the equation.

$$T_p = -2E + 2nH\cos i \tag{3.19}$$

3.4.3 Hyperbolic excess velocity

The hyperbolic excess velocities $V_\infty^{+/-}$, similar to the Tisserand parameter, are conserved during a purely ballistic gravity-assist trajectory. Moreover, literature [13] has proven that it is possible to construct a Tisserand graph without the use of the Tisserand parameter. Moreover, it suggests that the hyperbolic excess velocity and the Tisserand parameters are equivalent. Consider Equation 3.14, the velocity of the planet around the Sun is assumed constant and equal to the circular velocity (Section 3.2). This circular velocity is given by Equation 3.20

with μ_s the gravitational parameter of the Sun and r the orbital radius of the planet (for circular orbits, equal to the semi-major axis).

$$V_{\text{planet}}^2 = \frac{\mu_s}{r} \tag{3.20}$$

Substituting the above equation for the circular velocity, the vis-viva equation for the heliocentric velocity before the flyby V^- and the equation for the flightpath angle γ (e.g. Equations 3.20, 3.3 and 3.15) in Equation 3.14 for the hyperbolic excess velocity, one can rewrite this to the following new equation for the angular momentum:

$$H = -\left(V_\infty^2 - \frac{3\mu_1}{r} + \frac{\mu_1}{a}\right)\frac{1}{2\cos i}\sqrt{\frac{r^3}{\mu_1}} \tag{3.21}$$

Note that the constant angular velocity of the planet around the Sun is given by Equation 3.7. Now combining this equation with Equations 3.17 and 3.18 gives a new equation (3.22) for the Tisserand parameter in terms of hyperbolic excess velocity. An important consideration of this equation is that although the inclination is not present in the equation, it holds for all inclinations.

$$T_p = \frac{3\mu_1}{R_2} - V_\infty^2 \tag{3.22}$$

3.5 Tisserand graph

The previous sections showed that there are multiple ways to express or calculate the Tisserand parameter. These are useful when constructing the actual Tisserand graph. Because the Tisserand parameter is constant throughout a gravity assist, it is possible to build a graph considering multiple flyby planets and hyperbolic excess velocities that is very useful in designing multiple gravity-assist trajectories. First, the algorithm of constructing the Tisserand graph is explained, then the Tisserand graph of the outer Solar System is shown with an explanation of how it is used.

3.5.1 Construction

The inputs of a Tisserand graph are the pump angle α, the hyperbolic excess velocity V_∞ and the physical characteristics of the flyby bodies and central body (gravitational parameter, orbital radius and physical radius). Only the two-dimensional (coplanar) Tisserand graph is discussed here, so no inclinations are considered. A single point on the Tisserand graph is created in the following steps:

1. Determine the spacecraft's velocity with respect to the central body at the orbital radius of the flyby body Equation 3.12.
2. Use the vis-viva equation (3.3) to obtain the semi-major axis.
3. Calculate the orbital energy using Equation 3.17.
4. Calculate the Tisserand parameter using Equation 3.22.
5. Determine the angular momentum using Equation 3.19.
6. Calculate eccentricity by solving Equation 3.10.
7. Calculate the pericenter radius using Equation 3.16.

As said at the beginning of this subsection, the inputs of a Tisserand graph (apart from the physical characteristics of the central body and flyby bodies) are the pump angle and the hyperbolic excess velocity. For a full graph instead of a single point, a range for the pump angle from 0 to 180°is taken and for the hyperbolic excess velocities V_∞ most often steps of one km/s are taken. Then the algorithm is repeated for each hyperbolic excess velocity and every flyby body. In theory, there is no bound for the maximum hyperbolic excess velocity, but the effect of a single flyby will become smaller for large hyperbolic excess velocities. Moreover, large values for the hyperbolic excess velocity will result in a negative angular velocity. A negative angular velocity means a retrograde orbit around the central body. Considering the subject of this thesis report, retrograde orbits are not useful and thus excluded. The additional benefit of this is that the graph becomes clearer.

A full Tisserand graph consists of multiple contour lines representing a different value of hyperbolic excess velocity and flyby body. Figure 3.3 presents such a Tisserand graph of the outer Solar System.

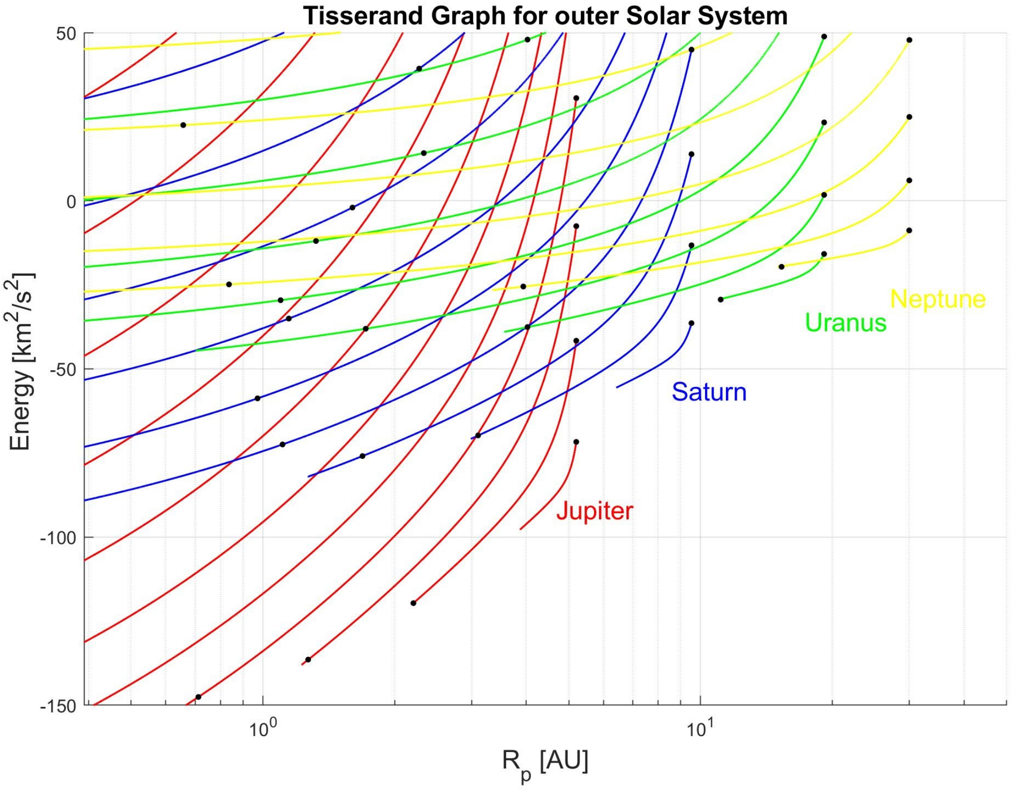

Figure 3.3: Tisserand graph of the outer Solar System. Thick marks on the contour lines illustrate the effect of a single gravity assist with the planet considered taking into account the maximum bending angle as a result of the minimum flyby altitude (six Jupiter radii for Jupiter, three Saturn radii for Saturn, and two planetary radii for Uranus and Neptune). Increments for the hyperbolic excess velocity are set to 2 km/s increasing from lower right to upper left.

The algorithm of the Tisserand graph was implemented in C++, tested for the Solar System and compared with results from literature [12, p.46] in Section 9.1. This is shown in a later chapter on verification and validation. Both results fully overlap and therefore is the algorithm considered validated. Then the physical characteristics of the Jovian system are implemented in the algorithm, taking into account the four Galilean moons (Io, Europe, Ganymede and Callisto) and Jupiter. Running the algorithm for this system resulted in the Tisserand graph presented in Figure 3.4. Other variations of the Tisserand graph also exist. For example, the orbital period or apocenter radius can be put on the y-axis instead of the orbital energy. This implies the same algorithm as outlined above but with an additional step of calculating the orbital period using Equation 3.23 or Equation 3.24. The downside of these versions of the Tisserand graph is that they can only be used for orbits that are closed around the central body (elliptical). Regarding the thesis topic in this report that treats the transition from open to closed orbits, these are less useful and therefore excluded from this

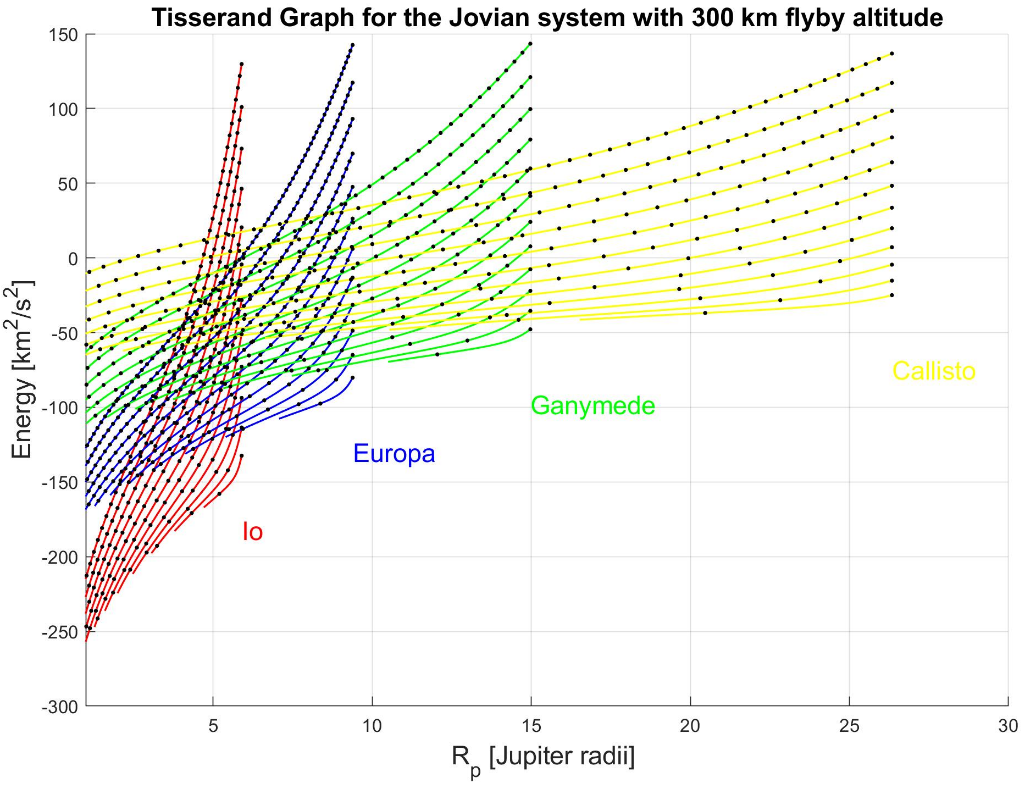

Figure 3.4: A Tisserand graph of the Jovian system taking into account the four large Galilean moons. The spacing between the tick marks illustrates a single flyby's effect with that particular moon, with that specific excess velocity at a flyby altitude of 300 km. Increments for the hyperbolic excess velocity are set to 1 km/s increasing from lower right to upper left.

report.

$$T = 2\pi\sqrt{\frac{a^3}{\mu}} = \pi\sqrt{\frac{\mu^2}{2E^3}} \tag{3.23}$$

$$r_a = a(1+e) \tag{3.24}$$

3.5.2 Using the Tisserand graph

A Tisserand graph is a useful tool for designing multiple gravity-assist trajectories. How this works precisely will be explained in this section employing an Earth-Venus-Earth-Earth-Jupiter or short EVEEJ trajectory. For this, a new Tisserand graph for the planets Venus up to Jupiter is created and shown in Figure 3.5.

By observing the Tisserand graph, one notices that some of Earth's contours intersect with other planets' contours. Such an intersection suggests that a spacecraft with that particular orbit (orbital energy and pericenter radius) can reach that particular planet's orbit. This makes it possible for the spacecraft to perform a flyby with that planet (considering the hyperbolic excess velocity specified by the contour of that planet). Each flyby (with minimum flyby radius) alters the orbit of the spacecraft to reach other planets without the use of propellant. Figure 3.6 illustrates this for the EVEEJ sequence.

Figure 3.6 shows the contour lines used for this particular sequence. The arrows in the graph indicate the orbital changes as a result of a single flyby and the cross marks the initial point. First, performing a flyby with Earth at a hyperbolic excess velocity of 3 km/s to reach the orbit of Venus. Then a flyby with Venus at V_∞ of 5 km/s to reach the orbit of Earth again. This does not violate energy conservation in the three-body problem since the spacecraft switches between two three-body systems and thus exchanges energy with another secondary (e.g.

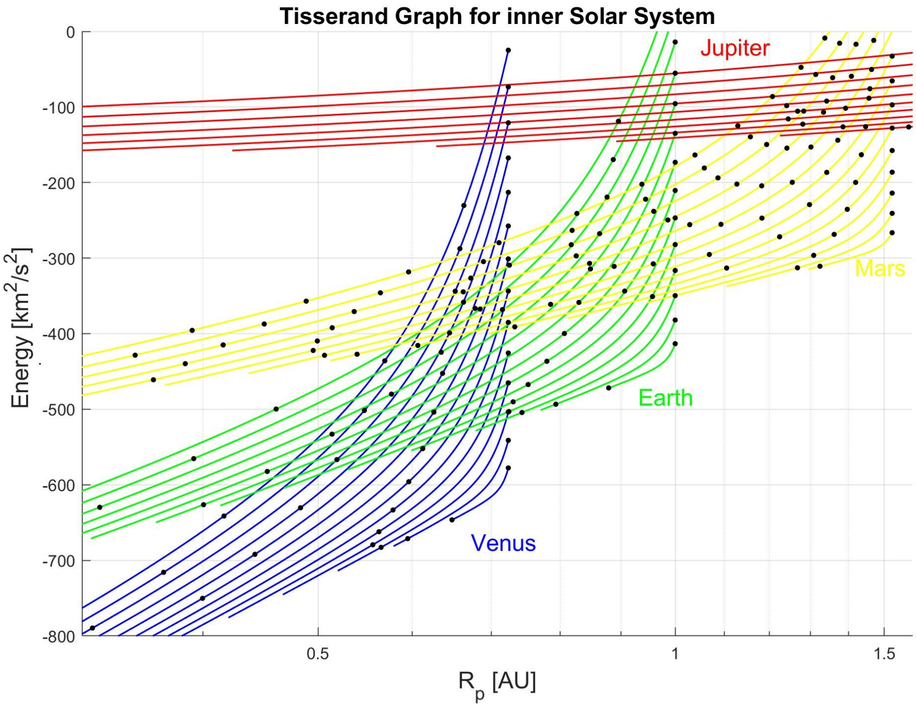

Figure 3.5: A Tisserand graph of planets Venus up to Jupiter. Thick marks on the contour lines illustrate the effect of a single gravity assist with the planet considered taking into account the maximum bending angle resulting from the minimum flyby altitude (200 km for Venus and Mars, 500 km for Earth and six Jovian radii for Jupiter). Increments for the hyperbolic excess velocity are set to 1 km/s.

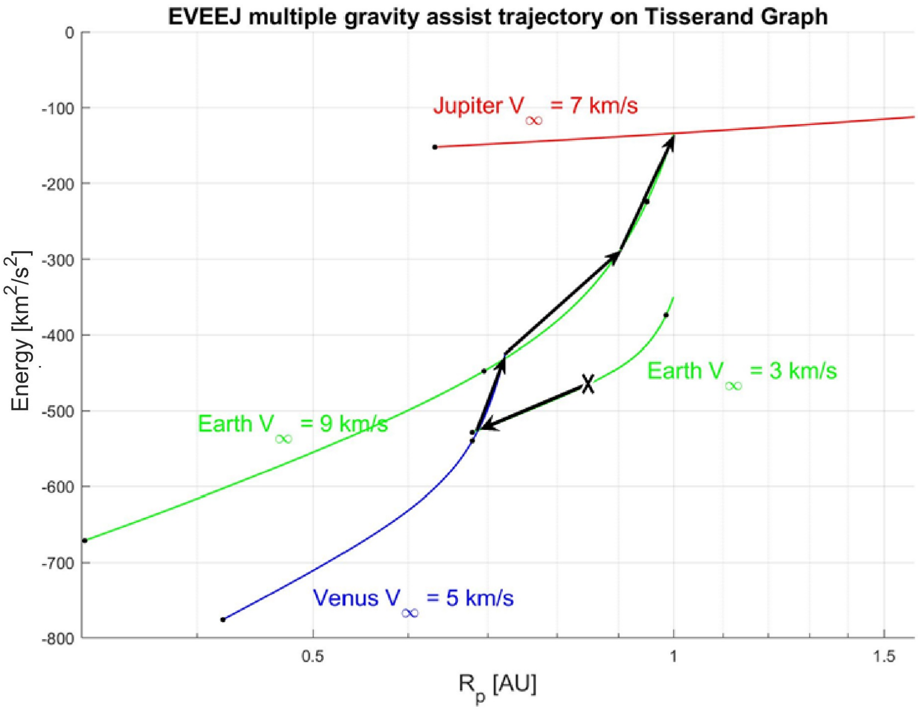

Figure 3.6: An EVEEJ multiple gravity-assist trajectory to the Jovian system. Cross indicates the initial point in Tisserand graph after launch from Earth.

planet). The spacecraft then performs two more flybys at a V_∞ of 9 km/s to reach the Jovian system at a V_∞ of 7 km/s.

3.5.3 Limitations

In the previous sections, both the Tisserand parameter and Tisserand graph have been derived and introduced. While doing so, several assumptions were made that influence the usage of the Tisserand graph. It is vital for the following chapters that the reader is aware of these as it will be reflected upon.

All Tisserand graphs considered so far do not include any form of thrust. The trajectories considered are purely ballistic, no intermediate maneuvers are considered. However, it has been proven [23] that including such an intermediate maneuver could significantly reduce the total mission cost. Powered gravity assists (Oberth maneuver [12, p.43]) are not considered. These change the V_∞ during the gravity assist what could positively affect the overall mission performance. However, the gains from these powered flyby's are much smaller than those resulting from intermediate maneuvers. From the Tisserand graph, one observes the change in orbital energy and pericenter radius due to a flyby. The Tisserand graph however does not give any insight into the moons' location, also called the phasing, which will be discussed in a later chapter. This could mean that a particular sequence only occurs once in a very long time but is possible from a purely energetic perspective. It is essential to consider that the lines on the Tisserand graphs shown so far illustrate how the Tisserand parameter can be used to construct multiple gravity-assist trajectories. In reality, a point that lies in between the lines represents an orbit with a specific V_∞ with respect to a particular flyby body. Of course, if the pericenter radius lies beyond the flyby body's orbital radius, the spacecraft can not perform a flyby with it.

Chapter 4

Capture trajectories in the Tisserand graph

This chapter investigates the possibilities of ballistic satellite-aided planetary capture in the Jovian system. Starting, a brief description of the basic principle of capturing a spacecraft into a closed orbit is given in Section 4.1. Then Section 4.2 explains the optimization routine used to find ballistic capture trajectories on the Tisserand graph. This holds the creation of a fitness function, choice of the optimization algorithm, and the algorithm's tuning. In Section 4.3 the results of single-, double- and triple-aided capture trajectories are presented and discussed. The chapter closes with some concluding remarks with respect to the result and methodology of this chapter.

4.1 Capturing a spacecraft

When a spacecraft arrives at the Jovian system with a hyperbolic excess velocity and orbital energy ($E > 0$) resulting from the foregoing heliocentric trajectory, it must lower its orbital energy towards the closed orbit (elliptic) regime ($E < 0$). This fundamental difference in orbital energy is illustrated in Figure 4.1.

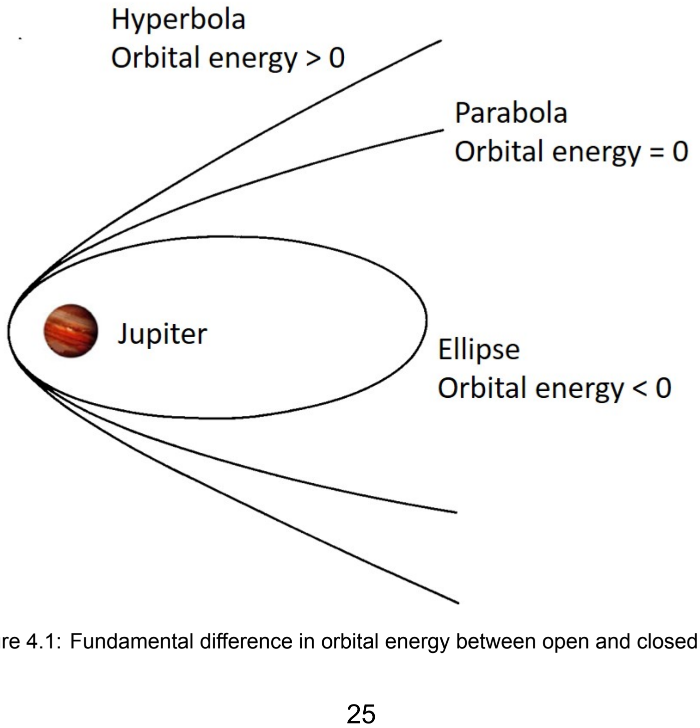

Figure 4.1: Fundamental difference in orbital energy between open and closed orbits.

From the three-body problem, [12, p27] it is known that a purely ballistic permanent capture around a planet in a Sun-planet-spacecraft three-body system is impossible. The reason for this is that almost every particle will pass arbitrary close to its initial position in phase-space. Therefore it will, at some point, escape the target planet again. For that reason, some sort of mechanism is required to close the orbit of the spacecraft permanently. The most straightforward way to do this is to perform an impulsive rocket thrusting or JOI maneuver (optimally performed at perijove of the hyperbolic trajectory), which closes the orbit and captures the spacecraft around Jupiter. However, this rocket thrusting requires a significant amount of propellant mass compared to the spacecraft's total mass. By performing a (sequence of) gravity assist(s) with one (or more of) the massive moon(s) of Jupiter, the orbital energy of the spacecraft could already be lowered such that the total propellant mass required for the JOI would be less. The greatest advantage of this is that these mass savings could be used for extra scientific payload, or for mission extensions.

4.2 Identifying capture trajectories in Tisserand graph

This section explains the methodology used to find the best satellite-aided planetary capture trajectories in the Jovian system. It starts with creating a fitness function that quantifies to what extent a particular trajectory is a good candidate to be used as satellite-aided capture trajectory. The fitness function uses the methodologies of the Tisserand parameter. From previous chapter it is known that the Tisserand parameter and moreover the Tisserand graph is a good tool for identifying multiple gravity assist trajectories. Earlier research [18],[16] uses a more simple patched conics approach without specifically using the Tisserand parameter. Then Subsection 4.2.4 briefly explains the choice of the optimization algorithm. This is further extended in Subsection 4.2.6 where the optimizer's tuning settings are discussed. A good selection of these tuning settings ensures fast convergence behavior of the optimizer, which is beneficial in terms of calculation time.

4.2.1 Fitness function

A fitness function or objective function summarizes to what extent a particular trajectory achieves a specific set of goals. Concerning satellite-aided planetary capture, this depends on the preferred captured orbit. For ensuring a long scientific lifetime of a mission to the Jovian system, it is beneficial to preserve as much orbital energy as possible. From literature [12] it becomes clear that a highly eccentric and long-periodic orbit (200 days) are satisfactory for this. Such an orbit has considerable orbital energy that can be preserved during the scientific part of the mission. In theory, there is no limit on the captured orbit period; however, longer than 200 days could result in perturbations acting on the spacecraft becoming relatively too large compared to Jupiter's gravitational acceleration and too long times of flights. Alternatively, it is also possible to capture the spacecraft into a shorter-period orbit. However, this requires a trade-off between reducing the flight time against increasing the JOI velocity increment (e.g., ΔV_{JOI}). As explained earlier, satellite-aided planetary capture uses flyby(s) with one or more of Jupiter's massive moons (e.g., Galilean moons) combined with an impulsive JOI to lower the spacecraft's orbital energy and close the orbit around Jupiter. These are steps towards the satisfactory capture orbit. To investigate the possibilities of this, the following objective function is created.

1. Obtain the initial perijove of the hyperbolic approach trajectory from the parameter vector. Together with the initial orbital energy, this makes the first point on the Tisserand graph.

2. Calculate the initial eccentricity using Equation 3.16.

3. Obtain the flyby moon from the preset flyby sequence. If the preset sequence demands a JOI, proceed to step 12.

4. Calculate the velocity V^- with respect to Jupiter using the vis-viva equation.

5. Calculate the mean angular motion of the flyby moon around Jupiter using Equation 3.7.
6. Determine the Tisserand parameter for the initial point (orbital energy and perijove) on the Tisserand graph using Equation 3.18.
7. Using the Tisserand parameter, calculate the angular momentum with Equation 3.19.
8. Obtain the hyperbolic excess velocity with respect to the flyby moon using Equation 3.14.
9. Obtain the minimum flyby altitude from the parameter vector and use it to calculate the turning angle with Equation 3.13.
10. Calculate the increment in orbital energy for this turning angle.
11. Update the orbital energy, semi-major axis, eccentricity and perijove. Proceed to step 15.
12. Calculate the velocity at perijove V_p using the vis-viva equation.
13. Obtain ΔV_{JOI} from the parameter vector; subtract ΔV_{JOI} from V_p.
14. Update the orbital energy using the vis-viva equation, semi-major using Equation 3.17 and eccentricity using Equation 3.16.
15. Repeat steps 2 up to 14 for the whole preset flyby sequence.

After the sequence is completed through the algorithm above, the fitness as a result of the parameter vector is defined by the last parameter in the parameter vector, that is ΔV_{JOI} plus the absolute difference in orbital energy from that of the desired 200-day periodic captured orbit. (Equation 4.1). A weight factor W of 1000 was added to ensure faster convergence. Due to the order of magnitude of the orbital energy compared to that of ΔV_{JOI} no weighting for the absolute difference in orbital energy was needed.

$$J = \Delta V_{JOI} * W + \Delta E \tag{4.1}$$

The fitness function in Equation 4.1 is the basic fitness function. It does not yet hold penalties. Penalties indicate that a particular set of parameters results in a faulty region in the solution space. Two cases for which a penalty is added are as follows:

P_{fb} A first penalty (flyby penalty) is added when the parameter vector leads to a point on the Tisserand graph where a subsequent flyby with the flyby moon in the preset sequence is not possible. This occurs if the spacecraft's perijove (with respect to Jupiter) is larger than the orbital radius of that moon. Because the perijove is the minimum radius with respect to Jupiter it is impossible for the spacecraft to reach the orbit of that particular moon. Therefore the results following would be undesired. The penalty is added and the algorithm above is broken to prevent the optimization to use the corresponding settings for the decision vector again.

P_{rad} A second penalty is given when the resulting perijove of the spacecraft reaches the harsh radiation environment of Jupiter as a result of a flyby (radiation penalty). Lower radiation capture trajectories have a minimum perijove of eight Jupiter radii [18]. Being closer to Jupiter results in a more intense radiation dose that could harm scientific equipment or increase spacecraft's mass due to radiation shielding material. Due to the orbital radius of Io, this penalty excludes possible flybys with Io.

For both cases the penalties are equal to 10^{12} and are added to the fitness function in Equation 4.1, and arrive at the complete fitness function:

$$J = \Delta V_{JOI} * W + \Delta E + P_{fb} + P_{rad} \tag{4.2}$$

4.2.2 Initial conditions

In the algorithm described above, the flyby sequence is preset. A previous version where this was not the case was also examined. However, this extended the search domain for the parameter vector to such an extent that the solutions found for a particular seed number initiation did not overlap with that of another seed number. Furthermore, the algorithm required too much function evaluations to get to a converged solution. Therefore, the author chose to preset flyby sequences. This gave the benefits that the potential gains for each possible flyby sequence could be investigated separately. The initial orbital energy is a result of a foregoing heliocentric trajectory. This thesis research assumed a direct Hohmann transfer from Earth. Figure 4.2 gives a schematic of such a trajectory. By assuming coplanar, circular planetary orbits, the spacecraft arrives at Jupiter with a relative velocity of 5.65 km/s. This relative velocity is equal to the hyperbolic excess velocity in the Jovian system. From this follows the initial condition for orbital energy. Equation 4.3 calculates the semi-major axis of this hyperbolic approach trajectory. Then Equation 4.3 gives the initial orbital energy as 16.347 $\mathrm{km}^2/\mathrm{s}^2$. Note the minus sign in Equation 4.3 as a result of the negative semi-major axis of a hyperbolic trajectory.

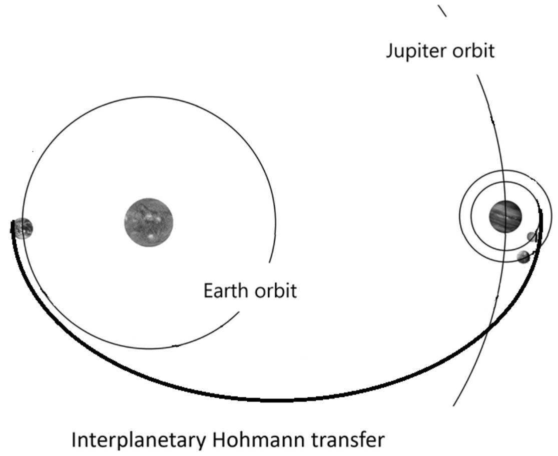

Figure 4.2: Illustration of interplanetary Hohmann transfer.

$$V_\infty = \sqrt{\frac{-\mu}{a}} \tag{4.3}$$

Another version was developed that did not preset the initial orbital energy but instead let the optimizer chose a value within a range of 13.005 and 19.006 $\mathrm{km}^2/\mathrm{s}^2$. The motivation for this was to investigate if an initial orbital energy higher than the nominal value could result in more effective flybys with particular moons, resulting in a larger orbital energy increment. The result was that all solutions converged towards the lower limit of the range. The author argued that this only increased the required function evaluations without any scientific benefits. Therefore, the initial orbital energy was preset to 16.347 $\mathrm{km}^2/\mathrm{s}^2$ which is the nominal value resulting from a foregoing interplanetary Hohmann transfer from Earth. From the 200 day period for the desired capture orbit, the semi-major axis a_c was calculated using Equation 3.23 and Equation 3.17 gives a desired orbital energy of -6.4251 $\mathrm{km}^2/\mathrm{s}^2$. Note this is a final condition, but it seemed convenient for the author to include it here.

4.2.3 Parameter vector

The parameter vector contains the initial perijove radius of the hyperbolic approach trajectory in the Jovian system, the flyby altitudes for each flyby and the ΔV_{JOI}. For completeness, the parameter vector is illustrated here for a triple-aided sequence:

$$\bar{X}_p = \{R_p, h_1, h_2, h_3, \Delta V_{JOI}\} \tag{4.4}$$

The search domain for the initial perijove is set to $8R_J$ to $30R_J$ to ensure that it includes the orbital radius of Europa ($9.39R_J$), Ganymede ($14.97R_J$) and Callisto ($26.34R_J$). This excludes Io, but the section on penalties had already explained this. The flyby altitudes are allowed to vary between a range of 500 and 4000 km. The motivation for this 500 km minimum flyby altitude is because of navigational concerns and ephemeride errors. As the Galilean moons orbit Jupiter at high velocity, an error in ephemerides at which the flyby is executed results in a deviation from the nominal flyby altitude. This error is then propagated towards following flybys, resulting in even larger errors. Therefore the minimum flyby altitude is set at 500 km, where the effects of these deviations are relatively small (acceptable). It is expected that optimal solutions will approach the lower limit of this flyby altitude because of the orbital energy increment dependency on the minimum flyby radius. However, it will become clear in the discussion on the results that it is of additional value to investigate the possibility of flyby altitudes other than the minimum. The domain for ΔV_{JOI} is set from zero to 1100 m/s. The lower limit of this is quite straightforward. The upper limit lies close to the required JOI when no flybys are used and the spacecraft is only captured by means of the JOI itself (i.e. 1069 m/s).

4.2.4 Optimization algorithm

This subsection explains the motivation for the choice of the optimization algorithm. It will not give an overview of all possible optimization algorithms. For more information on this the reader is referred to [12].

The optimization intends to find a global optimum in terms of required ΔV_{JOI} to insert the spacecraft in a desired (highly eccentric 200-days periodic orbit) as a result of the initial perijove radius of the hyperbolic approach trajectory and flyby altitudes. One could use a local optimizer when the search space is smooth, possibly even combined with multi-start methods. However, for a gravity-assist problem in the Tisserand graph, the search space is considered irregular [10] because the problem is of a higher order (e.g., more extended parameter vector). Therefore, global optimization is deemed the best choice.

A simple Monte Carlo or grid search optimizer requires an enormous sample size to arrive at a reliable optimum. This generally results in investigating parts of the search space that are not interesting, leading to unnecessary large numbers of function evaluations. Therefore the author chooses not to use this method for conducting the research.

Considering the (meta)heuristic methods with global search methods, the choice is made by considering availability and previous experiences with the algorithm. To cut down the time spent on programming and testing, the Parallel Global Multi-objective Optimizer (PaGMO) toolbox [2] was chosen. It holds most of the modern metaheuristic algorithms such as Differential Evolution (DE), Particle Swarm Optimization (PSO), Genetic Algorithm (GA) and Simulated Annaling (SA). Earlier research [22] concluded that DE outperforms PSO and GA algorithms. SA is, in most cases, not considered due to the fact that it does not handle widely varying solution spaces very well and often, because of this, does not converge towards the correct global optimum. Therefore DE is considered the best choice.

4.2.5 Differential Evolution

The previous section explained the choice for DE algorithm. Now the working principle of the DE is explained. DE is a population-based (meta-)heuristic optimization algorithm. A heuristic method uses the knowledge available from previous objective function evaluations to direct the parameter vector where to look in the search space for creating new populations. Because the algorithm uses a random component to make new populations, it is called a meta-heuristic algorithm. Furthermore, it is population-based because it uses a set of trail solutions or, in a word, a population.

The DE algorithm originates from [25] where concepts of evolution theory were used to solve the fitting Chebychev polynomials problem. Figure 4.3 gives an illustration of the DE algorithm through a flowchart. The terms used here originate from evolution theory. NP is the size of the population and P the population itself.

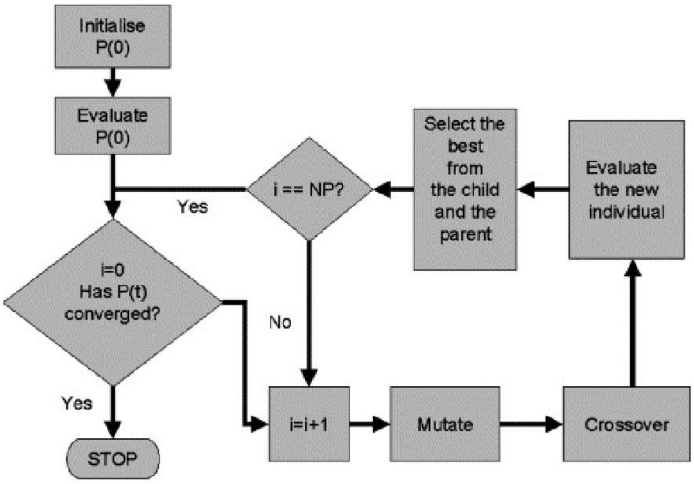

Figure 4.3: Flowchart of a simple DE algorithm [15].

The DE algorithm's essential steps illustrated in Figure 4.3 are the mutation, crossover, and selection. Therefore a brief explanation on these follows. One last thing to note is that the optimization problem is always a minimization problem. Optimizations that require maximization of the fitness can simply invert the fitness function ($Fitness^{-1}$).

Mutation

The mutation step creates a mutant or a donor vector using a base vector and a number of difference pairs. The following equation gives a random method with one difference pair. Ten different mutation methods will be tested in Subsection 4.2.6.

$$V_{i,G} = X_{r_1^i,G} + F\left(X_{r_2^i,G} - X_{r_3^i,G}\right) \tag{4.5}$$

In Equation 4.5 X is a decision vector of the population. The three X, indicated by the r subscript, are mutually exclusive random samples of the population. G indicates the generation number. The subscript i of X_i indicates the parent vector for which the mutant is made. Lastly, F is the mutation scale factor, a tuning parameter that generally has a large influence on the DE algorithm's overall performance. Typical values for the scale factor F are within the interval $[0.4, 1.0]$.

In earlier research [23] it was concluded that using the best-known decision vector instead of $X_{r_1^i}$ in Equation 4.5 can be beneficial. However, a strategy based on the best-known solution generally converges towards a sub-optimum rather than the overall optimum. Therefore, the random strategy is preferred over the best-known solution strategy.

Crossover

The mutant vector explained above needs to be combined with the parent vector to obtain the trail vector. The selection process then uses this trail vector. The notation of the trial vector is $U_{i,G}$. Both in PaGMO and the DE algorithm's original paper, two strategies for the crossover are considered. The first one is exponential crossover, which combines part of the mutant vector with the parent vector. The second strategy is binomial crossover, where every single element of the mutant vector has a probability of being placed in the trail vector. The difference between the two is illustrated in Figure 4.4. From [14] it is known that the binomial crossover should be at least as good as the exponential crossover, in some cases even better. Concerning the optimization problem described in this chapter, binomial crossover seems to be the better choice. However, this will still be investigated in Subsection 4.2.6. The parameter C_r defines the probability of crossover or simply ”crossover rate”. Similar as the mutation scale factor F, this has a strong influence on DE's overall performance. Typical

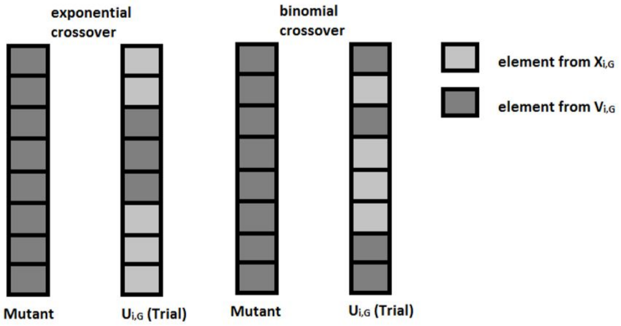

Figure 4.4: The difference between exponential and binomial crossover [25].

values of the crossover rate lie within the interval $[0, 1.0]$. The crossover rate is always smaller than 1, suggesting that there is only a minimal probability that no crossover will happen at all. When this is the case, none of the mutant vector elements are present in the trail vector. Therefore, the DE algorithm is designed to have at least one element from the mutant vector present in the trail vector. In Subsection 4.2.6 different settings for the crossover rate and scale factor and different mutation strategies are tested.

Selection

The selection step is the most straightforward in the algorithm. It follows the principle of ”survival of the fittest”. The objective function value (fitness) of the parent and the trail vector are compared with one another and the vector with the lowest fitness is added to the new generation. When it is the case that the fitnesses are equal, the trail vector is used to prevent the algorithm from getting stuck on a flat plane (equal fitness) in the search space. This strategy is named $DE/rand/1/bin$. The notation $rand$ refers to the fact that the base vector $X_{r_1^i,G}$ is chosen randomly. Other variations are $best$, which takes the best or $rand - to - best$, the integer 1 sets the number of difference pairs, and bin is short for the binomial crossover strategy (exp for exponential). Other variations for the mutation strategy are presented in Table 4.1 and tested in Subsection 4.2.6. The notation $best$ refers to the best known decision vector instead of $X_{r_1^i}$ in Equation 4.5. The $rand - to - best$ notation combines both the $best$ and $rand$ methods. In a DE iteration, the new members of the population are not inserted back into the old populations, but a secondary population is used to store the new members. Note that if the parent vector was better, the new members could also be the old members. So during a single iteration, the population does not change. An iteration is finalized when all members of the population have been a parent vector. This means that for each iteration of the DE algorithm, the objective function is calculated NP times and members of the population are stored with their respective fitness value. After a prescribed number of iterations (e.g., generations), the DE algorithm ends. There is also the possibility to use a criterion that decides that the optimization has converged. In the implementation of DE in PaGMO, there are two different criteria. The first one is a condition of the difference between all the members of a population. This refers to the maximum distance in the search space that should be smaller than a prescribed value (criterion). The second criterion checks the difference in fitness between the worst and best members of the population. If this difference is smaller than a prescribed value (criterion) the optimization is terminated. For the optimizations considered in this chapter, both stopping criteria are not used and one simply presets the total number of generations. This is done by simply setting both stopping criteria values too stringent.

1. DE/best/1/exp	6. DE/best/1/bin
2. DE/rand/1/exp	7. DE/rand/1/bin
3. DE/rand-to-best/1/exp	8. DE/rand-to-best/1/bin
4. DE/best/2/exp	9. DE/best/2/bin
5. DE/rand/2/exp	10. DE/rand/2/bin

Table 4.1: Different selection methods of DE algorithm tested for best tuning parameters.

4.2.6 Optimizer settings

The previous subsection explained the three main steps of a DE algorithm and how to tune them. In this subsection, one aims to find the best possible settings for these three steps. In Table 4.1 the different settings for $DE/x/y/z$ are presented. x refers to the method of selecting the base vector, y indicates the number of pairs used, and z indicates the crossover method used. Apart from the different selection methods presented in the table above, four combinations of two different values (0.33 and 0.67) for Cr and F are investigated for each of the methods presented in Table 4.1. The algorithm is tested for a Callisto-Ganymede-Europa-JOI triple-flyby sequence. The number of generations is set to 200, each with 5000 individuals to ensure convergence for each combination of tuning parameters. These high numbers are taken because there was no real restriction on computation time due to the analytical nature of the problem. Figure 4.5 shows the convergence behavior for each of the settings. Each plot holds the four combinations of Cr and F for a single method of the ones presented in Table 4.1 and indicated by the method number. To make the plots more clear the fitness will be plotted from the 20th generation onwards. The two convergence criteria are set to half of a percentage of the final fitness above and below the final fitness value. Convergence is said to be reached when the fitness is (and stays) between these two lines and the aim is to find tuning parameters that converge fastest.

From the results presented in Figure 4.5 one can conclude that methods one and six compete to have the best convergence behavior. Comparing both of these plots in more detail, the author concluded that method six with $Cr = 0.67$ and $F = 0.33$ has the best convergence behavior. The results shown in Figure 4.5 were generated using a seed number of 2222. The number of generations required to reach the optimal settings was 36. The author is aware that the difference between the first and sixth methods is only in the exponential or binomial crossover strategy. Moreover, the preset seed number could influence the convergence behavior. Therefore it was tested for three different seed numbers (2222, 3333 and 1234). The result was that although the number of generations needed to reach the convergence criteria could differ, the optimal settings for the tuning parameters stayed the same (method six with $Cr = 0.67$ and $F = 0.33$). Therefore these settings are used throughout the remainder of this chapter. For convenience all settings are summarized in Table 4.2.

Tuning parameter	Notation	Setting
Number of generations	$\mathrm{G_i}$	200
Number of individuals	NP	5000
Mutation scale factor	F	0.33
Crossover rate	$\mathrm{C_r}$	0.67
Selection method	$\mathrm{DE/x/y/z}$	DE/best/1/bin

Table 4.2: Summary of the tuning parameters for the DE optimization algorithm for a triple satellite-aided capture sequence. These are used for all the optimizations in this chapter.

To better illustrate the convergence of the optimization Figure 4.6 shows the fittest solution for every generation. As the number of generations increases, the solutions' lines start to overlap such that they appear as one line. The hyperbolic excess velocity for each flyby, the minimum flyby altitude and the flyby moon are also shown in the plot (only for the last

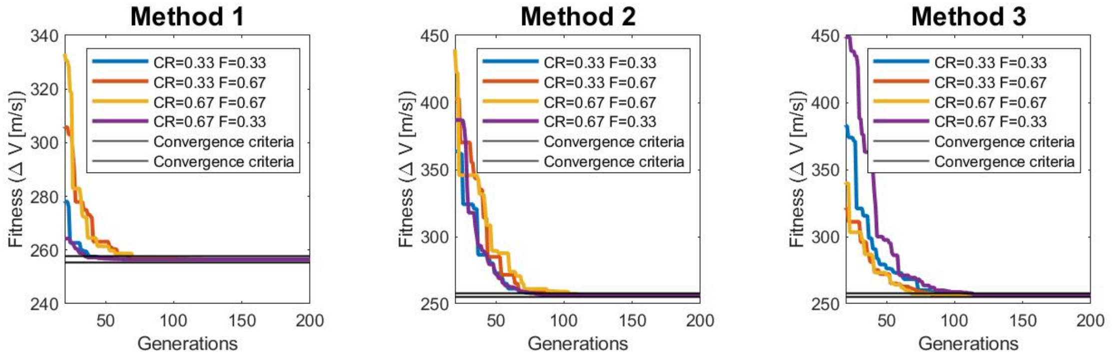

(a) Method 1 (b) Method 2 (c) Method 3

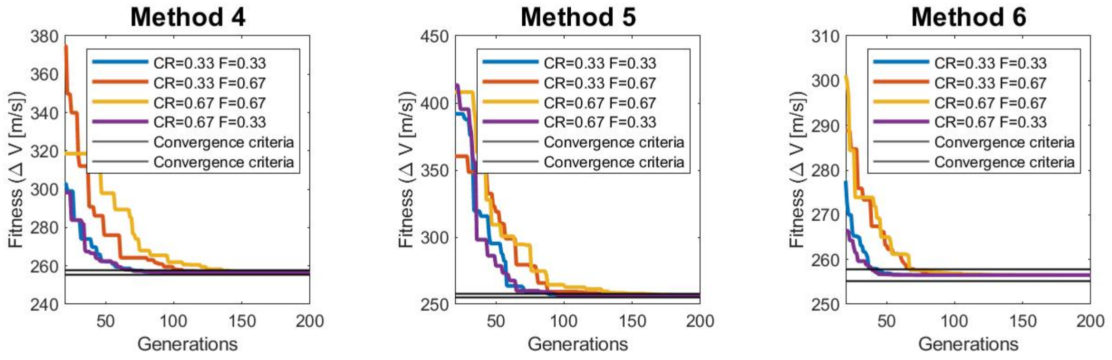

(d) Method 4 (e) Method 5 (f) Method 6

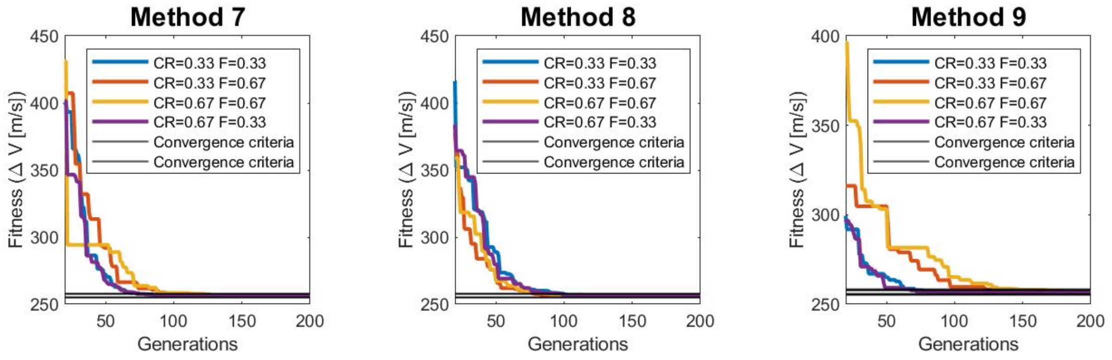

(g) Method 7 (h) Method 8 (i) Method 9

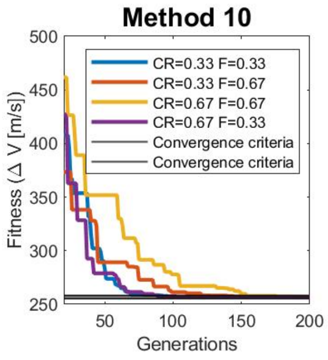

(j) Method 10

Figure 4.5: Convergence behaviour for different settings of the tuning parameters for a preset Callisto-Ganymede-Europa-JOI sequence.

generation). The final optimum presented in Figure 4.6 results in a final orbital energy of $-6.425\ \mathrm{km}^2/\mathrm{s}^2$, referring to the 200-day periodic capture orbit. Again as mentioned earlier in this section, the settings were tested for a Callisto-Ganymede-Europa-JOI capture sequence. This resulted in an impulsive ΔV_{JOI} of 275 m/s injected at the perijove of the trajectory and in the opposite direction of the spacecraft's velocity vector. The graph presented in Figure 4.6 will be repeated in Section 4.3 but only for the converged solution.

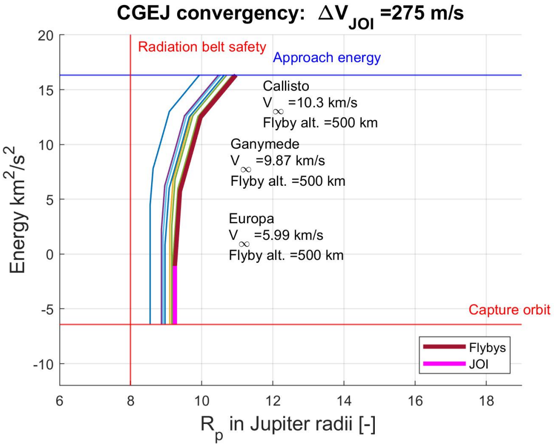

Figure 4.6: Optimal solution per generation for a Callisto-Ganymede-Europa-JOI satellite-aided planetary capture trajectory in Tisserand graph. Thick linewidth indicates the final solution, horizontal red line represents the desired capture orbit and the vertical red line the minimum allowable perijove radius due to the harsh radiation environment.

4.3 Results

This section presents the results for the satellite-aided planetary capture trajectory optimization in the Tisserand graph. Better solutions are the ones where the JOI is smaller. Important to consider is that no phasing considerations are applicable at this moment. The results are organized such that first the single-aided sequences are explained, then the double-aided and finally the triple-aided. The section closes with a summarizing table (Table 4.3) and conclusions in Section 4.4.
The results show the effect of the flybys in blue and the JOI in pink. Thinner lines in the plots indicate the complete Tisserand contours from Figure 3.4 for specific values of V_∞, on which the flyby is flown. The colors of the Tisserand contours are arranged similar to Figure 3.4. The sequence is indicated in the title of the plot with the first letter of the moon under consideration and the JOI with J.

4.3.1 Single-aided

The most simple satellite-aided capture trajectories are the ones that only imply a single flyby with one moon. Considering the orbital parameters of the Galilean moons and the minimum perijove radius due to the harsh radiation environment around Jupiter, it was already concluded that Io should not be used for a satellite-aided capture trajectory and is therefor not considered. For Callisto, Ganymede and Europa, the results present both a JOI before and after the flyby.

Callisto

Figure 4.7 presents the two optima for a Callisto-aided planetary capture sequence. The first thing to notice is that with a single Callisto flyby, the spacecraft can not be captured in a closed orbit around Jupiter without the use of an impulsive JOI. The JOI is always inserted at the perijove, which makes the flyby either inbound or outbound. Both options are presented in Figures 4.7a and 4.7b. Inbound flybys refer to the situation that the spacecraft is moving closer to Jupiter and on its path perfroms a flyby with one of the moons. Contrary, outbound flybys mean that the spacecraft is moving further away from Jupiter. This latter means that after the JOI is executed, all subsequent flybys are outbound. The results suggest that it is better to perform the flyby first (hence lowering the perijove and orbital energy), followed by a JOI of 902 m/s. The initial perijove (around $9R_J$) is such that after the flyby, the perijove is decreased to its minimum allowable value (e.g. $8R_J$). It is well known that an impulsive maneuver performs best when implemented when the spacecraft's velocity is maximum (e.g., the perijove). On the other hand, from the relations in Section 3.3 one learned that the effects of a gravity assist maximize when it is performed at zero flight-path angle γ and lowest relative velocity with respect to the flyby moon (Equations 3.3, 3.14, 3.12 and 3.13). From the optima presented in Figure 4.7a one can conclude that the combined effect of a JOI at perijove and a Callisto flyby is governed by more efficient impulsive JOI's at lower perijoves. The same reasoning holds when the JOI is implemented before the flyby (Figure 4.7b). This lowers the spacecraft's relative velocity with respect to the flyby moon, making flybys more effective and thus lowering the required JOI. However, the more efficient JOI at perijove results in an optimal perijove around $9.2R_J$ such that room is left in terms of perijove to perform the flyby. This results in an increase of the JOI to 926 m/s.

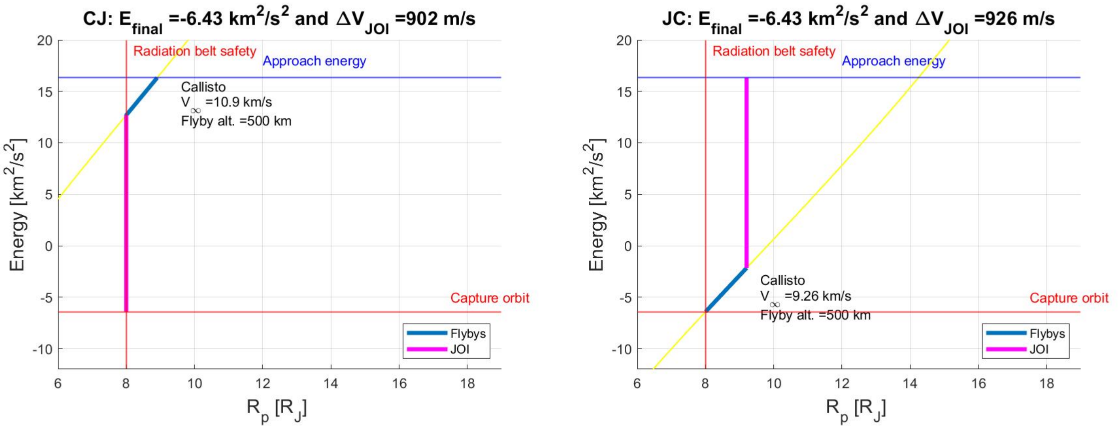

(a) Optimal Callisto-JOI planetary capture sequence in Tisserand graph.

(b) Optimal JOI-Callisto planetary capture sequence in Tisserand graph.

Figure 4.7: Results for Callisto-aided planetary capture trajectories.

Following the reasoning above, it is concludes that in the case of a Callisto-aided planetary capture trajectory, Callisto's high orbital radius makes the optima dominated by more efficient JOI's at lower perijoves.

Ganymede

The results of Ganymede-aided planetary capture trajectories are presented in Figure 4.8. Like Callisto, a gravity assist with Ganymede only is incapable of capturing the spacecraft in a closed orbit around Jupiter. A JOI is still inevitable and can be implemented before (Figure 4.8b) or after (Figure 4.8a) the flyby.

From the optima one can conclude that a JOI before the flyby results in the lowest ΔV of 643 m/s. This is due to a lower relative velocity with respect to Ganymede that makes the flyby more effective. Both optima have a perijove equal to the orbital radius of Ganymede right before the flyby. Thus the flyby is performed at the perijove with flight-path angle γ equal to zero and minimal relative velocity with respect to Ganymede. This makes the final perijove far above the radiation safety belt of $8R_J$. A higher perijove at which the JOI is executed means a less efficient impulsive maneuver. The author concludes that more effective flybys govern a Ganymede-aided capture trajectory instead of a more efficient JOI at lower perijove.

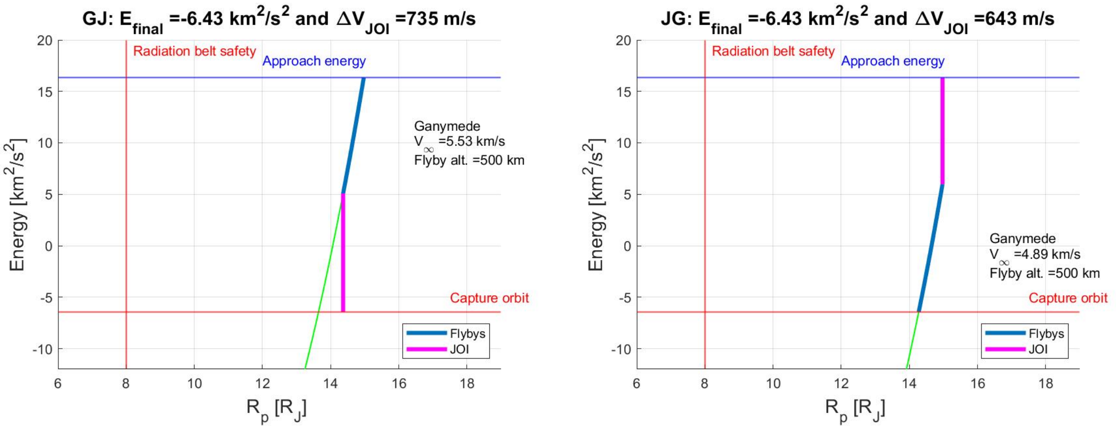

(a) Optimal Ganymede-JOI planetary capture sequence in Tisserand graph.

(b) Optimal JOI-Ganymede planetary capture sequence in Tisserand graph.

Figure 4.8: Results for Ganymede-aided planetary capture trajectories.

This is opposite to the optima found for the Callisto-aided sequences.

Europa

Similar to the Callisto and Ganymede optima, the results of both inbound- and outbound Europa flybys are given in Figure 4.9. This implies that a JOI is also inevitable for a Europa-aided capture trajectory. The outbound flyby has the lowest possible JOI of 788 m/s because of the lower relative velocity with respect to Europa. Both optima have a perijove equal to the orbital radius of Europa right before the flyby. Therefore setting the flight-path angle to zero and the relative velocity to a minimum makes the flyby most effective. The final captured orbit lies about $1.2R_J$ above the radiation safety belt. The JOI could theoretically be performed at lower perijove. However, from the optima in Figure 4.9 one learns that the minimal ΔV for the JOI is dominated by more effective Europa flybys instead of a more efficient JOI. The same was concluded for the Ganymede-aided planetary capture trajectories.

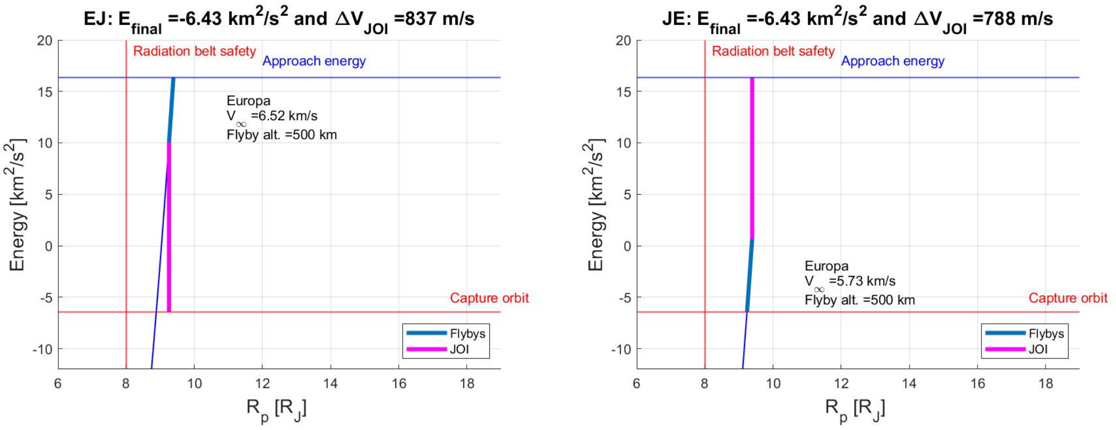

(a) Optimal Europa-JOI planetary capture sequence in Tisserand graph.

(b) Optimal JOI-Europa planetary capture sequence in Tisserand graph.

Figure 4.9: Results for Europa-aided planetary capture trajectories.

4.3.2 Double-aided

Slightly more complicated satellite-aided planetary capture trajectories are the ones that include two flybys in the sequence. Two gravity assists with a Galilean moon could lower the orbital energy towards the limit value of closed and open orbits (e.g., zero orbital energy or a parabolic orbit). However, capturing the spacecraft in the desired captured orbit around Jupiter would still require an impulsive JOI. Therefore, the results of double-aided capture trajectories are organized in three groups, each representing four possible combinations of two of the three Galilean moons with a JOI at perijove (excluding Io due to the radiation safety). First the Callisto-Ganymede, second the Ganymede-Europa and last the Callisto-Europa sequences are presented here.

Inbound-outbound

As explained in the paragraph above, each combination of two moons hold four possible sequences due to the arbitrary location of the JOI. In theory, six possible sequences could be investigated. However, these two additional sequences have no physical meaning due to the inbound-outbound problem. The inbound-outbound problem is illustrated in Figure 4.10 for a hypothetical JOI-Callisto-Ganymede sequence. Because the JOI is always executed at perijove, all subsequent flyby are outbound flybys. Referring to the fact that the spacecraft is mover further away from Jupiter. So, for the hypothetical JOI-Callisto-Ganymede sequence, after the JOI is executed the spacecraft can perform a flyby with Callisto. A subsequent Ganymede flyby is then geometrically impossible because Ganymede orbits Jupiter at smaller orbital radius and the spacecraft will therefore never reach the orbit of Ganymede.

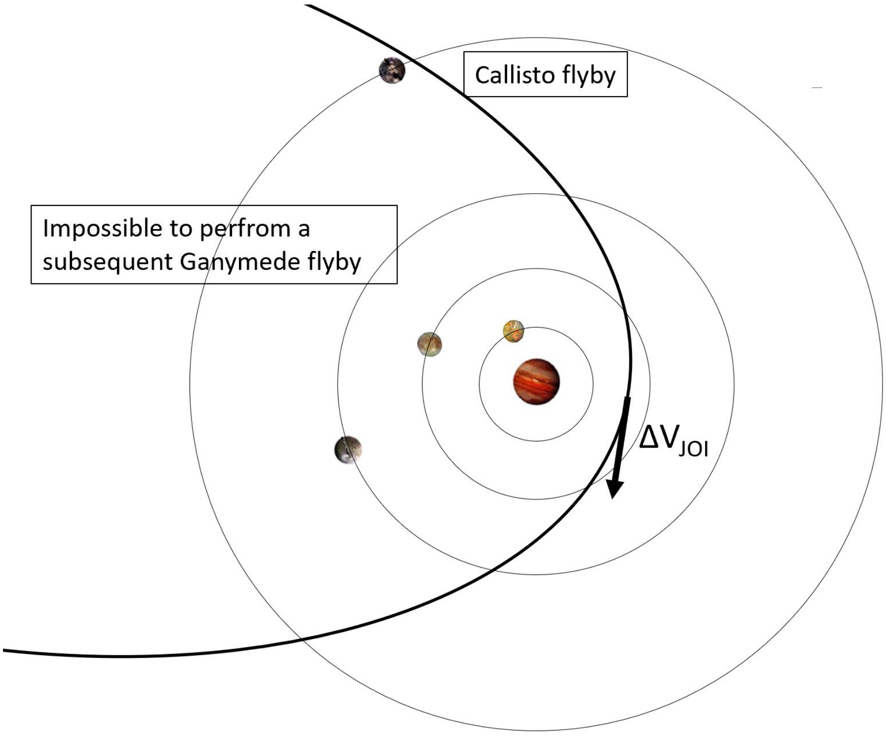

Figure 4.10: Illustration of the inbound-outbound problem by means of a hypothetical JOI-Callisto-Ganymede sequence.

Callisto-Ganymede

The results of the Callisto-Ganymede aided planetary capture trajectories are given in Figure 4.11. They hold four possible sequences due to arbitrary locations of the JOI in the sequence. The required ΔV_{JOI} varies between 359 m/s for the sequence when the JOI is inserted before the flybys and 433 m/s when it is done after. So the effect of having smaller relative velocities before the flybys as was explained in Subsection 4.3.1 is also valid for Callisto-Ganymede-aided planetary capture trajectories. Considering the orbital radius of Ganymede, one can observe that the optima converge to a perijove equal to Ganymede's orbital radius for every sequence thus performing the Ganymede flyby with zero flight-path angle. This makes the JOI and final captured orbit lie far above the radiation safety belt.

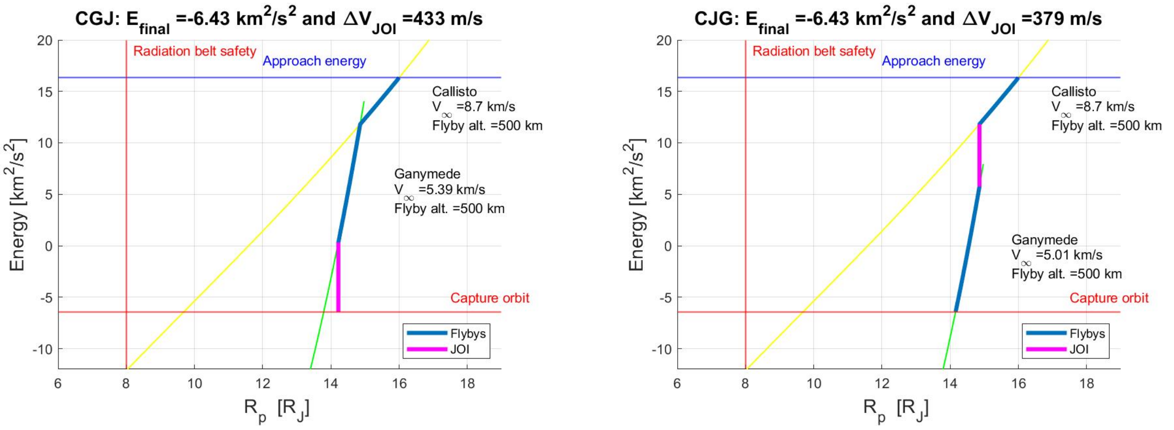

(a) Optimal Callisto-Ganymede-JOI planetary capture sequence in Tisserand graph.

(b) Optimal Callisto-JOI-Ganymede planetary capture sequence in Tisserand graph.

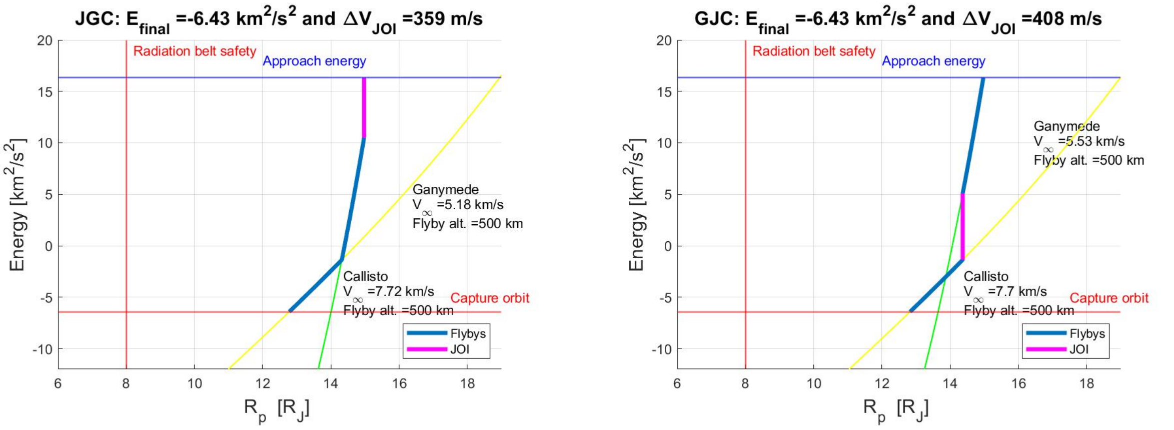

(c) Optimal JOI-Ganymede-Callisto planetary capture sequence in Tisserand graph.

(d) Optimal Ganymede-JOI-Callisto planetary capture sequence in Tisserand graph.

Figure 4.11: Optimal for Callisto-Ganymede-aided planetary capture trajectories in Tisserand graph.

Therefore, the author argues that the optima for all Callisto-Ganymede capture sequences are governed by more effective flybys at lower relative velocity with respect to the flyby moons and a zero flight-path angle with the most inner flyby moon.

Ganymede-Europa

With ΔV_{JOI} ranging from 455 to 491 m/s (Figure 4.13), the Ganymede-Europa-aided planetary capture trajectories perform worse (in terms of ΔV_{JOI}) than Callisto-Ganymede-aided trajectories. This is mainly due to Europa being less massive than Callisto, although the orbital velocity of Europa is far larger than that of Callisto.

The optima are again bound to the orbital radius of the most inner moon Europa instead of a more efficient JOI at a lower perijove. The absolute minimum for JOI is found for the JOI-Europa-Callisto sequence holding only outbound flybys. Thus similar to the case for

Callisto-Ganymede, optima are dominated by more effective flybys due to lower relative velocities and zero flight-path angle.

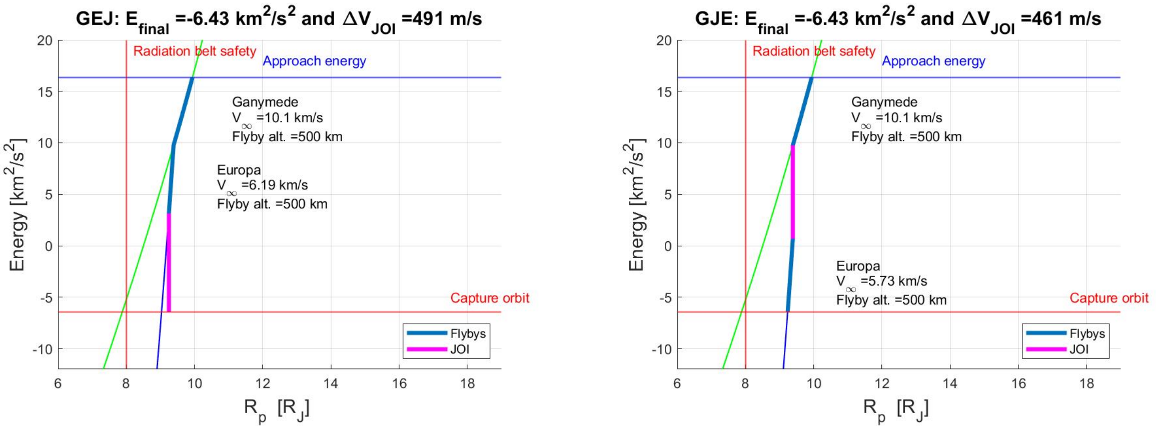

(a) Optimal Ganymede-Europa-JOI planetary capture sequence in Tisserand graph.

(b) Optimal Ganymede-JOI-Europa planetary capture sequence in Tisserand graph.

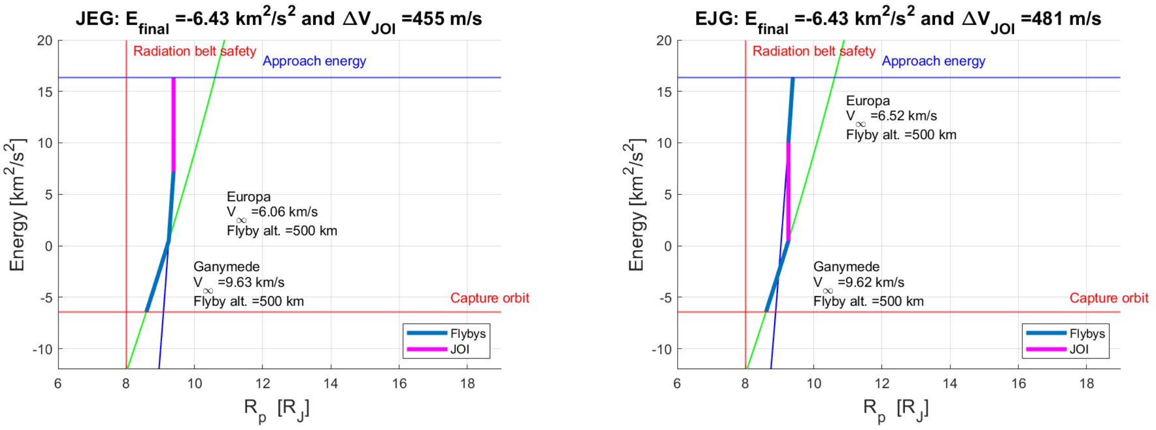

(c) Optimal JOI-Europa-Ganymede planetary capture sequence in Tisserand graph.

(d) Optimal Europa-JOI-Ganymede planetary capture sequence in Tisserand graph.

Figure 4.12: Optimal for Ganymede-Europa-aided planetary capture trajectories in Tisserand graph.

Callisto-Europa

The optimal Callisto-Europa-aided planetary capture trajectories are given in Figure 4.13. ΔV_{JOI} varies from 582 to 638 m/s what makes them the worst from all three possible combinations of the double-aided sequences. The large difference in orbital radius between Callisto and Europa worsens the effectiveness of (one of) the flybys. Every optimum converged towards a perijove equal to the orbital radius of Europa right before the Europa flyby. Consequently, enlarging the flight-path angle and relative velocity at the Callisto flyby makes it less effective.

The reasoning for the Ganymede-Europa sequences also applies to the Callisto-Europa-JOI- and Callisto-JOI-Europa sequences (e.g., Figures 4.13a and 4.13b). Therefore, it will not be repeated here for brevity. In short, the more effective flybys (flight-path angle and relative velocity) govern the optima found for a Callisto-Europa-aided planetary capture trajectory.

For the JOI-Europa-Callisto and Europa-JOI-Callisto sequences in Figures 4.13c and 4.13d the optima in terms of more efficient JOI at lower perijove and a more effective Europa flyby at Europa's orbital radius seem to coincide. Therefore the final perijove of the captured orbits lies exactly on the radiation safety belt of $8R_J$.

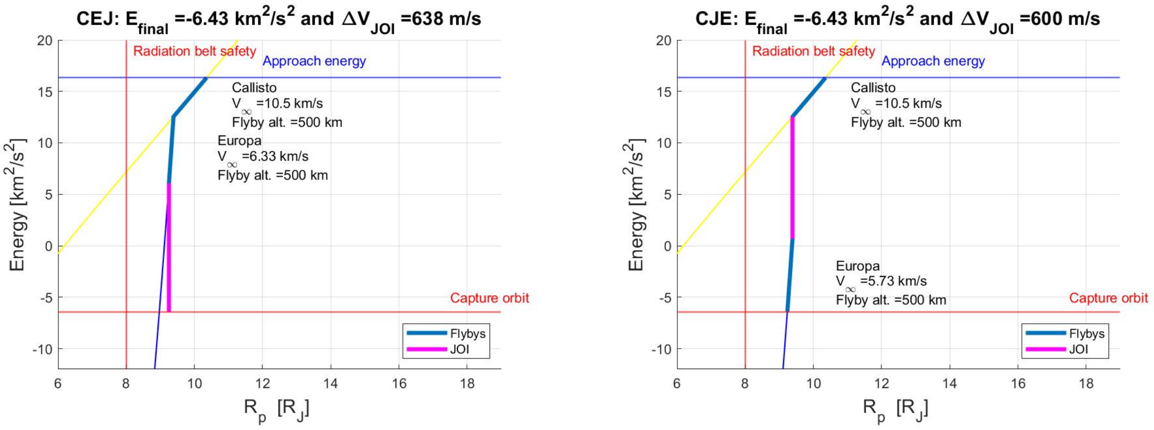

(a) Optimal Callisto-Europa-JOI planetary capture sequence in Tisserand graph.

(b) Optimal Callisto-JOI-Europa planetary capture sequence in Tisserand graph.

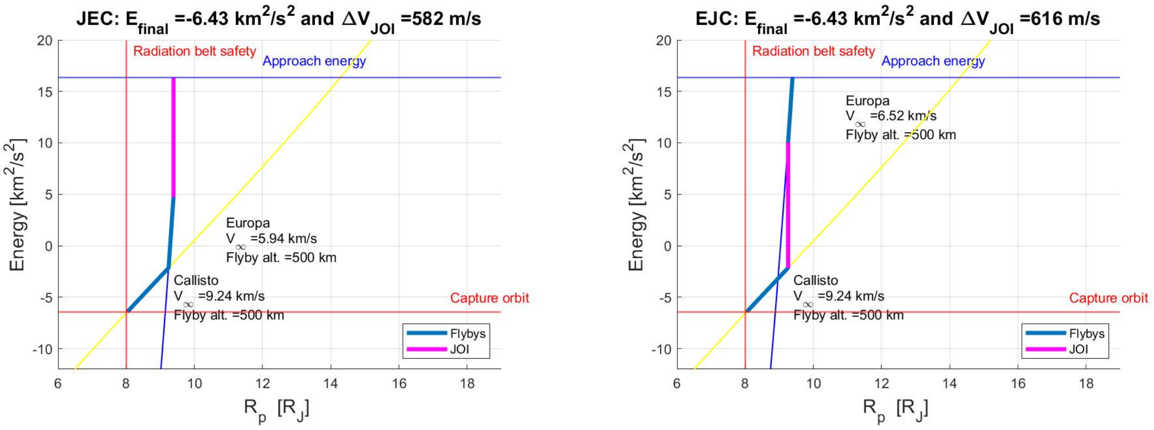

(c) Optimal JOI-Europa-Callisto planetary capture sequence in Tisserand graph.

(d) Optimal Europa-JOI-Callisto planetary capture sequence in Tisserand graph.

Figure 4.13: Optimal for Callisto-Europa-aided planetary capture trajectories in Tisserand graph.

4.3.3 Triple-aided

Figures 4.14 and 4.15 present the results of all possible triple-aided planetary capture trajectories. Triple-aided capture trajectories could potentially capture a spacecraft in a closed orbit. However, the captured orbit would have a very long orbital period that is generally not desired regarding the time of flight. As stated earlier, a desired captured orbit would have an orbital period of 200 days (indicated by the red line in the graphs). Therefore also for triple-aided capture trajectories, a JOI is demanded. With JOI's ranging from 258 to 374 m/s it makes the triple-aided capture trajectories perform best.

Like the double-aided sequences, the optimum lies at perijoves equal to the orbital radius of the most inner moon right before the flyby with that inner moon. For the triple-aided sequences that is always Europa. Europa's orbital radius of $9.4R_J$ has a downside though. With the radiation safety belt set to $8R_J$, there is only a small region in perijove to incorporate flybys. Flybys with Callisto and Ganymede have more effect on the perijove in this region on the Tisserand graph compared to Europa flybys. Therefore it is better to place Callisto and Ganymede in front of the sequence. This results in optima with larger final perijoves, meaning that a larger range of initial perijoves (smaller than the optimum) can potentially be flown.
For the JOI-Europa-Ganymede-Callisto and Europa-JOI-Ganymede-Callisto sequence, the Callisto flyby is not flown at the minimum flyby altitude of 500 km. Both cases have a

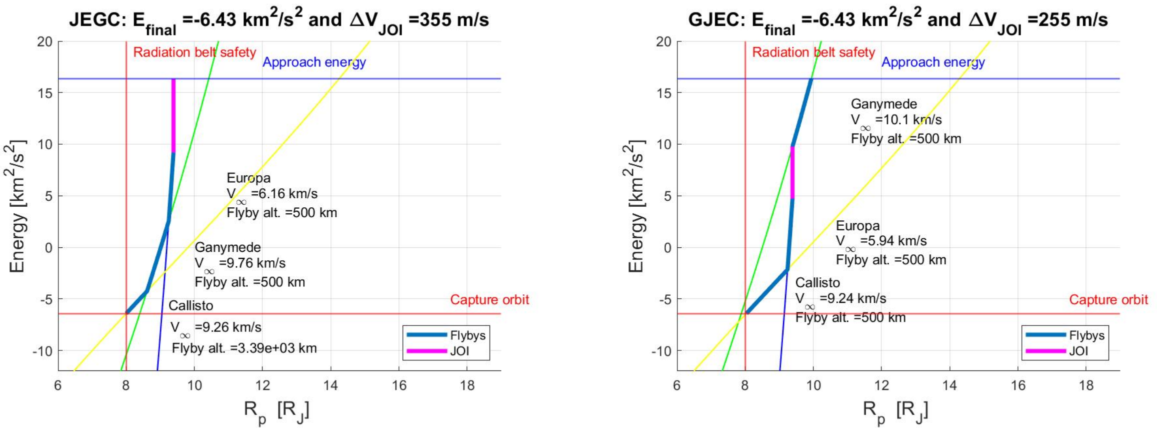

(a) Optimal JOI-Europa-Ganymede-Callisto planetary capture sequence in Tisserand graph.

(b) Optimal Ganymede-JOI-Europa-Callisto planetary capture sequence in Tisserand graph.

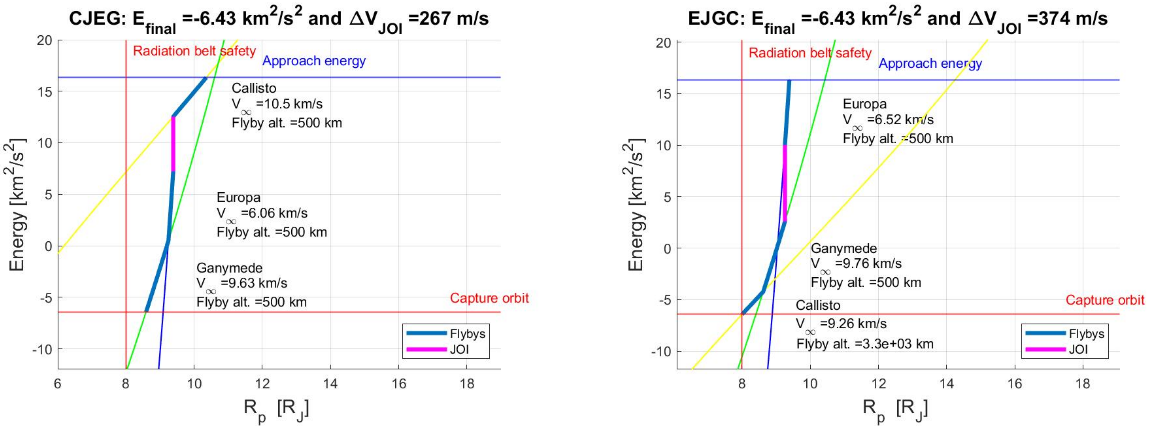

(c) Optimal Callisto-JOI-Europa-Ganymede planetary capture sequence in Tisserand graph.

(d) Optimal path for a Europa-JOI-Ganymede-Callisto planetary capture sequence in Tisserand graph.

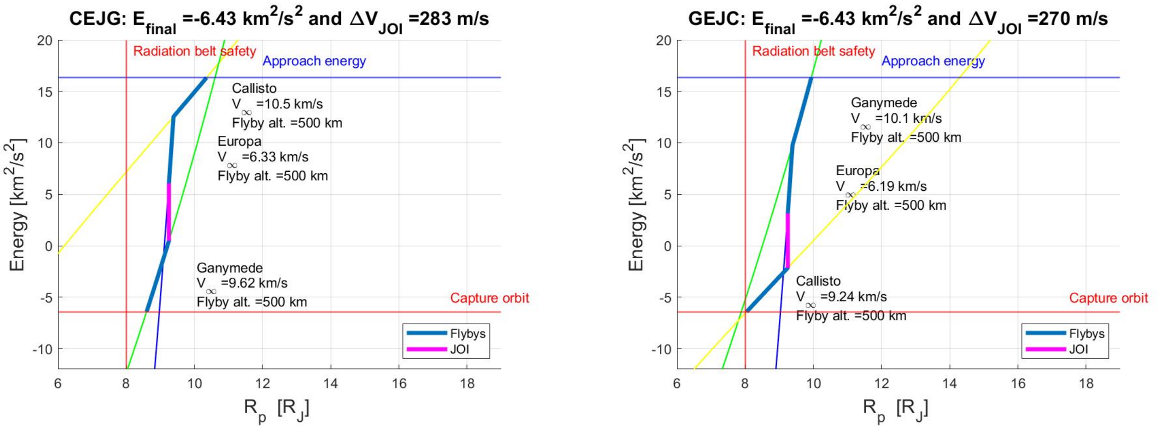

(e) Optimal Callisto-Europa-JOI-Ganymede planetary capture trajectory in Tisserand graph.

(f) Optimal path for a Ganymede-Europa-JOI-Callisto planetary capture sequence in Tisserand graph.

Figure 4.14: Optimal triple-aided planetary capture trajectories in Tisserand graph (part 1).

Callisto flyby altitude above 3300 km. This is to limit the perijove increment delivered by the Callisto flyby. However, this also limits the energy increment and thus causes an increase in the required JOI. This is why these two sequences have a higher ΔV_{JOI} result than all other triple-aided scenarios.

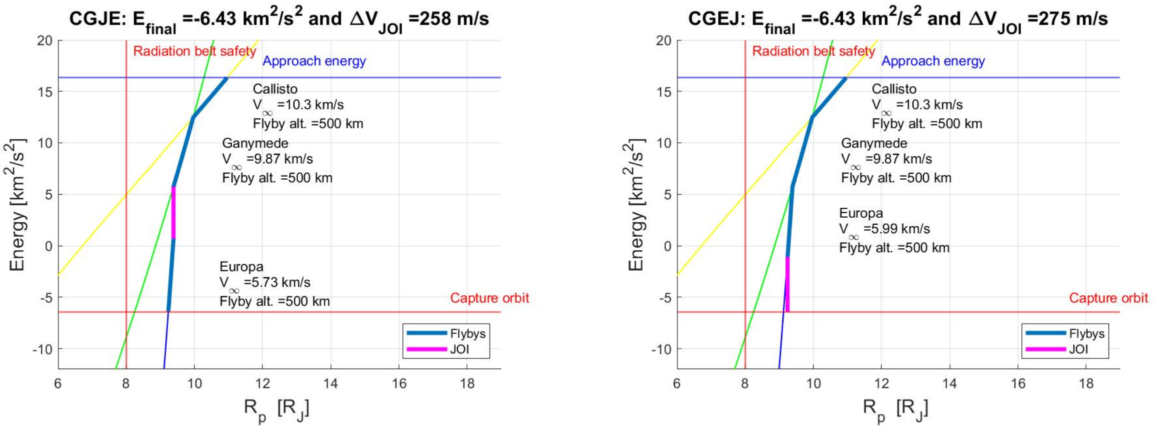

(a) Optimal Callisto-Ganymede-JOI-Europa planetary capture trajectory in Tisserand graph.

(b) Optimal path for a Callisto-Ganymede-Europa-JOI planetary capture trajectory in Tisserand graph.

Figure 4.15: Optimal triple-aided planetary capture trajectories in Tisserand graph (part 2).

4.3.4 Summary

The results of all sequences are summarised in Table 4.3. The table shows the required JOI in terms of ΔV_{JOI} and propellant mass. The required propellant mass is calculated using the well-known “Tsiolkovsky rocket equation” [7] including only high-thrust (Equation 4.6).

$$M_{prop} = M_{initial}\left(1 - e^{-\frac{\Delta V_{JOI}}{g_0 I_{sp,HT}}}\right) \tag{4.6}$$

The above equation uses the following values. The initial spacecraft mass, $M_{initial}$ is set to 4000 kg, the high-thrust specific impulse equal to 300 s and the gravitational acceleration at the surface of Earth, g_0 = 9.81 m/s^2.

Single-aided planetary capture sequence required propellant for the JOI ranging from 785 kg for a JOI-Ganymede to 1080 kg for a JOI-Callisto sequence. The propellant mass for Europa-aided capture lies in between these two. Compared with not-aided capture, this already meant potential mass savings from 138 to 433 kg (11 to 35%). The orbital radius of the flyby moon was the primary cause of this wide range. Nonetheless, this already showed that a single flyby upon capture could lead to significant mass savings for the spacecraft.
The addition of an extra flyby to fly double-aided capture sequences further lowered the overall propellant needs. Combining Callisto and Ganymede performed best: with required propellant masses going from 460 kg for JOI-Ganymede-Callisto to 547 kg for Callisto-Ganymede-JOI. Compared with the reference of 1218 kg, these are mass savings from 671 to 758 kg. That is 55 to 62% of the propellant mass for not-aided capture. Other combinations performed (slightly) less with mass savings from 603 to 645 kg (49 to 53%) for Ganymede-Europa and 438 to 501 kg (36 to 41%) for Callisto-Europa.
The triple-aided capture sequence lowered the propellant mass even further. The Europa-JOI-Ganymede-Callisto sequence required a propellant mass of 477 kg, saving up to 741 kg (60%). The best triple-aided sequence was the Ganymede-JOI-Europa-Callisto that required 331 kg propellant, and with it, saving of 887 kg (or 73%).

	ΔV_{JOI} [m/s]	$M_{prop,min}$ [kg]	$\%\mathrm{M}_{\mathrm{prop,direct}}$ [-]
Direct			
-	1069	1218	100
Single-aided			
Callisto			
CJ	902	1056	87
JC	926	1080	89
Ganymede			
GJ	735	945	78
JG	643	785	64
Europa			
EJ	837	990	81
JE	788	939	77
Double-aided			
Callisto-Ganymede:			
CGJ	433	547	45
CJG	379	484	40
JGC	359	460	38
GJC	408	517	42
Ganymede-Europa			
GEJ	491	615	50
GJE	461	580	48
JEG	455	573	47
EJG	481	603	50
Callisto-Europa			
CEJ	638	780	64
CJE	600	738	61
JEC	582	717	59
EJC	616	755	62
Triple-aided			
CGEJ	275	357	29
CGJE	258	336	28
CEJG	283	366	30
CJEG	267	347	28
GEJC	270	351	29
GJEC	255	331	27
EJGC	374	477	39
JEGC	355	454	37

Table 4.3: Summary of the results of all double- and triple-aided capture sequences. Results hold the amount of ΔV_{JOI} and propellant mass for the JOI.

4.4 Conclusions

This chapter implemented the methodology and theory of the Chapter 3 to investigate the possibilities of satellite-aided planetary capture trajectory within the Jovian system. This was done through a fitness function that evaluates the required ΔV_{JOI}. A short evaluation of optimization algorithms suggested that the differential evolution algorithm (DE) was the best option. Additionally, the DE algorithm was tuned in its settings for the mutation (F), crossover (CR) and the selection method to guarantee the fastest convergence behavior. As a result the combiniation, CR=0.67, F = 0.33 and selection method six (DE/x/y/z) came out as the best option.

Three cases were investigated: single-, double- and triple satellite-aided capture trajectories. One conclusion was that a spacecraft arriving at the Jovian system due to an interplanetary

Hohmann transfer could not properly capture itself in the Jovian system through one-, two or three gravity assists alone. This implies that an impulsive JOI would always be required. For singe-aided trajectories, a Ganymede flyby would serve as the best solution to lower the required JOI maneuver. When considering two gravity assists, the combinations of Callisto and Ganymede perform best.

A trajectory incorporating three flybys can capture the spacecraft into a closed orbit around Jupiter without the use of any JOI. However, to insert it into the desired 200-day periodic, high eccentric orbit around Jupiter, an impulsive JOI is still required. Overall the triple-aided trajectories perform better than the double-aided trajectories. Sequences that have Europa as the first flyby have the problem of reaching beyond the radiation safety belt. An increase in flyby altitude prevents this. The best option for conventional satellite-aided capture trajectory would be the Ganymede-JOI-Europa-Callisto sequence with a JOI of only 255 m/s which requires only 27% of the propellant for direct capture.

Chapter 5

Low-thrust Tisserand graph

This chapter presents a fast method to include low-thrust legs in the Tisserand graph. It starts with the characteristics of low-thrust (electric) propulsion in Section 5.1. This is quantitatively extended with the equations of motion in Section 5.3. Then in Section 5.4 reference trajectories are created to verify the method in this chapter. This section also explains the effects of low thrust on the Tisserand graph. Section 5.5 presents the actual method (Taylor-series expansion) for the inclusion of low-thrust legs in the Tisserand graph. The chapter closes with some concluding remarks that are relevant for the following chapter.

5.1 Characteristics of low-thrust electric propulsion

A low-thrust electric propulsion system typically referes to a propulsion system that is only capable of producing very low thrust levels (in the order of mN) and comes with a separate electrical power unit. This power unit could be a solar array, which generally refers to a Solar-Electric-Propulsion system or short, SEP. The thrust capabilities of a SEP are therefore related to the solar power available. Another option for the power unit might be a nuclear fission reactor. This then refers to a Nuclear-Electric-Propulsion system or short NEP. For missions to the outer planets where the power available from the Sun diminishes with the orbital radius of the target planet, a NEP system is preferred over a SEP.
The advantage of a low-thrust propulsion system comes from the very high exhaust velocity $V_{exhaust}$. A very high $V_{exhaust}$ results in a very high specific impulse through Equation 5.1. In this equation, g_0 is equal to the gravitational acceleration on Earth at sea level. For example, the BepiColombo [1] spacecraft's thrusters have a specific impulse of 4022 s compared to only 300 s for the Messenger spacecraft [19].

$$I_{sp} = \frac{V_{exhaust}}{g_0} \tag{5.1}$$

A low-thrust electrical propulsion system typically has three methods of accelerating the propellant. The first one is by electrical heating, which refers to an electrothermal propulsion system. Another technique is an electrostatic propulsion system. By letting ionized atoms pass through a static electric field, a strong Coulomb force is created that accelerates these atoms to high exhaust velocities. The third method for accelerating the propellant mass is using a magnetic field. This uses the Lorentz force to accelerate the atoms, referring to an electromagnetic propulsion system [29]. As mentioned above, a very high efficiency comes from the very high exhaust velocity. However, this is at the cost of very low thrust levels and thus, long thrust times to reach a certain amount of ΔV. Again, the BepiColombo spacecraft has a maximum thrust level of around 270 mN (Section 5.2) against 670 N for the Messenger spacecraft. This is a very significant difference in thrust level. However, due to the high specific impulse of low-thrust propulsion and very low propellant mass flow, low-thrust propulsion systems allow for very long thrusting times. This makes the modeling of low-thrust trajectories more challenging compared to that of high thrust trajectories. An example of a low-thrust propulsive trajectory modelled in the Solar System for 1.5 years is given in Figure 5.1. A constant thrust acceleration of 10^{-4}m/s^2 is assumed, resulting in a constant mass of the spacecraft. How this trajectory is modeled is explained in the following section. Concerning this thesis report's topic, that is low-thrust natural satellite-aided planetary capture in the Jovian system: a NEP system is considered the best option due to limited solar power available. A NEP propulsion system can then also be used throughout the scientific phase of the mission.

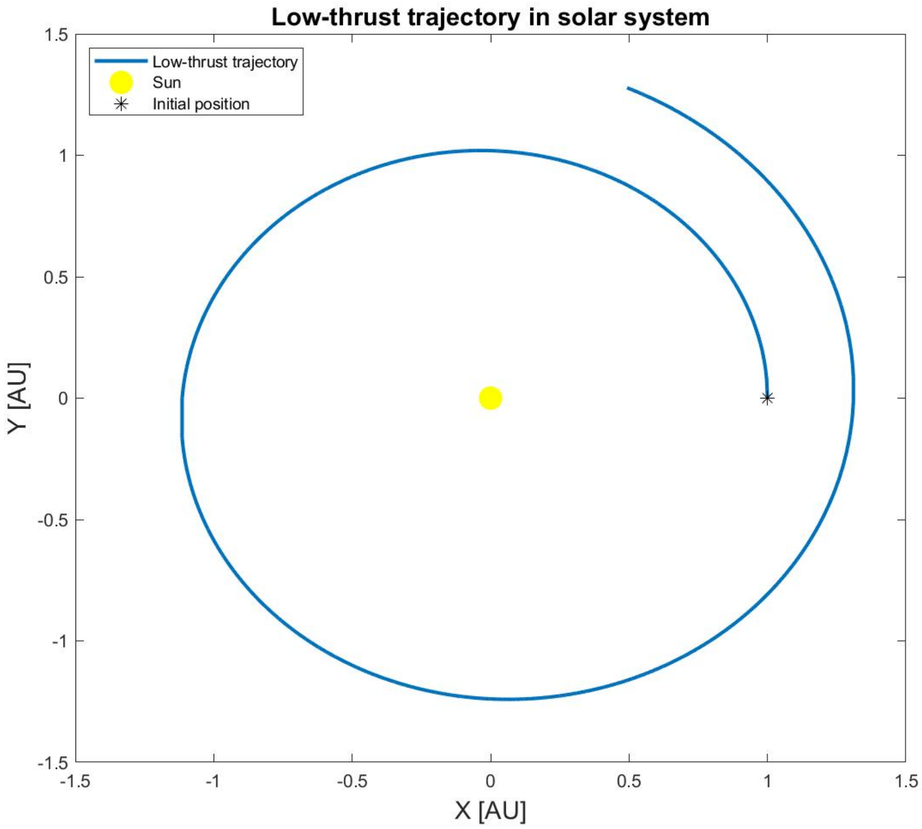

Figure 5.1: Example of low-thrust trajectory in modelled in the Solar System for 1.5 year. Initial conditions are taken to match (circular) orbit of Earth and the thrust acceleration is set at 10^{-4} m/s^2.

5.2 BepiColombo

An example of a low-thrust propulsive mission is the BepiColombo mission. The BepiColombo mission was the first European mission to employ SEP in combination with seven flybys (one with Earth, two with Venus and four with Mercury) to reach an inner planet (Mercury). It was launched on an Ariane 5 rocket from Kourou, French Guiana at 01:45:28 UT on 20 October 2018 [1]. It was first intended to be launched on 9 July 2014. The baseline of this intended interplanetary transfer is shown in Figure 5.2. The figure shows the orbits of Earth, Venus and Mercury. Black lines represent coasting arcs (SEP turned off) and red lines represent thrusting arcs (SEP turned on). After the four Mercury flybys the spacecraft performed six final low-thrust arcs to lower the relative velocity with respect to Mercury. This had the advantage that if the planned impulsive Mercury Orbit Insertion (MOI) should fail, the spacecraft would still be weakly captured around Mercury.

The basic characteristics of the SEP of BepiColombo are presented in Table 5.1.

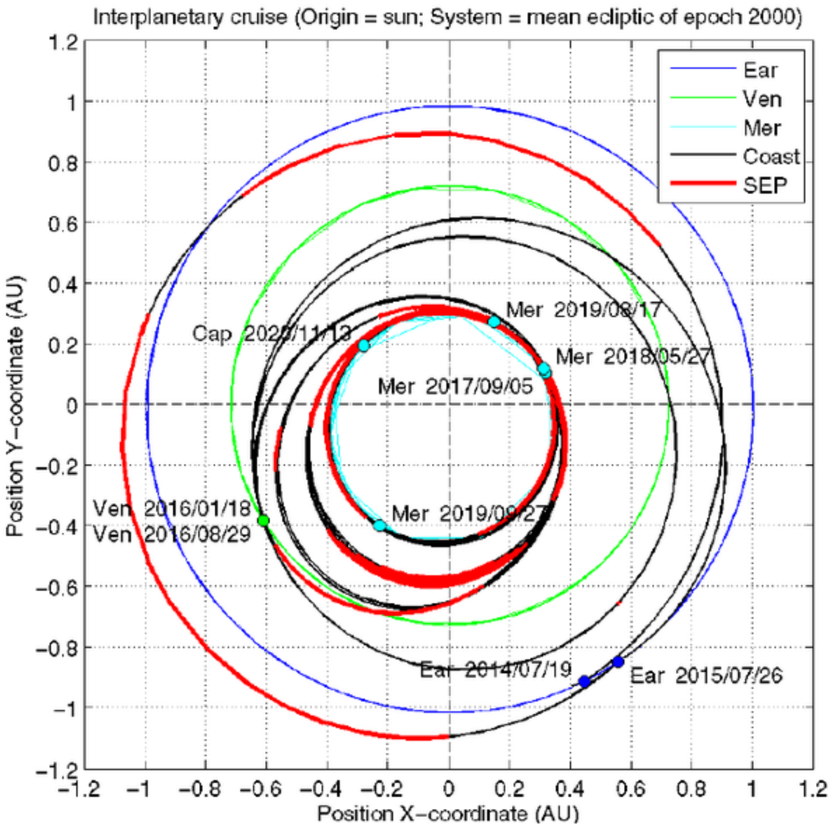

Figure 5.2: An example of a low-thrust mission is the BepiColombo mission. Red arcs in the graph represent trajectory legs where solar electric propulsion is turned on [1].

Characteristic	Value	Unit
Initial mass	4100	kg
Thrust level	261 to 290	mN
Specific impulse	4100	s
Acceleration	0.7×10^{-4}	$\mathrm{m/s^2}$
Total ΔV_{LT}	4.254	km/s

Table 5.1: Characteristics of BepiColombo SEP (and spacecraft initial mass) [1].

5.3 Equations of motion

The previous section briefly explained the characteristics of low-thrust propulsion. Due to the very low thrust levels, the accelerations are very small. However, they are still an order of magnitude larger than the perturbing accelerations [12]. This is why when modeling low-thrust trajectories, the assumption that these perturbing accelerations can be neglected is valid. With this in mind, the equations of motion read:

$$\ddot{\bar{r}} + \frac{\mu}{r^3}\bar{r} = \bar{a}_T \tag{5.2}$$

The vector $\bar{r}$ represents the radius to the central body, μ is the gravitational parameter of that central body. The thrust acceleration is given by the vector $\bar{a_T}$. Vectors are indicated by means of the bar above the symbol and the double derivatives (w.r.t. time) by the double dots. Equation 5.2 is in general always valid. The downside of it is that a very high-order integration method is needed to ensure trustworthy results for many problems. Therefore another approach that uses information that is already known about the orbit could be beneficial. As was explained in Section 5.1, the levels of accelerations are low. Because of this, the effects of these accelerations on the shape of the orbit are small. Some literature suggests that a low-thrust acceleration could be regarded as a perturbing acceleration, despite the fact that they are an order of magnitude larger than these natural perturbing accelerations. From [29] it is known that the effects of perturbations on orbital elements can be modeled using the Gauss form of planetary equations, or short the Gauss equations. These expressions in terms of Kepler elements are given here from Equation 5.3 to 5.8.

$$\frac{da}{dt} = \frac{2e\sin(\theta)}{n\sqrt{1-e^2}}F_R + \frac{2a\sqrt{1-e^2}}{nr}F_\theta \tag{5.3}$$

$$\frac{de}{dt} = \frac{\sqrt{1-e^2}}{na}\left[\sin(\theta)F_R + \left(\cos(\theta) + \frac{e+\cos(\theta)}{1+e\cos(\theta)}\right)F_\theta\right] \tag{5.4}$$

$$\frac{di}{dt} = \frac{r\cos(u)}{na^2\sqrt{1-e^2}}F_\perp \tag{5.5}$$

$$\frac{d\Omega}{dt} = \frac{r\sin(u)F_\perp}{na^2\sqrt{1-e^2}\sin(i)} \tag{5.6}$$

$$\frac{d\omega_p}{dt} = \frac{\sqrt{1-e^2}}{nae}\left[-\cos(\theta)F_R + \frac{2+e\cos(\theta)}{1+e\cos(\theta)}\sin(\theta)F_\theta\right] - \frac{r\sin(u)}{H\tan(i)}F_\perp \tag{5.7}$$

$$\frac{d\theta}{dt} = \sqrt{\frac{\mu}{p^3}}(1+e\cos\theta)^2 + \frac{\sqrt{1-e^2}}{nae}\cos(\theta)F_R - \frac{\sqrt{1-e^2}}{nae}\frac{2+e\cos(\theta)}{1+e\cos(\theta)}F_\theta \tag{5.8}$$

For the thrust accelerations, F_R is directed along the radius vector and its positive direction points outwards. F_θ lies in the orbital plane and points in the direction of motion of the spacecraft. $F_\perp$ is perpendicular to the orbital plane and points in the direction of the angular momentum vector. From [12] it is known that Kepler elements have the disadvantage that they contain singularities at $i = 0°$ or $i = 180°$ and at $e = 0$ or $e = 1$. A solution for avoiding these is to use the Modified Equinoctial Elements (MEE) [29] [12]. These MEE are defined from the conventional Kepler elements by means of Equations 5.9 to 5.14.

$$p = a\left(1-e^2\right) \tag{5.9}$$

$$f = e\cos\left(\omega_p + \Omega\right) \tag{5.10}$$

$$g = e\sin\left(\omega_p + \Omega\right) \tag{5.11}$$

$$h = \tan(i/2)\cos\Omega \tag{5.12}$$

$$k = \tan(i/2)\sin\Omega \tag{5.13}$$

$$L = \Omega + \omega_p + \theta \tag{5.14}$$

It is possible to combine these MEE with the Gauss planetary equations and so create the Gauss equations in MEE. These are given by Equations 5.15 to 5.20:

$$\frac{dp}{dt} = \sqrt{\frac{p}{\mu}}\frac{2pF_\vartheta}{C_1} \tag{5.15}$$

$$\frac{df}{dt} = \sqrt{\frac{p}{\mu}}\left[F_R \sin(L) + \frac{[(C_1+1)\cos(L)+f]\,F_\vartheta}{C_1} - \frac{g(h\sin(L)-k\cos(L))F_\perp}{C_1}\right] \tag{5.16}$$

$$\frac{dg}{dt} = \sqrt{\frac{p}{\mu}}\left[-F_R \cos(L) + \frac{[(C_1+1)\sin(L)+g]\,F_\vartheta}{C_1} - \frac{f(h\sin(L)-k\cos(L))F_\perp}{C_1}\right] \tag{5.17}$$

$$\frac{dh}{dt} = \sqrt{\frac{p}{\mu}}\frac{C_2 F_\perp}{2C_1}\cos(L) \tag{5.18}$$

$$\frac{dk}{dt} = \sqrt{\frac{p}{\mu}}\frac{C_2 F_\perp}{2C_1}\sin(L) \tag{5.19}$$

$$\frac{dL}{dt} = \sqrt{p\mu}\left(\frac{C_1}{p}\right)^2 + \sqrt{\frac{p}{\mu}}\frac{(h\sin(L)-k\cos(L))F_\perp}{C_1} \tag{5.20}$$

In these equations, C_1 is given by $C_1 = p/r = 1 + f\cos(L) + g\sin(L)$ and C_2 by $C_2 = 1 + h^2 + k^2$. Although the MEE prevent the singularities occurring in the conventional Kepler elements, they have the major disadvantage that they do not give a direct or easy insight into what is happening in a certain model. This is because they do not represent a physical quantity (except for the semi-latus rectum and true longitude) such as the Kepler elements. Therefore, the use of Kepler elements is still preferred if the nature of the problem allows it. With respect to the thesis topic in this report where the eccentricity is expected to go through the singularity of $e = 1$, it is strongly encouraged to use the MEE.

5.4 Reference trajectory

In order to get an idea of what the effects are of low-thrust propulsion in the Tisserand graph, some reference trajectories are integrated forward in time using the Gauss planetary equations which are available and ready to use in Tudat. These same initial conditions will be used to verify a method of creating low-thrust legs in the Tisserand graph that does not require integration in time but rather in true longitude. This will speed up the calculation time in the optimizations of Chapter 6.

5.4.1 Relations for tangential thrust

The first thing to mention is that all initial conditions used in the integration hold an inclination, Right Ascension of the Ascending Node, argument of pericenter and true anomaly (thus also the true longitude, Equation 5.14) set to zero. Then only the eccentricity (e) and semi-major axis (a) remain. These are also the only quantities required to create a Tisserand graph. The exact values of them are given in Table 5.2. For these reference trajectories a constant thrust acceleration of $10^{-4}\mathrm{m/s^2}$ was assumed which implies a constant mass of the spacecraft. Whether this assumption is valid will be shown in later sections. The corresponding thrust level has been proven to be achievable in earlier missions (Section 5.1). Also, it is assumed that the thrust acts only in tangential direction. This is to reduce the complexity of the method developed in Section 5.5. Because the thrust is acting parallel to the velocity vector (tangential) its direction is dependent on the flight-path angle (γ). Figure 5.3 gives an illustration of how this flight-path angle is defined along a trajectory within the orbital plane. By means of Equations 5.21 and 5.22 the flight-path angle can be defined as a function of

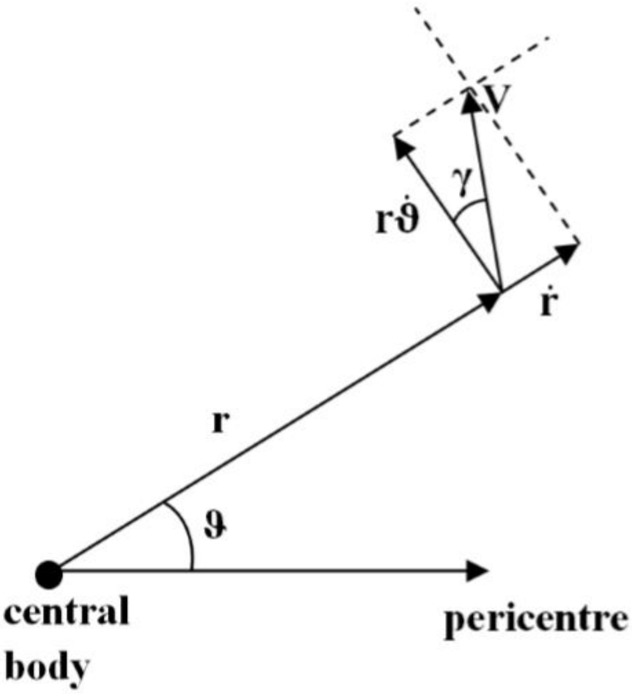

Figure 5.3: The flight-path angle defined in the orbital plane of a trajectory [10].

Kepler elements.

$$V \sin\gamma = V_r = \sqrt{\frac{\mu}{p}}(e \sin\vartheta) \tag{5.21}$$

$$V \cos\gamma = V_T = \sqrt{\frac{\mu}{p}}(1 + e \cos\vartheta) \tag{5.22}$$

As stated before, the use of MEE is preferred over conventional Kepler elements because they avoid the singularities around zero inclination and eccentricities close to zero and one. Therefore Equations 5.21 and 5.22 are converted into MEE:

$$V^2 = \mu\left(\frac{2}{r} - \frac{1}{a}\right) = \mu\left(\frac{2(1 + f\cos L + g\sin L)}{p} - \frac{1 - f^2 - g^2}{p}\right) \tag{5.23}$$

$$r = \frac{p}{1 + e\cos\vartheta} = \frac{p}{1 + f\cos L + g\sin L} \tag{5.24}$$

$$\begin{aligned} e\sin\vartheta &= \sqrt{f^2 + g^2}\sin\left(L - \tan^{-1}\frac{g}{f}\right) \\ &= \sqrt{f^2 + g^2}\left(\frac{\sin L}{\sqrt{\left[\frac{g}{f}\right]^2 + 1}} + \frac{\frac{g}{f}\cos L}{\sqrt{\left[\frac{g}{f}\right]^2 + 1}}\right) \\ &= f\sin L - g\cos L \end{aligned} \tag{5.25}$$

Now that the flight-path angle is expressed in terms of MEE, the two components of the tangential thrust acceleration that are used in the Gauss planetary equations (Equations 5.3 to 5.20) are given by Equations 5.26 and 5.27.

$$F_R = F_T \sin\gamma \tag{5.26}$$

$$F_\vartheta = F_T \cos\gamma \tag{5.27}$$

5.4.2 Integrator

The integrator used for creating the reference trajectories is a Runge-Kutta 4 (RK4) method. It has a comparable accuracy of a fourth-order Taylor expansion [21]. Although the RK4 integrator is generally not known as the most efficient one to use, it performs well enough to provide reference orbits against which the method developed in Section 5.5 (accurate up to second-order polynomial) can be tested. The main advantages of using the RK4 method are that it is a straightforward method to implement, produces results very quickly, and is already available in Tudat. The RK4 integrator is a fixed step size method. This implies that faster dynamics will be the main source of the integration error. Considering that the only disturbing force acting on the spacecraft is the thrust, none of these faster dynamics (for example, a gravity assist) are expected to be present during the reference trajectory integration. Also, using the MEE instead of cartesian coordinates avoids the presence and severity of faster dynamics.

Before creating the reference orbits, it is worth investigating what a good accuracy might be for them. The first thing to consider is the error that arises during the integration due to the time steps of the numerical integration. This error is shown in Figure 5.4. The figure shows the relative difference in radial position with respect to a 10 s time step integration of the trajectory that is shown in Figure 5.1 (1.5 sidereal year).

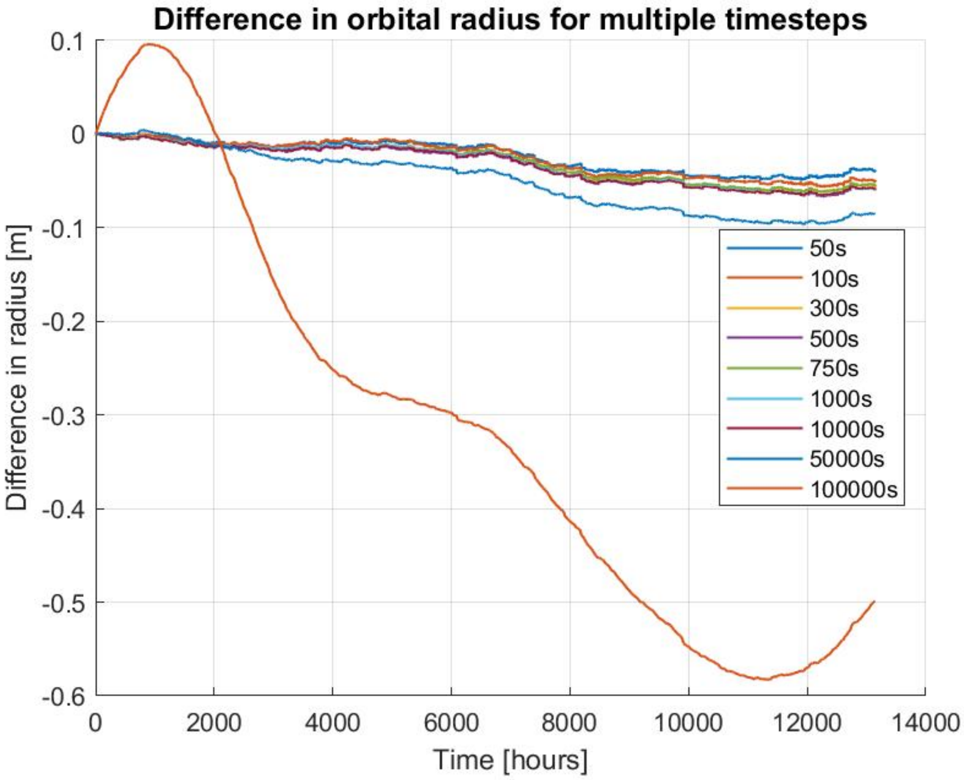

Figure 5.4: Relative difference in orbital radius for nine different time steps compared with a reference with 10 seconds time step.

By observing Figure 5.4, it is concluded that there is no need to choose time steps smaller than 50000 seconds in terms of accuracy. However, it is argued here that having a significant number of data points for verifying the methods presented further in this chapter is of great importance. A smaller time step would require more memory on the computer and is therefore avoided. After a brief evaluation of the different time steps, the author concluded that a time step of 300 s is the best choice. This was also concluded after a similar investigation in [10].

5.4.3 Integration results

The relations explained in Subsection 5.4.1 and the integration scheme described in the previous section need six initial conditions that will be integrated forward in time. Three different values for the semi-major axis are taken that will result in three different energy regions in the Tisserand graph; and two values for the eccentricity. Combining these results in six different reference trajectories on the Tisserand graph. The precise values for the eccentricity and semi-major axis are presented in Table 5.2.

	Eccentricity [-]	Semi-major axis [AU]
IC1	0.1	1.05
IC2	0.4	1.05
IC3	0.1	2.8
IC4	0.4	2.8
IC5	0.1	3.8
IC6	0.4	3.8

Table 5.2: Initial conditions (IC) of the reference trajectories in terms of eccentricity and semi-major axis.

Figure 5.5 shows the result on the Tisserand graph. Note that the initial conditions five and six are integrated five sidereal years forward in time and the other four only for two sidereal years. This was done because integrating them only for two sidereal years would not visualize the effects of low-thrust propulsion on the Tisserand graph. On the other hand, integrating the other four initial conditions for five sidereal years would make the graph too chaotic to be used for proper comparison with the method developed in Section 5.5.

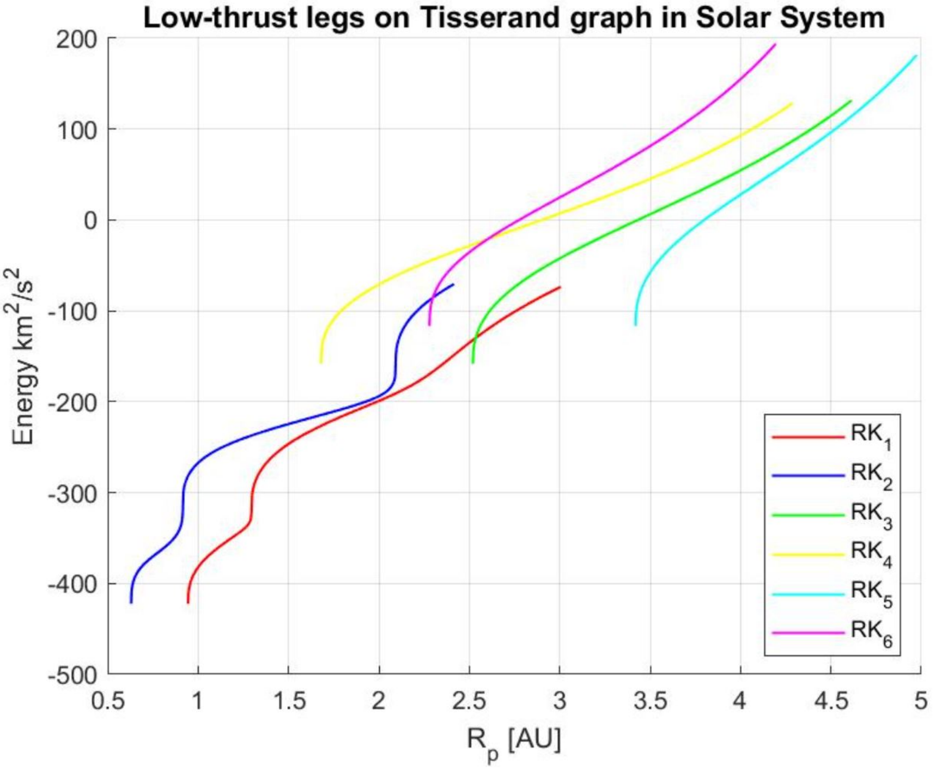

Figure 5.5: Integrated low-thrust trajectories on the Tisserand graph. Integration was done by RK4 with 300 seconds step size.

Observing Figure 5.5 one notices a curved shape in each line. To better explain these, the second initial condition RK_2 and the subsequent trajectory is plotted separately in Figure 5.6 with indications for the true anomaly on it. The true anomaly gives more direct insight into

where the spacecraft is located along the orbit. In Figure 5.6 the black stars indicate a true anomaly of 0° or 360°, thus the start of a new orbit (w.r.t. the initial orbit). The purple stars indicate a true anomaly of 180°. Using these two, one can distinguish two parts of a trajectory. The first one is located close to the pericenter, where the energy increases, but the pericenter radius does not. This results in the vertical sections of the lines on the Tisserand graph. The second part is located close to the apocenter, indicated by the purple stars. The pericenter radius increases relatively faster around these points than the orbital energy, which translates into more horizontal sections of the lines on the Tisserand graph.
The point where the transition between these two parts occurs is known to be difficult and case dependent. In Figure 5.6, two angles per bent are indicated. These two angles indicate two true anomalies in between which the bend usually occurs. The first two are 90° and 135°. The reversed transition (bend) usually occurs at 225° and 270°. Again, finding a general rule for the location at which this bend occurs is challenging. Between the true anomalies mentioned in this paragraph, the spacecraft passes the semi-minor axis of the trajectory. One could argue that the true anomaly corresponding with the bend also corresponds with the true anomaly of semi-minor axis passage. However, this does not hold for higher orbital energies.

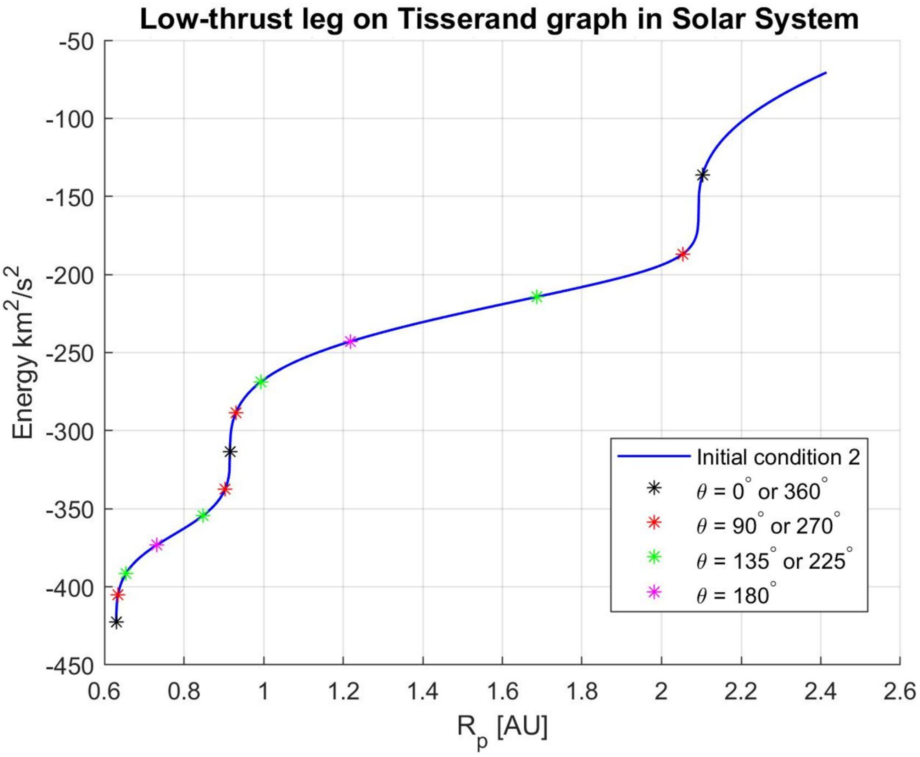

Figure 5.6: Separate plot of initial condition 2 from Figure 5.5 including extra indications for the true anomaly.

5.5 Taylor-series expansion of orbital elements

This section presents a simple and computationally fast method to include low-thrust propulsive legs in a Tisserand plot. The aim is to reproduce the same trajectories as shown in Figure 5.5. As discussed in the foregoing section, one can separate three parts in a full revolution on the Tisserand plot. The first part is around the pericenter where the energy is increased and the pericenter radius stays approximately the same. A second part is around the apocenter where the increase in pericenter occurs relatively fast with a small increase in orbital energy. The third part is the transition between these, also known as the ”bend”. It is expected that a second-order Taylor expansion should be able to model this ”bend” accurately enough. Ideally, it should be possible to resolve a trajectory analytically using only one Taylor-series expansion for all three parts. One full revolution would then consist of 5 parabolas. A first for the initial pericenter passage, a second for the first bend, a third for the apocenter passage, a fourth for the second bend and the fifth from the bend to the next pericenter passage. By patching these together, an approximation of a low-thrust trajectory (one full revolution) on the Tisserand graph is created. The method will be developed using a second-order Taylor-series expansion of the relevant Gauss planetary equations. The reason for choosing a second-order Taylor-series expansion instead of a direct numerical integration lies in the computational speed. The next chapter will combine this method with the optimizations from Chapter 4 to find optimal low-thrust satellite-aided planetary capture trajectories. A direct numerical integration would result in much longer computational time and is therefor avoided. In [10] three different Taylor-series expansions were investigated: one using conventional Kepler elements, a second using the argument of latitude and the last based on the MEE. First a brief discussion follows on the motivation of using the MEE instead of the Kepler elements with true anomaly or argument of latitude as running parameter. For brevity, only the motivation will be given in this report and the reader is referred to [10] for a quantitative explanation and relations when using the Kepler elements. Then the relevant equations are derived for the MEE and results are compared with those from RK4 integration in Subsection 5.5.4.

5.5.1 Limitations using Kepler elements

The limitations of conventional Kepler elements were already mentioned before. The first is that circular orbits cannot be integrated. This, however, does not seem to be a problem for satellite-aided planetary capture trajectories on the Tisserand graph since the orbits considered would be far beyond circular. Moreover, a Tisserand graph is a useful tool for designing multiple gravity assist trajectories under the forgoing assumption of the Tisserand parameter that the orbits of the secondary bodies are all circular. Therefore, if the orbit of the spacecraft would be circular, no combination of the orbital radius of the spacecraft and the secondary could suggest a proper gravity assist. This is also the region where no V_∞ lines are defined on the Tisserand graph (e.g., the region in the lower right corner). Another limitation is that conventional Kepler elements are singular for the transition between closed and open orbits (e.g., parabolic orbits). Concerning low-thrust satellite-aided planetary capture trajectories, this is a region of great interest. Moreover, as was shown in Figure 3.3, there are possible sequences of gravity assists where the spacecraft gets orbital energy greater than zero (i.e. an open orbit). Even more important is that these trajectories have already been flown in the past by the Voyager (one and two) spacecraft [3]. The last and most important limitation of using the conventional Kepler elements for the Taylor-series expansion is that the true anomaly at a certain point could start to decrease due to the increasing argument of pericenter. When this occurs, the Taylor-series is no longer valid and is stopped. This problem often occurs at higher orbital energy levels or for nearly circular orbits. Considering the high orbital energy levels of a low-thrust satellite-aided planetary capture trajectory and the orbital energies of the Galilean moons used in the previous chapter, it is expected that this last limitation of conventional Kepler elements will raise problems. Because conventional Kepler elements will not be used in the Taylor-series expansion due to the limitations mentioned above, the relations will not be mentioned in this report for brevity. For more information the reader is referred to [10].

5.5.2 Limitations using argument of latitude

The previous section explained the limitations of using the Kepler elements in a Taylor expansion describing low-thrust trajectories. The most crucial problem was that the true anomaly does not always increase under the influence of thrust. This is due to a fast-changing argument of periapsis, which at its turn occurs for nearly circular orbits or long thrust periods at the apocenter. When these long thrust periods occur, the orbit considered becomes circular before becoming elliptic again, which means that the apocenter and pericenter have switched places. In the Tisserand graph this corresponds to curves that are closely located to the regions where the Tisserand graph is not defined (e.g. circular orbits for the spacecraft). A solution to this problem is to combine (Equation 5.28) the true anomaly with the argument of pericenter and so create the Argument Of Latitude (AOL). Because the argument of latitude is defined with respect to a fixed point in space, it is always increasing. Therefore using the AOL as the running parameter will ensure that no maximum is reached and thus that the Taylor-series expansion is valid in more regions of the Tisserand graph.

$$u = \theta + \omega_p \tag{5.28}$$

In [10] the accuracy of using the AOL as running parameter was investigated and it became clear that it performed better for orbits at higher energies under the influence of tangential thrust. However, for nearly circular orbits, the error in pericenter radius and orbital energy still becomes large [10]. Because the Taylor-series expansion using the AOL as running parameter uses the conventional Kepler elements, singularities arise at energies close to zero (e.g., parabolic orbits). A Tisserand graph does not indicate any limitations on the orbital energy and concerning low-thrust satellite-aided planetary capture, this region is of great interest. Therefore, a method that is both more accurate and valid in all energy regions is preferred. Because conventional Kepler elements with the AOL as running parameter will not be used in the Taylor-series expansion due to the limitations mentioned above, the Taylor-series expansions will also not be mentioned in this report for brevity. For more information, the reader is referred again to [10].

5.5.3 Taylor-series expansion using MEE

The singularities that occur when using the Kepler elements (true anomaly or AOL as running parameter) around parabolic orbital energies are critical regarding this thesis report's topic. Low-thrust satellite-aided planetary capture trajectories go from a positive to a negative energy regime. In other words, they go through the regions where the Kepler elements become singular. Therefore the use of MEE is considered the only possible approach for implementing them in the Taylor-series expansion. In the MEE the true longitude (L) is the running parameter. By assuming that there is no out-of-plane thrust the true longitude behaves in the same way as the AOL does, which avoids that the derivatives become negative. This already clears out the problems of using the true anomaly as the running parameter.

First, the Gauss equations in MEE of the relevant parameters are repeated here. Because no out-of-plane thrust is considered ($F_\perp = 0$) the only relevant parameters are p, f, g and L. The other two MEE have zero derivatives when only applying thrust in the orbital plane and are therefore not repeated here.

$$\frac{dp}{dt} = \sqrt{\frac{p}{\mu}}\frac{2pF_\vartheta}{C_1} \tag{5.29}$$

$$\frac{df}{dt} = \sqrt{\frac{p}{\mu}}\left[F_R \sin(L) + \frac{[(C_1+1)\cos(L)+f]\,F_\vartheta}{C_1}\right] \tag{5.30}$$

$$\frac{dg}{dt} = \sqrt{\frac{p}{\mu}}\left[-F_R \cos(L) + \frac{[(C_1+1)\sin(L)+g]\,F_\vartheta}{C_1}\right] \tag{5.31}$$

$$\frac{dL}{dt} = \sqrt{p\mu}\left(\frac{C_1}{p}\right)^2 \tag{5.32}$$

where:

$$C_1 = p/r = 1 + f\cos(L) + g\sin(L) \tag{5.33}$$

The first-order derivatives with respect to the true longitude are obtained by dividing the appropriate Gauss equations in MEE. In other words, dividing Equations 5.29,5.30 and 5.31 by 5.32. Then the second order total derivatives are given by:

$$\frac{d}{dL}\left(\frac{dp}{dL}\right) = \frac{\partial}{\partial L}\left(\frac{dp}{dL}\right) + \frac{dp}{dL}\frac{\partial}{\partial p}\left(\frac{dp}{dL}\right) + \frac{df}{dL}\frac{\partial}{\partial f}\left(\frac{dp}{dL}\right) + \frac{dg}{dL}\frac{\partial}{\partial g}\left(\frac{dp}{dL}\right) \tag{5.34}$$

$$\frac{d}{dL}\left(\frac{df}{dL}\right) = \frac{\partial}{\partial L}\left(\frac{df}{dL}\right) + \frac{dp}{dL}\frac{\partial}{\partial p}\left(\frac{df}{dL}\right) + \frac{df}{dL}\frac{\partial}{\partial f}\left(\frac{df}{dL}\right) + \frac{dg}{dL}\frac{\partial}{\partial g}\left(\frac{df}{dL}\right) \tag{5.35}$$

$$\frac{d}{dL}\left(\frac{dg}{dL}\right) = \frac{\partial}{\partial L}\left(\frac{dg}{dL}\right) + \frac{dp}{dL}\frac{\partial}{\partial p}\left(\frac{dg}{dL}\right) + \frac{df}{dL}\frac{\partial}{\partial f}\left(\frac{dg}{dL}\right) + \frac{dg}{dL}\frac{\partial}{\partial g}\left(\frac{dg}{dL}\right) \tag{5.36}$$

Now, the quotient rule gives the partial derivatives that occur in these equations. Please note that d is referred to as a total derivative and ∂ a partial derivative. The partial derivatives are given here in Equations 5.37 to 5.48.

$$\frac{\partial}{\partial L}\left(\frac{dp}{dL}\right) = \frac{\partial}{\partial L}\left[\left(\frac{dL}{dt}\right)^{-1}\cdot\frac{dp}{dt}\right] = \left(\frac{dL}{dt}\right)^{-1}\cdot\frac{\partial}{\partial L}\left(\frac{dp}{dt}\right) - \frac{dp}{dt}\cdot\left(\frac{dL}{dt}\right)^{-2}\cdot\frac{\partial}{\partial L}\left(\frac{dL}{dt}\right) \tag{5.37}$$

$$\frac{\partial}{\partial L}\left(\frac{df}{dL}\right) = \frac{\partial}{\partial L}\left[\left(\frac{dL}{dt}\right)^{-1}\cdot\frac{df}{dt}\right] = \left(\frac{dL}{dt}\right)^{-1}\cdot\frac{\partial}{\partial L}\left(\frac{df}{dt}\right) - \frac{df}{dt}\cdot\left(\frac{dL}{dt}\right)^{-2}\cdot\frac{\partial}{\partial L}\left(\frac{dL}{dt}\right) \tag{5.38}$$

$$\frac{\partial}{\partial L}\left(\frac{dg}{dL}\right) = \frac{\partial}{\partial L}\left[\left(\frac{dL}{dt}\right)^{-1}\cdot\frac{dg}{dt}\right] = \left(\frac{dL}{dt}\right)^{-1}\cdot\frac{\partial}{\partial L}\left(\frac{dg}{dt}\right) - \frac{dg}{dt}\cdot\left(\frac{dL}{dt}\right)^{-2}\cdot\frac{\partial}{\partial L}\left(\frac{dL}{dt}\right) \tag{5.39}$$

$$\frac{\partial}{\partial p}\left(\frac{dp}{dL}\right) = \frac{\partial}{\partial p}\left[\left(\frac{dL}{dt}\right)^{-1}\cdot\frac{dp}{dt}\right] = \left(\frac{dL}{dt}\right)^{-1}\cdot\frac{\partial}{\partial p}\left(\frac{dp}{dt}\right) - \frac{dp}{dt}\cdot\left(\frac{dL}{dt}\right)^{-2}\cdot\frac{\partial}{\partial p}\left(\frac{dL}{dt}\right) \tag{5.40}$$

$$\frac{\partial}{\partial p}\left(\frac{df}{dL}\right) = \frac{\partial}{\partial p}\left[\left(\frac{dL}{dt}\right)^{-1}\cdot\frac{df}{dt}\right] = \left(\frac{dL}{dt}\right)^{-1}\cdot\frac{\partial}{\partial p}\left(\frac{df}{dt}\right) - \frac{df}{dt}\cdot\left(\frac{dL}{dt}\right)^{-2}\cdot\frac{\partial}{\partial p}\left(\frac{dL}{dt}\right) \tag{5.41}$$

$$\frac{\partial}{\partial p}\left(\frac{dg}{dL}\right) = \frac{\partial}{\partial p}\left[\left(\frac{dL}{dt}\right)^{-1}\cdot\frac{dg}{dt}\right] = \left(\frac{dL}{dt}\right)^{-1}\cdot\frac{\partial}{\partial p}\left(\frac{dg}{dt}\right) - \frac{dg}{dt}\cdot\left(\frac{dL}{dt}\right)^{-2}\cdot\frac{\partial}{\partial p}\left(\frac{dL}{dt}\right) \tag{5.42}$$

$$\frac{\partial}{\partial f}\left(\frac{dp}{dL}\right) = \frac{\partial}{\partial f}\left[\left(\frac{dL}{dt}\right)^{-1}\cdot\frac{dp}{dt}\right] = \left(\frac{dL}{dt}\right)^{-1}\cdot\frac{\partial}{\partial f}\left(\frac{dp}{dt}\right) - \frac{dp}{dt}\cdot\left(\frac{dL}{dt}\right)^{-2}\cdot\frac{\partial}{\partial f}\left(\frac{dL}{dt}\right) \tag{5.43}$$

$$\frac{\partial}{\partial f}\left(\frac{df}{dL}\right) = \frac{\partial}{\partial f}\left[\left(\frac{dL}{dt}\right)^{-1}\cdot\frac{df}{dt}\right] = \left(\frac{dL}{dt}\right)^{-1}\cdot\frac{\partial}{\partial f}\left(\frac{df}{dt}\right) - \frac{df}{dt}\cdot\left(\frac{dL}{dt}\right)^{-2}\cdot\frac{\partial}{\partial f}\left(\frac{dL}{dt}\right) \tag{5.44}$$

$$\frac{\partial}{\partial f}\left(\frac{dg}{dL}\right) = \frac{\partial}{\partial f}\left[\left(\frac{dL}{dt}\right)^{-1}\cdot\frac{dg}{dt}\right] = \left(\frac{dL}{dt}\right)^{-1}\cdot\frac{\partial}{\partial f}\left(\frac{dg}{dt}\right) - \frac{dg}{dt}\cdot\left(\frac{dL}{dt}\right)^{-2}\cdot\frac{\partial}{\partial f}\left(\frac{dL}{dt}\right) \tag{5.45}$$

$$\frac{\partial}{\partial g}\left(\frac{dp}{dL}\right) = \frac{\partial}{\partial g}\left[\left(\frac{dL}{dt}\right)^{-1}\cdot\frac{dp}{dt}\right] = \left(\frac{dL}{dt}\right)^{-1}\cdot\frac{\partial}{\partial g}\left(\frac{dp}{dt}\right) - \frac{dp}{dt}\cdot\left(\frac{dL}{dt}\right)^{-2}\cdot\frac{\partial}{\partial g}\left(\frac{dL}{dt}\right) \tag{5.46}$$

$$\frac{\partial}{\partial g}\left(\frac{df}{dL}\right) = \frac{\partial}{\partial g}\left[\left(\frac{dL}{dt}\right)^{-1}\cdot\frac{df}{dt}\right] = \left(\frac{dL}{dt}\right)^{-1}\cdot\frac{\partial}{\partial g}\left(\frac{df}{dt}\right) - \frac{df}{dt}\cdot\left(\frac{dL}{dt}\right)^{-2}\cdot\frac{\partial}{\partial g}\left(\frac{dL}{dt}\right) \tag{5.47}$$

$$\frac{\partial}{\partial g}\left(\frac{dg}{dL}\right) = \frac{\partial}{\partial g}\left[\left(\frac{dL}{dt}\right)^{-1}\cdot\frac{dg}{dt}\right] = \left(\frac{dL}{dt}\right)^{-1}\cdot\frac{\partial}{\partial g}\left(\frac{dg}{dt}\right) - \frac{dg}{dt}\cdot\left(\frac{dL}{dt}\right)^{-2}\cdot\frac{\partial}{\partial g}\left(\frac{dL}{dt}\right) \tag{5.48}$$

These equations also contain other partial derivatives. The ones derived with respect to the true longitude are given by Equations 5.49 to 5.52:

$$\frac{\partial}{\partial L}\left(\frac{dp}{dt}\right) = \sqrt{\frac{p}{\mu}}\frac{2p}{C_1^2}(f\sin L - g\cos L)F_\vartheta \tag{5.49}$$

$$\begin{aligned}\frac{\partial}{\partial L}\left(\frac{df}{dt}\right) = \sqrt{\frac{p}{\mu}}\Bigg[&F_R\cos L + \frac{F_\vartheta}{C_1}(g\cos(2L) - f\sin(2L) - 2\sin(L)) \\ &+ \frac{[(C_1+1)\cos(L)+f]\,F_\vartheta}{C_1^2}(f\sin(L) - g\cos(L))\Bigg]\end{aligned} \tag{5.50}$$

$$\begin{aligned}\frac{\partial}{\partial L}\left(\frac{dg}{dt}\right) = \sqrt{\frac{p}{\mu}}\Bigg[&F_R\sin L + \frac{F_\vartheta}{C_1}(g\sin(2L) + f\cos(2L) + 2\cos(L)) \\ &+ \frac{[(C_1+1)\sin(L)+g]\,F_\vartheta}{C_1^2}(f\sin(L) - g\cos(L))\Bigg]\end{aligned} \tag{5.51}$$

$$\frac{\partial}{\partial L}\left(\frac{dL}{dt}\right) = -2\sqrt{\frac{\mu}{p^3}}C_1(f\sin(L) - g\cos(L)) \tag{5.52}$$

Following up, the partial derivatives with respect to p are given by:

$$\frac{\partial}{\partial p}\left(\frac{dp}{dt}\right) = 3\sqrt{\frac{p}{\mu}}\frac{F_\vartheta}{C_1} \tag{5.53}$$

$$\frac{\partial}{\partial p}\left(\frac{df}{dt}\right) = \frac{1}{2p}\frac{df}{dt} \tag{5.54}$$

$$\frac{\partial}{\partial p}\left(\frac{dg}{dt}\right) = \frac{1}{2p}\frac{dg}{dt} \tag{5.55}$$

$$\frac{\partial}{\partial p}\left(\frac{dL}{dt}\right) = -\frac{3}{2}\sqrt{\frac{\mu}{p^5}}C_1^2 \tag{5.56}$$

The ones with respect to f are given by:

$$\frac{\partial}{\partial f}\left(\frac{dp}{dt}\right) = -2\sqrt{\frac{p^3}{\mu}}\frac{F_\vartheta}{C_1^2}\cos L \tag{5.57}$$

$$\frac{\partial}{\partial f}\left(\frac{df}{dt}\right) = \sqrt{\frac{p}{\mu}}\frac{F_\vartheta}{C_1}\left[1 + \cos^2 L - \frac{([C_1+1]\cos(L)+f)\cos(L)}{C_1}\right] \tag{5.58}$$

$$\frac{\partial}{\partial f}\left(\frac{dg}{dt}\right) = \sqrt{\frac{p}{\mu}}\frac{F_\vartheta}{C_1}\left[\frac{1}{2}\sin(2L) - \frac{([C_1+1]\sin(L)+g)\cos(L)}{C_1}\right] \tag{5.59}$$

$$\frac{\partial}{\partial f}\left(\frac{dL}{dt}\right) = 2\sqrt{\frac{\mu}{p^3}}C_1\cos(L) \tag{5.60}$$

and the ones with respect to g are given by:

$$\frac{\partial}{\partial g}\left(\frac{dp}{dt}\right) = -2\sqrt{\frac{p^3}{\mu}}\frac{F_\vartheta}{C_1^2}\sin L \tag{5.61}$$

$$\frac{\partial}{\partial g}\left(\frac{df}{dt}\right)=\sqrt{\frac{p}{\mu}}\frac{F_\vartheta}{C_1}\left[\frac{1}{2}\sin(2L)-\frac{([C_1+1]\cos(L)+f)\sin(L)}{C_1}\right] \tag{5.62}$$

$$\frac{\partial}{\partial g}\left(\frac{dg}{dt}\right)=\sqrt{\frac{p}{\mu}}\frac{F_\vartheta}{C_1}\left[1+\sin^2 L-\frac{([C_1+1]\sin(L)+g)\sin(L)}{C_1}\right] \tag{5.63}$$

$$\frac{\partial}{\partial g}\left(\frac{dL}{dt}\right)=2\sqrt{\frac{\mu}{p^3}}C_1\sin(L) \tag{5.64}$$

With all the partial derivatives combined to create the total derivatives of all the relevant MEE, one can write down the second-order Taylor-series expansion of p, f and g.

$$p_n(L)=p_{n-1}+\frac{\mathrm{d}p}{\mathrm{d}L}(L_n-L_{n-1})+\frac{d}{dL}\left(\frac{dp}{dL}\right)\frac{(L_n-L_{n-1})^2}{2} \tag{5.65}$$

$$f_n(L)=f_{n-1}+\frac{\mathrm{d}f}{\mathrm{d}L}(L_n-L_{n-1})+\frac{d}{dL}\left(\frac{df}{dL}\right)\frac{(L_n-L_{n-1})^2}{2} \tag{5.66}$$

$$g_n(L)=g_{n-1}+\frac{\mathrm{d}g}{\mathrm{d}L}(L_n-L_{n-1})+\frac{d}{dL}\left(\frac{dg}{dL}\right)\frac{(L_n-L_{n-1})^2}{2} \tag{5.67}$$

All these expressions are implemented in Tudat and use the same initial conditions as in Figure 5.5 to create the same reference trajectories on the Tisserand graph. The result is shown in Figure 5.7. All the curves in the figure represent low-thrust legs with initial conditions as stated in Table 5.2. The dashed lines represent the results of the second-order Taylor-series expansion and the full lines are the same results of the RK4 integration as presented in Figure 5.5. In Figure 5.7 one notices that there is a very good overlap in the beginning of the propagation. Depending on the initial condition, there is an increasing difference between the Taylor-series expansion and the RK4 integration. This is further quantified in the following section on accuracy. For now, the most important thing to notice is the smooth transition from a closed orbit (with negative orbital energy) towards an open orbit (with positive orbital energy). This is important with respect to this thesis research topic and the aim of using the MEE elements instead of Kepler elements.

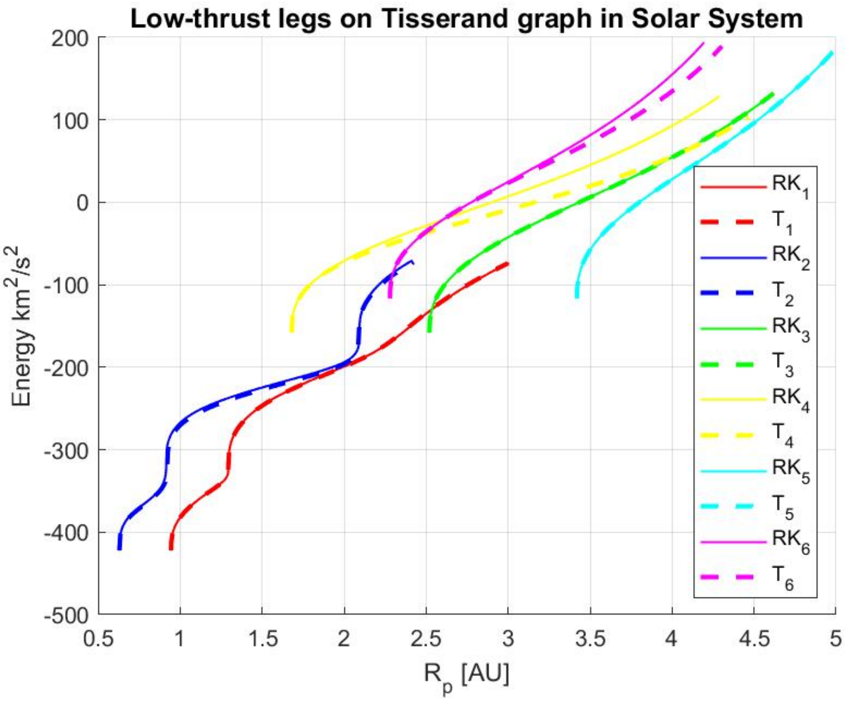

Figure 5.7: Trajectories with tangential thrust with initial conditions equal to Figure 5.5. Result of both the RK4 integration and Taylor-series expansion in terms of MEE are shown.

5.5.4 Accuracy

The Taylor expansion method results are plotted using Matlab to give a simple comparison between the results of the RK4 integration. This is done by sampling 100 values of the true longitude. This holds a range from zero to the final true longitude. This final true longitude is different for all initial conditions but in general corresponds to the time frame of two sidereal years. For initial conditions one and two the final true longitude is cut of at six to make the graph more clear. Since different initial conditions correspond to a different orbital period, the maximum values for true longitude of each initial condition propagated forward in time will be different. For all values of the true longitude (100 points), the radius is calculated using the MEE resulting from the Taylor-series expansion. The same is done with the results from the RK4 integration and the difference between them is calculated and presented in Figure 5.8. The errors shown a representation of the differences between the dashed- and full lines of Figure 5.7. The colors used for each initial condition are the same as in Figure 5.7. From both Figures 5.7 and 5.8 one learns that initial conditions holding a higher eccentricity behave less than lower eccentricities. Different initial orbital energies (e.g., semi-major axis) do not seem to have a large impact on the accuracy. Figure 5.8 also shows a relatively large increase of the error in radius for initial condition four. A radial error of 0.16 AU for an orbit with a pericenter at 4.25 AU is a relative error of 3.76%. This, however, is an error that arises after two sidereal years. This error will not be of any concern with respect to low-thrust satellite-aided planetary capture trajectories since these trajectories usually hold much shorter propagation times (order of days instead of years). Therefore the author expects that the second-order Taylor-series expansion can be combined with the method from Chapter 4 for analyzing low-thrust satellite-aided planetary capture trajectories in the Tisserand graph.

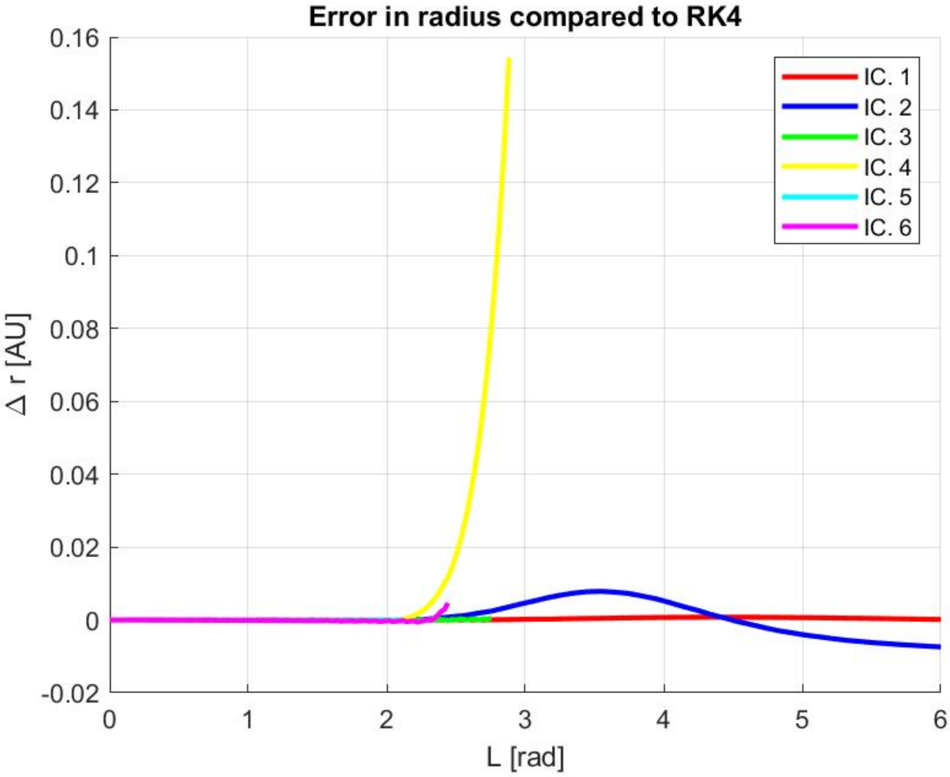

Figure 5.8: Comparison of radius using second-order Taylor-series expansion with RK4 results.

Chapter 6

Low-thrust capture sequences

This chapter combines the ballistic satellite-aided planetary capture trajectory optimization with low-thrust legs in the Tisserand graph. Section 6.1 presents the fitness function. Then the initial conditions are reevaluated and the results are presented similarly as in Chapter 4. The chapter closes with some concluding remarks in Section 6.4.

6.1 Fitness function

By combining the method for low-thrust legs presented in the previous chapter with the ballistic fitness function explained in Subsection 4.2.1 it is possible to find optimal flyby sequences in the Tisserand graph with forgoing, intermediate, and subsequent low-thrust legs. This section explains this new fitness function. Note that the acceleration of the low-thrust propulsion system is 10^{-4}m/s^2 and the spacecraft's initial mass is 4000 kg, equal to the characteristics used in the previous chapter.

1. Obtain initial perijove of the hyperbolic approach trajectory from parameter vector. Together with the initial orbital energy, this creates the first point on the Tisserand graph.
2. Calculate the initial eccentricity using Equation 6.3
3. Create a range for the true longitude with the initial value set to -0.95 times the hyperbolic limit value. Set the number of data points equal to 10000.
4. Obtain the flyby moon from the preset flyby sequence. If the preset sequence demands a JOI, proceed to step 7.
5. Propagate the trajectory over the range in true longitude using the low-thrust propulsion Taylor-series expansion and check if the spacecraft's radial position along the trajectory comes in the vicinity (SOI) of the orbital radius of the flyby moon. The radius is calculated using Equation 5.24.
6. When the spacecraft enters the SOI of the flyby moon, calculate the new orbital elements resulting from the flyby using steps 3 to 10 in the algorithm from Subsection 4.2.1.
    5.1 Calculate the velocity V^- with respect to Jupiter using the vis-viva equation.
    5.2 Calculate the mean angular velocity of the flyby moon around Jupiter using Equation 3.7.
    5.3 Determine the Tisserand parameter using Equation 3.18.
    5.4 Using the Tisserand parameter, calculate the angular momentum with Equation 3.19.
    5.5 Obtain the hyperbolic excess velocity with respect to the flyby moon using Equation 3.14.
    5.6 Obtain the minimum flyby altitude from the parameter vector and use it to calculate the maximum turning angle with Equation 3.13.

    5.7 Calculate the increment in orbital energy for this maximum turning angle.
    5.8 Update the orbital energy and obtain semi-major axis and eccentricity, thus updating perijove.
    5.9 Return to step 4.0.

7. Propagate the trajectory towards the perijove and calculate the perijove velocity V_p using the vis-viva equation.
8. Obtain ΔV_{JOI} from the parameter vector and subtract it from V_p.
9. Update the orbital energy using the vis-viva equation, semi-major using Equation 3.17 and eccentricity using Equation 3.16.
10. Return to step 4.0 for the rest of the sequence.
11. Propagate the trajectory until the limit value of the true longitude. Note that when the trajectory is closed along the sequence, the limit value for true longitude is 2π radian. The propagation also ends when the perijove approaches the radiation belt safety value ($8R_J$).

As was stated earlier in this section, the algorithm described above is a combination of the earlier used algorithm from Subsection 4.2.1 and the second-order Taylor-series expansion for low-thrust legs in the Tisserand graph. Thus also including the same penalties from Subsection 4.2.1. These will therefore not repeated here; only the complete fitness function is given here in Equation 6.1.

$$J = \Delta V_{JOI} * W + \Delta E + P_{fb} + P_{rad} \tag{6.1}$$

6.1.1 Initial conditions

The previous section's algorithm uses the same initial conditions as the ballistic algorithm from Subsection 4.2.1. The initial orbital energy resulting from the interplanetary trajectory (Hohmann transfer) is still $16.347\text{km}^2/\text{s}^2$. The minimal allowable flyby altitude is 500 km. The motivation of this value is again due to navigational and ephemerides concerns. Again, the author expects the optimization to converge towards this minimal flyby altitude since this results in the largest energy increment. However, from the results in Chapter 4, it was concluded that larger flyby altitudes hold the optimum for some sequences. The algorithm described above mentioned that the range in true longitude starts at $-0.95L_{limit}$, where L_{limit} is determined by Equation 6.2 with e_0 the initial eccentricity. This eccentricity is given by Equation 6.3. Note that r_p and a are the initial perijove as set by the parameter vector and the initial semi-major axis is set by the initial orbital energy due to the foregoing interplanetary trajectory.

$$L_{limit} = acos(-1/e_0) \tag{6.2}$$

$$e_0 = 1 - \frac{r_p}{a} \tag{6.3}$$

There are two reasons for choosing this value for the initial true longitude. The first is because low-thrust legs starting at L_{limit} of the incoming hyperbolic trajectory occur at infinity with respect to Jupiter. This introduces large errors because the low-thrust legs considered close to this L_{limit} represent very long thrusting periods compared to thrust legs performed at or near the perijove. The second reason is to ensure that the spacecraft first properly enters the SOI of Jupiter. This prevents solar radiation pressure or third-body perturbations acting relatively intense on the trajectory of the spacecraft. Equation 6.4 determines the SOI of a particular celestial body to a central body. In the Sun-Jupiter system, the SOI of Jupiter is around 687 Jovian radii. The initial radial position of the incoming hyperbolic trajectory can be calculated using Equation 5.24. The overall radial position corresponding to $-0.95L_{limit}$ is for all optimizations around 300 Jovian radii. With this in mind, the author expects that this initial true longitude will create reliable results.

6.1.2 Sphere of Influence

In the algorithm described at the beginning of this chapter, a flyby is initiated when the spacecraft approaches the orbital radius of the flyby moon considered. With the expression ”in the vicinity”, it is meant that the spacecraft is located between the orbital radius of the flyby moon plus and minus the SOI of that moon. The SOI of each moon is calculated using Equation 6.4 and is presented for all four of the Galilean moons in Table 6.1. This equation was already briefly mentioned by Equation 3.9, but for completeness repeated here. The mass m_1 is the mass of the moon under consideration, m_2 the mass of Jupiter and a_m is the semi-major axis of the moon under consideration.

$$\frac{R_{SOI}}{a_m} = \left(\frac{m_1}{m_2}\right)^{2/5} \tag{6.4}$$

Galilean moon	R_{SOI} [km]
Io	7834
Europe	9722
Ganymede	24350
Callisto	37681

Table 6.1: Spheres of influences of the Galilean moons.

6.2 Optimizer settings

The optimizations of the low-thrust satellite-aided capture trajectories mostly use the same optimizer settings as in Table 4.1. Due to the numerical nature of the second-order Taylor-series expansion, the computation time drastically increased when using the same number of generations and individuals per generation. Therefore, the number of generations and individuals per generation was reduced to 120 and 1000, respectively. The mutation scale factor, crossover rate and selection method were kept the same as Table 4.1. Table 6.2 summarizes the optimization settings used in this chapter.

Tuning parameter	Notation	Setting
Number of generations	G_i	120
Number of individuals	NP	1000
Mutation scale factor	F	0.33
Crossover rate	C_r	0.67
Selection method	DE/x/y/z	DE/best/1/bin

Table 6.2: Summary of the tuning parameters for the DE optimization algorithm for the low-thrust satellite-aided capture trajectories. These are used for all the optimizations in this chapter.

6.3 Results

This section presents the optimal low-thrust satellite-aided planetary capture trajectories in the Tisserand graph. First for the single-, secondly for a double- and last for the triple-aided sequences. Direct trajectories that only incorporate low-thrust and an impulsive JOI are not discussed because they hold no additional value with respect to the research sub-questions. It is important to note that all the results and methods explained in this chapter do not hold any accountability with the phasing of the moons. They are just a representation of what could be possible from an energetic point of view. The next chapter treats the phasing problem for both ballistic and low-thrust capture trajectories. Both velocity increments as results of low-thrust (ΔV_{LT}) and the impulsive JOI (ΔV_{JOI}) are indicated above each graph. Each graph consists of three different lines. The uppermost right point with the somewhat curved shape represents the incoming hyperbola's low-thrust leg. Then either a gravity assist (sloped straight lines) or an impulsive JOI (straight vertical line) follow. There is also a short thrusting phase for low-thrust propulsion between two gravity assists or a gravity assist and JOI. Because these low-thrust legs are relatively short, they do not deliver significant energy- and perijove increment. Therefore they are clearly not visible on the graphs, although they are present.

6.3.1 Low-thrust single-aided

First, the most simple satellite-aided capture trajectories are discussed, now with low-thrust incorporated. In other words, low-thrust single-aided capture trajectories. Similar to Chapter 4, considering the orbital parameters of the Galilean moons and the radiation safety belt Io is again not deemed feasible. The results for Europa, Ganymede and Callisto low-thrust single-aided capture trajectories are presented here.

Callisto

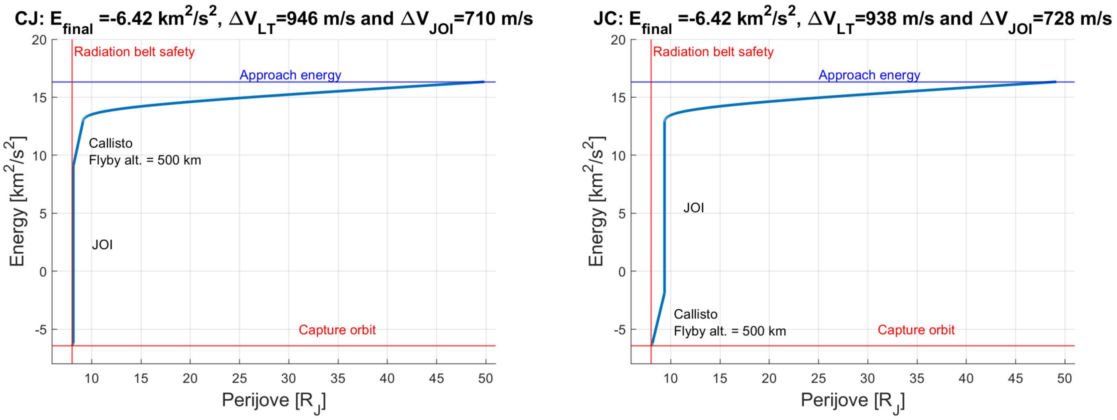

(a) Optimal low-thrust Callisto-JOI planetary capture sequence in Tisserand graph.

(b) Optimal low-thrust JOI-Callisto planetary capture sequence in Tisserand graph.

Figure 6.1: Results for low-thrust Callisto-aided planetary capture trajectories.

The combination of low-thrust propulsion and a single Callisto flyby cannot capture a spacecraft in a (desired) closed orbit around Jupiter; thus, a JOI will still be required (710 or 728 m/s). A low-thrust Callisto-aided planetary capture trajectory takes full benefits from a high initial perijove (around $49 R_J$). Therefore, the spacecraft follows a longer trajectory, which gives the low-thrust propulsion a longer time of flight to deliver ΔV_{LT} (938 and 946 m/s). The presence of low-thrust propulsion along the trajectory lowers the required JOI around 200 m/s compared to the optima in Figure 4.7a. The low-thrust leg is followed by the Callisto flyby (Figure 4.7a) or the JOI (Figure 6.1b). For both cases, the Callisto flyby does not occur at the orbital radius of Callisto (or at zero flight-path angle γ). This latter is similar for the ballistic optima in Figure 4.7. In short, a JOI executed at a lower perijove has more advantages than performing the Callisto flyby at the orbital radius of Callisto. This makes the JOI for both cases to be initiated at the lowest possible perijove. Therefore, after both the JOI and the Callisto flyby (independent of the order), the perijove lies at the radiation belt safety altitude. Thus no extra low-thrust leg is needed or allowed. Also, note that both Callisto flybys hold the minimum flyby altitude of 500 km.

Ganymede

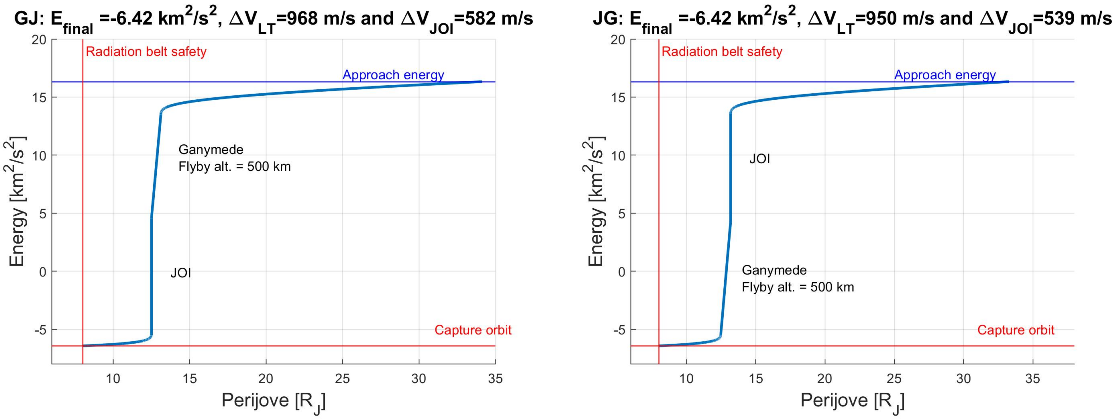
GJ: E_{final} =-6.42 km^2/s^2, ΔV_{LT}=968 m/s and ΔV_{JOI}=582 m/s

JG: E_{final} =-6.42 km^2/s^2, ΔV_{LT}=950 m/s and ΔV_{JOI}=539 m/s

(a) Optimal low-thrust Ganymede-JOI planetary capture sequence in Tisserand graph.

(b) Optimal low-thrust JOI-Ganymede planetary capture sequence in Tisserand graph.

Figure 6.2: Results for low-thrust Ganymede-aided planetary capture trajectories.

Similar as for the low-thrust Callisto-aided results, capturing a spacecraft in a 200-day periodic orbit using low-thrust propulsion and a Ganymede flyby still requires an impulsive JOI. Figure 6.2 presents both results of a low-thrust Ganymede aided capture trajectory with the JOI placed before or after the Ganymede flyby. The low-thrust propulsion lowers the amount of ΔV_{JOI} to 582 m/s for the inbound Ganymede flyby and 539 m/s for the outbound Ganymede flyby. A low-thrust Ganymede-aided capture trajectory also takes many benefits of the higher initial perijove that results in long thrusting times for the low-thrust propulsion. However, the orbital radius of Ganymede restricts the maximum possible initial perijove. For both inbound and outbound flybys, the optimum does not converge towards flybys with Ganymede at a perijove equal to Ganymede's orbital radius. Instead, the Ganymede flyby is for both optima executed at a perijove of around $13R_J$. This implies that the combination of low-thrust propulsion, a Ganymede flyby and an impulsive JOI results in a more collaborative optimum of more effective flybys, more efficient JOI and the energy increment due to low-thrust propulsion. Contrary to the low-thrust Callisto-aided results, after both the JOI and the Ganymede flyby are executed, there is still room in terms of perijove. Therefore, an extra low-thrust leg up to the radiation belt safety altitude that saves some extra ΔV_{JOI} can be added. This is also the reason that despite low-thrust Callisto-aided trajectories have higher initial perijove, a low-thrust Ganymede-aided trajectory delivers more ΔV_{LT}.

Europa

A capture trajectory that combines low thrust and a Europa flyby also requires the additional JOI. The presence of low-thrust propulsion along the trajectory lowers the required JOI to 720 m/s for the inbound (Figure 6.3a) and 679 m/s for the outbound (Figure 6.3b) flyby. The initial perijove is for both cases around $13R_J$. This gives the low-thrust propulsion room to lower the orbital energy and consequently also the perijove radius up to the orbital radius of Europa. The combined effect of low-thrust propulsion, Europa flyby and impulsive JOI converges towards the most effective Europa flyby. After both JOI and Europa flyby are executed, the perijove lies above the radiation belt safety and thus a low-thrust leg that further lowers the ΔV_{JOI} can be added.

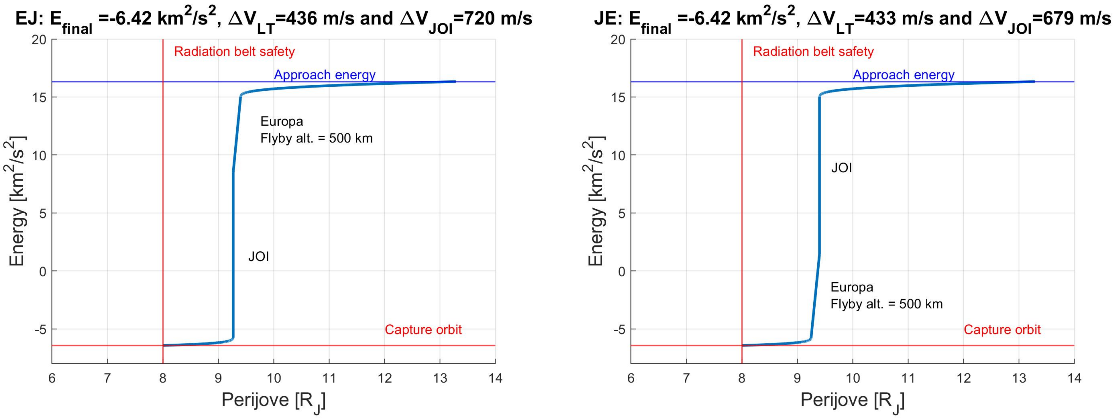

(a) Optimal low-thrust Europa-JOI planetary capture sequence in Tisserand graph.

(b) Optimal low-thrust JOI-Europa planetary capture sequence in Tisserand graph.

Figure 6.3: Results for low-thrust Europa-aided planetary capture trajectories.

6.3.2 Low-thrust double-aided

Now the results for low-thrust double-aided planetary capture trajectories are presented. Again Io is not deemed as a feasible flyby candidate and will not be considered. First, all Callisto-Ganymede sequences are presented and discussed, then Ganymede-Europa and next Callisto-Europa. For each low-thrust combination, a JOI is required and each arbitrary location of this JOI in the sequence will be presented (four cases).

Callisto-Ganymede

The required JOI for the low-thrust Callisto-Ganymede-aided sequences varies from 285 m/s for the low-thrust JOI-Ganymede-Callisto trajectory and 365 m/s for the low-thrust Callisto-Ganymede-JOI. This latter indicates that first performing the JOI requires less ΔV_{JOI}. The orbital radius of Ganymede limits the initial perijove to around $33-34R_J$. Similar to Figure 6.2 the optima do not converge towards a Ganymede flyby at the perijove equal to Ganymede's orbital radius. After the flybys and JOI are executed, there is still room in terms of perijove towards the radiation belt safety, such that low-thrust propulsion can further limit the required ΔV_{JOI}. When Callisto is placed at the end of the sequence (Figures 6.4c and 6.4d), this room in perijove is smaller and therefore less ΔV_{LT} could be delivered compared to when Callisto is placed at the beginning of the sequence (Figures 6.4a and 6.4b).

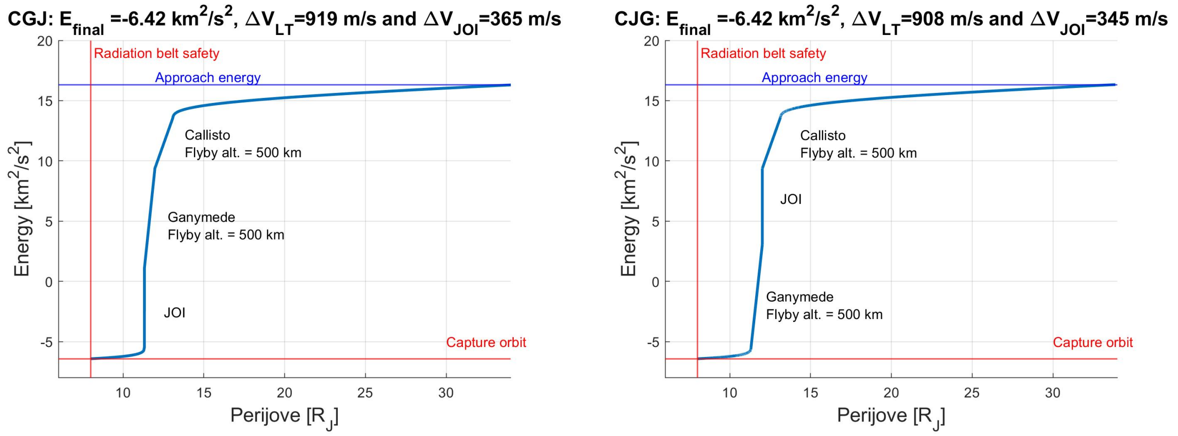

(a) Optimal low-thrust Callisto-Ganymede-JOI planetary capture sequence in Tisserand graph.

(b) Optimal low-thrust Callisto-JOI-Ganymede planetary capture sequence in Tisserand graph.

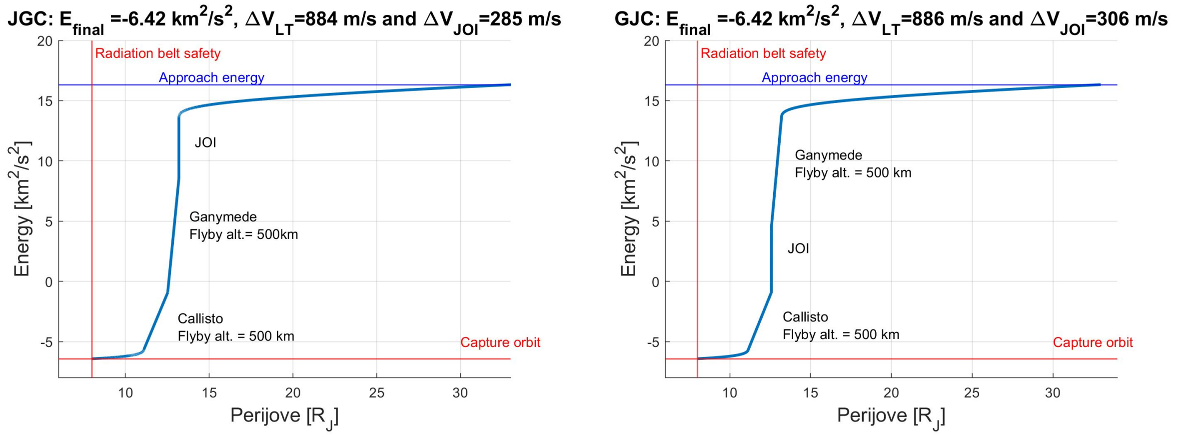

(c) Optimal low-thrust JOI-Ganymede-Callisto planetary capture sequence in Tisserand graph.

(d) Optimal low-thrust Ganymede-JOI-Callisto planetary capture sequence in Tisserand graph.

Figure 6.4: Optima for low-thrust Callisto-Ganymede-aided planetary capture trajectory in Tisserand graph.

Ganymede-Europa

Low-thrust Ganymede-Europa-aided capture trajectories require a JOI from 342 m/s for the low-thrust Ganymede-JOI-Europa and 373 m/s for the low- thrust Europa-JOI-Ganymede sequence, respectively. Placing the JOI first in the sequence does not provide the most optimal trajectory in terms of ΔV_{JOI}. Compared with the results from Figure 4.13 one concludes that the low-thrust propulsion lowers the ΔV_{JOI} with approximately 100-120 m/s, which indicates the benefits that low-thrust propulsion could provide. The initial perijoves are limited by a maximum of $14R_J$ to ensure the spacecraft reaches the orbital radius of Europa along the trajectory. Therefore less ΔV_{LT} can be delivered by the low-thrust propulsion compared to a low-thrust Callisto-Ganymede sequence. The initial perijove limitation also implies that all optima converge towards the most effective flyby at Europa. Similar to the low-thrust Callisto-Ganymede sequences, there is a low-thrust leg after the JOI and two flybys are executed. The fact that the perijove after the JOI and flybys is above the radiation belt safety allows for this later. Also observe smaller ΔV_{LT} for sequences with Ganymede placed at the end (Figures 6.5c and 6.5d). The Ganymede flyby lowers the perijove and thus limits the low-thrust leg at the end of the sequence.

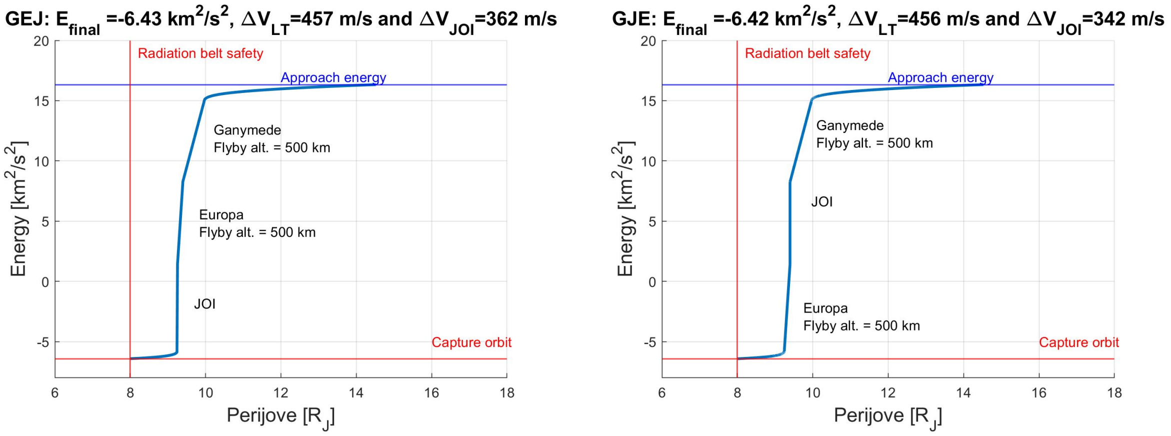

(a) Optimal low-thrust Ganymede-Europa-JOI planetary capture sequence in Tisserand graph.

(b) Optimal low-thrust Ganymede-JOI-Europa planetary capture sequence in Tisserand graph.

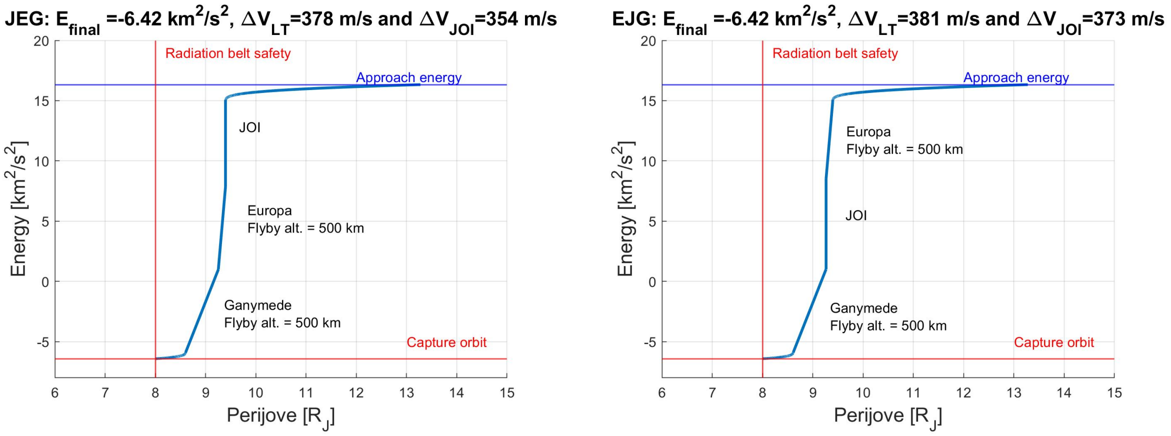

(c) Optimal low-thrust JOI-Europa-Ganymede planetary capture sequence in Tisserand graph.

(d) Optimal low-thrust Europa-JOI-Ganymede planetary capture sequence in Tisserand graph.

Figure 6.5: Optima for low-thrust Ganymede-Europa-aided planetary capture trajectory in Tisserand graph.

Callisto-Europa

Figure 6.6 presents the low-thrust Callisto-Europa-aided capture trajectories. With the required JOI from 478 m/s for the low-thrust Callisto-JOI-Europa sequence to 522 m/s for the low-thrust Europa-JOI-Callisto sequence, the combination Europa-Callisto performs worst of the three possible double-aided sequences. Compared to the ballistic optima (no low thrust), the ΔV_{JOI} is lowered by approximately 110-130 m/s, thus indicating the benefits of adding low-thrust propulsion. Like Ganymede-Europa, the initial perijoves are limited by reaching the orbital radius of Europa in the sequence. Moreover, the optima converge towards the most effective Europa flyby (flight-path angle). Note that when the Callisto flyby occurs at the end of the sequence, no room in terms of perijove is left to add an additional low-thrust leg. This latter, combined with the lower initial perijove, explains the lower ΔV_{LT}.

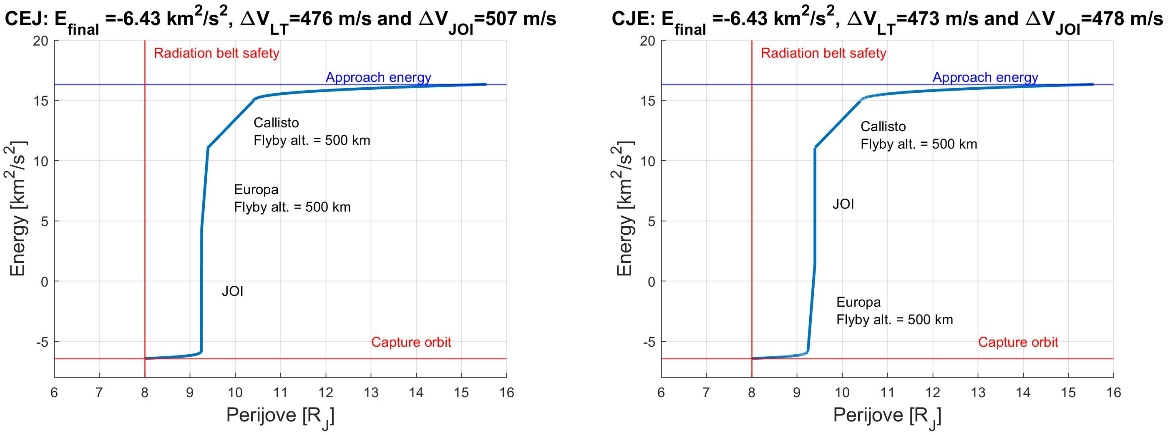

(a) Optimal low-thrust Callisto-Europa-JOI planetary capture sequence in Tisserand graph.

(b) Optimal low-thrust Callisto-JOI-Europa planetary capture sequence in Tisserand graph.

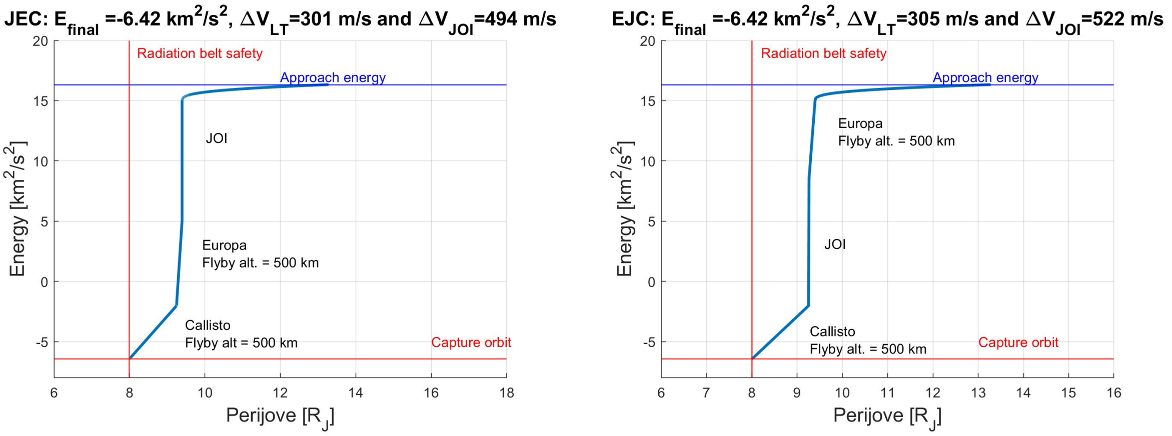

(c) Optimal low-thrust JOI-Europa-Callisto planetary capture sequence in Tisserand graph.

(d) Optimal low-thrust Europa-JOI-Callisto planetary capture sequence in Tisserand graph.

Figure 6.6: Optima for low-thrust Ganymede-Europa-aided planetary capture trajectory in Tisserand graph.

6.3.3 Low-thrust triple-aided

From the results in Section 4.3, one learned that it is possible to capture a spacecraft in a closed orbit around Jupiter through three flybys. However, to reach the desired 200-day periodic orbit, an impulsive JOI is still required. For the results presented in this section, one is interested in the extent to which the low-thrust propulsion reduces this JOI.

The optima of every possible low-thrust triple-aided capture trajectories are presented in Figures 6.7 and 6.8. The ΔV_{JOI} differs from 123 m/s for a low-thrust Callisto-Ganymede-JOI-Europa sequence to 286 m/s for a low-thrust Europa-Ganymede-Callisto sequence. Placing the JOI at the beginning of the sequence even performs second-worst (273 m/s). The reason for the relatively large ΔV_{JOI} for the low-thrust JOI-Europa-Ganymede-Callisto and Europa-JOI-Ganymede-Callisto sequences lies in the (much) higher minimal flyby altitude of the Callisto flyby. The argumentation for this is the same as explained for the ballistic case and will not be repeated here. All six other sequences have flybys with the minimum altitude equal to 500 km and therefore much smaller ΔV_{JOI}. The initial perijoves are again limited by ensuring the spacecraft can reach the orbital radius of Europa to perform a flyby with it. Moreover, the Europa flyby is always such that the most considerable energy (and perijove) increment can be delivered (zero flight-path angle). The amount of ΔV_{LT} also varies significantly for the different sequences. A higher initial perijove and a low-thrust leg after the sequence in-

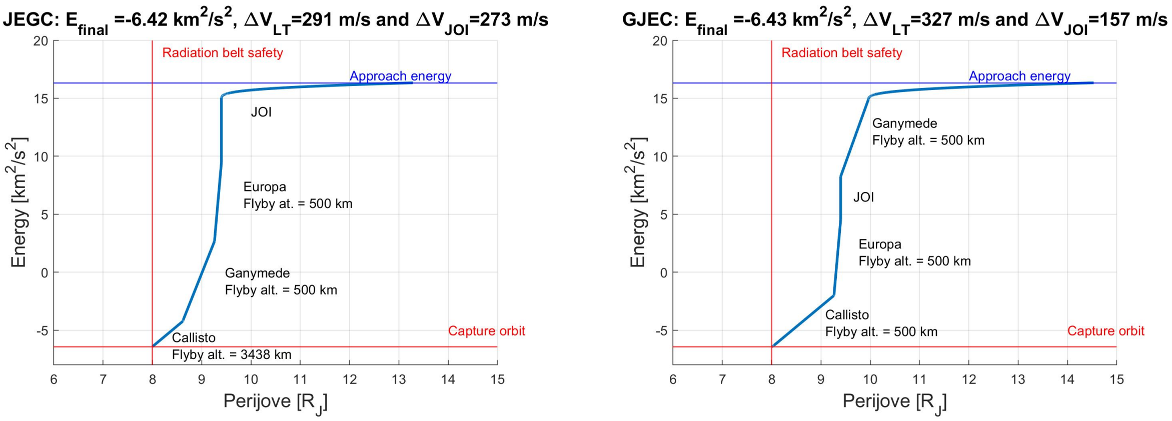

(a) Optimal low-thrust JOI-Europa-Ganymede-Callisto planetary capture sequence in Tisserand graph.

(b) Optimal low-thrust Ganymede-JOI-Europa-Callisto planetary capture sequence in Tisserand graph.

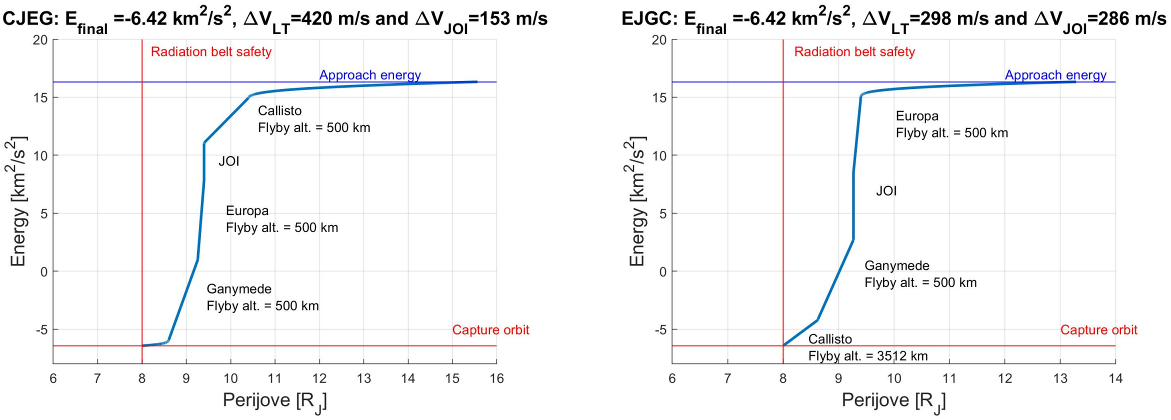

(c) Optimal low-thrust Callisto-JOI-Europa-Ganymede planetary capture sequence in Tisserand graph.

(d) Optimal low-thrust Europa-JOI-Ganymede-Callisto planetary capture sequence in Tisserand graph.

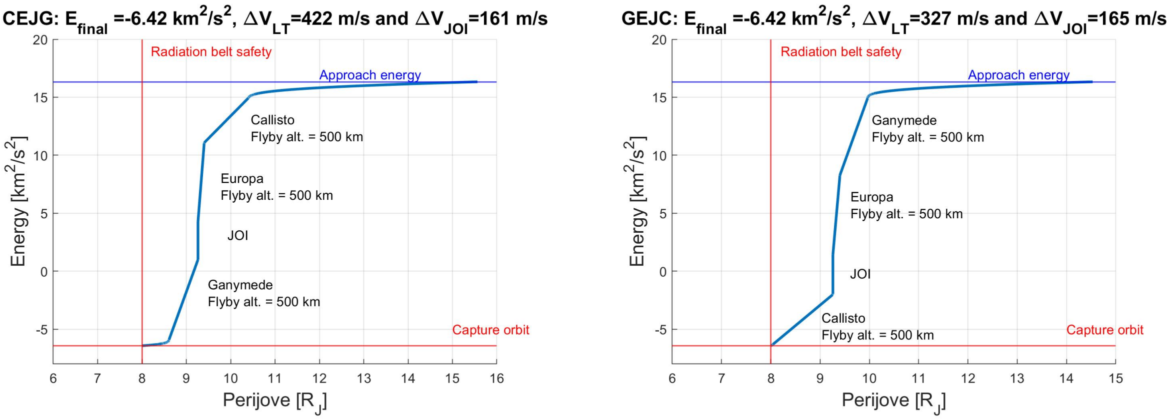

(e) Optimal low-thrust Callisto-Europa-JOI-Ganymede planetary capture trajectory in Tisserand graph.

(f) Optimal low-thrust Ganymede-Europa-JOI-Callisto planetary capture sequence in Tisserand graph.

Figure 6.7: Optimal low-thrust triple-aided planetary capture trajectories in Tisserand graph (part 1).

crease the ΔV_{LT}. This latter reduces the required ΔV_{JOI} thus declaring that the best low-thrust triple-aided capture sequences are given by the low-thrust Callisto-Ganymede-JOI-Europa and Callisto-Ganymede-Europa-JOI sequences (Figures 6.8a and 6.8b).

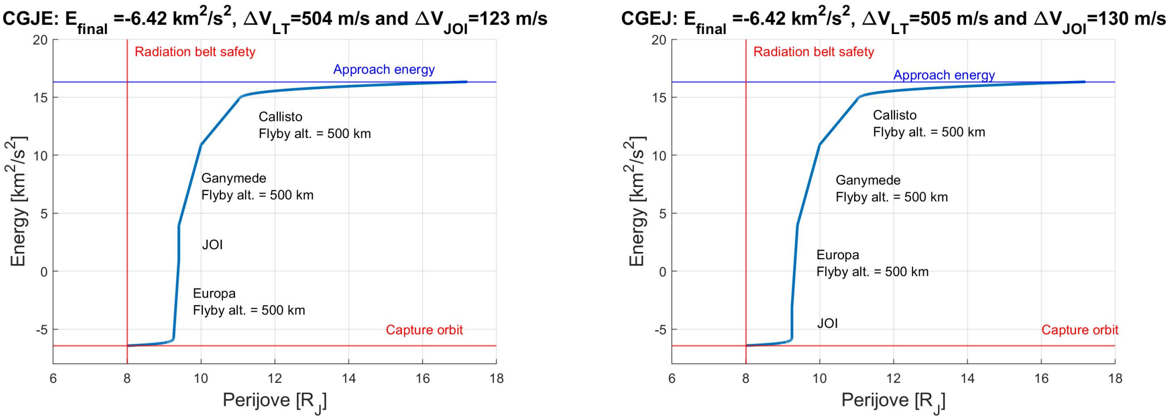

(a) Optimal low-thrust Callisto-Ganymede-JOI-Europa planetary capture trajectory in Tisserand graph.

(b) Optimal path for a Callisto-Ganymede-Europa-JOI planetary capture trajectory in Tisserand graph.

Figure 6.8: Optimal low-thrust triple-aided planetary capture trajectories in Tisserand graph (part 2).

6.3.4 Summary

The results of all low-thrust capture trajectories are presented in Table 6.3. The amounts of ΔV_{LT} and ΔV_{JOI} shown and combined in the propellant mass using the following equation:

$$M_{prop} = M_{initial}\left(1 - e^{-\frac{\Delta V_{HT}}{g_0 I_{sp,HT}} - \frac{\Delta V_{LT}}{g_0 I_{sp,LT}}}\right) \tag{6.5}$$

In the equation above, $I_{sp,HT}$ and $I_{sp,LT}$ represent the specific impulse of the high-thrust and low-thrust propulsion respectively. $M_{initial}$ is the initial spacecraft mass and g_0 is the gravitational acceleration on Earth (at the surface). The same values as in Chapter 6 are used here but extended with the low-thrust specific impulse of 4000 seconds.

Low-thrust single-aided capture sequences demand a total propellant mass from 749 kg for JOI-Ganymede up to 950 kg for JOI-Callisto. Compared to the not-aided capture, this represents a decrease of 22 to 39% in propellant mass. This is slightly more than the conventional single-aided results. Hence the benefits of using low-thrust propulsion along the trajectory.
A second flyby is added to investigate low-thrust double-aided capture. Here Callisto-Ganymede and Ganymede-Europa performed comparably: a propellant mass of 450 kg for JOI-Ganymede-Callisto saving 768 kg or 63% against not-aided. However, only 10 kg extra savings compared to a conventional JOI-Callisto-Ganymede sequence were observed. Thus the benefits of adding low thrust are rather limited for this sequence. Moreover, for the Callisto-JOI-Ganymede sequence, the addition of low-thrust propulsion requires an extra propellant mass of 40 kg. The author argues that this is due to the nature of the problem. The spacecraft entered the SOI of Jupiter with a very high initial perijove ($32R_J$), resulting in a very long flight time. The methodology in the low-thrust satellite-aided planetary capture optimizations assumed that the low-thrust engine was turned on along the whole trajectory. The ΔV_{JOI} did become smaller compared to the ballistic double-aided sequence. However, the low-thrust propellant mass due to the 884 m/s velocity increment becomes of significance (89 kg, considering only low-thrust) and therefore diminishes the effect of lower ΔV_{JOI}. The best low-thrust Ganymede-Europa sequence was Ganymede-JOI-Europa: a propellant mass of 480 kg, saving 738 kg or 61% against the impulsive capture and an extra 100 kg against the ballistic Ganymede-JOI-Europa capture. Like the ballistic case, the low-thrust Callisto-Europa sequences performed worst of the (low-thrust) double-aided cases. With 640 kg for Callisto-JOI-Europa, saving 578 kg (47%) against not-aided capture and an extra 98 kg compared to ballistic.
Again, adding a third flyby to the (low-thrust) sequence further lowered the total propellant mass. The low-thrust Europa-JOI-Ganymede-Callisto sequence again performed worst of all

triple-aided sequences. A propellant mass of 398 kg meant saving 820 kg or 67 % against the not-aided capture and an extra mass saving of 79 kg against ballistic triple-aided. Callisto-Ganymede-JOI-Europa was the best low-thrust triple sequence. A propellant mass of 213 kg meant saving 1005 kg or 83% and 123 kg compared to ballistic Callisto-Ganymede-JOI-Europa-aided capture.

	ΔV_{LT} [m/s]	ΔV_{JOI} [m/s]	$\mathrm{M}_{\mathrm{prop,min}}$ [kg]	$\%\mathrm{M}_{\mathrm{prop,direct}}$ [-]
Single-aided				
Callisto				
CJ	946	710	932	76
JC	938	728	950	78
Ganymede				
GJ	968	582	798	66
JG	950	539	749	61
Europa				
EJ	436	720	903	74
JE	433	679	859	71
Double-aided				
Callisto-Ganymede:				
CGJ	919	365	548	45
CJG	908	345	524	43
JGC	884	285	450	37
GJC	886	306	475	39
Ganymede-Europa				
GEJ	457	362	504	41
GJE	456	342	480	39
JEG	378	354	487	40
EJG	381	373	510	42
Callisto-Europa				
CEJ	476	507	674	55
CJE	473	478	640	53
JEC	301	494	644	53
EJC	305	522	676	56
Triple-aided				
CGEJ	505	130	222	18
CGJE	504	123	213	17
CEJG	422	161	253	21
CJEG	420	153	243	20
GEJC	327	165	249	20
GJEC	327	157	239	20
EJGC	298	286	398	33
JEGC	291	273	381	31

Table 6.3: Summary of the ΔV and total propellant mass results of all low-thrust satellite-aided capture sequences.

6.4 Conclusion

This chapter combined two methods from the preceding chapters into a heuristic algorithm. The first one is optimizing using gravity assists with one, two or three of the Galilean moons (excluding Io) as explained in Chapter 4. The second method was to include low-thrust propulsion in the Tisserand graph. Important to mention at the end of this chapter is that all the methods and results presented in this chapter did not take the moons' phasing into account. They are just a representation of what is possible from an energetic point of view. The phasing problem is treated in the following chapter. The combination of low-thrust and a single gravity assist could not capture the spacecraft in a closed orbit and thus not in the desired long-period high eccentric orbit. An impulsive JOI is still required but is reduced due to the low-thrust propulsion. For low-thrust double-aided planetary capture trajectories, some combinations of moons could potentially close the orbit and thus capture the spacecraft. However, for the desired 200-day periodic orbit, the impulsive JOI is still required. However, the presence of low-thrust propulsion reduces this JOI. This reduction in JOI does not always translate itself into a decrease of propellant mass when compared to conventional satellite-aided capture. Those sequences should best be flown without low-thrust propulsion. For low-thrust triple-aided planetary capture trajectories, it is possible to close the orbit around Jupiter without a JOI. However, for the 200-day periodic orbit, a JOI is still inevitable (but reduced due to the presence of low-thrust). The best low-thrust satellite-aided capture sequence is the Callisto-Ganymede-JOI-Europa scenario. With a ΔV_{JOI} of 213 m/s. Combined with the ΔV_{LT} this only requires 17% of the propellant mass for direct capture.

Chapter 7

Phasing problem formulation

The previous chapters investigated the abilities of natural satellite-aided planetary capture trajectories on a purely energetic base. This chapter will discuss the phasing problem of such trajectories. The phasing problem generally deals with the location of the moons. In order to actually fly the sequences found in previous chapters, the moons need to be correctly aligned. This is done in two steps. First, the relative phasing is investigated in Section 7.1. The relative phasing results are then transferred to an ephemerides search to investigate when these trajectories can be flown.

7.1 Phase angles

The theory of phase angles lies at the heart of the phasing problem. A ”phase angle” is the angle between two celestial bodies relative to a central body at a certain point in time. With respect to this thesis research topic, the central body is Jupiter and the other celestial bodies are the Galilean moons used for the capture sequences found in previous chapters and the Sun. The point in time is always the time of flyby with the first moon. Please note that just as for the optima found in the previous chapter (on a purely energetic base), no retrograde capture trajectories are considered, only prograde trajectories. This is because all Galilean moons orbit Jupiter in prograde directions. When considering retrograde capture

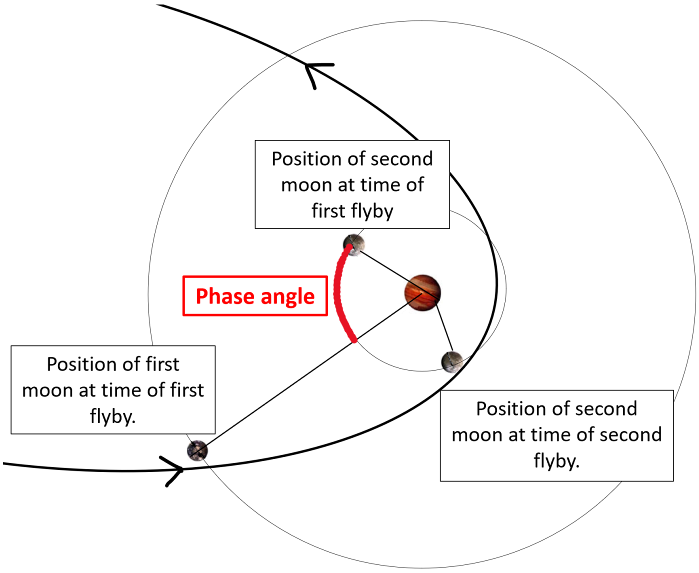

Figure 7.1: Illustration of the angle between two celestial bodies w.r.t. a central body at a certain point in time or in general, a phase angle.

trajectories, V_∞ would be too high and, therefore, diminish the effect of a flyby. In Figure 7.1 a schematic representation of a purely inbound capture trajectory is given. The figure shows the location of the moons at the time that the flyby with that moon is executed. The JOI maneuver is left out as the figure only serves to illustrate the physical meaning of a phase angle.

The purpose of the phasing problem is finding the moons' angular locations with respect to the angular location (true longitude) of the first flyby moon at the time of the first flyby. This essentially means backward propagating the moons under consideration to the point in time that corresponds to the first flyby. Therefore, the first flyby location needs to be determined, which goes hand in hand with determining the orientation of the incoming hyperbola.

7.2 Ballistic relative phasing

This section explains the methodology used for determining the relative phase angles for (ballistic) satellite-aided planetary capture trajectories.

7.2.1 First flyby

In a simplified circular coplanar assumption, the phase angle is, by definition, the difference in true longitude of the moons considered. The reason for using the true longitude instead of the true anomaly is because the argument of perijove changes due to the flyby. This strongly affects the true anomaly, leading to faulty phasing results. Using the true longitude instead, which is with respect to a fixed reference in space, resolves this issue.

Consider the moment in time just before the first flyby. This point is said to be described in space by the orbital elements θ_0, ω_0, a_0, e_0, Ω_0 and i_0. The out-of-plane elements Ω_0 and i_0 are assumed zero by the coplanar assumption. Therefor only θ_0, ω_0, a_0 and e_0 are of importance. Combining the true anomaly, the argument of perijove and in theory also the right ascension of the ascending node gives the true longitude of the first flyby.

$$L_0 = \theta_0 + \omega_0 + \cancel{\Omega}_0 \tag{7.1}$$

7.2.2 Orientation of incoming hyperbola

To define the point of the first flyby in both time and space, an asymptotic body-fixed frame is created. In an asymptotic Jupiter-fixed frame, the incoming asymptote of the hyperbolic approach trajectory aligns with the negative x-axis. This is shown in Figure 7.2. The next step is to determine the argument of perijove at the moment that the spacecraft enters the SOI of Jupiter or at the moment of the first flyby. This latter is essentially the same for ballistic satellite-aided planetary capture trajectories and given by Equation 7.2.

$$\omega_0 = \pi + acos\left(\frac{-1}{e_0}\right) \tag{7.2}$$

Please note that the orientation of the incoming hyperbole and thus also the orientation of the Jupiter-fixed asymptotic frame can still be arbitrary in the Jupiter-Sun frame.

7.2.3 Second flyby

Now using the patched-conics equations from Chapter 3, the first flyby with the first moon is executed. This results in new orbital elements (θ_1, ω_1, a_1 and e_1) that should, due to the zero sphere of influence approximation (patched-conics), still represent the same location and point in time as the orbital elements right before the first flyby. Hence we recognize the motivation of using the true longitude instead of the true anomaly for calculating phase angles. However, consider the true longitude (and thus the point in space) just after the first flyby defined by $L_1 = \theta_1 + \omega_1 + \cancel{\Omega}_1$. Propagating the trajectory towards the (orbit of the) second moon, the true longitude is defined as $L_2 = \theta_2 + \omega_2 + \cancel{\Omega}_1$. Because the inter-moon

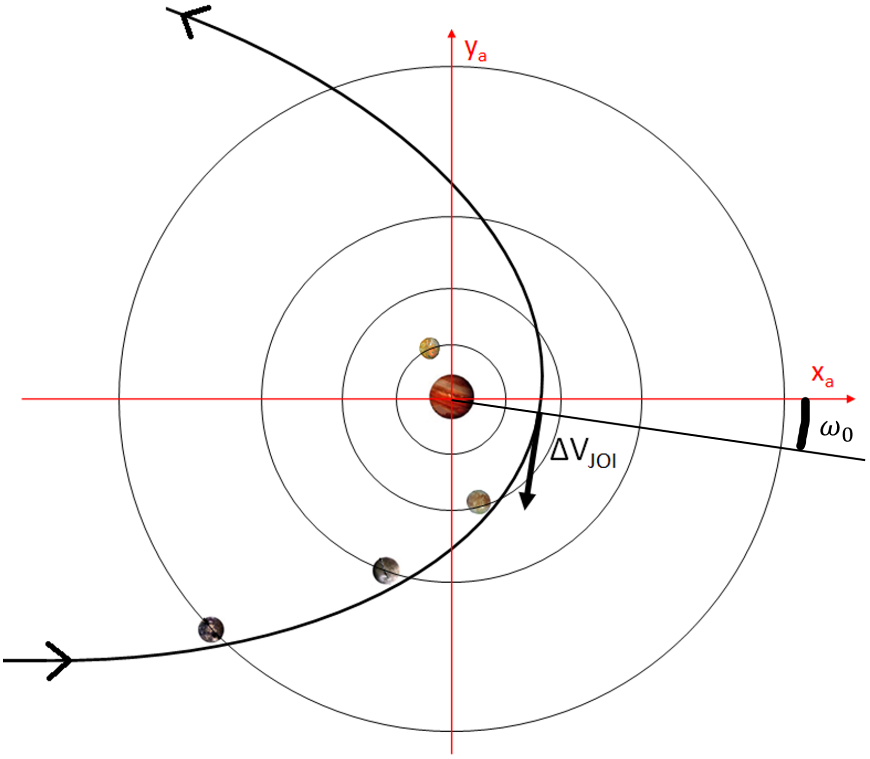

Figure 7.2: Schematic of the orientation of approach hyperbola (ω_0) in the asymptotic frame.

trajectories are considered as purely conic sections, the argument of perijove stays constant ($\omega_1 = \omega_2$). Therefore the angle between the two moons at two different points in time (first flyby and second flyby) is defined by Equation 7.3. θ_1 and θ_2 are given by Equation 7.4. The negative or positive sign on the righthand side of Equation 7.4 is defined by whether the flyby is executed before or after (respectively) the JOI. As the JOI is always inserted at the perijove, flyby's following after JOI are always outbound and occur at true anomalies greater than zero.

$$L_{21} = L_2 - L_1 = \theta_2 + \omega_1 - (\theta_1 + \omega_1) = \theta_2 - \theta_1 \tag{7.3}$$

$$\theta_n = \pm acos\left[\frac{a_n(1-e_n^2) - a_{moon,n}}{e_n a_{moon,n}}\right] \tag{7.4}$$

Important to note is that L_{21} is not the phase angle. A phase angle is defined at one point in time. Therefore, a time-of-flight correction needs to be added to account for the travel time from flyby one to flyby two. When the spacecraft is in hyperbolic orbit, the time-of-flight of the intermoon trajectory is given by Equations 7.5 and 7.6.

$$t_{21} = \sqrt{\frac{-a_1^3}{\mu_J}}\left[\left(e_1 \sinh H_{moon,2} - H_{moon,2}\right) - \left(e_1 \sinh H_{moon,1} - H_{moon,1}\right)\right] \tag{7.5}$$

$$H_{moon} = -\cosh\left(\frac{a_1 - a_{moon}}{a_1 e_1}\right) \tag{7.6}$$

A different description applies if the intermoon trajectory has already become elliptic due to flybys or impulsive JOI maneuver. In that case, the time of flight for the intermoon trajectory is calculated by means of Equations 7.7 and 7.8.

$$t_{21} = \sqrt{\frac{a_1^3}{\mu_J}}\left[\left(e_1 \sin E_{moon,2} - E_{moon,2}\right) - \left(e_1 \sin E_{moon,1} - E_{moon,1}\right)\right] \tag{7.7}$$

$$E_{moon} = -\cos\left(\frac{a_1 - a_{moon}}{a_1 e_1}\right) \tag{7.8}$$

$$n_{moon} = \sqrt{\frac{\mu_J}{a_{moon}^3}} \tag{7.9}$$

In the above equations, μ_J is the gravitational parameter of Jupiter and a_{moon} the semi-major axis or due to the circular coplanar assumption, the orbital radius of the moon under consideration. H_{moon} and E_{moon} are the hyperbolic and eccentric anomaly respectively. Now using the mean angular motion of the moon for which the time-of-flight correction needs to be added (Equation 7.9, this equation was already mentioned in Chapter 3 by Equation 3.7 but repeated here for convenience), the relative phase angle of the second moon with respect to the first moon, at the time of the first flyby (ΔL_{21}) is given by:

$$\Delta L_{21} = (\theta_2 - \theta_1) - n_{moon,2} t_{21} \tag{7.10}$$

7.2.4 Third flyby

Adding a third flyby is done relatively straightforward but now with two correction terms for the times of flight. The first one corrects for the angular motion of the third moon during two inter-moon transfers; the second corrects for the angular motion of the second moon. If this second correction term were not added, the phase angle would be defined with respect to the location of the second moon at the time of the first flyby moon. Adding the time of flight correction (now positive) of the second moon resolves this. Now the phase angle of the third moon (ΔL_{41}) is defined with respect to the location of the first moon at the time of the first flyby moon.

$$\Delta L_{41} = (\theta_4 - \theta_3) - n_{moon,3}(t_{21} + t_{43}) + n_{moon,2} t_{21} \tag{7.11}$$

The geometric definition of all the angles discussed in this section is shown in Figure 7.3. The phase angles are positive in counterclockwise direction, meaning that both ΔL_{21} and ΔL_{41} are negative for this case.

7.2.5 JOI

The impulsive JOI can be implemented at any location in the sequence by means of logic. Consider two separate trajectory legs with the same ω but different θ, a and e. Two times of flights (t_{np} and $t_{p,n+1}$) can be calculated, one before the JOI and one after the JOI as illustrated in Figure 7.4. The subscript p indicates the perijove. These are then added to create the time-of-flight correction term for the corresponding moon (e.g., n+1). Note that all flybys occurring after the JOI are outbound flybys.

7.3 Low-thrust relative phasing

The optimizations of low-thrust satellite-aided capture trajectories from Chapter 6 use the advantage of a second-order Taylor-series expansion with the true longitude as a running parameter. By doing so, the computational time is reduced to a minimum while maintaining reasonable accuracy. However, this raises problems for the low-thrust phasing problem because nothing is known about the inter-moon time-of-flight. Moreover, since the trajectory is not ballistic due to the low-thrust propulsion, Equations 7.7 and 7.5 cannot be used. Therefor a similar second-order Taylor-series expansion is developed for time with the true longitude as running parameter. This Taylor-series is presented in Equation 7.12. The total- and partial derivatives in the equation are given by Equations, 7.13-7.16. In Equation 7.12, the first-order derivative is simply given by the Gauss equation Equation 5.20. The second-order derivatives are constructed using the same procedure as was applied for the other second-order derivatives in Subsection 5.5.3.

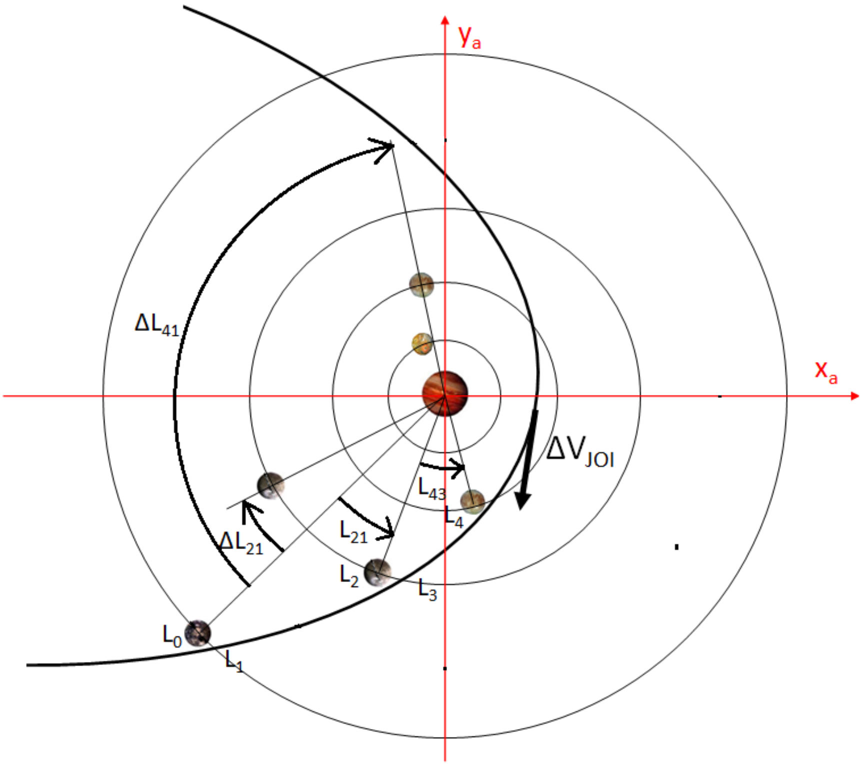

Figure 7.3: Schematic of the geometric definition of phase angles for a triple-aided Callisto-Ganymede-Europa-JOI capture trajectory in the $x_a - y_a$ asymptotic Jupiter-centered reference frame. All angles are positive in counterclockwise direction. This means that the phase angles ΔL_{41} and ΔL_{21} are negative in this case.

$$\Delta t_n = \frac{dt}{dL}(L_n - L_{n-1}) + \frac{d}{dL}\left(\frac{dt}{dL}\right)\frac{(L_n - L_{n-1})^2}{2} \tag{7.12}$$

$$\frac{d}{dL}\left(\frac{dt}{dL}\right) = \frac{\partial}{\partial L}\left(\frac{dt}{dL}\right) + \frac{dp}{dL}\frac{\partial}{\partial p}\left(\frac{dt}{dL}\right) + \frac{df}{dL}\frac{\partial}{\partial f}\left(\frac{dt}{dL}\right) + \frac{dg}{dL}\frac{\partial}{\partial g}\left(\frac{dt}{dL}\right) \tag{7.13}$$

$$\frac{\partial}{\partial p}\left(\frac{dt}{dL}\right) = -\left(\frac{dL}{dt}\right)^{-2} \cdot \frac{\partial}{\partial p}\left(\frac{dL}{dt}\right) \tag{7.14}$$

$$\frac{\partial}{\partial f}\left(\frac{dt}{dL}\right) = -\left(\frac{dL}{dt}\right)^{-2} \cdot \frac{\partial}{\partial f}\left(\frac{dL}{dt}\right) \tag{7.15}$$

$$\frac{\partial}{\partial g}\left(\frac{dt}{dL}\right) = -\left(\frac{dL}{dt}\right)^{-2} \cdot \frac{\partial}{\partial g}\left(\frac{dL}{dt}\right) \tag{7.16}$$

Using Equation 7.12 the time can be integrated along with the three other elements p, f and g as a function of true longitude. To ensure a minimal error, the same integration procedure as in Subsection 5.5.3 is used. This is shown in Equation 7.17 or in short in Equation 7.18.

$$t_n(L) = t_{n-1} + \frac{dt}{dL}(L_n - L_{n-1}) + \frac{d}{dL}\left(\frac{dt}{dL}\right)\frac{(L_n - L_{n-1})^2}{2} \tag{7.17}$$

$$t_n(L) = t_{n-1} + \Delta t \tag{7.18}$$

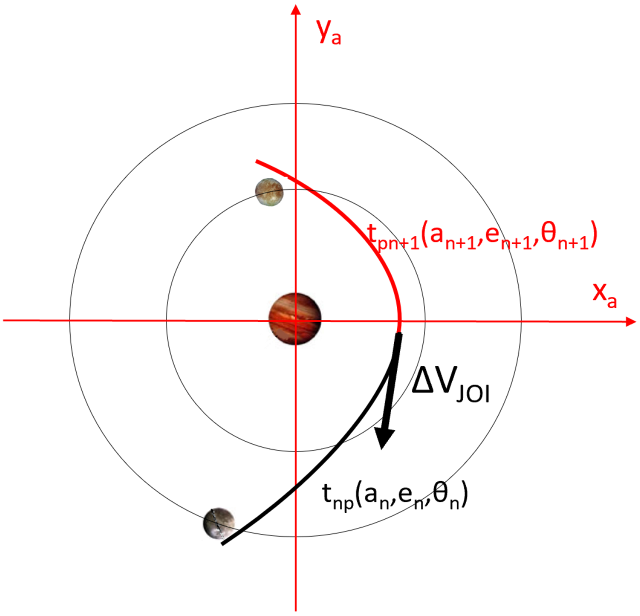

Figure 7.4: Illustration of how the time of flight is calculated for an intermoon trajectory leg with an intermediate JOI executed at perijove.

By having the numerical progression of the time over the true longitude available now, the relative phasing for double- and triple low-thrust satellite-aided capture trajectories can easily be solved by means of Equations 7.19 and 7.20.

$$\Delta L_{21} = (L_2 - L_1) - n_{moon,2}(t_2 - t_1) \tag{7.19}$$

$$\Delta L_{41} = (L_4 - L_3) + n_{moon,3}(t_{12} + t_{34}) - n_{moon,2}(t_2 - t_1) \tag{7.20}$$

Again note that L_0 is essentially assumed to have the value same as L_1. The same holds for the other pair L_2 and L_3. This was already explained earlier in this chapter and shown in Figure 7.3. The second-order Taylor-series expansion for time presented here also has another use for itself. With the progression of time over longitude available, the (constant) thrust acceleration a_T can also be integrated with p, f and g. By doing so, the velocity increment of the low-thrust propulsion (ΔV_{LT}) becomes available. This is shown during the verification of the assumption of constant mass of the low-thrust propulsion in Subsection 9.4.4.

7.4 Absolute phasing

In the two previous sections of this chapter, the moons' phase angles were determined relative to the first flyby. All directions were defined in a Jupiter-centered asymptotic reference frame. Note that this asymptotic frame is still oriented in an arbitrary way with respect to the Sun-Jupiter frame. This implies that the approach hyperbola also might be arbitrary directed. To ensure this approach hyperbola results from a heliocentric Hohmann transfer, the reference for the relative phase angles, that is, the first flyby longitude (L_0), should be defined with respect to the Sun-Jupiter line.

A spacecraft arriving at the Jovian system from a heliocentric Hohmann transfer enters Jupiter's SOI before it's velocity vector with a velocity that is slower than the velocity of Jupiter. So the asymptote of the incoming hyperbola aligns with the velocity vector of Jupiter. Assuming that Jupiter orbits the Sun in a circular orbit, Jupiter's velocity vector and the Sun-Jupiter line are perpendicular with respect to each other. Therefor, the true longitude of the first flyby moon at the time of the first flyby (L_0) should be increased by 90°. This is to align the negative x-axis of the assymptotic frame with the velocity vector of Jupiter. The phase angles of the subsequent moons are left the same since they are all calculated relative to L_0. When doing so, all the angles required for an ephemerides search are available.

7.5 Ephemerides search

As stated at the end of the previous section, both relative and absolute phasing needs to be solved. The goal now is to perform an ephemerides search over the time interval from 2025 to 2065. Its purpose is to find the times at which the proper phasing (relative and absolute) of the moons occurs. In other words, the time windows at which the satellite-aided planetary capture trajectories could actually be flown.

7.5.1 Ephemeris file

An ephemerides file *jup310.bsp* is available from [11]. It holds the locations of the Galilean moons in a Jupiter-fixed reference frame. Figure 7.5 shows the propagation of them for a time interval from January 1th 2024 up to May 1th 2024. This time window was chosen arbitrarily with a reasonable length to ensure that the Sun's position is also clearly visible.

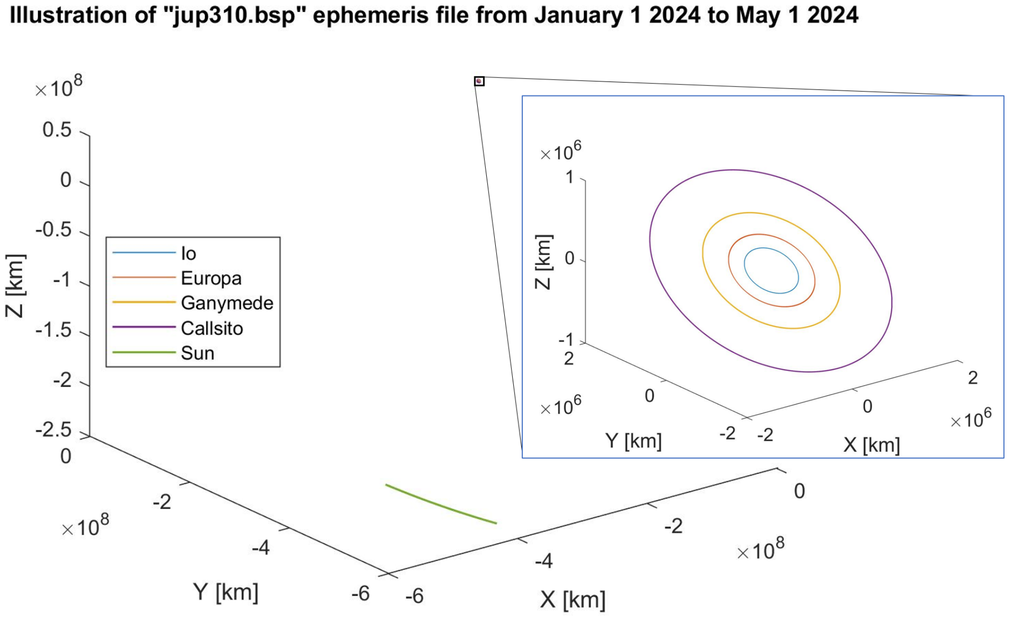

Figure 7.5: Illustration of the data available in the 'jup310.bsp' ephemeride file.

As explained in Section 7.4 for ensuring that the incoming trajectories result from a heliocentric Hohmann transfer, the Jupiter-Sun line is of great importance. The advantage of the ephemeride file available is that it also includes the location of the Sun with respect to the Jupiter-centered reference frame.

7.5.2 Ephemerides phase angle

Using the position vectors of Callisto, Ganymede, Europa and the Sun it is possible to calculate the phase angles through the following equations [18][16][17]:

$$\Delta L_{\text{Ga,Ca},ephem} = \text{Sgn}\left(\hat{\mathbf{n}} \bullet \mathbf{r}_{\text{Ca}} \times \mathbf{r}_{\text{Ga}}\right) \cos^{-1}\left(\frac{\mathbf{r}_{\text{Ca}} \bullet \mathbf{r}_{\text{Ga}}}{\|\mathbf{r}_{\text{Ca}} \cdot \mathbf{r}_{\text{Ga}}\|}\right) \tag{7.21}$$

$$\Delta L_{\mathrm{Ca,Sun},ephem} = \mathrm{Sgn}\left(\hat{\mathbf{n}} \cdot \mathbf{r}_{\mathrm{Sun}} \times \mathbf{r}_{\mathrm{Ca}}\right) \cos^{-1}\left(\frac{\mathbf{r}_{\mathrm{Sun}} \cdot \mathbf{r}_{\mathrm{Ca}}}{\|\mathbf{r}_{\mathrm{Sun}}\| \, \|\mathbf{r}_{\mathrm{Ca}}\|}\right) \tag{7.22}$$

In these equations $\Delta L_{\mathrm{Ga,Ca},ephem}$ and $\Delta L_{\mathrm{Ca,Sun},ephem}$ are the Ganymede-Callisto and Callisto-Sun phase angles at a particular time (e.g. the time of the Callisto flyby or in general the first subscript w.r.t. the second subscript), $\mathbf{r}_{\mathrm{Sun}}$, $\mathbf{r}_{\mathrm{Ca}}$ and $\mathbf{r}_{\mathrm{Ga}}$ are the Jupiter-centered position vectors of the representative celestial body. The Sgn (Signum) function combined with the triple scalar product make sure that the signs of the phase angles calculated are compatible with Equations 7.10 and 7.11. Then the arccosine of the unit dot product is taken to determine the actual magnitude of the phase angles. The orbital normal $\hat{\mathbf{n}}$ is easily calculated using two successive positions of Ganymede ($\mathbf{r}_{\mathrm{Ga},1}$ and $\mathbf{r}_{\mathrm{Ga},2}$ differing 25 minutes). In reality, one could calculate the orbital normal of all three moons considered in this thesis report (not Io). The moons lie almost in the same orbital plane (within one degree with respect to each other). Moreover, as stated before, the orbital normal is only used in the Sgn function to ensure consistent signs for the phase angles. Therefore, the calculation of only the orbital normal of Ganymede is considered enough and could be used for the other phase angles as well [16]. To prove this latter, the orbital normal vectors of Callisto, Ganymede and Europa are calculated and the three components (x,y,z) are plotted over each other in Figure 7.6. As can be observed, they almost completely overlap. Therefore it is considered valid just to use one of the orbital normal vectors.

$$\hat{\mathbf{n}} = \frac{\mathbf{r}_{\mathrm{Ga},1} \times \mathbf{r}_{\mathrm{Ga},2}}{\left\|\mathbf{r}_{\mathrm{Ga},1} \times \mathbf{r}_{\mathrm{Ga},2}\right\|} \tag{7.23}$$

It is important to keep in mind during calculation of phase angles from the ephemeride file that for the Ganymede-Callisto phase angle, Callisto is the first flyby moon. Thus, the Callisto-Sun angle is of importance in the ephemerides search instead of the Ganymede-Sun phase angle. The Ganymede-Sun angle becomes of interest when Ganymede is the first flyby moon. When a third flyby is considered (Europa), Europa-Callisto phase angles need to be calculated as well. The phase angles assuming Callisto, Ganymede and Europa as the first flyby moon are plotted from January 5th, 2020 to February 4th, 2020 in Figure 7.7. One can observe that opposite phase angles (e.g., Callisto-Ganymede vs. Ganymede-Callisto) evolve in the opposite direction. The Sun-moon phase angle always evolves in positive direction. This is the result of all three moons having prograde orbits around Jupiter. Furthermore, when Callisto is the first flyby moon as in Figure 7.7a, all three phase angles evolve in a positive direction. The Callisto-Sun due to Callisto's prograde orbit but the Europa-Callisto and Ganymede-Callisto because Ganymede and Europe orbit much closer to Jupiter and thus have shorter orbital periods. This theory also works the other way around. Observing Figure 7.7c where Europa is the first flyby moon, the Europa-Sun phase angle evolves

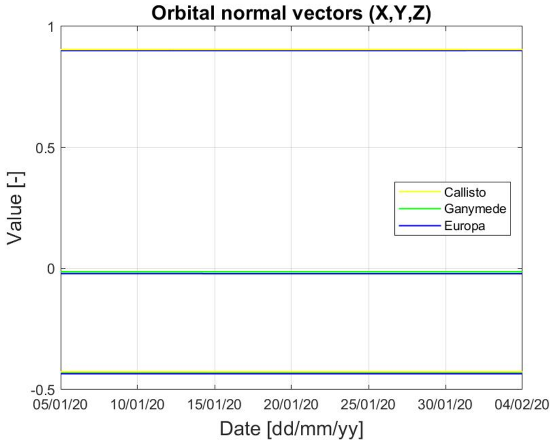

Figure 7.6: Illustration of marginal differences between the orbital normal vectors of Callisto, Ganymede and Europa.

in positive direction due to Europa's prograde orbit but the Callisto-Europa and Ganymede-Europa evolve in negative direction because Ganymede and Callisto have much longer orbital periods and will therefore always lack the orbit of Europa. The combined effect of this can be observed in Figure 7.7b where again the Ganymede-Sun phase angle propagates in positive direction due to the prograde orbit of Ganymede around Jupiter. The Callisto-Ganymede phase angle matures in negative direction because the longer orbital period of Callisto compared to Ganymede. It is the other way around for the Europa-Ganymede phase angle due to the shorter orbital period of Europa compared to Ganymede.

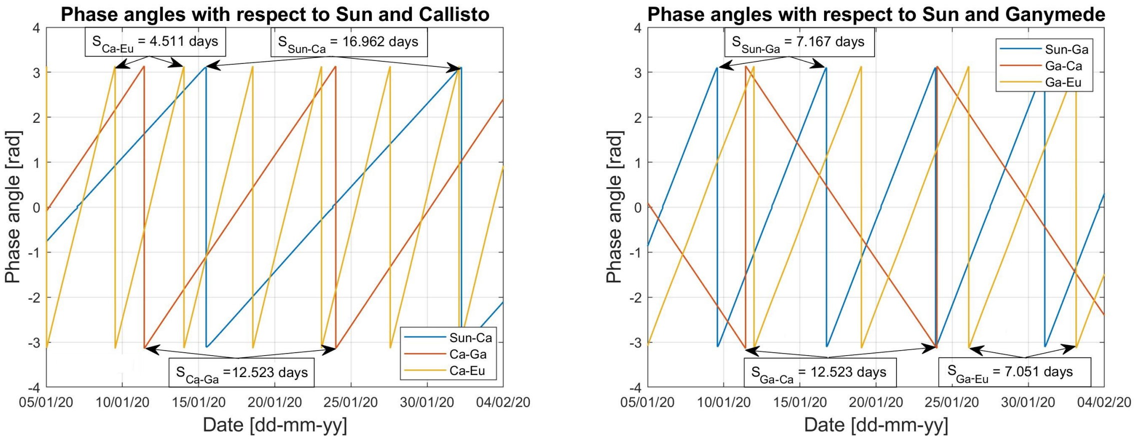

(a) Phase angles for Callisto as first flyby moon.

(b) Phase angles for Ganymede as first flyby moon.

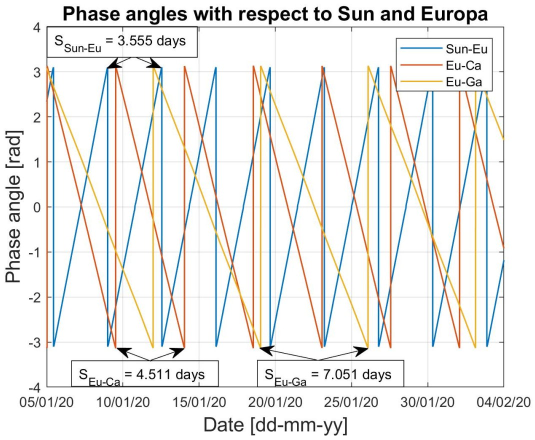

(c) Phase angles for Europa as first flyby moon.

Figure 7.7: Phase angles considering Sun and Callisto, Sun and Ganymede and Sun and Europa as reference. Phase angles are calculated from position vectors given by the 'jup310.bsp' file with dates ranging from January 5th 2020 up to February 4th 2020 as illustration.

7.5.3 Synodic period

Geometrically speaking, a particular phase angle between two moons only occurs every synodic period. This is the time that the phase angles evolve from 0 to 2π. The synodic period is calculated using Equation 7.24.

$$S = \frac{2\pi}{n_1 - n_2} \tag{7.24}$$

In Equation 7.24, S represents the synodic period in days, n_1 the mean angular motion of the innermost moon, and n_2 the mean angular motion of the outer moon. This has to be arranged in this way to ensure a positive sign for the outcome of the synodic period. The synodic periods for the three sequences relevant in this thesis research (excluding Io) are given in Table 7.1.

Sequence	T_1 [days]	n_1 [deg/day]	T_2 [days]	n_2 [deg/day]	S [days]
Europa-Ganymede	3.552	101.375	7.155	50.317	7.051
Europa-Callisto	3.552	101.375	16.689	21.571	4.511
Ganymede-Callisto	7.155	50.317	16.689	21.571	12.523
Europa-Sun	3.552	101.375	4332.589	0.083	3.555
Ganymede-Sun	7.155	50.317	4332.589	0.083	7.167
Callisto-Sun	16.689	21.571	4332.589	0.083	16.962

Table 7.1: Synodic periods between Callisto, Ganymede, Europa and the Sun. These numbers are also indicated in Figure 7.7.

This synodic period is indicated in Figure 7.7. Moreover, the individual orbital periods should nearly match the ”synodic” period between the first flyby moon and the Sun. Therefore it is also indicated in Figure 7.7. It serves as a verification method to gain more confidence in the methodology used to calculate the ephemerides phase angles. It will not be repeated in the chapter on verification and validation because it is already included here.

7.5.4 Ephemerides search

The ephemerides search is performed between 2025 and 2065. This 40-year interval is divided into 20 two-year intervals with timesteps of one minute. This division into two-year intervals was necessary because of the limiting array length in Matlab. An interval of two years holds about 1.05 million minutes. This times 20 years equals 21 million minutes to be analyzed. Therefore it is emphasized to choose proper logic that limits useless calculations and data loading.

The ephemerides search starts with the phasing of the first flyby moon. Using Equation 7.22 calculates the location of the first moon (in the case of Equation 7.22 it is Callisto) with respect to the Jupiter-Sun line. A Matlab script iterates over al 8.4 million minutes and checks when this first phase angle is satisfied. The first phasing is said to be satisfied when it is within a range of one hour (3600 seconds) times the angular velocity of the moon under consideration. It is emphasized that for the first moon the foregoing interplanetary Hohmann transfer allows for some trajectory correction maneuvers (TCM). TCMs generally alter the time of arrival at the first moon. Since the Galilean moons orbit at different orbital radii, their velocity and thus angular velocity is different. Taking the same angular range that the moon should be in for every moon would not give thrust-worthy results.

The phasing criterion of the first moon immediately eliminates a large portion of the time interval that is investigated. For the moments in time when this desired first phasing is found, the algorithm proceeds into checking if the second phasing is satisfied as well (Equation 7.21). If not, the algorithm proceeds to the next epoch for which the first phasing was satisfied. For the second (and possibly third) moon, a time window of only a half hour (1600 seconds) is taken. This time window is smaller because of the limiting times of flight between the moons wherein TCMs could be implemented.

This also eliminates a large portion of the epochs for which the first phasing was satisfied. When a third phasing is added, an extra phasing check is performed in the same way as the second phasing, reducing the number of valid epochs even further. In the end, the complete time interval of 40 years will be reduced to only a few dates. It goes without saying that the solution space holding the valid epochs would be more extensive for double flyby sequences compared to the triple flyby sequences. Generally, the more moons added to the sequence, the more severe the geometrical constraints are.

From the optimizations performed in Chapter 4 it was learned that it would most often converge towards an initial perijove that results in a zero flight-path angle and smallest relative velocity when at that most inner flyby moon. This implies that the flyby with the most inner moon is performed at the perijove of the spacecraft’s trajectory. In other words, the spacecraft's perijove just before the flyby with the most inner moon is performed equals the orbital radius of that moon. Therefore, the phasing problem was fed a range in perijove from $[0.9R_{p_{opt}}, 1.0R_{p_{opt}}]$ with 30 steps. The result would be a much wider solution space in terms of valid first flyby epochs instead of just searching for the optima found in Chapter 4. The range of initial perijove is limited to only 30 steps to limit the amount of computational time. However, the author expects that this would suffice to get insight into the effects of varying perijove on available first flyby times for performing (low-thrust) satellite-aided planetary capture trajectories.

Chapter 8

Phasing results

This chapter presents the results of the methodologies discussed in the previous chapter. First, the ballistic case (satellite-aided) results are given in Section 8.1, and then the case incorporating low-thrust along the trajectory in Section 8.2. Some of the sequences are not discussed in this chapter because they would hold the same reasoning as forgoing sequences.

8.1 Satellite-aided results

This section will present the results of the phasing problem of the satellite-aided planetary capture trajectories. This holds the combination of flybys with two or three of Jupiter's Galilean moons combined with a JOI. For brevity, only sequences with the JOI first will be discussed. Results of other sequences are presented in Appendix A. In general the results hold the required JOI maneuver in terms ΔV and propellant mass and the dates for which the flyby sequence can be flown. All results are given for a range of initial perijoves. A third graph presenting the flyby altitudes is also included when relevant.

8.1.1 Double-aided

Here the results for double satellite-aided planetary capture trajectories are presented. It starts with the combination Callisto-Ganymede, then Ganymede-Europa and finally Callisto-Europa.

Callisto-Ganymede

In Figure 8.1 the required JOI for a JOI-Ganymede-Callisto capture sequence is presented. This JOI is given in terms of ΔV and propellant mass. The JOI ensures that when the full sequence is flown, the spacecraft is captured in a (highly eccentric) 200-day periodic orbit. The JOI is plotted for the range of initial perijove for which the phasing problem is sampled and solutions were found for in the ephemerides search. Because the impulsive JOI is the only contribution to propellant mass, the progressions of both ΔV and propellant mass are similar.

In Figure 8.1 one can notice the decreasing behavior of the JOI as the initial perijove approaches its optimum. This optimum is the same optimum as was found in the optimizations of Chapter 4. It corresponds with a perijove equal to Ganymede's orbital radius just before the Ganymede flyby is executed. At higher perijoves the spacecraft would not reach the orbit of Ganymede and perform a flyby. Conventionally, a JOI executed at a lower perijove would require less propellant. That is for the case that no flybys are used and the JOI is the only mechanism that ensures the spacecraft is captured in the desired orbit. When flybys are used and the initial perijove is decreased beyond its optimum, the JOI would indeed be implemented at a lower perijove. However, due to the increasing flight-path angle (angle between the velocity vector of Ganymede and spacecraft) and relative velocity at the point where the flyby with Ganymede is executed, the effect (orbital energy and perijove increment)

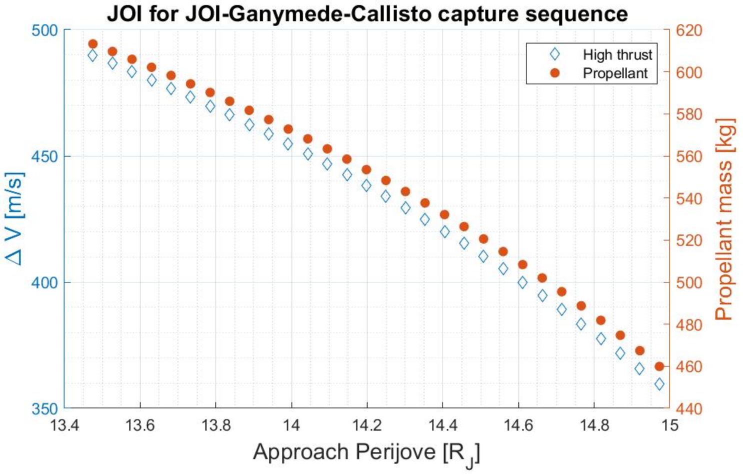

Figure 8.1: Required JOI maneuver in terms of ΔV and propellant mass considering a JOI-Ganymede-Callisto capture sequence for varying initial perijove.

of the flyby decreases. So, as was concluded from the results in Chapter 4, the combined effect of decreasing perijove and less effective flybys is dominated by the less effective flyby's and therefore results in increasing ΔV and propellant mass for the JOI. From Figure 8.1 one also learns that for every perijove value that was sampled, all flyby's were performed with minimum flyby altitude. This means that trajectories holding lower initial perijoves do not have the problem that their perijove decreases beyond the radiation safety belt (e.g., $8R_J$). If this would be the case, one or both flyby altitudes could be increased to prevent this. This would result in less effective flybys for lower perijoves. The effect would be noticeable as changing slopes for both ΔV and propellant mass. This phenomenon will become clear in the discussion of a Europa-Ganymede capture sequence.

Figure 8.2 presents the ephemerides results of a JOI-Ganymede-Callisto capture sequence for the range of initial perijoves sampled through the phasing problem. The first thing to notice is the (almost) vertical arrangement of the results. These arrangements are called flyby windows. They indicate a range of dates for which the desired phasing is found in the ephemerides search. The more vertical these windows are, the more strict the launch- and arrival dates are to the flyby sequence. One notices that for higher initial perioves, the desired phasing occurs later than for smaller initial perijove. This slightly narrows the gap between two flyby windows, making it easier to fly the sequence in terms of dates, but also makes the perijove requirement more strict. For mission planning, it is most desired to have both a wide perijove and date distribution.

The theory for these flyby windows lies in the dynamics of Callisto and Ganymede. The orbital period of Callisto (16.69 days), the synodic period of Callisto and Ganymede (12.52 days), and the orbital period of Ganymede (7.155 days) are very close to a 3:4:7 resonance or so-called *"near-orbital resonance"*. This near-orbital resonance has a (near) resonance period of approximately 50.3 days ($3T_{Ca}$ or $7T_{Ga}$). Near-orbital resonance implies that there is a mismatch. This mismatch, M_{Ca-Ga}, per (near) resonance period can be calculated using Equation 8.1 [18]. Here S_{Ca-Ga} is the synodic period between Callisto and Ganymede in days, T_{Ca} the orbital period of Callisto in days and n_{Ga} the angular velocity of Ganymede in degrees per day.

$$M_{Ca-Ga} = (4S_{Ca-Ga} - 3T_{Ca})n_{Ga} = 0.50317^{\circ}/\text{resonanceperiod} \tag{8.1}$$

In that same amount of time, Jupiter orbits around the Sun with an orbital period of $T_{Jup} = 4332.589\text{days}$, resulting in an additional mismatch:

$$M_{Sun} = \frac{360^{\circ}3T_{Ca}}{T_{Jup}} = 4.15^{\circ}/\text{resonanceperiod} \tag{8.2}$$

One can conclude that the mismatch between flyby's for a Callisto-Ganymede sequence is governed by Jupiter's orbit around the Sun. The total mismatch is calculated by subtracting

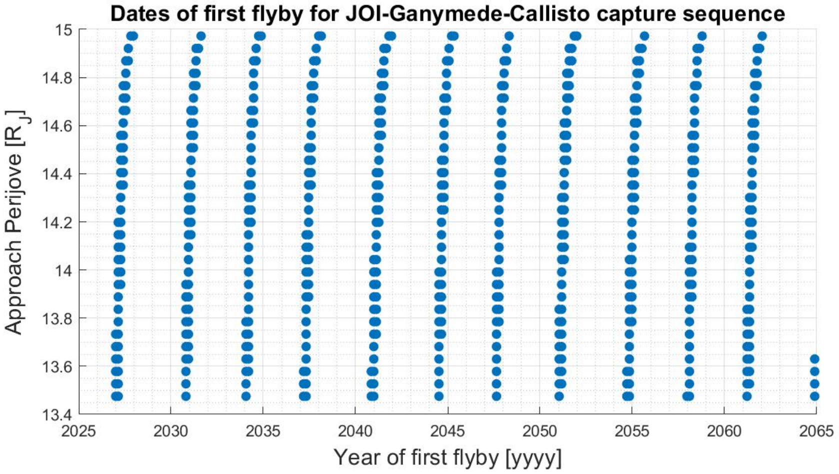

Figure 8.2: Ephemerides results within the 2025-2065 time interval considering a JOI-Ganymede-Callisto capture sequence for varying initial perijove. The vertical patterns represent four flyby windows that repeat every 13.523 years.

one from another:

$$M_{tot} = M_{Sun} - M_{Ca-Ga} = 3.6468°/50.3\text{days} = 0.07294°/\text{day} \tag{8.3}$$

This implies that when a flyby window has just occurred, a full 360°of mismatch needs to be filled to make the flyby window occur again. Or in other words, the flyby window repeat period, $T_{window,Ca-Ga}$ which is calculated using Equation 8.4.

$$T_{window,Ca-Ga} = \frac{360°}{M_{tot}} = 4935.7935 \text{ days} = 13.523 \text{ years} \tag{8.4}$$

Observing Figure 8.2 one may notice that these flyby windows occur much more often than once every 13.523 years. However, one (near) resonance period holds four synodic periods. This means that from the definition of the synodic period, the desired relative phasing of Callisto and Ganymede occurs four times during one (near) resonance period. One should simply wait until one of them coincides with the absolute phasing. Observing Figure A.6, the four most left flyby windows each reoccur after 13.523 years.

A JOI-Ganymede-Callisto capture sequence offers great advantages in terms of required JOI. Due to both Callisto and Ganymede's orbital radius, a wide range of initial perijoves hold valid satellite-aided planetary capture trajectories. In terms of valid dates at which the sequence could actually be flown, one should consider if a certain flyby window coincides with a particular interplanetary Hohmann transfer. This is highly dependent on forgoing mission planning. Because the flyby windows are not too strict (not completely vertical), a JOI-Ganymede-Callisto sequence could be attractive for mission planning as well.

Ganymede-Europa

The required JOI considering a JOI-Europa-Ganymede capture sequence for various initial perijove is shown in Figure A.11. They hold the sample points for which solutions were found in the ephemerides search. Similar as for a JOI-Callisto-Ganymede capture sequence, the JOI decreases as it approaches the optimum initial perijove. This is due to the combined effect of a less efficient JOI at higher perijove and more efficient flybys; governed by the more efficient flybys. For a JOI-Europa-Ganymede capture sequence one notices that for lower initial perijove the slope of the sample points differs from that of higher initial perijove. The reason for this lies in the flyby altitudes at which flybys are executed. For convenience these are shown in Figure 8.4. For lower initial perijoves the flyby altitudes differ from the minimum allowable altitude (500 km). This is to prevent the final captured orbit from having a perijove

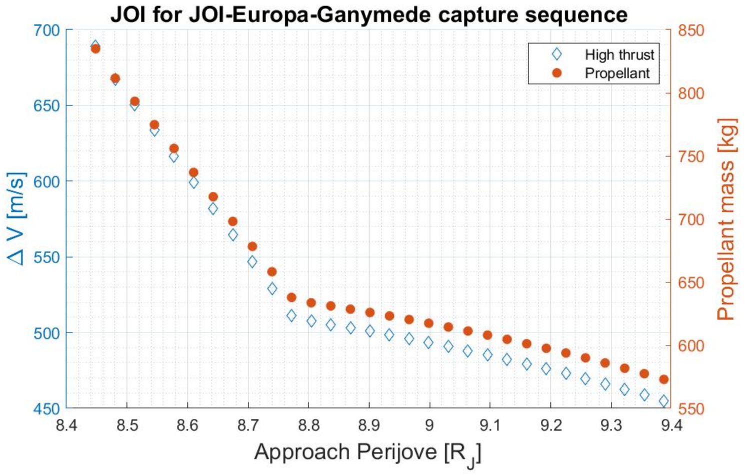

Figure 8.3: Required JOI maneuver in terms of ΔV and propellant mass considering a JOI-Europa-Ganymede capture sequence for varying initial perijove.

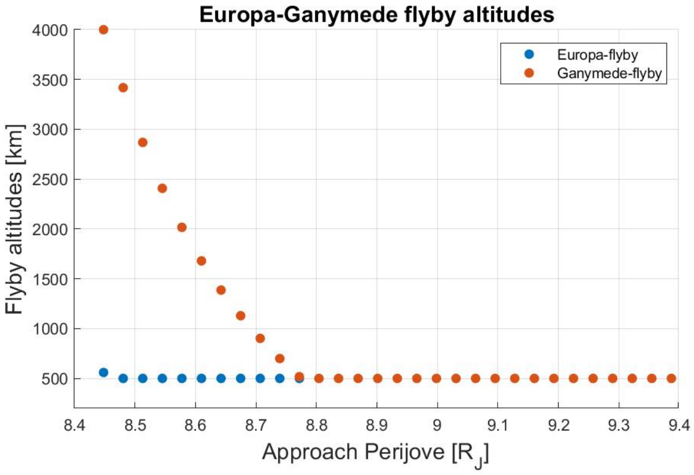

Figure 8.4: Flyby altitudes for a JOI-Europa-Ganymede capture sequence.

smaller than the radiation safety belt. However, it also limits the amount of orbital energy increment that one flyby could deliver (less effective flybys). This results in a more significant JOI to capture the spacecraft into the desired capture orbit above the earlier mentioned effect of increasing flight-path angles. Thus we obtain a more steep slope for these sample points. Again because the JOI is the only contribution in propellant mass, the progression of both ΔV and propellant mass is comparable. Figure 8.5 shows the ephemerides results of a JOI-Europa-Ganymede capture sequence. In this case, one can again see that dates at which the sequence can be flown coincide with certain flyby windows. Although these flyby windows appear to be more strict than for the JOI-Ganymede-Callisto sequence, they occur often. For that, it is worth taking a look into the dynamics of Ganymede and Europa.

Ganymede and Europa are in a 2:1 *orbital resonance*. Their synodic period and resonance period are both equal to Ganymede's orbital period, which means that every combination of phase angles only occurs once during every resonance period. With the orbital periods of both Ganymede and Europa, the mismatch can be calculated using Equation 8.5. Here T_{Eu} and T_{Ga} is the orbital period of Europa and Ganymede, respectively and n_{Eu} the angular velocity of Europa.

$$M_{Ga-Eu} = (2T_{Eu} - T_{Ga})n_{Eu} = -0.72246°/\text{resonanceperiod} \tag{8.5}$$

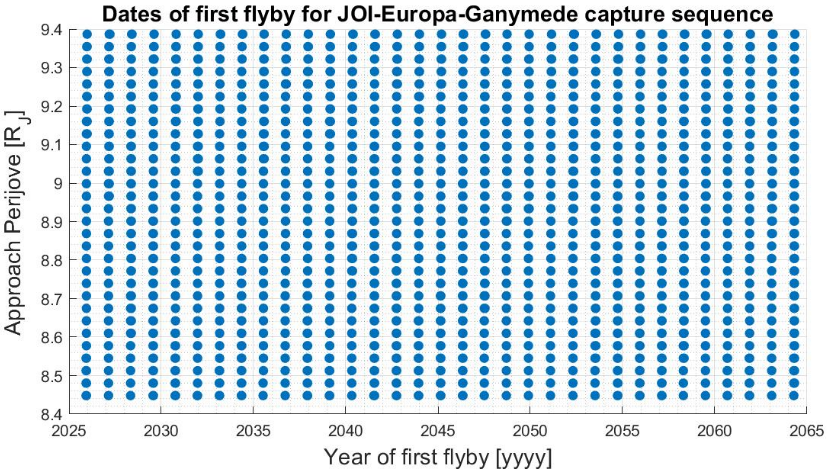

Figure 8.5: Ephemerides results within the 2025-2065 time interval for varying perijove considering a JOI-Europa-Ganymede capture sequence for varying initial perijove. The vertical patterns represent four flyby windows that repeat every 1.224 year.

Combining this with the mismatch due to Jupiter's orbit around the Sun:

$$M_{Sun} = \frac{360° T_{Ga}}{T_{Jup}} = 0.5945°/\text{resonanceperiod} \tag{8.6}$$

$$M_{tot} = M_{Sun} - M_{Ga-Eu} = 5.7646°/\text{resonanceperiod} = 0.8057°/\text{day} \tag{8.7}$$

So when a certain flyby window gets at its end, the time it takes for Ganymede and Europa to phase themselves again correctly is given by:

$$T_{window,Ga-Eu} = \frac{360°}{M_{tot}} = 446.8287\text{days} = 1.2242 \text{ year} \tag{8.8}$$

This 1.2242 year gap is clearly visible in Figure 8.5. Unlike Callisto and Ganymede, the proper relative phasing of Callisto and Ganymede only occurs once every resonance period, which is equal to the synodic period. The foregoing also holds for all other sequences that combine Europa and Ganymede in a capture sequence. These are not discussed here for brevity but shown in Appendix A.

In general, a JOI-Ganymede-Europa capture sequence offers fewer advantages than a Callisto-Ganymede capture sequence in terms of ΔV and propellant mass. For lower initial perijoves, higher flyby altitudes are required to prevent the final capture orbit from reaching below the radiation safety belt. In terms of valid dates on which the sequences can be flown, a Ganymede-Europa capture sequence offers more flyby windows that could align with a preceding interplanetary Hohmann transfer. Keep in mind that these flyby windows are more strict (vertical) than for a JOI-Ganymede-Callisto sequence.

Callisto-Europa

Figure 8.6 presents the required JOI for a JOI-Europa-Callisto capture sequence. Similar to the JOI-Europa-Ganymede scenario, one notices the decreasing progression towards its optimum initial perijove in two slopes. Therefore the flyby altitudes are presented in Figure 8.7. At the lowest initial perijove, both flyby altitudes approach the maximum (4000 km). The idea of increasing the flyby altitude(s) has its limits. When the flyby altitudes are increased such that they approaches their maximum value (4000 km) but the spacecraft is still captured in an orbit that has its perijove lower than the radiation safety belt, the sampling of this particular initial perijove is not fed to the phasing problem. This reduces the number of sampling points that appear in Figure 8.6.

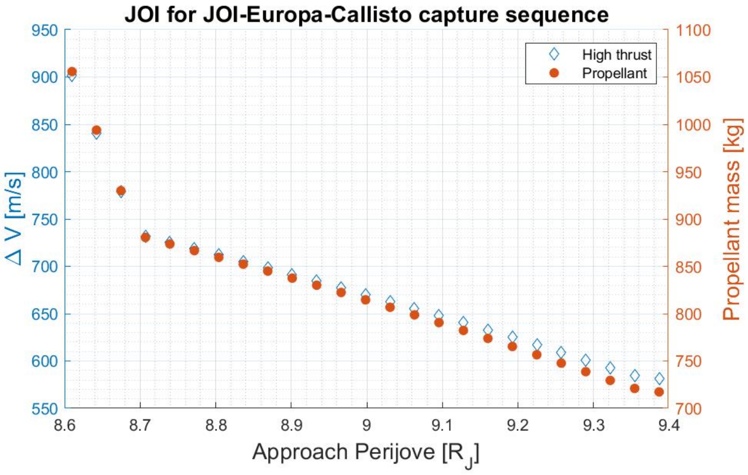

Figure 8.6: Required JOI maneuver in terms of ΔV and propellant mass considering a JOI-Europa-Callisto capture sequence.

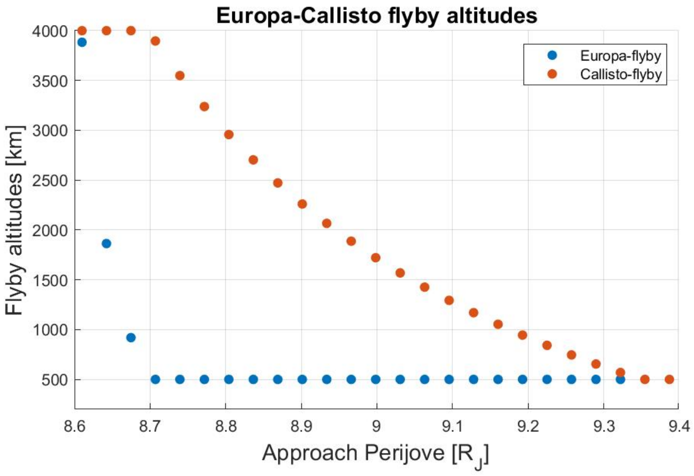

Figure 8.7: Flyby altitudes for a JOI-Europa-Callisto capture sequence

In Figure 8.8 the ephemerides results of the JOI-Europa-Callisto sequence are shown. Contrary to the Callisto-Europa and Callisto-Ganymede sequences, there appear to be no vertical alignments as in Figures 8.2 and 8.5. For JOI-Europa-Callisto, there is a more continuous behavior of possible dates on which the sequence can be flown. Also, there are multiple initial perijoves at which the trajectories could be flown at these particular dates. So we observe both a good date and initial perijove distribution for a JOI-Europa-Callisto sequence.
Observing Figure 8.8 closer, one can notice some periodicity in the pattern. For the JOI-Europa-Callisto sequence, this pattern appears in the ”no solution” areas. However, for each time the pattern returns on later dates it is shifted a bit towards higher initial perijoves although the shape is more or less the same. The author of this thesis research argues that this shifting is because of some long-periodic mechanism. Due to the limited time interval on which the ephemerides search is performed, there was no thorough investigation of this. However, the return of the pattern or the so-called ”short periodicity” will be investigated by estimating how long this ”short” period is. Multiple combinations of the orbital period with synodic periods, orbital period with orbital period and synodic period with synodic periods were tested in this estimate. It turned out that the combination of two synodic periods gave the best result. Considering the Sun-Callisto, S_{Sun-Ca} and Callisto-Europa S_{Ca-Eu} synodic periods from Table 7.1. One can observe that they are close to a rather long 37:10 resonance:

$$\frac{S_{Sun-Ca}}{S_{Ca-Eu}} = 3.714 \approx \frac{37}{10} \tag{8.9}$$

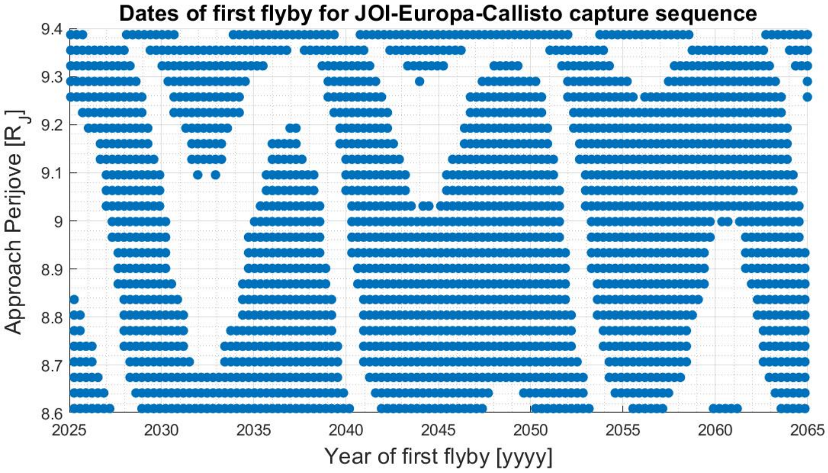

Figure 8.8: Ephemerides results within the 2025-2065 time interval considering a JOI-Europa-Callisto capture trajectory for varying initial perijove. A short and long periodicity are observed in the patterns. The short periodicity repeats every 12.2 years.

Similar to the Callisto-Ganymede and Ganymede-Europa sequences, a mismatch is calculated:

$$M_{Ca-Eu} = \frac{37S_{Ca-Eu} - 10S_{Sun-Ca}}{10S_{Sun-Ca}} n_{Sun-Ca} = -0.0809°/\text{day} \tag{8.10}$$

Because the synodic period between Callisto and the Sun already takes the mismatch due to Jupiter's orbit around the Sun, it is not required to take it into account here. Therefore the period for the short-periodic pattern appearing in Figure 8.8 is given by:

$$T_{pattern,Ca-Eu} = \frac{360°}{M_{Ca-Eu}} = 4452.2355\text{days} = 12.1979 \text{ years} \tag{8.11}$$

This 12.1979 years can also be seen in Figure 8.8.

In general, a Callisto-Europa capture sequence offers less advantages in terms of ΔV and propellant mass. Most of the sequences require higher flyby altitudes to stay above the radiation belt of Jupiter. In terms of ephemerides results, a more continuous behavior of opportunities arises for both dates and initial perijoves. Contrary to the case that flyby windows appear, an interplanetary Hohmann transfer will generally always align with a possible phasing. Although at a particular date, not all initial perijoves will find solutions in the ephemerides search. This makes the requirements on the initial perijove slightly stricter.

8.1.2 Triple-aided

Here the results of a JOI-Europa-Ganymede-Callisto (triple)-aided capture sequence are presented. Figure 8.9 shows very strong dependency on the initial perijove for the JOI and propellant mass (860 to 460 kg). Also notice the different slopes that indicate changing flyby altitudes. The progression of these flyby altitudes is shown in Figure 8.10. However one important aspect to notice is the limited number of sample points that appear in the graph. From the 30 initial perijoves sampled, only ten of them have a solution in the ephemerides search. There are two reasons for this. The first one is due to the strong geometrical constraints that arise for a triple flyby sequence. The second is the orbital radius of Europa and the radiation safety belt that limit the range in which initial perijoves can be sampled. This latter was already argued in the discussion of the results from Chapter 4.

In terms of JOI, a triple flyby sequence can further decrease the amount of ΔV and thus propellant mass. However, due to the limiting range in initial perijove, navigational issues might become so severe that intense TCMs will be needed when flying the sequence.

Figure 8.11 shows the ephemerides results for the JOI-Europa-Ganymede-Callisto sequence. One can notice the vertical arrangements of the solutions that indicate the presence of flyby

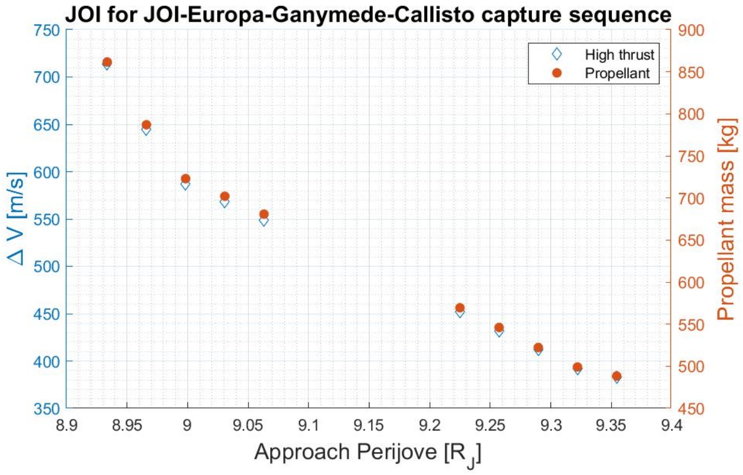

Figure 8.9: Required JOI maneuver in terms of ΔV and propellant mass considering a JOI-Europa-Callisto capture sequence for varying initial perijove.

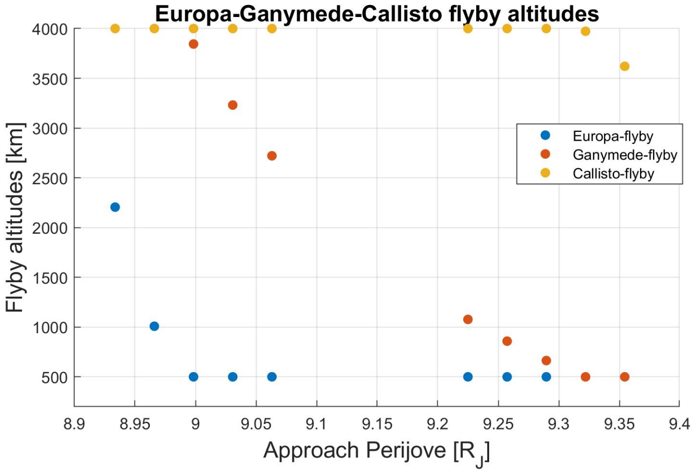

Figure 8.10: Flyby altitudes for a JOI-Europa-Ganymede-Callisto capture sequence.

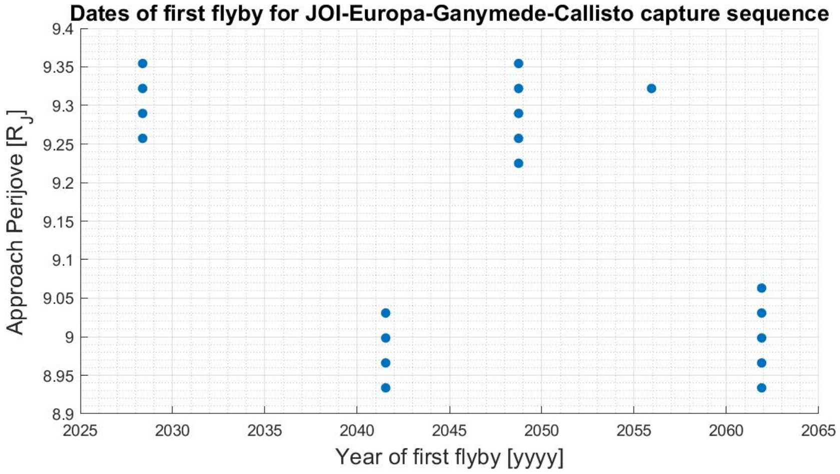

Figure 8.11: Ephemerides results within the 2025-2065 time interval considering a JOI-Europa-Ganymede-Callisto capture trajectory for varying initial perijove.

windows. Compared to the double flyby sequences, one concludes that the strong geometrical constraints given by a third flyby limit the number of dates on which the triple flyby sequence can be flown. The similar method as for double-aided sequences was used to investigate the periodicity of these triple-aided sequences.

$$\frac{S_{Ca,Ga}}{S_{Ga,Eu}} = 1.77606 \approx 1.777.. = \frac{16}{9} \tag{8.12}$$

$$M_{Ca,Ga,Eu} = (16S_{Ga,Eu} - 9S_{Ca,Ga})n_{Ca} = 2.3512°/\text{resonanceperiod} = 0.020841°/\text{day} \tag{8.13}$$

$$T_{window,Ca,Ga,Eu} = \frac{360°}{M_{Ca,Ga,Eu}} = 17273.2719 days = 47.32 \text{ years} \tag{8.14}$$

The synodic period of the two systems Callisto-Ganymede and Ganymede-Europa is given by:

$$S_{Ca,Ga,Eu} = \frac{2\pi}{\frac{2\pi}{S_{Ga,Eu}} - \frac{2\pi}{S_{Ca,Ga}}} = 16.13 \text{ days} \tag{8.15}$$

One resonance period is given by $16S_{Ga,Eu}$ = 112.816 days. This implies that there are 112.816/16.13 = 7 synodic periods in one near-orbital resonance period, or seven flyby windows in $T_{window,Ca,Ga,Eu}$. The time between two of these seven flyby windows is equal to 6.714 years. This is approximately the separation between the vertical arrangements in Figure 8.11. Although a good estimation was made here, a wider time interval needs to be examined to be sure. The author leaves this latter for future work and recommendations.

In general, a third flyby can further lower the required JOI. However, because of the orbital radius of Europa and radiation safety belt, the range of initial perijove in which the flybys can be flown is rather limited. Lower initial perijoves require flybys at higher altitude, making them less effective. Due to a third flyby, the geometrical events required from the ephemerides search are very strict. Therefore, the number of dates at which the flybys could be flown is very limited. It is emphasized that a triple flyby sequence will require more TCMs. The ΔV required for this might overshadow the benefits of a third flyby. Therefore, at this point, the author of this thesis research argues that a double flyby sequence looks more promising.

8.1.3 Summary of satellite-aided results

The results of all satellite-aided planetary capture sequences are summarized in Table 8.1. The table is essentially an extension of Table 4.3. ΔV_{JOI} is left out and two phasing grades are added: One that reflects upon the date distribution (0-5) in the results of the ephemerides search and one upon the perijove distribution (0-5). Both are added up to a total phasing score. By evaluating both the propellant mass and phasing, one could estimate what particular sequences are attractive in mission planning.

The not-aided and single-aided all score very well for phasing, because they hold almost no geometrical constraints. The constraint there is the initial perijove due to the orbital radius of the moon. However, they perform worst in terms of propellant mass. For single-aided capture, it appears that a JOI-Ganymede clearly requires the least propellant mass and therefore, the author argues that this sequence should be preferred (between all single-aided trajectories).

For the double aided scenario, the Callisto-Europa sequences perform worst of the three possible combinations (of two moons). Moreover, their phasing score is also marginal. Thus, these should not be preferred. The Callisto-Ganymede and Ganymede-Europa sequences have comparable phasing scores. However, the Callisto-Ganymede-sequences clearly require the least amount of propellant mass. The author argues that a Callisto-Ganymede sequence should be preferred for a double-aided trajectory, moreover, a JOI-Ganymede-Callisto sequence.

	$M_{prop,min}$ [kg]	Date [0-5]	Perijove [0-5]	Total [0-10]
Direct				
-	1218	5	5	10
Single-aided				
Callisto				
CJ	1056	5	5	10
JC	1080	5	5	10
Ganymede				
GJ	945	5	4	9
JG	785	5	4	9
Europa				
EJ	990	5	3	8
JE	939	5	3	8
Double-aided				
Callisto-Ganymede:				
CGJ	547	3	4	7
CJG	484	3.5	4	7.5
JGC	460	3.5	4	7.5
GJC	517	3	4	7
Ganymede-Europa				
GEJ	615	4	4	8
GJE	580	4	4	8
JEG	573	4	3	7
EJG	603	4	3	7
Callisto-Europa				
CEJ	780	1.5	3	4.5
CJE	738	3.5	3	6.5
JEC	717	5	3	8
EJC	755	4	3.5	7.5
Triple-aided				
CGEJ	N/A	0	0	0
CGJE	378	0.5	2	2.5
CEJG	N/A	0	0	0
CJEG	396	0.5	1.5	2
GEJC	404	0.5	1.5	2
GJEC	337	0.5	0.5	1
EJGC	545	2	2	4
JEGC	478	2.5	1.5	4

Table 8.1: Results of all satellite-aided capture trajectories. Two grades reflecting on the valid dates and perijove distribution to reflect upon the advantages for mission planning. The sequence is indicated with the first letters of the flyby moons and J for the JOI.

Triple-aided trajectories were all given a low phasing score due to the strict geometrical constraints that come with a third flyby. Both Callisto-Europa-JOI-Ganymede and Callisto-Ganymede-JOI-Europa had no solutions in the ephemerides search. Therefore they received a phasing score of zero, and the propellant mass was set at N/A. The highest phasing score that was granted for the triple aided was for the sequences with Europa in the beginning. Although comparing the propellant mass with the Callisto-Ganymede double-aided sequences, the author argues that one should not want to fly a triple-aided capture sequence. Also note that for some of the sequences, the ephemerides search could not find solutions for the optimum found in Chapter 4. This is why for some of the sequences the minimum propellant mass in Table 8.2 differs from that presented in Table 4.3.

8.2 Low-thrust satellite-aided results

This section discusses the phasing results of low-thrust satellite aided planetary capture trajectories. That is, combining two or three flybys, a JOI maneuver and low-thrust propulsion along the trajectory. Similar to the ballistic case from the previous section, the results hold two or three graphs, one for the ΔV (low-thrust and JOI) and total propellant mass, one for the ephemerides results and if necessary, a third graph that shows the flyby altitudes. First, the low-thrust double-aided results are given, then the low-thrust triple-aided trajectories and the section closes with a summary of all results and conclusions.

8.2.1 Low-thrust double-aided

The low-thrust double-aided results are given in the same order as for the ballistic results. First the combination Callisto-Ganymede, then Ganymede-Europa and finally, Callisto-Europa.

Low-thrust Ganymede-Callisto

In Figure 8.12 the ΔV and propellant mass results are shown for a JOI-Ganymede-Callisto low-thrust capture sequence.

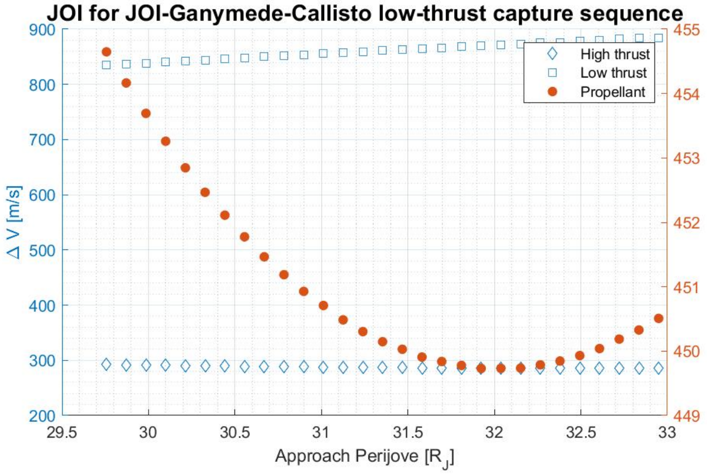

Figure 8.12: Required JOI and low-thrust ΔV combined in total propellant mass considering a low-thrust JOI-Ganymede-Callisto capture sequence for varying initial perijove.

In the figure, one can see that the progression of the required ΔV_{JOI} is constant around 290 m/s. This suggests no (strong) dependency of the JOI on the initial perijove, which is contradictory to the ballistic case (Figure 8.1). 290 m/s is generally smaller than any of the results for the ballistic case. The presence of low-thrust along the trajectory further decreases the required ΔV_{JOI}. The ΔV_{LT} shows an increase from 840 to 880 m/s along with increasing initial perijoves. This due to the spacecraft flying a longer trajectory giving the low-thrust propulsion more time to deliver ΔV_{LT}. As mentioned earlier, these two ΔV's are combined in one total propellant mass for the whole trajectory which slightly varies from 453.5 to 449.8 kg. This could be interesting for mission planning, considering possible deviations from nominal initial perijoves. Note that the minimum amount of propellant mass does not coincide with the optimum initial perijove in terms of ΔV_{JOI}. The minimum propellant mass lies at 32 R_J; increasing this with one R_J gives the low-thrust propulsion a longer trajectory and thus more time to insert ΔV. This has no effect on ΔV_{JOI}. Hence the small increase in propellant mass after $32R_J$. The ephemerides results of the JOI-Ganymede-Callisto low-thrust capture sequence are presented in Figure 8.13. One notices the presence of flyby windows. These were also observed in the ballistic case (Figure 8.2) but now slightly shifted to later dates.
A second difference from the flyby windows in Figure 8.2 is that the flyby windows over the full range of initial perijove are more compressed (e.g., vertical patterns are more vertical).

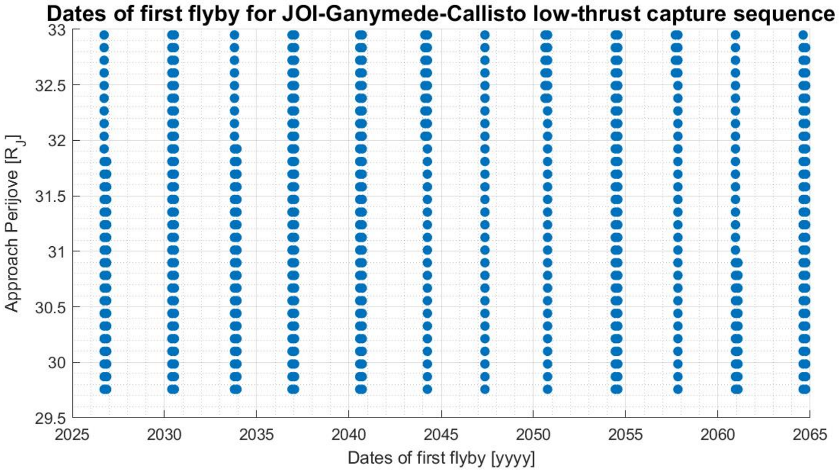

Figure 8.13: Ephemerides results within the 2025-2065 time interval for varying perijove considering a low-thrust JOI-Ganymede-Callisto capture sequence. The vertical patterns represent four flyby windows that repeat every 13.523 years.

This could be beneficial when a spacecraft arrives at the planned date but the initial perijove differs from its nominal. However, this increases the gap between two flyby windows, which is generally not beneficial for mission planning. The periodicity at which these flyby windows occur is independent of the type of flown trajectory (e.g. with or without low-thrust). Ephemerides are only dependent on the dynamics of the moons considered. Therefore, the estimation of the periodicity obtained in Subsection 8.1.1 also holds here and will not be repeated.

In general, one can conclude that a JOI-Ganymede-Callisto low-thrust capture trajectory further decreases the JOI compared to the ballistic case. There appears to be no dependency of the JOI on the initial perijove and thus, the required propellant mass only slightly varies for different perijoves. The dynamics of Ganymede and Callisto and the low-thrust phasing requirements result in more compressed flyby windows. These need to coincide with a foregoing interplanetary trajectory to actually fly the sequence.

Low-thrust Ganymede-Europa

A JOI-Europa-Ganymede low-thrust capture trajectory shows a strong dependence on the initial perijove for both the impulse JOI (ΔV_{JOI}) and the low-thrust (ΔV_{LT}). Consequently, there is a strong dependency of the total propellant mass on the initial perijove (ranging from 590 to 490 kg in Figure 8.14).

The impulsive JOI shows the same behavior as for the ballistic case. It decreases towards the optimum initial perijove in two slopes as a result of increasing flyby altitude. This increase in flyby altitudes is shown in Figure 8.15. ΔV_{LT} increases towards the optimal initial perijove due to the increasing time of flight. Because of the high specific impulse of the low thrust, an increase in ΔV_{LT} has minimal effect on the total propellant mass. A strong dependence of the propellant mass (due to increasing ΔV_{JOI}) on the initial perijove is generally less desired for mission planning.

Figure 8.16 shows the ephemerides results. The implementation of low-thrust on a JOI-Europa-Ganymede capture sequence appears to have a marginal influence on the flyby windows. This was concluded by comparing Figures 8.5 and 8.14.

A JOI-Europa-Ganymede low-thrust capture sequence is less attractive for mission planning when considering propellant mass (compared to other low-thrust double-aided sequences). In terms of dates at which the sequence can be flown, there is hardly any difference from the ballistic case (flyby windows and periodicity).

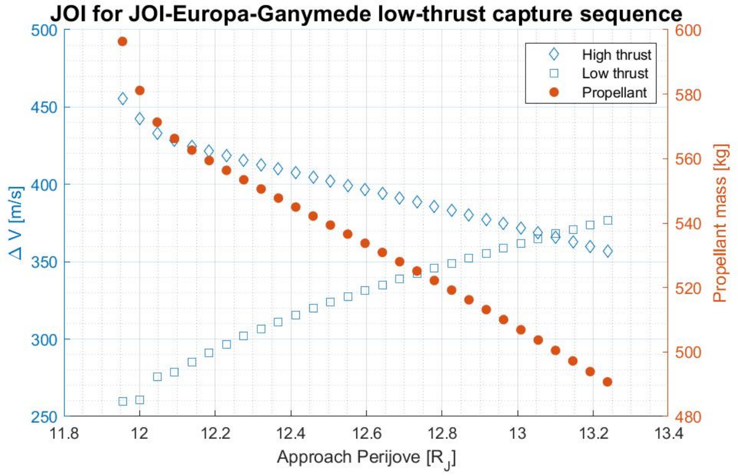

Figure 8.14: Required JOI and low-thrust ΔV combined in total propellant mass considering a low-thrust JOI-Europa-Ganymede capture sequence for varying initial perijove.

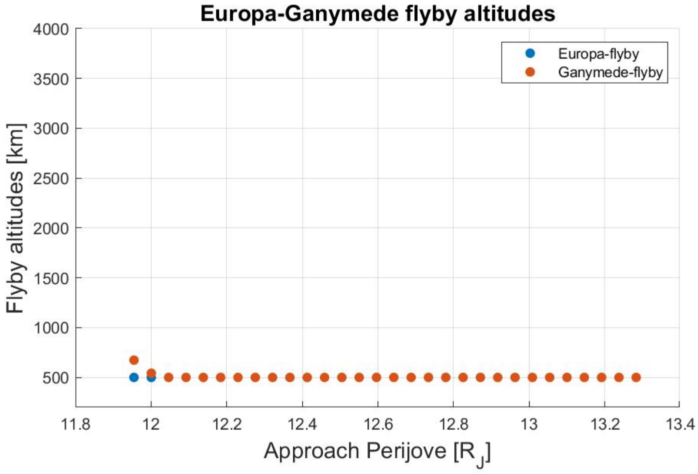

Figure 8.15: Flyby altitudes considering a low-thrust JOI-Europa-Ganymede capture sequence for varying initial perijove.

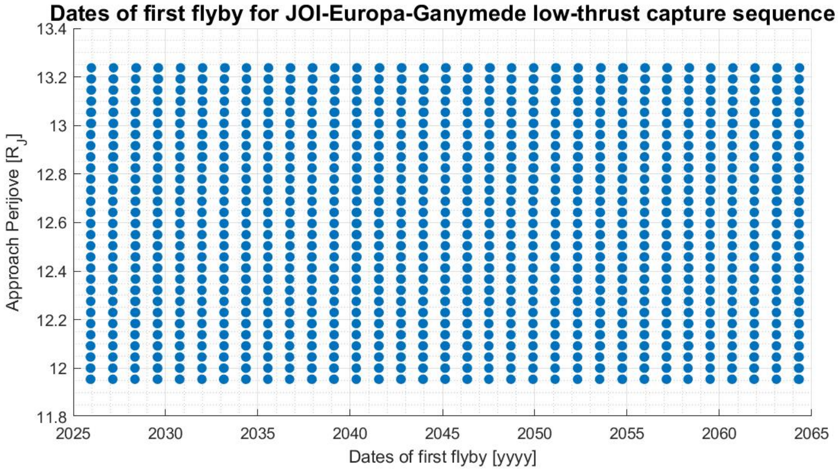

Figure 8.16: Ephemerides results within the 2025-2065 time interval considering a low-thrust JOI-Europa-Ganymede capture sequence for varying initial perijove. The vertical arrangements represent four flyby windows that repeat every 1.224 year.

Low-thrust Europa-Callisto

The ΔV results and total propellant mass for a JOI-Europa-Callisto capture sequence are shown in Figure 8.17. The impulsive JOI shows a strong dependence on the initial perijove (decreasing towards the optimum initial perijove), which is considered undesirable for mission planning. ΔV_{LT} is less dependent on the initial perijove and, together with its high specific impulse, makes the ΔV_{LT} have minimal influence on the progression of total propellant mass. Therefore, identical to the JOI-Europa-Ganymede low-thrust sequence, a JOI-Europa-Callisto low-thrust sequence shows a strong dependency of the total propellant mass on the initial perijove (815 to 630 kg). The presence of low thrust decreases the amount of propellant mass compared to the ballistic JOI-Europa-Callisto. Still, a JOI-Europa-Callisto low-thrust sequence performs worse than both a JOI-Ganymede-Callisto- and JOI-Europa-Ganymede low-thrust capture trajectory. This latter was also concluded for the ballistic case.

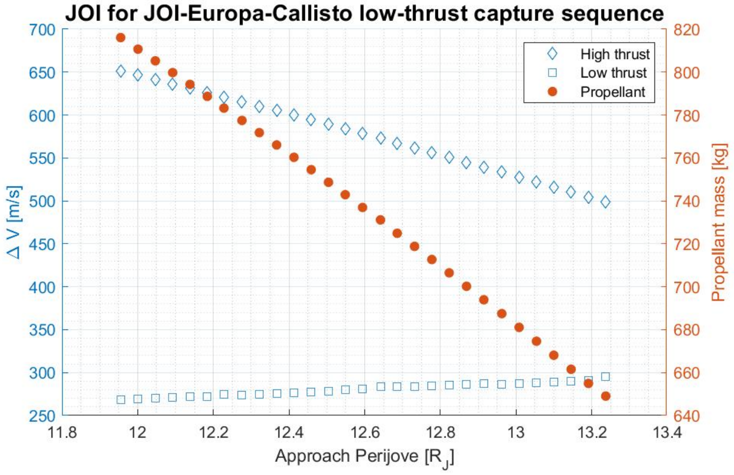

Figure 8.17: Required JOI and low-thrust ΔV combined in total propellant mass considering a low-thrust JOI-Europa-Callisto capture sequence for varying initial perijove.

Considering the flyby altitudes of a JOI-Europa-Callisto sequence, Figure 8.17 does not show any multiple slopes for ΔV_{JOI} and total propellant mass. This suggests that each flyby is flown at minimum flyby altitudes. However, plotting both the Europa and Callisto flyby altitudes (Figure 8.18) one observes that the Callisto flyby altitude decreases over the whole range of approach perijove. This explains the strong dependence on the initial perijove for both ΔV_{JOI} and propellant mass. Contradictory to the ballistic JOI-Europa-Callisto sequence, the flyby altitudes do not reach their maximum allowable value. Figure 8.19 shows the ephemerides results of the JOI-Europa-Callisto low-thrust capture sequence. Apart from higher initial perijoves as in Figure 8.8 due to low thrust, no real differences can be observed in both graphs. Therefore, the reasoning on the ephemerides results from Section 8.1.1 also holds here. For mission planning, a JOI-Europa-Callisto low-thrust capture sequence is less beneficial in terms of ΔV_{JOI} (and thus also propellant mass) compared to the other low-thrust sequences. However, the presence of low-thrust shows its benefits over the ballistic sequence. Moreover, due to low thrust, the ephemerides results show a wider range of initial perijoves. For valid dates on which the sequences could be flown, a more continuous behavior is observed. However, not every date holds solutions for the full range of initial perijoves sampled.

8.2.2 Low-thrust triple-aided

Figure 8.20 shows the ΔV and propellant mass result for a JOI-Europa-Ganymede-Callisto low-thrust capture sequence. Similar to the ballistic triple-aided results, only a limited number of sample points appear in the graph: only nine of the 30 initial perijoves sampled gave results in the ephemeride search. From this one can conclude the same as for the triple bal-

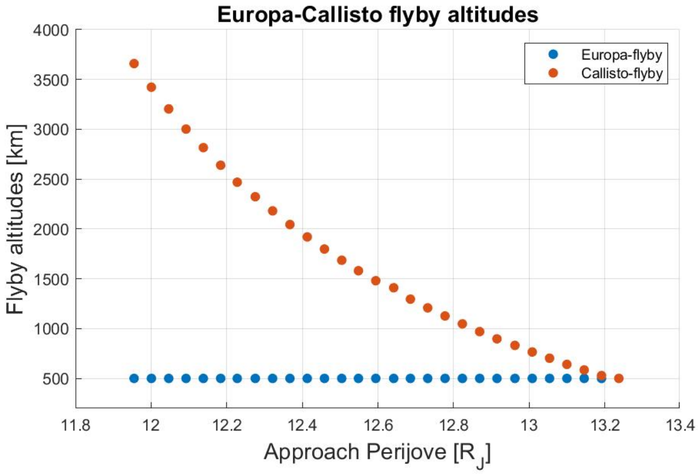

Figure 8.18: Flyby altitudes considering a low-thrust JOI-Europa-Callisto capture sequence for varying initial perijove.

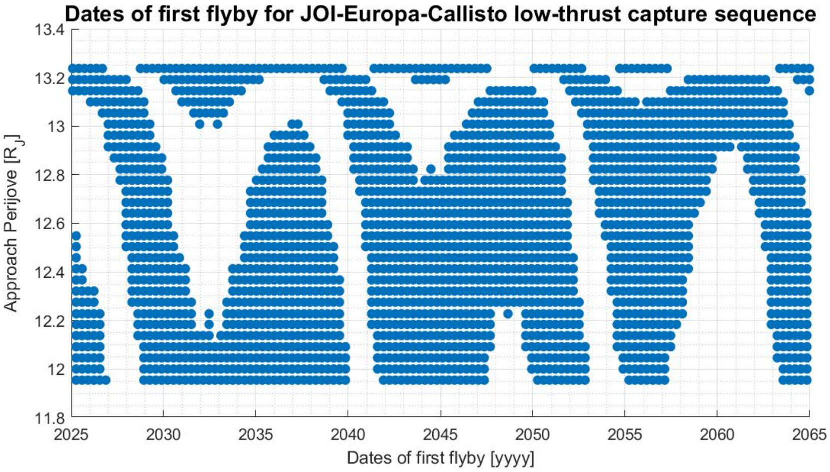

Figure 8.19: Ephemerides results within the 2025-2065 time interval considering a JOI-Europa-Callisto capture trajectory for varying initial perijove.

listic sequences, that due to a third flyby, the geometrical constraints are simply too strict. Moreover the orbital radius of Europa and the radiation belt safety narrow down the range in which the initial perijove can be sampled. Compared to the ballistic JOI-Europa-Ganymede-Callisto sequence, the presence of low thrust does show its benefits in terms of minimum propellant mass. The progression of ΔV_{LT} is rather constant over the initial perijoves. Because of decreasing flyby altitudes towards increasing perijove, ΔV_{JOI} and total propellant mass show a strong decrease. To clarify this, the three flyby altitudes are presented in Figure 8.21. Please note that around initial perijove of $12.65 R_J$, Figure 8.21 shows an outlier. This is also visible for in Figure 8.20. The reader should be aware that this is due to the numerical nature of the problem.

Figure 8.22 presents the ephemeride results of the JOI-Europa-Ganymede-Callisto low-thrust capture sequence. Compared to the ballistic ephemerides results in Figure 8.11, less solutions were found by the ephemeride search. The number of dates at which the sequence could be flown stays approximately the same, but the requirements on initial perijove become very strict.

In general, the presence of low-thrust propulsion could further lower the total propellant mass compared to a ballistic JOI-Europa-Ganymede-Callisto sequence. However, in terms of phasing, the low-thrust phasing requirements become more strict compared to the ballistic triple-aided trajectories. For mission planning, a low-thrust triple-aided capture trajectory

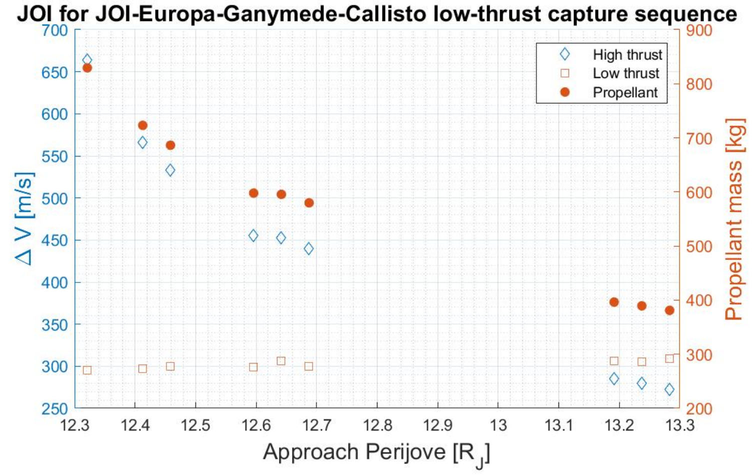

Figure 8.20: Required JOI and low-thrust ΔV combined in total propellant mass considering a low-thrust JOI-Europa-Ganymede-Callisto capture sequence for varying initial perijove.

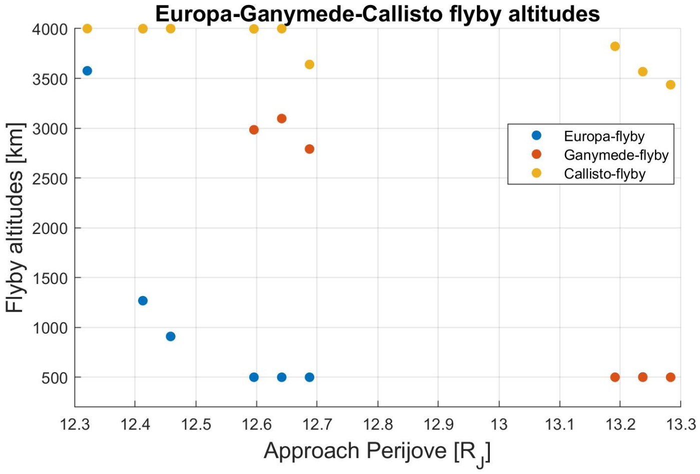

Figure 8.21: Flyby altitudes for a JOI-Europa-Ganymede-Callisto low-thrust capture sequence.

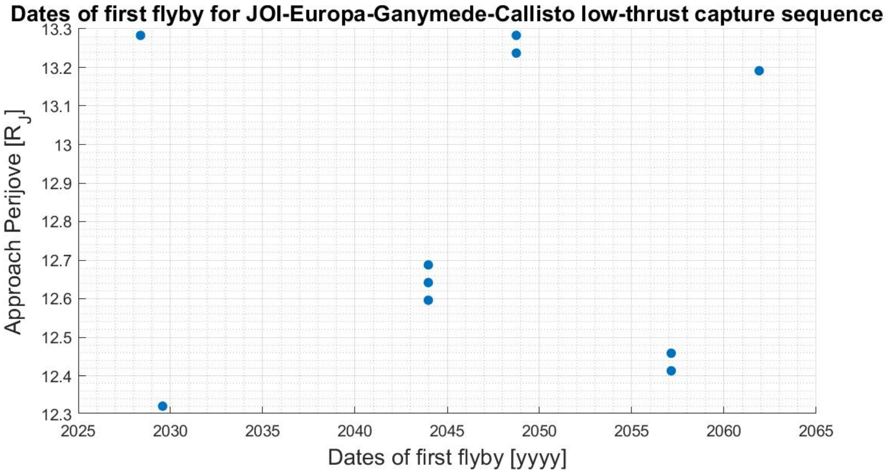

Figure 8.22: Ephemerides results within the 2025-2065 time interval considering a JOI-Europa-Ganymede-Callisto capture trajectory for varying initial perijove.

should not be preferred over a low-thrust double-aided trajectory.

8.2.3 Low-thrust satellite-aided results

	$M_{prop,min}$ [kg]	Date [0-5]	Perijove [0-5]	Total [0-10]
Single-aided				
Callisto				
CJ	932	5	5	10
JC	950	5	5	10
Ganymede				
GJ	798	5	4	9
JG	749	5	4	9
Europa				
EJ	903	5	3.5	8.5
JE	859	5	3.5	8.5
Double-aided				
Callisto-Ganymede:				
CGJ	548	3	4	7
CJG	524	3.5	4	7.5
JGC	450	3	4.5	7.5
GJC	475	3	4	7
Ganymede-Europa				
GEJ	505	4	4	8
GJE	480	4	4	8
JEG	487	4	3	7
EJG	510	4	3	7
Callisto-Europa				
CEJ	677	1.5	3	4.5
CJE	640	3.5	3	6.5
JEC	649	5	3	8
EJC	673	4	3.5	7.5
Triple-aided				
CGEJ	N/A	0	0	0
CGJE	258	0.5	3	3.5
CEJG	N/A	0	0	0
CJEG	243	0.5	0.5	1
GEJC	273	0.5	0.5	1
GJEC	238	1	1	2
EJGC	422	1	1	2
JEGC	378	2.5	1	3.5

Table 8.2: Results of all low-thrust satellite-aided capture sequences. Two grades reflecting on the valid dates and perijove distribution to reflect upon the advantages for mission planning.

The results of all low-thrust satellite-aided planetary capture sequences are presented in Table 8.2. Again, all sequences were given a phasing score based on the date and perijove distribution. The direct low-thrust trajectory was not examined.

All low-thrust single-aided trajectories have a relatively high phasing score. The only geometrical constraint that arises here is that the orbital radius of the flyby moon limits the initial perijove. This is why Callisto has a maximum phasing score and Europa only an 8.5. However in terms of propellant mass, sequences with Callisto score worst and Europa best. For mission planning the JOI-Ganymede low thrust sequence scores best. This was also the case for the ballistic case and the author suggests that this sequence should again be preferred.

For low-thrust double-aided capture, the Callisto-Europa combinations score worst in terms of propellant mass. Also the orbital radius of Europa limits the initial perijove and therefore these sequences should not be preferred. The low-thrust Callisto-Ganymede and and Ganymede-Europa sequence again have comparable phasing score. This is observed against a lower propellant mass for Callisto-Ganymede. Thus the author suggests that for low-thrust double-aided capture, the Callisto-Ganymede sequences should first be considered. This was also concluded for the ballistic double-aided capture results.
The low-thrust triple-aided trajectories score overall score best in terms of propellant mass. However, they are all granted a very low phasing score. The Callisto-Ganymede-JOI-Europa- and Callisto-Ganymede-Europa-JOI sequences again did not find solutions in the ephemerides search. Therefor they can not be considered and the lowest phasing score (zero) was given to them. Comparable to the ballistic case, the sequences with Europa placed first in the sequence or right after the JOI (which is then the first) could be considered. Other than the ballistic triple-aided sequences, these have a lower propellant mass. For the low-thrust JOI-Europa-Ganymede-Callisto sequence this could save 72 to 170 kg in propellant mass compared to the low-thrust Callisto-Ganymede sequences. However a phasing score of three is still considered very low and the author argues again that a low-thrust triple-aided capture sequence should not be preferred.

Chapter 9

Verification and Validation

This chapter explains the verification and validation methods used throughout the thesis research. Some verification efforts were already shown through the report and, therefore, not repeated here. First, the methodology of the Tisserand graph is validated in Section 9.1. Then the ballistic optimization algorithm is verified and validated in Section 9.2. Then some verification efforts on the low-thrust optimizations in Section 9.4.

9.1 Tisserand graph

Here the methodology of creating a Tisserand graph is validated by means of comparison. First the Tisserand from Figure 3.3 will be repeated here in Figure 9.1 for convenience. The graph includes the planets from Jupiter up to Neptune. The same Tisserand graph was found in [26]. Only here Pluto is also included. Besides from that, the two plots show that the algorithm from Subsection 3.5.1 produces the correct Tisserand graph.

9.2 Ballistic optimization

This section explains the verification and validation efforts for the optimizations of Chapter 4. This is crucial to gain confidence in the methodologies in Chapter 4 and the results of the optimizations.

9.3 Verification of ballistic optimization algorithm

Three efforts are taken for verification. First, the algorithm is tested for zero flybys, then results from different seed numbers are compared with each other and lastly, for all three seed numbers, a short investigation of the perijove penalty.

9.3.1 Direct

As a first attempt of testing the optimization algorithm, it is tested towards the case that no flybys are used to capture the spacecraft in the desired orbit around Jupiter. This implies that the Jupiter orbit insertion is the only mechanism that ensures this. The amount of ΔV_{JOI} required to insert the spacecraft into the desired orbit is calculated using Equation 9.1. In this equation, r_p is the initial perijove. This is also the final perijove since an impulsive JOI at perijove generally does not change the initial perijove. It is known that an impulsive maneuver is most efficient at lower perijoves. Thus taking into account the radiation belt safety, r_p should be equal to $8R_J$. The eccentricity of the approach hyperbola e is calculated using Equation 6.3 which is repeated here in Equation 9.2 for convenience. a_i is the initial semimajor axis of the approach hyperbola and given by Equation 9.3. The same for Equation 3.23 in Equation 9.4 that gives the semimajor axis of the 200-day periodic capture orbit.

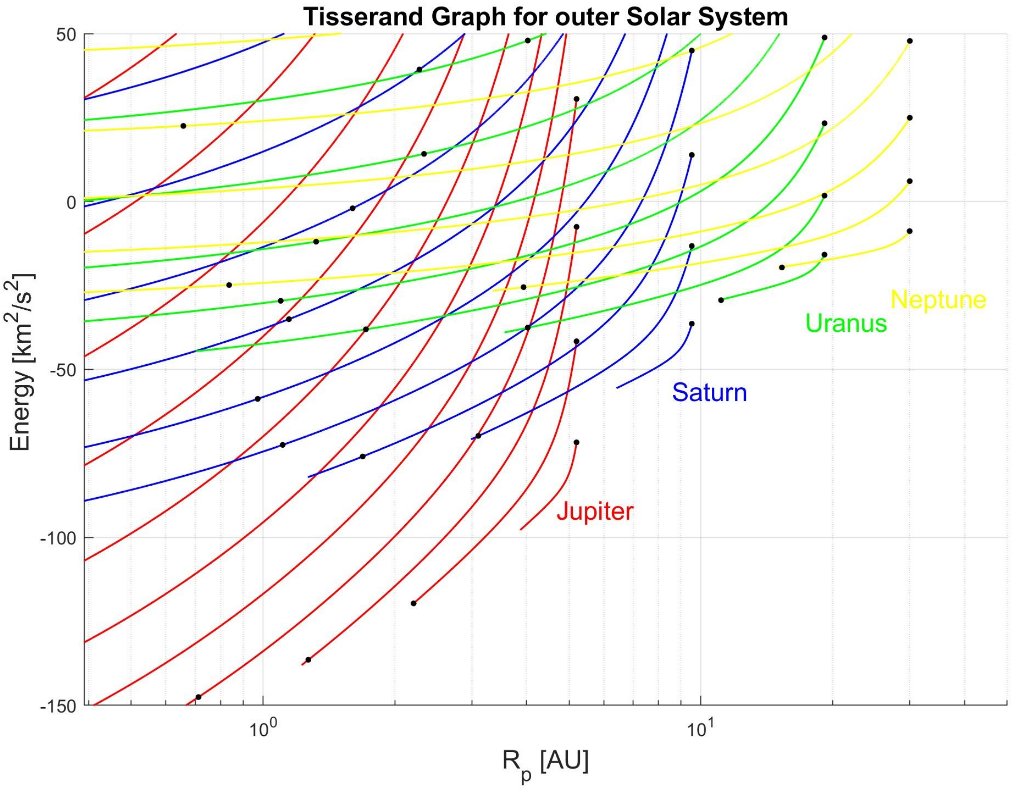

Figure 9.1: Tisserand graph of the outer Solar System. Thick marks on the contour lines illustrate the effect of a single gravity assist with the planet considered taking into account the maximum bending angle as a result of the minimum flyby altitude (six Jupiter radii for Jupiter, three Saturn radii for Saturn, and two planetary radii for Uranus and Neptune). Increments for the hyperbolic excess velocity are set to 2 km/s increasing from right at 1 km/s below to the upper left.

$$\Delta V_{JOI} = \sqrt{\frac{\mu_J}{r_p}\left(2 - \frac{r_p}{a_c}\right)} - \sqrt{\frac{\mu_J}{r_p}(1 + e_0)} \tag{9.1}$$

$$e_0 = 1 - \frac{r_p}{a_i} \tag{9.2}$$

$$a_i = \frac{\mu_J}{2E_i} \tag{9.3}$$

$$T = 2\pi\sqrt{\frac{a_c^3}{\mu_J}} \tag{9.4}$$

Using the above equations and the initial conditions from Subsection 4.2.2, a non-aided planetary capture trajectory requires 1069.42 m/s for the impulsive JOI. Setting the number of flybys in the fitness function of Subsection 4.2.1 equal to zero gave the same result. Moreover, the initial perijove also converged toward the minimum allowable, that is, eight Jupiter radii.

9.3.2 Different seed numbers

The results from three different seed numbers are compared for three different triple-aided capture sequences. A seed number is initialized at the beginning of the optimization and its purpose is to guarantee the reproduciblity of the results in the future. To better visualize any possible differences, the linewidth is set thinner than in the actual results of Chapter 4.

By observing Figure 9.3 one concludes that there are no visual differences between the solutions. This excellent overlap gave confidence in the results of the optimizations in Chapter 4.

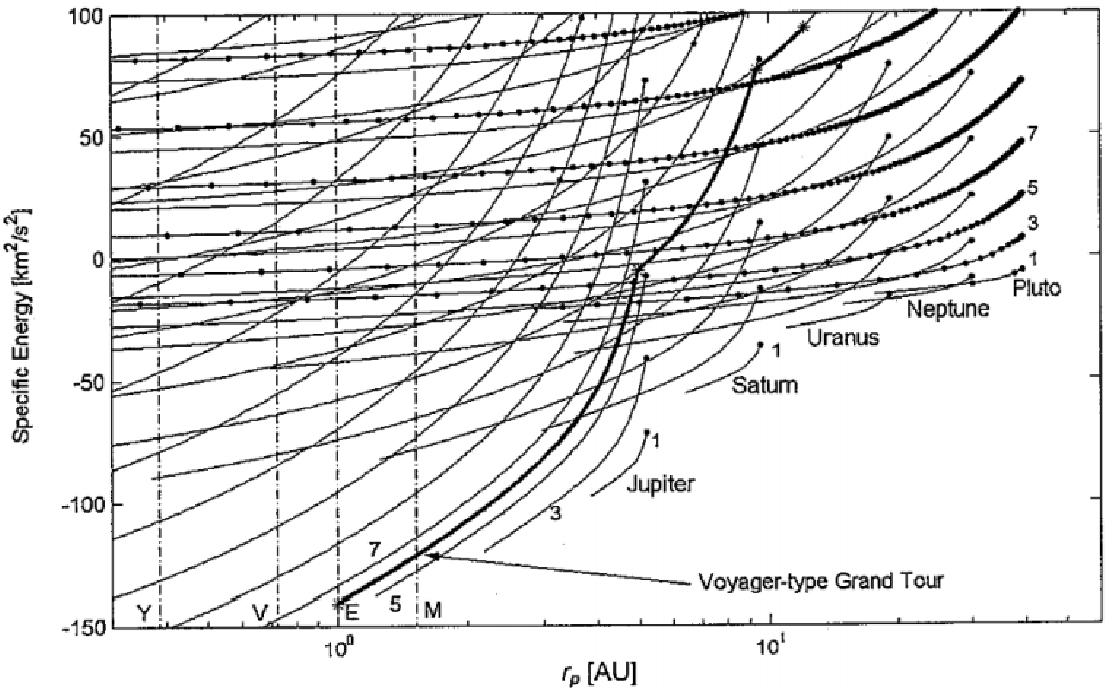

Figure 9.2: Tisserand graph of the outer Solar System from literature. This was included to validate the results of Figure 3.3 by means of comparison.

9.3.3 Penalties

The algorithm explained in Subsection 4.2.1 holds that a penalty is added in some cases to prevent the optimization from approaching non-favorable results. This penalty is in all cases 1000 km/s for the ΔV_{JOI} required to insert the spacecraft in the desired capture orbit. This was chosen after a brief investigation of the convergence behavior with different values for the penalty. When the penalty should be added, the loop over the preset flyby sequence breaks out and the resulting fitness will be the difference in orbital energy plus the penalty.

The purpose of the penalty is to guide the optimization out of non-favorable regions on the Tisserand graph. When plotting the number of times a penalty is granted against the number of generations, one should see a decrease in it. This is exactly what can be seen in Figure 9.4 for the same three seeds as in Figure 9.3. After this, one is confident that the penalty works appropriately.

9.3.4 Validation of ballistic optimization

Validation of the methodologies in Chapter 4 is done by reproducing results from earlier research. In [24] they used interplanetary trajectory constraints and combined that with a high-fidelity, double-aided satellite capture design algorithm. The motion of the spacecraft was numerically integrated by a system of second-order equations of motion. The characteristics of two solutions from [24] are presented in Tables 9.1 and 9.2. These are a Callisto-JOI-Ganymede and Callisto-JOI-Europa capture sequences, respectively. Keep in mind that in the high-fidelity numerical model, they did not assume a coplanar assumption and perfect circular orbits for the Galilean moons. Therefore, the solutions in [24] are expected to differ from the solutions obtained with the methodologies in Chapter 4. However, the differences should be within a reasonable order of magnitude. The solutions presented in Figures 9.5 and 9.6 are created by narrowing down the parameters in the decision vector in the algorithm from Subsection 4.2.1 such that the JOI-perijove (e.g. $r_{p,JOI}$) and flyby altitudes are equal to the value of the high fidelity solution. When doing so, the validity of the

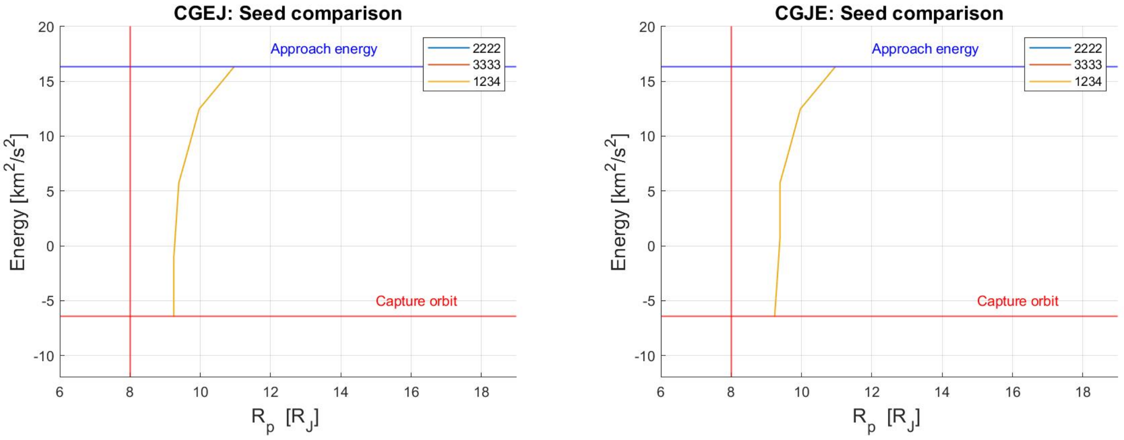

(a) Seed comparison for
Callisto-Ganymede-Europa-JOI capture sequence

(b) Seed comparison for
Callisto-Ganymede-JOI-Europa capture sequence

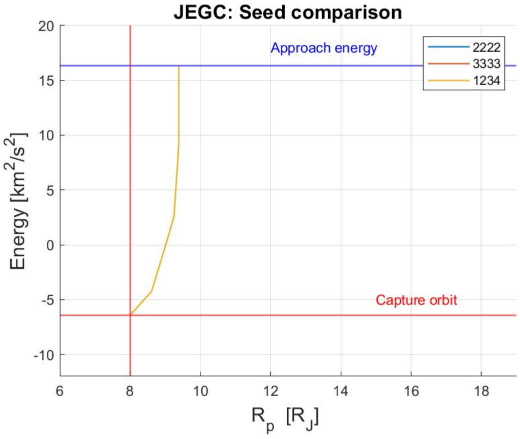

(c) Seed comparison for
JOI-Europa-Ganymede-Callisto capture sequence

Figure 9.3: Comparison of the optima from three different seeds for three different triple-aided capture sequences.

algorithm in Subsection 4.2.1 can be tested. Please note the differences in capture orbits period and second flyby altitude for both cases. For the Callisto-JOI-Europa sequence solution, the radiation belt safety was temporarily not considered but still shown in Figure 9.6.

Parameter	Value	Units
E_0	16.348	km^2/s^2
Flyby moon 1	Callisto	[-]
Flyby altitude 1	500	km
$r_{p,JOI}$	9.2	R_J
JOI	674	m/s
Flyby moon 2	Ganymede	[-]
Flyby altitude	1000	km
Capture period	190	days
Capture orbital energy	-6.665	km^2/s^2

Table 9.1: Characteristics of Callisto-JOI-Ganymede capture solution resulting from a high fidelity satellite-aided capture design in [24].

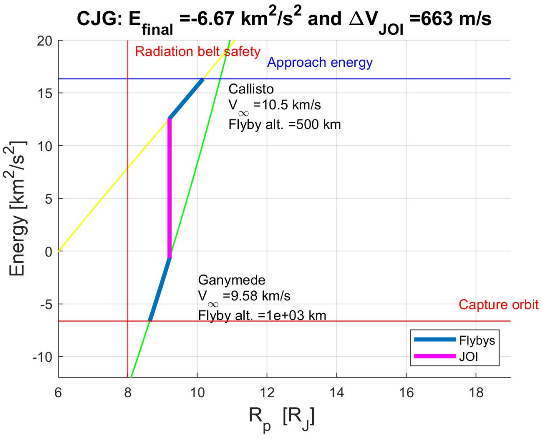

Figure 9.5: Solution of Callisto-JOI-Ganymede capture sequence resulting from methodologies in Chapter 4.

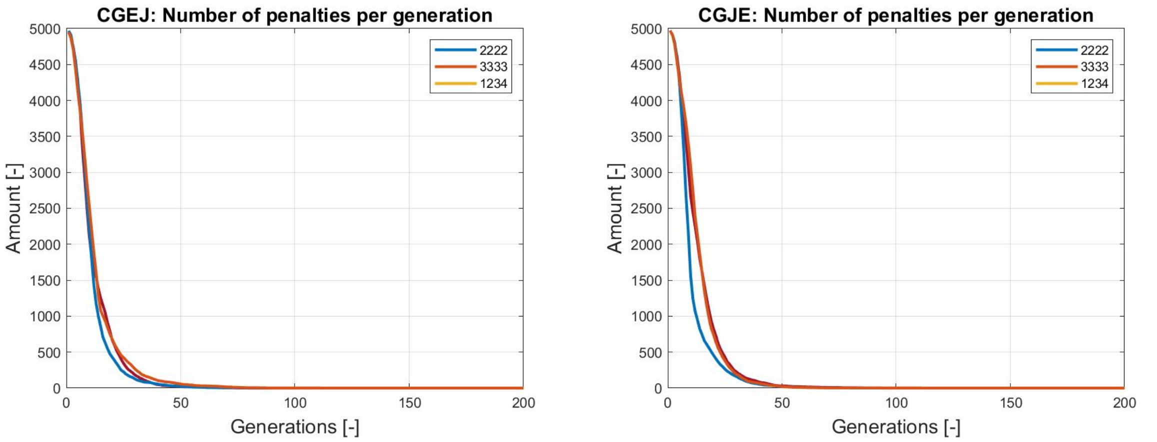

(a) Number of penalties assigned per generation for a Callisto-Ganymede-Europa-JOI sequence optimization.

(b) Number of penalties assigned per generation for a Callisto-Ganymede-JOI-Europa sequence optimization.

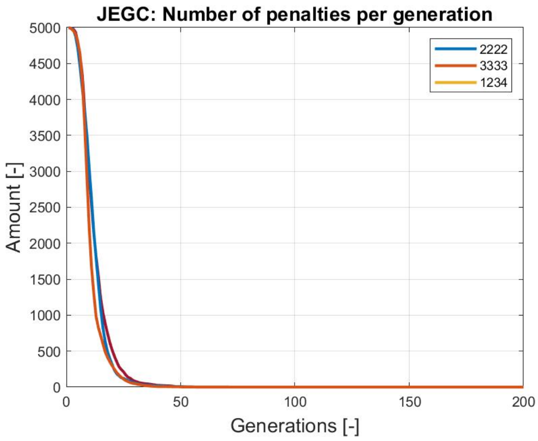

(c) Number of penalties assigned per generation for a JOI-Europa-Ganymede-Callisto sequence optimization.

Figure 9.4: Number of penalties assigned per generation for three different capture sequence optimizations. Results are shown for the same seeds from Figure 9.3.

Parameter	Value	Units
E_0	16.348	km^2/s^2
Flyby moon 1	Callisto	[-]
Flyby altitude 1	500	km
$r_{p,JOI}$	6.5	R_J
JOI	688	m/s
Flyby moon 2	Europa	[-]
Flyby altitude	500	km
Capture period	200	days
Capture orbital energy	-6.425	km^2/s^2

Table 9.2: Characteristics of Callisto-JOI-Europa capture solution resulting from a high fidelity satellite-aided capture design in [24].

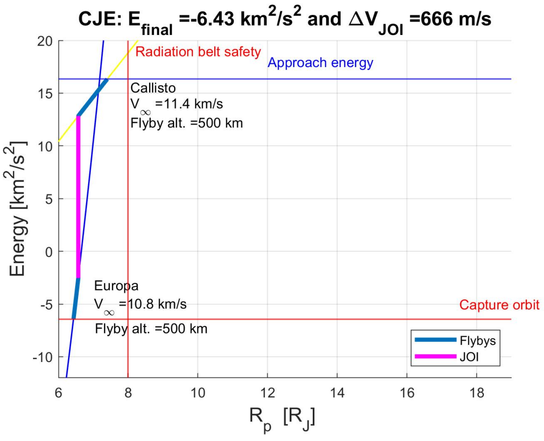

Figure 9.6: Solution of Callisto-JOI-Europa capture sequence resulting from methodologies in Appendix A.

Comparing the high-fidelity solution with the patch conics solution from Chapter 4 one notices some differences (11 m/s for Callisto-JOI-Ganymede and 22 m/s for Callisto-JOI-Europa). The author argues that the results are expected to be less favorable by considering relative inclinations compared to the coplanar case. Furthermore, in [24] they added the note with the results that for the particular launch period they considered, they assumed the worst-case values over the entire launch period. From this one concludes that the results from [24] are a bit over-designed.

The author concludes that considering the assumptions taken for the methodology in Chapter 4, the solutions are comparable with those found in [24]. Differences between the solutions can be explained due to limitations set by the assumptions.

9.4 Low-thrust optimization

This section explains the verification and validation efforts for the optimizations of Chapter 6. This is crucial to gain confidence in the methodologies and justify any evaluations on the results obtained with the methods from Chapter 6.

9.4.1 Verification of low-thrust optimization algorithm

The low-thrust optimization algorithm's verification efforts consist of comparing the optima resulting from different seed numbers and counting the number of penalties for each generation to see if the optimization pushes its solutions away from unfavorable regions.

9.4.2 Different seed number

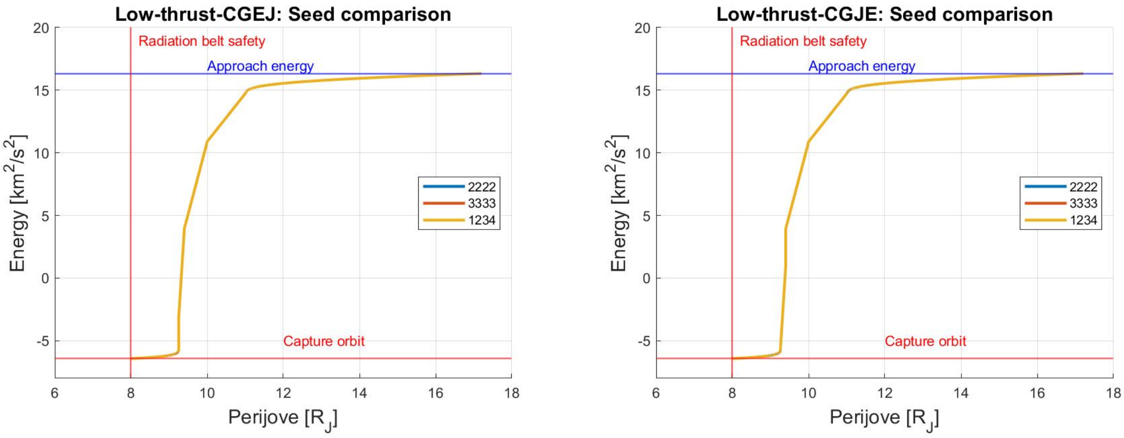

(a) Seed comparison for low-thrust Callisto-Ganymede-Europa-JOI capture sequence

(b) Seed comparison for low-thrust Callisto-Ganymede-JOI-Europa capture sequence

Figure 9.7: Comparison of the optima from three different seeds for two different low-thrust triple-aided capture sequences.

Similar as was done in Subsection 9.3.2, the optimization of low-thrust satellite-aided capture trajectories is repeated for three different seed numbers and three low-thrust triple-aided capture trajectories. The optima are plotted over each other on the Tisserand graph and the result is shown in Figure 9.7.

As can be seen, there are no visual differences between the optima origin from different seed settings. The author is motivated that this overlap gives more confidence in the results from Section 6.3.

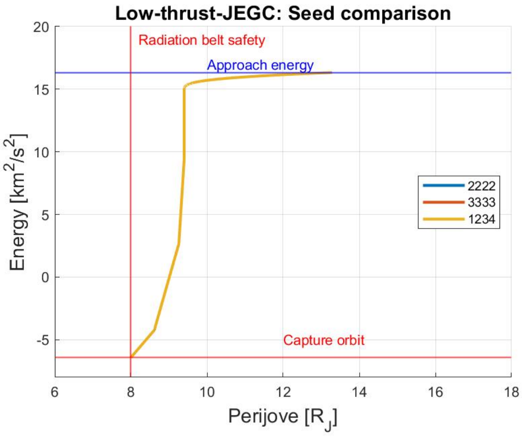

Figure 9.8: Seed comparison for low-thrust JOI-Europa-Ganymede-Callisto capture sequence

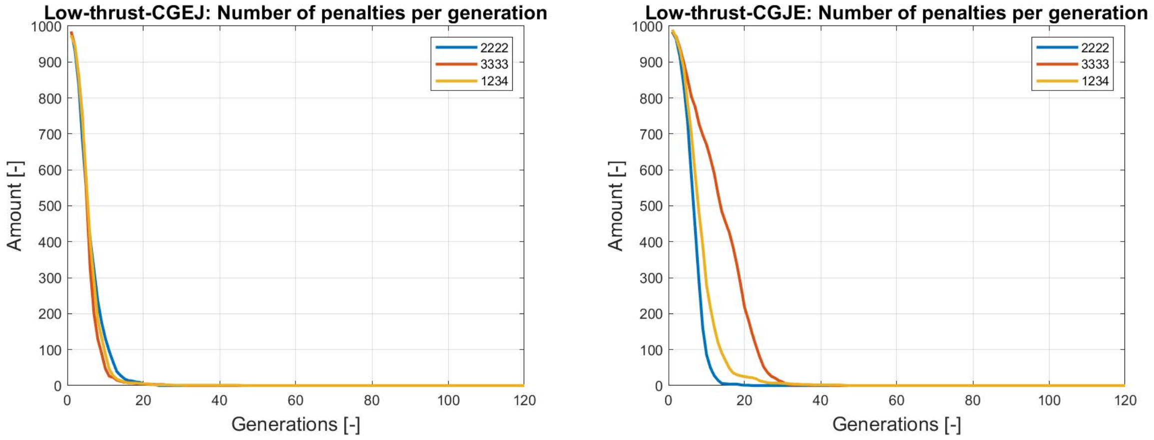

(a) Number of penalties assigned per generation for a low-thrust Callisto-Ganymede-Europa-JOI sequence optimization.

(b) Number of penalties assigned per generation for a low-thrust Callisto-Ganymede-JOI-Europa sequence optimization.

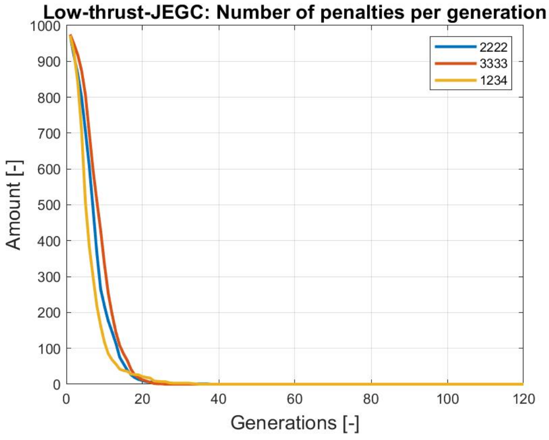

(c) Number of penalties assigned per generation for a low-thrust JOI-Europa-Ganymede-Callisto sequence optimization.

Figure 9.9: Number of penalties assigned per generation for three different low-thrust capture sequence optimizations. Results are shown for the same seeds from Figure 9.7.

9.4.3 Penalty

The allocation of penalties for the low-thrust optimizations is also verified in the same way as in Subsection 9.3.3. The results are shown in Figure 9.4. Figure 9.9 shows a decrease of the number of penalties for each sequence optimization. This indicates that the penalty also works for the low-thrust optimization algorithm.

9.4.4 Constant mass

All low-thrust legs in presented in this report assume a constant mass for the spacecraft. In other words, the mass expelled by the low-thrust propulsion is considered negligible. The mass ratio ($m_{final}/m_{initial}$) of the spacecraft is calculated along a hyperbolic trajectory in the Jovian system to prove that this is a reasonable assumption. This is usually done through the rocket equation (Equation 9.8) and the velocity increment delivered by the low-thrust propulsion ΔV_{LT}. Before doing so, the ΔV_{LT} delivered by the low-thrust propulsion is calculated using Equation 9.5.

$$\Delta V_{LT} = \int_{t_{initial}}^{t_{final}} F_T dt \tag{9.5}$$

This raises problems since time is not used as a running parameter in the second-order Taylor series expansion. Instead, the true longitude is used. Therefore, Equation 9.5 is rewritten into Equation 9.6 to hold the true longitude as running parameter.

$$\Delta V_{LT} = \int_{L_{initial}}^{L_{final}} a_T \left(\frac{\mathrm{d}t}{\mathrm{d}L}\right) \mathrm{d}L \tag{9.6}$$

Since Equation 9.6 has the problem that is cannot be solved analytical, the second-order Taylor expansion for time, developed in Section 7.3 is used here again and by assuming a constant thrust acceleration a_T, it is possible to rewrite Equation 9.6 into Equation 9.7.

$$\Delta V_{LT} = a_T \Delta t \tag{9.7}$$

Now the acceleration, a_T is integrated simultaneously with the other three orbital elements p, f and g. Knowing the velocity increment delivered by the low-thrust propulsion, the relative mass with respect to the spacecraft's initial mass can be calculated by means of the well known *"Tsiolkovsky rocket equation"* (e.g., Equation 9.8). This relative mass is shown for a low-thrust hyperbolic trajectory in Figure 9.10 with respect to both time and true longitude.

$$\Delta V_{LT} = g_0 I_{sp} ln\left(\frac{m_{initial}}{m_{final}}\right) \tag{9.8}$$

The shape of the curves differs from each other because of the propagating over the true longitude. When a spacecraft orbiting Jupiter with an eccentricity other than zero is relatively shorter at its perijove than regions located away from its perijove. In other words, sections of true longitude further away represent longer time steps than a section at the perijove, which means that more mass can be expelled.

From this figure, one learns that after the full range in true longitude is executed, the amount of mass that the spacecraft expelled is around two percent of the spacecraft's total mass. With this in mind, the author expects that constant mass assumption during low-thrust legs is valid.

Note that this says nothing about the mass expelled due to the impulsive JOI maneuver. This was not taken into account in the optimizations and was due to limited time not examined. The effect of this would be a slightly different low-thrust acceleration after the JOI maneuver. The author is aware that this "mistake" is present and leaves this for future recommendations.

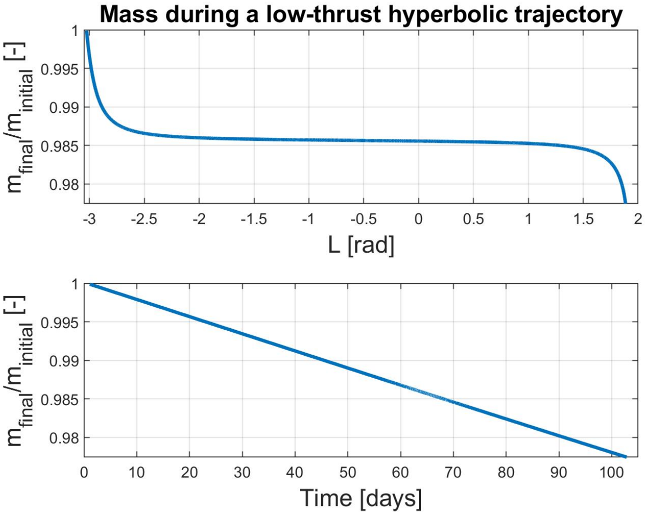

Figure 9.10: relative mass of the spacecraft along a low-thrust hyperbolic trajectory as a function of the true longitude. Initial spacecraft mass was 4000 kg.

9.4.5 Validation of low-thrust optimization

The combination of satellite-aided planetary capture trajectories considering an impulsive JOI at perijove and low-thrust propulsion along its trajectory was not thoroughly investigated before. Solutions from earlier research could not be found. The algorithm in Section 6.1 could therefore not be validated. However, both methods from which the low-thrust satellite-aided capture design consists are separately validated. The verification-validation of low-thrust propulsion was done by means of a reference trajectory in Chapter 5. Differences using the Taylor series expansion were considered to be within a reasonable range. The satellite-aided capture design is validated in the previous section. With These two and the verification efforts in the previous subsection, the author expects that the low-thrust satellite-aided capture design works therefore and adequately justifies any evaluation on the results with respect to the research questions presented in Subsection 2.2.2.

Chapter 10

Conclusions and recommendations

This chapter is the final chapter of this thesis report and gives the conclusions with respect to the research question from Subsection 2.2.2. Recommendations are also mentioned as a propose to improve the research and methodologies.

10.1 Conclusions

This thesis research was centered around low-radiation, low-thrust satellite-aided planetary capture trajectories in the Jovian system. More specifically, the goal was to investigate how the addition of low thrust along a capture trajectory could be beneficial. This was investigated by means of a central research problem that was presented in Subsection 2.2.1. The results followed from comparing the low-thrust performance with both purely impulsive capture and conventional satellite-aided capture. For this, the following research question and sub-questions were created:

> *What are the performance improvements of using low radiation satellite-aided planetary capture trajectories in the Jovian system compared to a purely impulsive capture maneuver and how could these further be improved by incorporating low-thrust electric propulsion?*

This research question was split up into three sub-questions:

- What are the potential propellant mass savings for low-radiation satellite-aided planetary capture trajectories compared to purely impulsive capture trajectories?
- What are the potential propellant mass savings for low-radiation satellite-aided planetary capture trajectories when low-thrust propulsion along the trajectory is added?
- Which of the promising trajectories could be considered most useful with respect to mission panning?

The thesis work started with a study on the Tisserand parameter and the Tisserand graph. Using the Tisserand graph for the Jovian system, a fitness function was created to identify potential optimal satellite-aided capture sequences in terms of ΔV_{JOI} and propellant mass for all possible combinations of the three moons Europa, Ganymede and Callisto. One of the objectives of this thesis research was to aim for low-radiation capture. Consequently, Io was excluded as a possible flyby moon. These first optimizations did not yet incorporate low-thrust propulsion; only a JOI in combination with one, two or three flybys with the Galilean moons was considered. Moreover, the positions of the moons with respect to Jupiter were also not considered. This first study aims to investigate the capabilities of satellite-aided planetary capture on an energy base solely.

Table 4.3 summarizes the results of this first study. As a reference, the not-aided (purely impulsive) capture is also included in the table. The ΔV_{JOI} executed at the border of the radiation safety belt ($8R_J$) is equal to 1069 m/s and in terms of propellant mass, that corresponds to 1218 kg.

The single-aided results showed that it is not possible to capture the spacecraft into a closed orbit around Jupiter and thus also not into the desired 200-day period orbit. However, single-aided capture trajectories do lower the required propellant mass for the JOI with 11 to 35% of the propellant mass needed for direct capture.
Double-aided capture sequences would also require a JOI for properly capturing the spacecraft around Jupiter. Although they lower the propellant mass for the JOI. Best mass savings appear for the JOI-Ganymede-Callisto scenario (62%) and worst for the Callisto-Europa-JOI scenario (36%). The double-aided results also showed the effects of placing the JOI at the beginning of the sequence. When doing so, the JOI already lowered the relative velocity of the spacecraft with respect to the flyby moon what made the flyby more effective.

The location of the JOI had a different effect on the optima for the triple-aided sequences. Both the Europa-JOI-Ganymede-Callisto- and JOI-Europa-Ganymede-Callisto sequences had the problem that they ended up below the radiation safety belt when flown at a minimum allowable flyby altitude for the Callisto flyby (500 km). An increase of the Callisto flyby altitude solved this. However, this translated into a more significant JOI maneuver and thus more propellant mass. Therefore contrary to the double-aided case, the best triple-aided sequence was not the one with the JOI placed in the beginning. The best option for conventional satellite-aided planetary capture is a Ganymede-JOI-Europa-Callisto sequence with a JOI of only 255 m/s which requires only 27% of the propellant mass for direct capture. This first study on (conventional) satellite aided planetary capture answered the first research sub-question. However, the results also serve as a second reference for the low-thrust satellite-aided planetary capture trajectories.

The second study of this thesis research was to expand the foregoing towards low-thrust satellite-aided planetary capture trajectories. A fast (second-order Taylor-series expansion) method could represent low-thrust legs in the Tisserand graph. The method needed to be fast because it was combined with the (conventional) ballistic satellite-aided capture optimizations. When doing so, it created a new fitness function for the low-thrust satellite-aided planetary capture optimizations. Results of these are summarized in Table 6.3. One of the objectives of the second research sub-question objectives was to compare low-thrust capabilities with both the direct capture and aided capture.
Low-thrust single-aided capture trajectories all require a JOI to close the orbit around Jupiter and moreover, to capture it in the desired long-periodic orbit. The presence of low-thrust propulsion along the trajectory further lowers the total propellant mass. The best low-thrust single-aided trajectory is the JOI-Ganymede scenario with 749 kg of propellant mass, that is a decrease of 39% of the propellant mass for direct capture. Which means saving an extra 3% due to the presence of low-thrust. The worst low-thrust single-aided capture sequence is the JOI-Callisto scenario. With a propellant mass of 950 kg, it saves 22 % of the propellant mass for direct transfer which is an extra 11% due to low-thrust.
Low-thrust double-aided planetary capture trajectories could potentially close the orbit around Jupiter and thus capture the spacecraft. However, to reach the desired 200-day periodic orbit, the impulsive JOI is still required. The presence of low-thrust propulsion reduces this JOI. This reduction in JOI does not always translate itself into a decrease of propellant mass when compared to conventional satellite-aided capture. Those sequences should best be flown without low-thrust propulsion. The best low-thrust double-aided sequence is the JOI-Ganymede-Callisto scenario. With a total propellant mass of 450 kg it saves up to 63% of the propellant mass for direct capture which is generally an additional 1% due to low-thrust propulsion. The worst low-thrust double aided is the Europa-JOI-Callisto scenario. With 676 kg of total propellant mass it saves up to 44% which is an extra 6% due to low-thrust propulsion.
Low-thrust triple-aided planetary capture trajectories, could close the orbit around Jupiter without a JOI. However, for the 200-day periodic orbit, a JOI is still inevitable but reduced due to the presence of low-thrust. The best scenario for low-thrust triple-aided capture is Callisto-Ganymede-JOI-Europa with a total propellant mass of only 17% of that for direct capture.

This is an extra saving of 11% due to low-thrust propulsion. The worst low-thrust triple-aided capture sequence is Europa-JOI-Ganymede-Callisto. Requiring 33% of the propellant mass for direct capture which is an extra reduction of 6% due to low-thrust.

Both optimization results (ballistic and low-thrust) concluded the first two research sub-question. The third research sub-question focuses on the phasing of the moons and more specifically, on mission planning. A particular sequence can look promising in terms of propellant mass. Flying the sequence would demand that the moons are aligned properly. This is where the phasing problem comes in line. This was solved for both the ballistic (analytical) and the low-thrust (numerical) satellite-aided capture sequences. From the phasing problem followed the relative and absolute locations of the moons to fly a certain sequence. These were fed to an ephemerides search to find proper epochs (e.g., dates) between 2025 and 2065. Then one could evaluate when and how often particular sequences could be flown. The phasing problem was fed a range of initial perijoves, and therefore one could also evaluate how strict the initial perijove requirements were. Both of these criteria were given a grade from one to five. These are added up with each other to a total phasing grade that reflects upon mission planning.

Both the ballistic and low-thrust satellite-aided capture sequences are summarized in Table 8.1 and Table 8.2 respectively. Comparing both results concludes that there was no significant difference in the date distribution between ballistic and low-thrust satellite-aided capture. Although some arrangements of flyby windows were shifted to later dates.

Single-aided (with or without low-thrust) were granted a very high phasing score. The phasing of these trajectories is only dependent on the period of the moon under consideration. Therefore there are no real restrictions for them. However, Europa's orbital radius lies relatively close to the radiation safety belt. This limits the range in initial perijove at which Europa-aided trajectories could be flown. Therefore, the total phasing score for the single-aided trajectories was solely influenced by the moon's orbital radius. All single-aided (ballistic and low-thrust) trajectories are considered useful for mission planning. Although they provide limited propellant mass savings.

The date distribution of double-aided sequences was highly dependent on the dynamics of the two moons under consideration. Europa and Ganymede are in orbital resonance; moreover, Ganymede and Callisto are in near-orbital resonance. Due to this, the date distribution appeared into flyby windows. Flyby windows are generally good for perijove distribution since a wide range of initial perijove could be flown when arriving at the Jovian system. Although depending on the kind of orbital resonance, these flyby windows could occur often or less. The dynamics of Europa-Ganymede translated itself in flyby windows that occur every 1.22 years. Because of Europa's orbital radius, the range in initial perijove is rather strict but not too strict. Therefore all Ganymede-Europa sequences (with or without low thrust) are beneficial for mission planning. Considering the extra mass savings that low thrust could deliver, one should certainly consider using low-thrust propulsion for all Ganymede-Europa-aided capture sequences. The most promising is the low-thrust Ganymede-JOI-Europa scenario. The near-orbital resonance of Ganymede-Callisto showed that every 3.4 years a flyby window opens. Therefore the date distribution is less beneficial than Ganymede-Europa sequences. The perijove distribution of Callisto-Ganymede was slightly better than Ganymede-Europa. The overall phasing score of Callisto-Ganymede ended up to to be slightly less than Ganymede-Europa. When a Callisto-Ganymede sequence is demanded it is better not to consider low-thrust propulsion due to the limiting mass savings or even negative mass savings. For Callisto and Europa, the date and perijove distribution strongly differ between all four sequences. For mission planning, the JOI-Europa-Callisto and Europa-JOI-Callisto should be preferred, with the absolute preference of JOI-Europa-Callisto. Then considering the extra mass saving that low-thrust propulsion can deliver, it should also be considered. Between all (low-thrust) double-aided sequences, the author's most favorite goes to a low-thrust Ganymede-JOI-Europa capture sequence.

Ephemerides results for triple-aided capture sequences show little or sometimes even no results. Therefore they are all given a very low phasing score. The author argues that despite

their potential propellant mass savings, they should not be considered or preferred.
To summarise, a satellite-aided planetary capture trajectory could result in great mass savings for the spacecraft. However, these mass savings could differ significantly between the moons under consideration. The addition of low-thrust has proven to be beneficial for most sequences. Although, if the orbital radius of the flyby moon(s) is large, the mass saving could diminish due to the propellant mass of the low-thrust propulsion itself. From all results and the discussion above, the author argues that a low-thrust Ganymede-JOI-Europa sequence should be preferred.

10.2 Future work and recommendations

This thesis research represents an analysis of the capabilities (low-thrust) satellite-aided planetary capture trajectories. However, some elements and methodologies could have been done different and improved this thesis research. These are briefly described here.

- **Inclination:** The techniques used in the optimizations and moreover the Tisserand graphs itself considered the coplanar case. It is, however, possible to include the inclination in the Tisserand graph. This would make the V_∞ lines in the Tisserand graph appear as contours. Reading and understanding these Tisserand graphs would be challenging. However it might be possible to include the inclination in the optimizations.
- **Thrust vector:** The thrust acceleration in the optimizations always acts along the velocity vector of the spacecraft. By considering the three-dimensional case that takes into account the inclination the thrust could also act in arbitrary direction. This would however significantly complicate the problem.
- **Thrust acceleration:** The low-thrust satellite-aided planetary capture optimizations assumed a constant mass for the spacecraft. This is a reasonable assumption for the low-thrust propulsion as was shown in Chapter 9. An impulsive JOI would expel a fair amount of propellant mass and change the low-thrust acceleration when constant thrust (force) is assumed. Due to a limited time at the closure of this thesis research, this was not anymore taken into account.
- **Time frame:** Finding periodicity in the ephemerides results of triple-aided capture sequences was not successful. The author argues that investigating a wider time frame would maybe better visualize any patterns.
- **Thrust on/off:** The optimizations considered that the low-thrust propulsion was always be turned on. If this would not be the case, a spacecraft could avoid thrusting close to apojove. This could limit the decrease in perijove and thus better avoiding the radiation safety belt.
- **Future missions:** By investigating how future missions will arrive at the Jovian system (for example, JUICE), the theory could be practical more practical.
- **Launch date:** Linking In this report one assumed that the spacecraft arrived from a foregoing Hohmann transfer. However, other trajectories could also arrive at the Jovian system. It might be worth it to make an effort when these (Hohmann) trajectories should be flown.

Appendix A

Ballistic phasing results

A.1 Double-aided

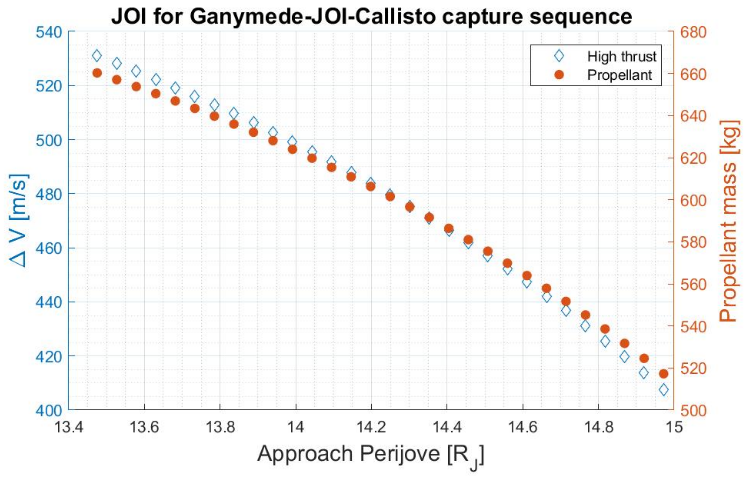

Figure A.1: Required JOI maneuver in terms of ΔV and propellant mass considering a Ganymede-JOI-Callisto capture sequence for varying initial perijove.

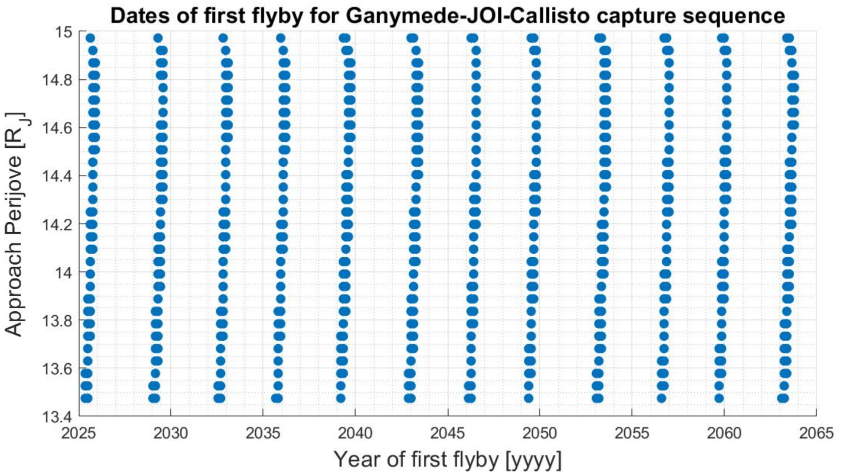

Figure A.2: Ephemerides results within the 2025-2065 time interval for varying perijove considering a Ganymede-JOI-Callisto capture sequence. The vertical patterns represent four flyby windows that repeat every 13.523 years.

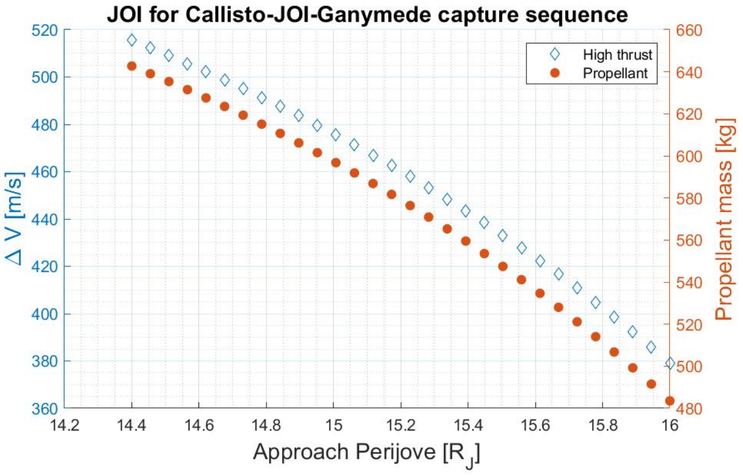

Figure A.3: Required JOI maneuver in terms of ΔV and propellant mass considering a Callisto-JOI-Ganymede capture sequence for varying initial perijove.

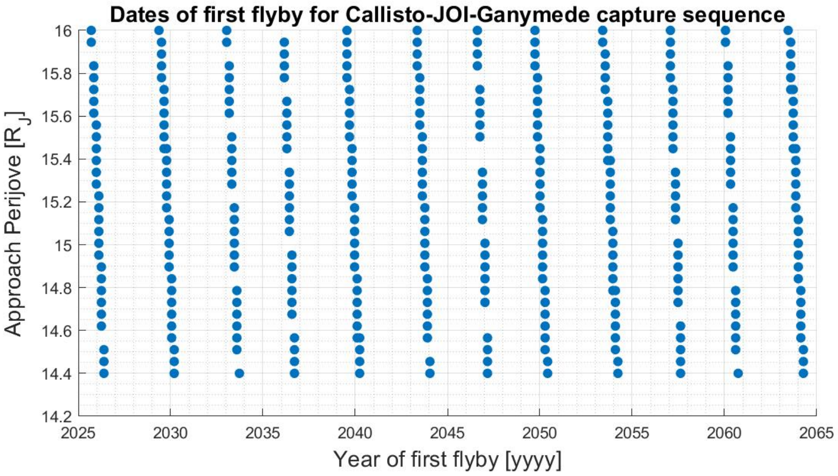

Figure A.4: Ephemerides results within the 2025 2045 time interval for varying perijove considering a Callisto-JOI-Ganymede capture sequence. The vertical patterns represent four flyby windows that repeat every 13.523 years.

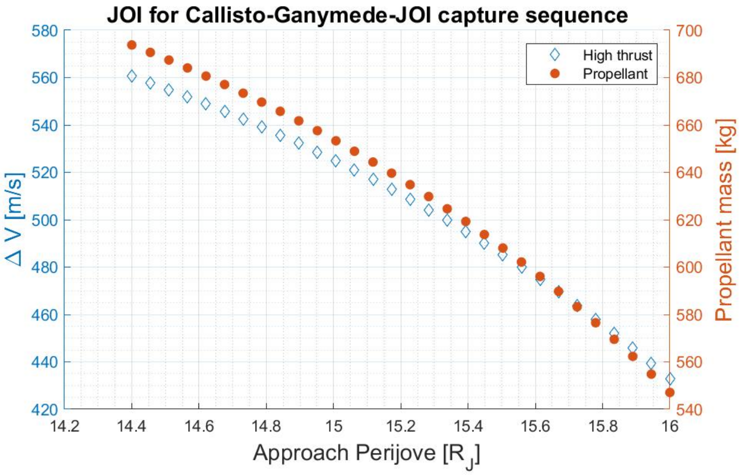

Figure A.5: Required JOI maneuver in terms of ΔV and propellant mass considering a Callisto-Ganymede-JOI capture sequence for varying initial perijove.

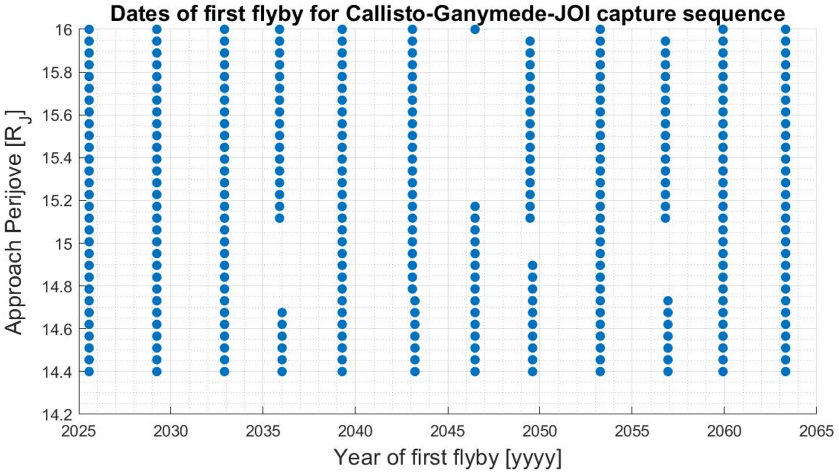

Figure A.6: Ephemerides results within the 2025 2045 time interval for varying perijove considering a Callisto-Ganymede-JOI capture sequence. The vertical patterns represent four flyby windows that repeat every 13.523 years.

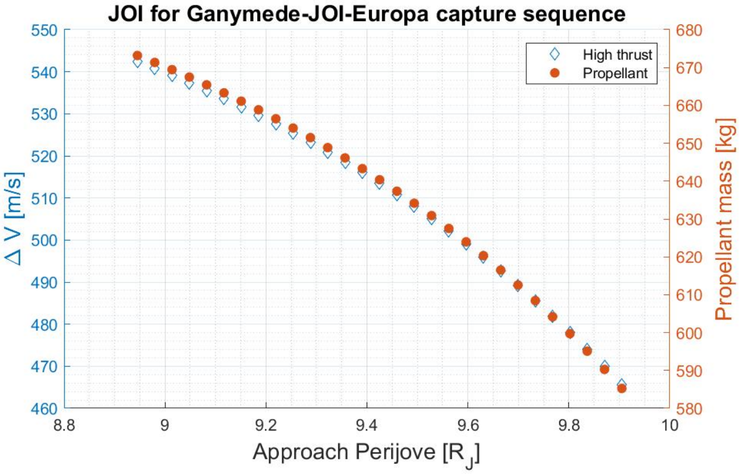

Figure A.7: Required JOI maneuver in terms of ΔV and propellant mass considering a Ganymede-JOI-Europa capture sequence for varying initial perijove.

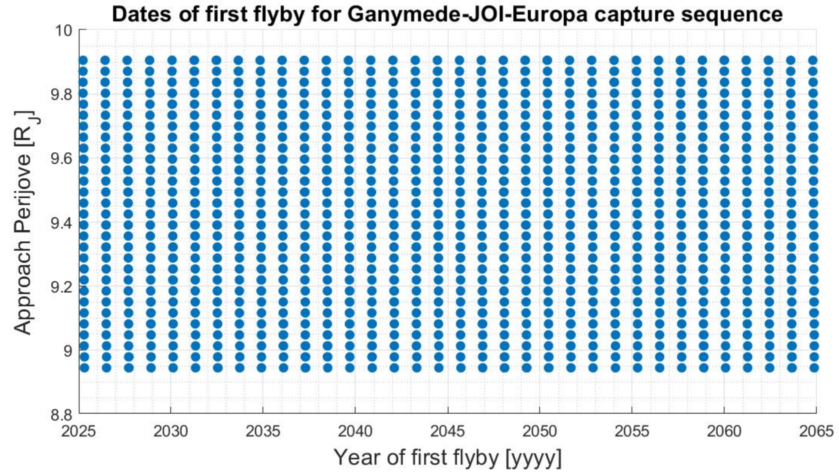

Figure A.8: Ephemerides results within the 2025-2065 time interval for varying perijove considering a Ganymede-JOI-Europa capture sequence. The vertical patterns represent one flyby window that repeats every 1.22 year.

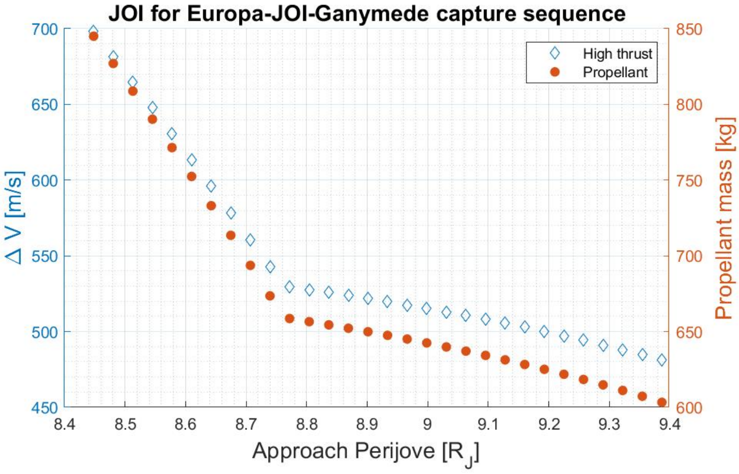

Figure A.9: Required JOI maneuver in terms of ΔV and propellant mass considering a Europa-JOI-Ganymede capture sequence for varying initial perijove.

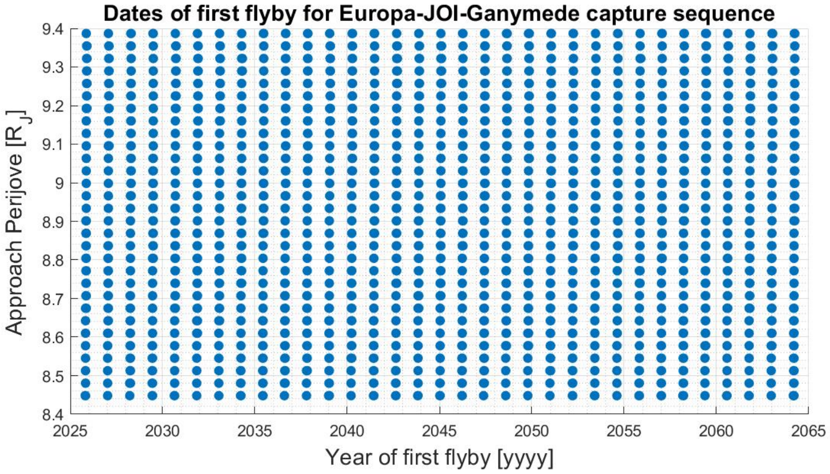

Figure A.10: Ephemerides results within the 2025-2065 time interval for varying perijove considering a Europa-JOI-Ganymede capture sequence. The vertical patterns represent one flyby window that repeats every 1.22 year.

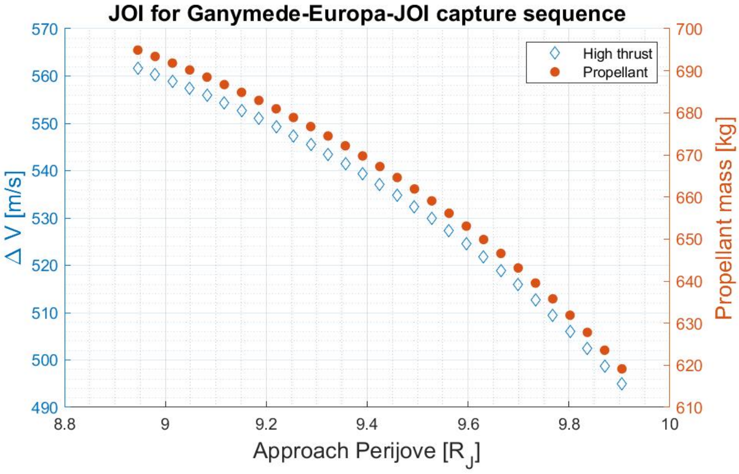

Figure A.11: Required JOI maneuver in terms of ΔV and propellant mass considering a Ganymede-Europa-JOI capture sequence for varying initial perijove.

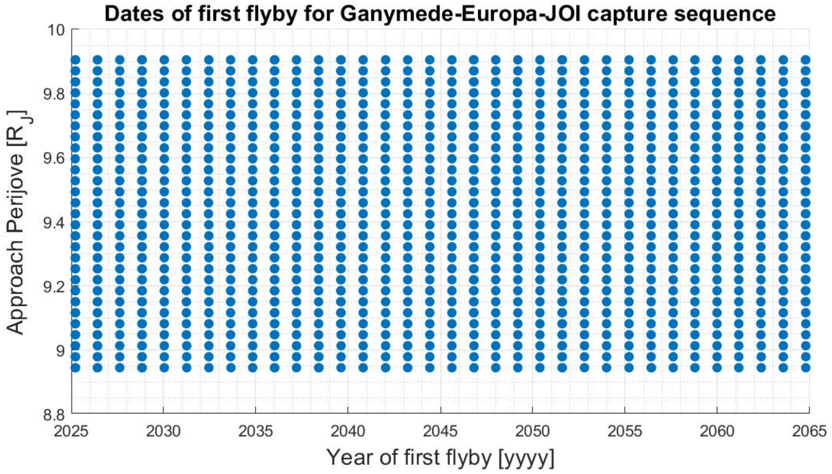

Figure A.12: Ephemerides results within the 2025-2065 time interval for varying perijove considering a Ganymede-Europa-JOI capture sequence. The vertical patterns represent one flyby window that repeats every 1.22 year.

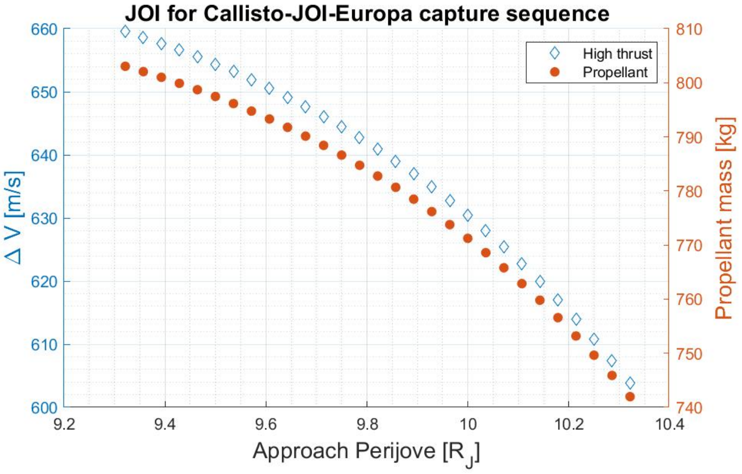

Figure A.13: Required JOI maneuver in terms of ΔV and propellant mass considering a Callisto-JOI-Europa capture sequence for varying initial perijove.

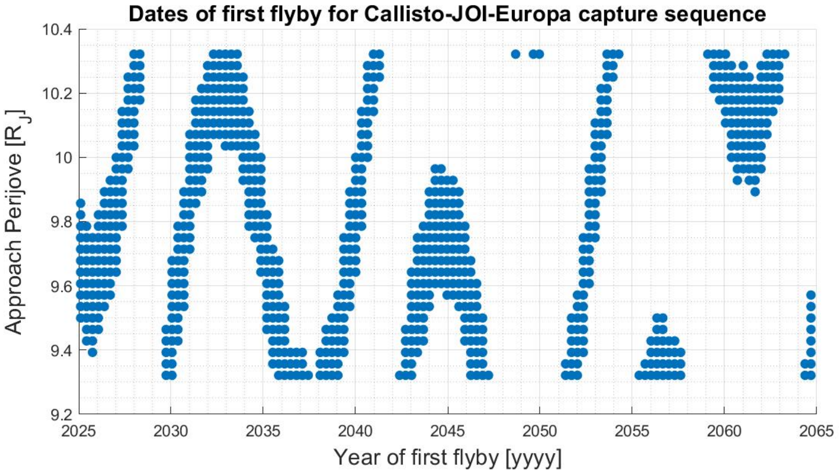

Figure A.14: Ephemerides results within the 2025-2065 time interval for varying perijove considering a Callisto-JOI-Europa capture sequence. Short periodic pattern repeats every 12.20 years.

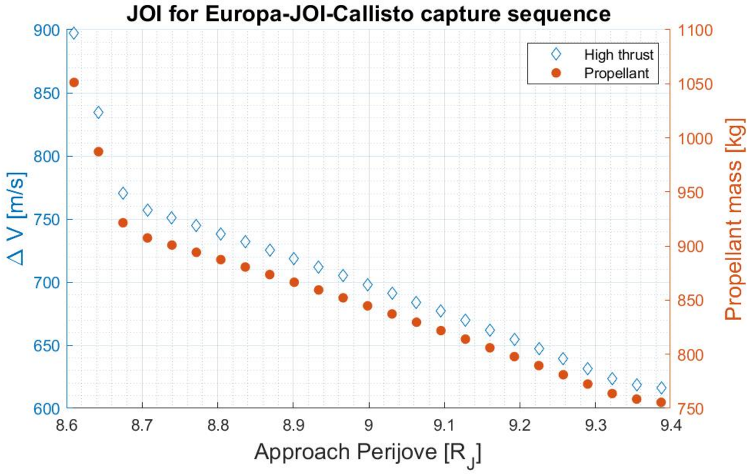

Figure A.15: Required JOI maneuver in terms of ΔV and propellant mass considering a Europa-JOI-Callisto capture sequence.

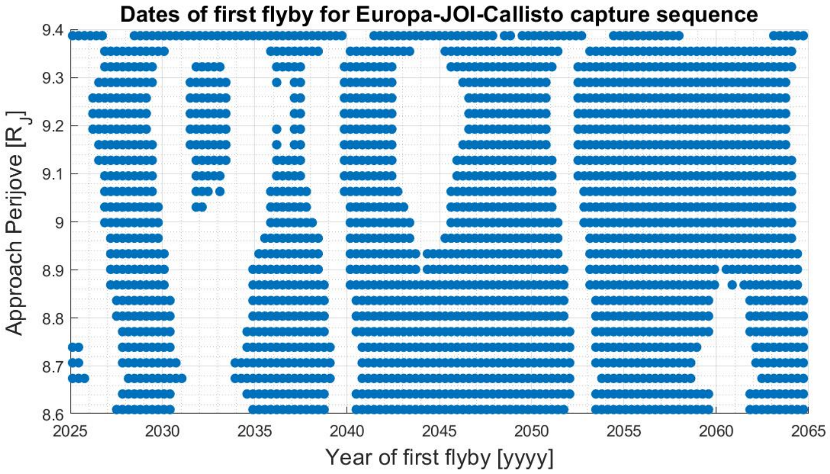

Figure A.16: Ephemerides results within the 2025-2065 time interval for varying perijove considering a Europa-JOI-Callisto capture sequence. Short periodic pattern repeats every 12.20 years.

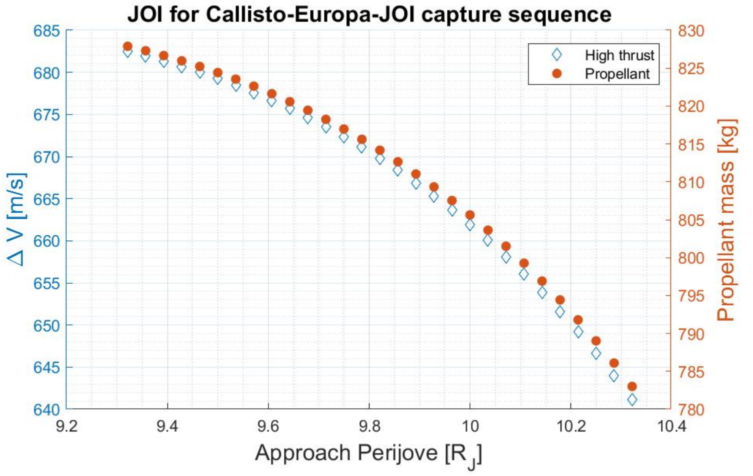

Figure A.17: Required JOI maneuver in terms of ΔV and propellant mass considering a Callisto-Europa-JOI capture sequence.

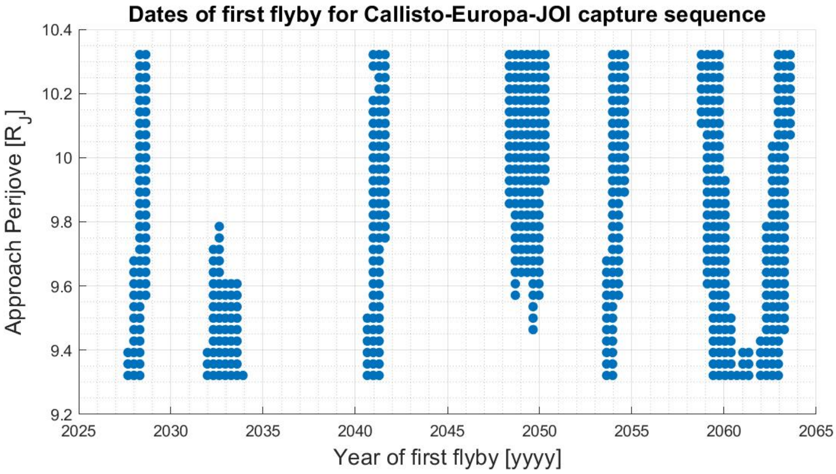

Figure A.18: Ephemerides results within the 2025-2065 time interval for varying perijove considering a Callisto-Europa-JOI capture sequence. Short periodic pattern repeats every 12.20 year.

A.2 Triple-aided

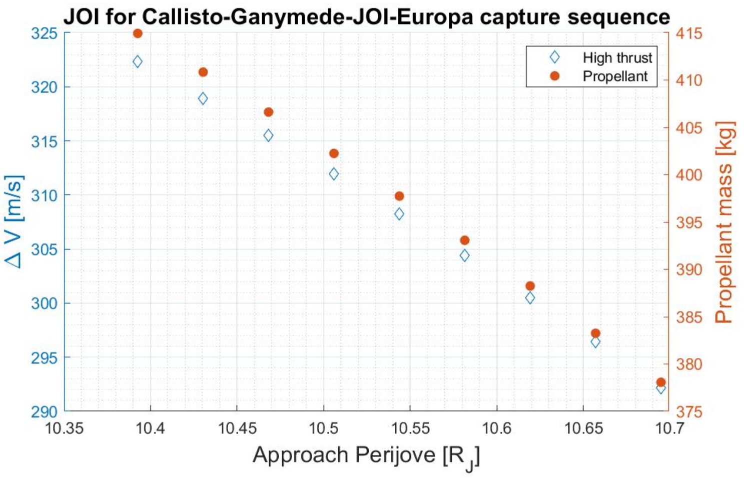

Figure A.19: Required JOI maneuver in terms of ΔV and propellant mass considering a Callisto-Europa-JOI-Ganymede capture sequence.

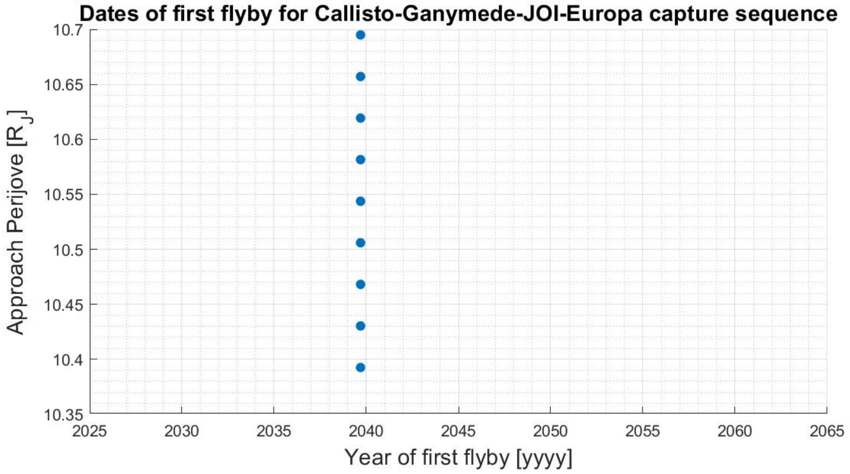

Figure A.20: Ephemerides results within the 2025-2065 time interval for varying perijove considering a Callisto-Europa-JOI-Ganymede capture sequence.

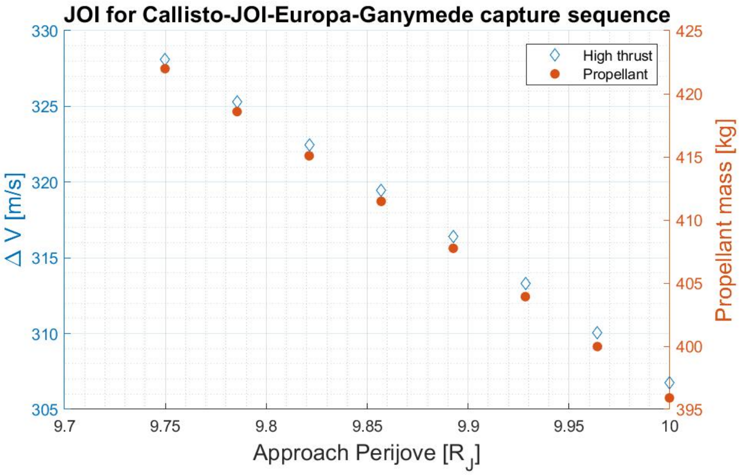

Figure A.21: Required JOI maneuver in terms of ΔV and propellant mass considering a Callisto-JOI-Europa-Ganymede capture sequence.

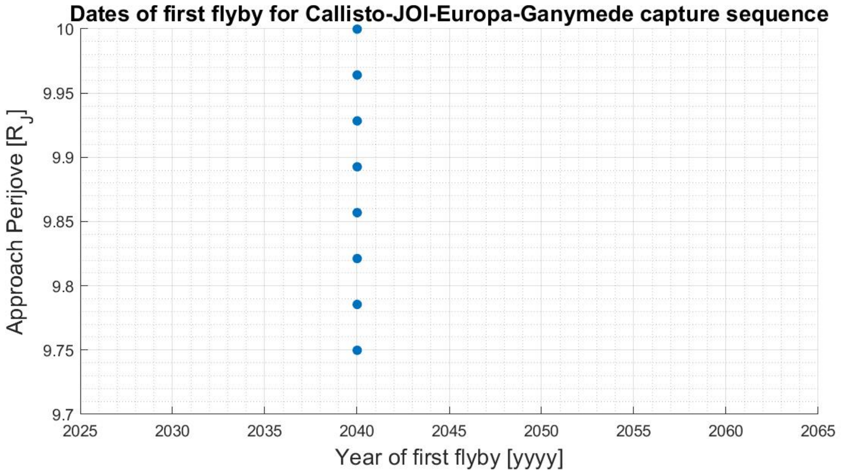

Figure A.22: Ephemerides results within the 2025-2065 time interval for varying perijove considering a Callisto-JOI-Europa-Ganymede capture sequence.

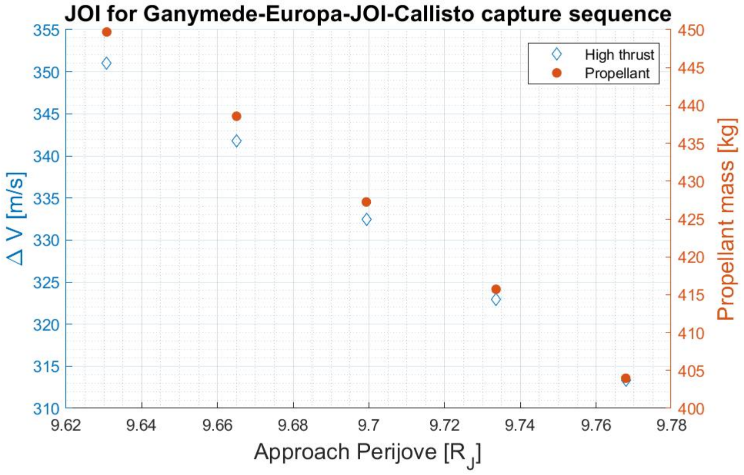

Figure A.23: Required JOI maneuver in terms of ΔV and propellant mass considering a Ganymede-Europa-JOI-Callisto capture sequence.

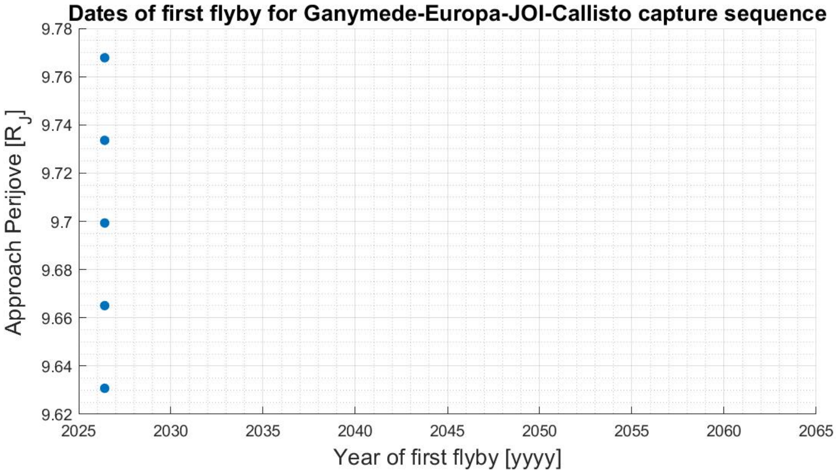

Figure A.24: Ephemerides results within the 2025-2065 time interval for varying perijove considering a Ganymede-Europa-JOI-Callisto capture trajectory.

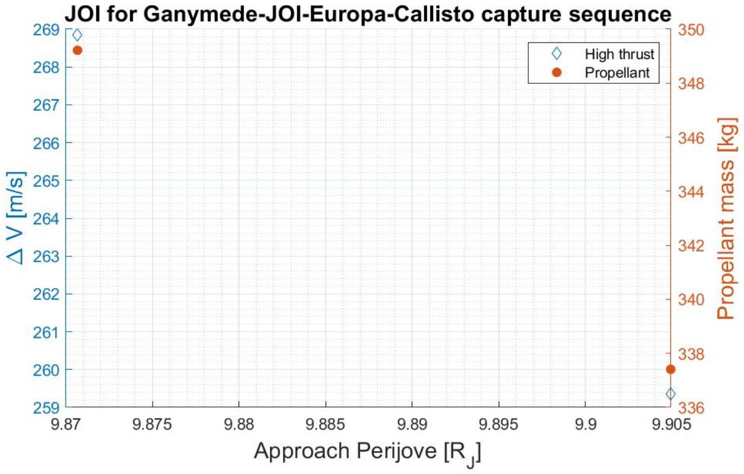

Figure A.25: Required JOI maneuver in terms of ΔV and propellant mass considering a Ganymede-JOI-Europa-Callisto capture sequence.

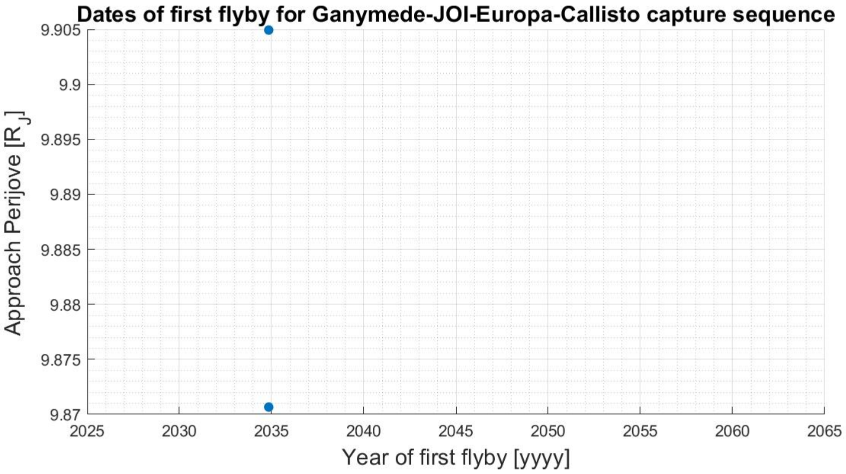

Figure A.26: Ephemerides results within the 2025-2065 time interval for varying perijove considering a Ganymede-JOI-Europa-Callisto capture trajectory.

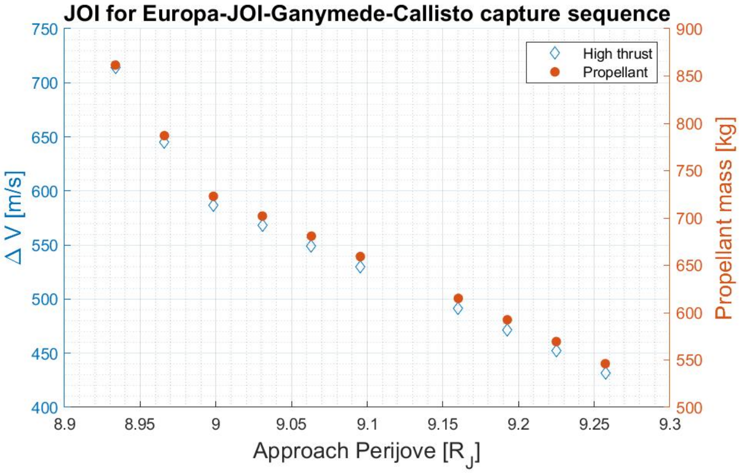

Figure A.27: Required JOI maneuver in terms of ΔV and propellant mass considering a Europa-JOI-Ganymede-Callisto capture sequence.

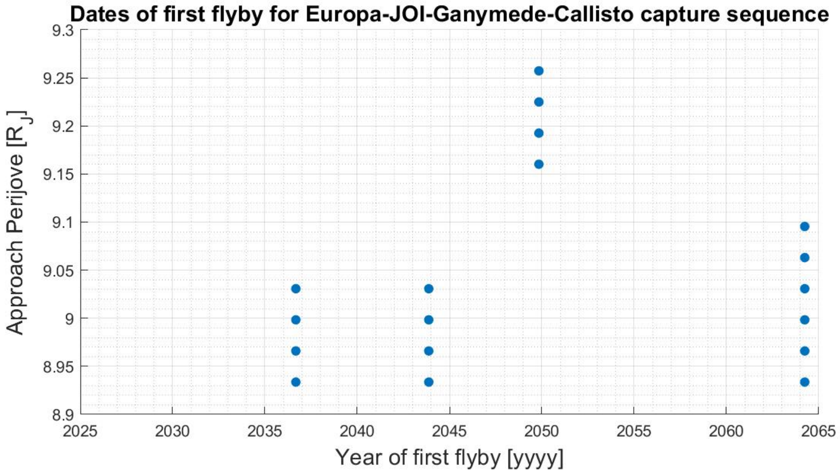

Figure A.28: Ephemerides results within the 2025-2065 time interval for varying perijove considering a Europa-JOI-Ganymede-Callisto capture trajectory.

Appendix B

Low-thrust phasing results

B.1 Low-thrust double-aided

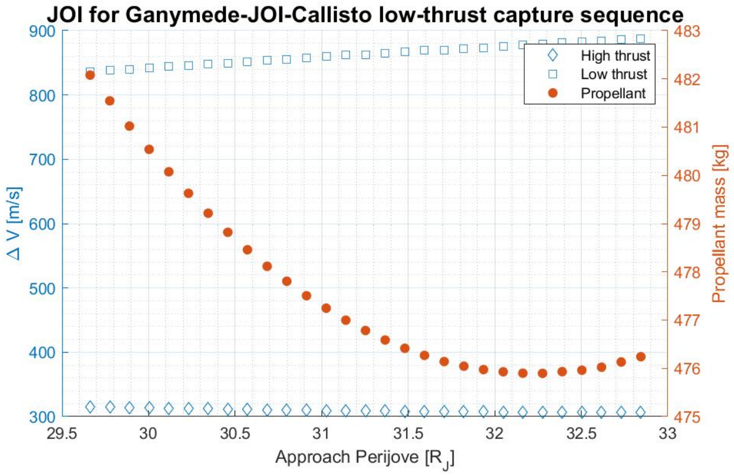

Figure B.1: Required JOI maneuver in terms of ΔV and propellant mass considering a Ganymede-JOI-Callisto low-thrust capture sequence for varying initial perijove.

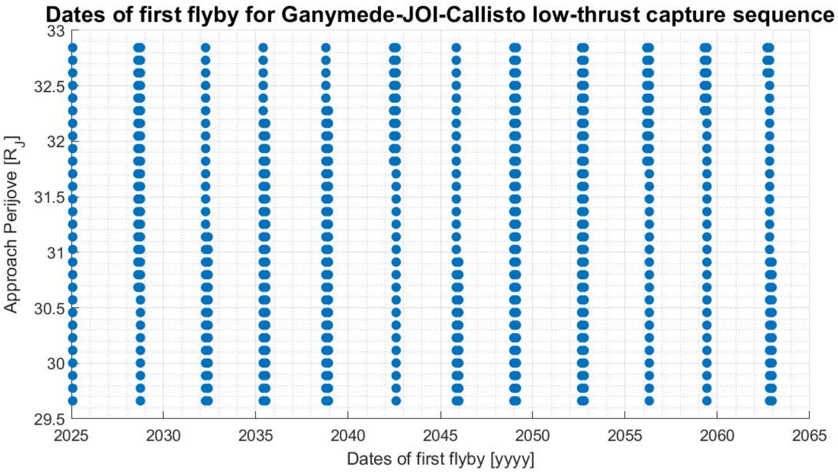

Figure B.2: Ephemerides results within the 2025-2065 time interval for varying perijove considering a Ganymede-JOI-Callisto low-thrust capture sequence. The vertical patterns represent four flyby windows that repeat every 13.523 years.

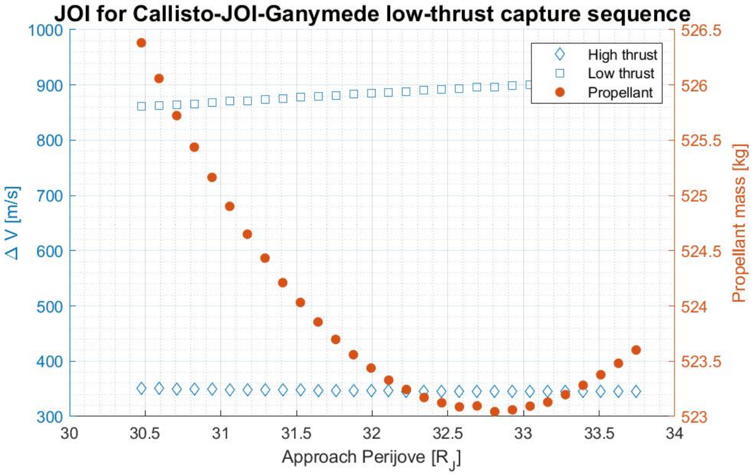

Figure B.3: Required JOI maneuver in terms of ΔV and propellant mass considering a Callisto-JOI-Ganymede low-thrust capture sequence for varying initial perijove.

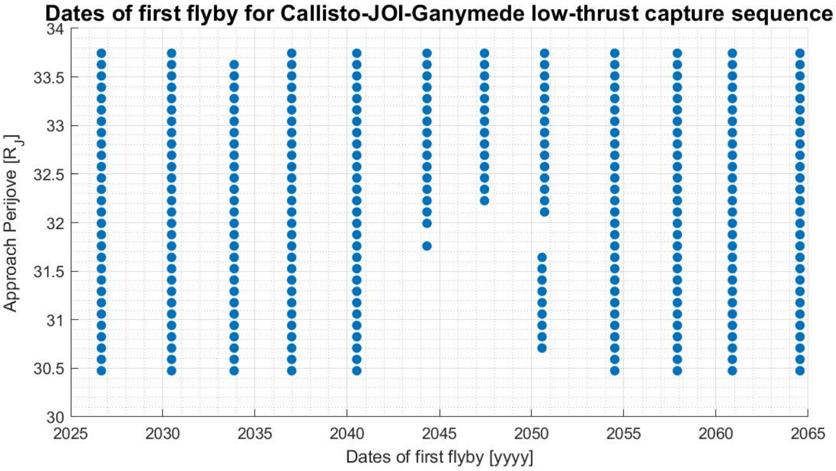

Figure B.4: Ephemerides results within the 2025 2045 time interval for varying perijove considering a Callisto-JOI-Ganymede low-thrust capture sequence. The vertical patterns represent four flyby windows that repeat every 13.523 years.

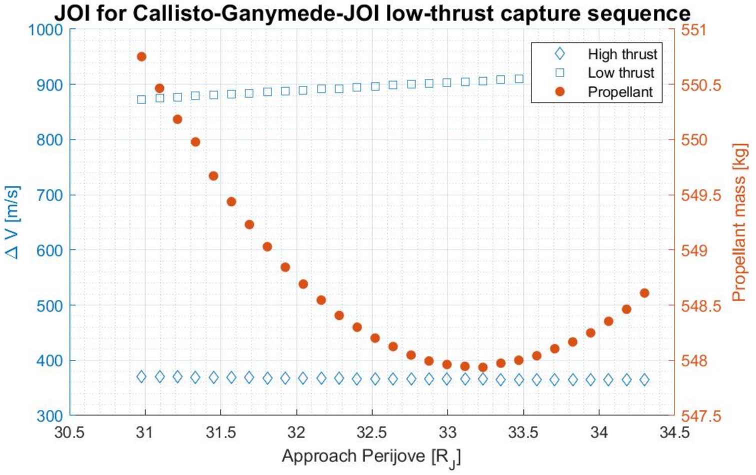

Figure B.5: Required JOI maneuver in terms of ΔV and propellant mass considering a Callisto-Ganymede-JOI low-thrust capture sequence for varying initial perijove.

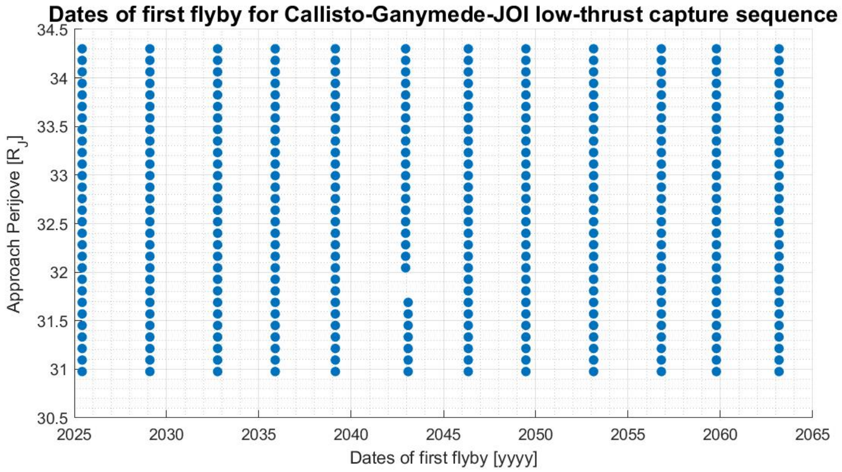

Figure B.6: Ephemerides results within the 2025 2045 time interval for varying perijove considering a Callisto-Ganymede-JOI low-thrust capture sequence. The vertical patterns represent four flyby windows that repeat every 13.523 years.

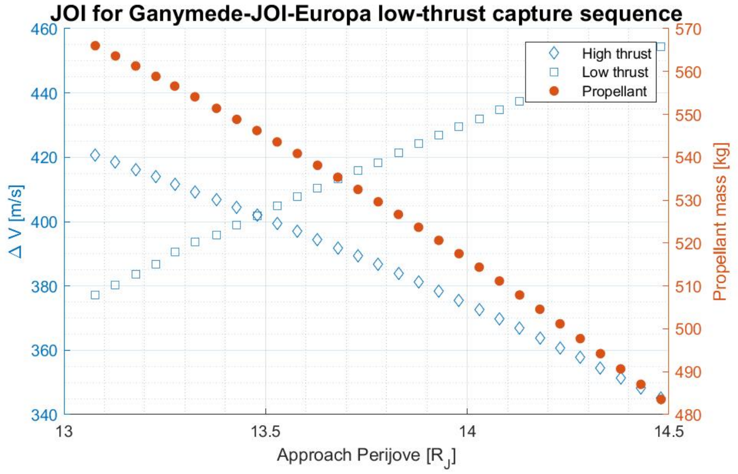

Figure B.7: Required JOI maneuver in terms of ΔV and propellant mass considering a Ganymede-JOI-Europa low-thrust capture sequence for varying initial perijove.

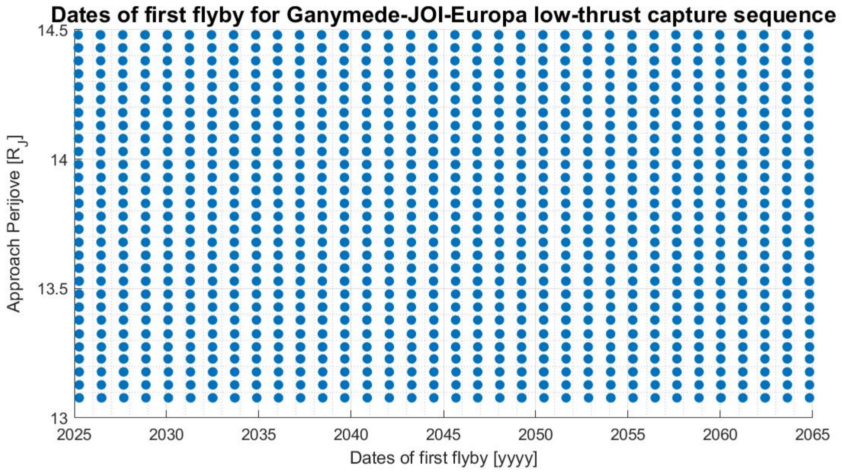

Figure B.8: Ephemerides results within the 2025-2065 time interval for varying perijove considering a Ganymede-JOI-Europa low-thrust capture sequence. The vertical patterns represent one flyby window that repeats every 1.22 year.

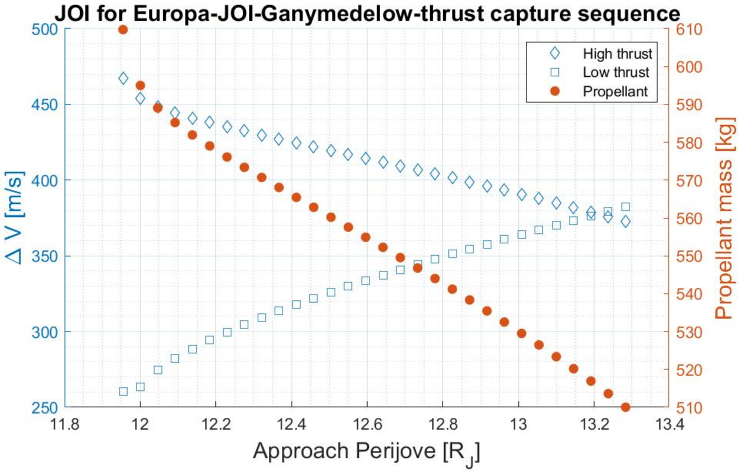

Figure B.9: Required JOI maneuver in terms of ΔV and propellant mass considering a Europa-JOI-Ganymede low-thrust capture sequence for varying initial perijove.

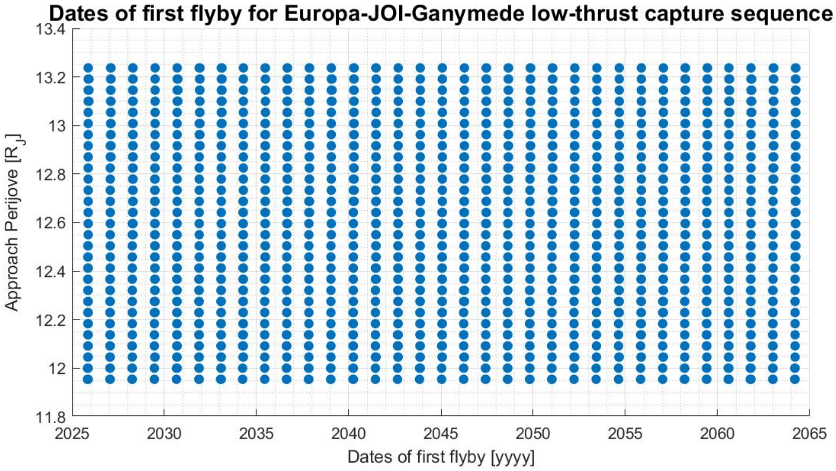

Figure B.10: Ephemerides results within the 2025-2065 time interval for varying perijove considering a Europa-JOI-Ganymede low-thrust capture sequence. The vertical patterns represent one flyby window that repeats every 1.22 year.

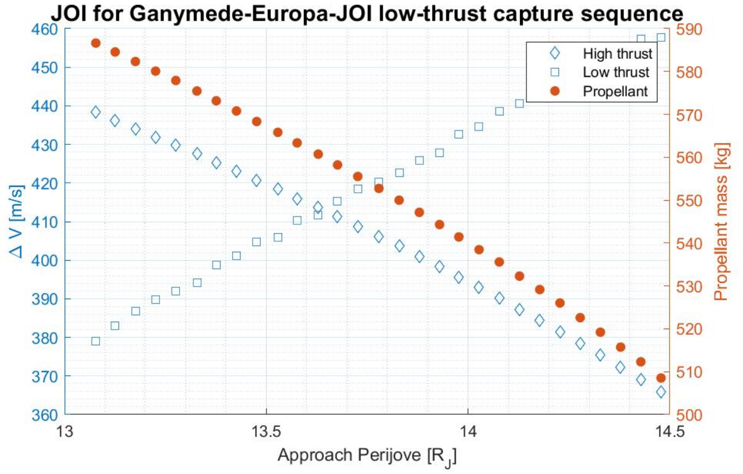

Figure B.11: Required JOI maneuver in terms of ΔV and propellant mass considering a Ganymede-Europa-JOI low-thrust capture sequence for varying initial perijove.

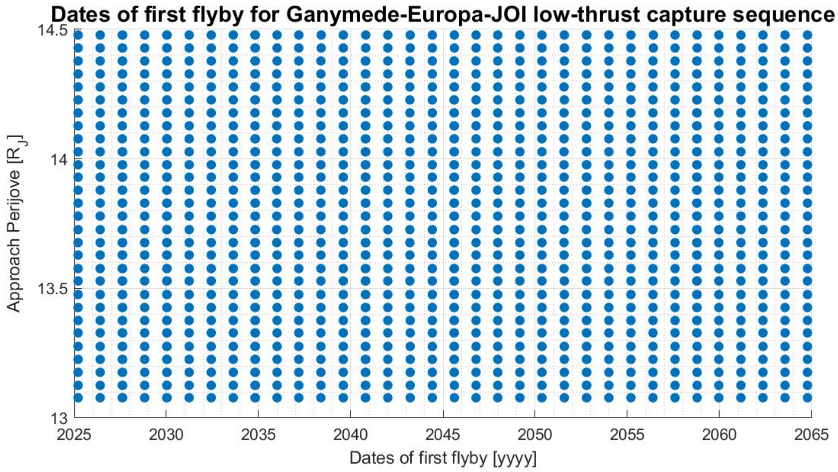

Figure B.12: Ephemerides results within the 2025-2065 time interval for varying perijove considering a Ganymede-Europa-JOI low-thrust capture sequence. The vertical patterns represent one flyby window that repeats every 1.22 year.

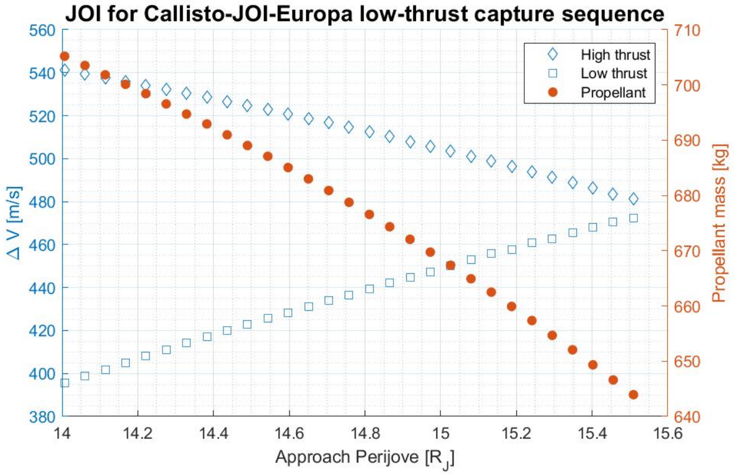

Figure B.13: Required JOI maneuver in terms of ΔV and propellant mass considering a Callisto-JOI-Europa low-thrust capture sequence for varying initial perijove.

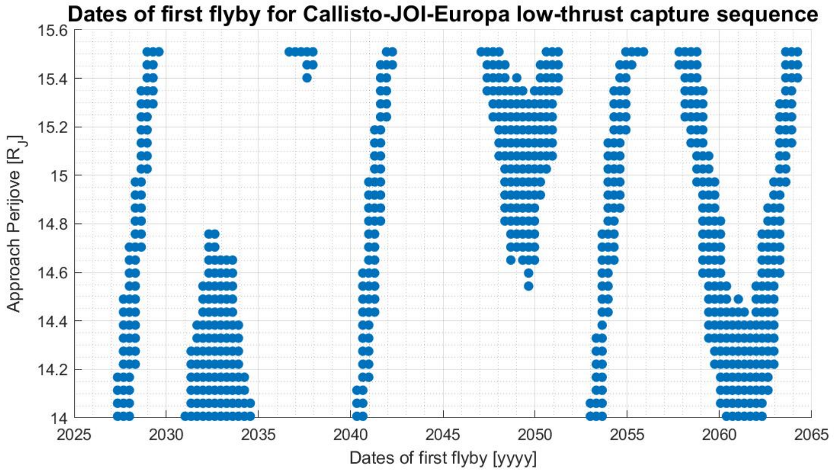

Figure B.14: Ephemerides results within the 2025-2065 time interval for varying perijove considering a Callisto-JOI-Europa low-thrust capture sequence. Short periodic pattern repeats every 12.20 years.

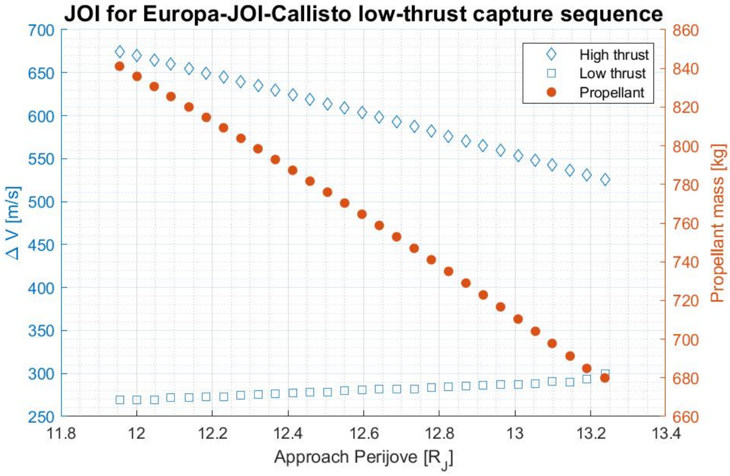

Figure B.15: Required JOI maneuver in terms of ΔV and propellant mass considering a Europa-JOI-Callisto low-thrust capture sequence.

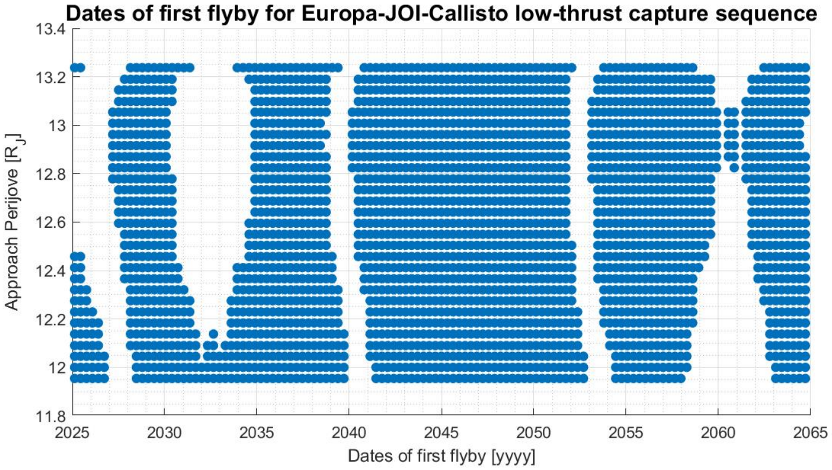

Figure B.16: Ephemerides results within the 2025-2065 time interval for varying perijove considering a Europa-JOI-Callisto low-thrust capture sequence. Short periodic pattern repeats every 12.20 years.

B.2 Low-thrust triple-aided

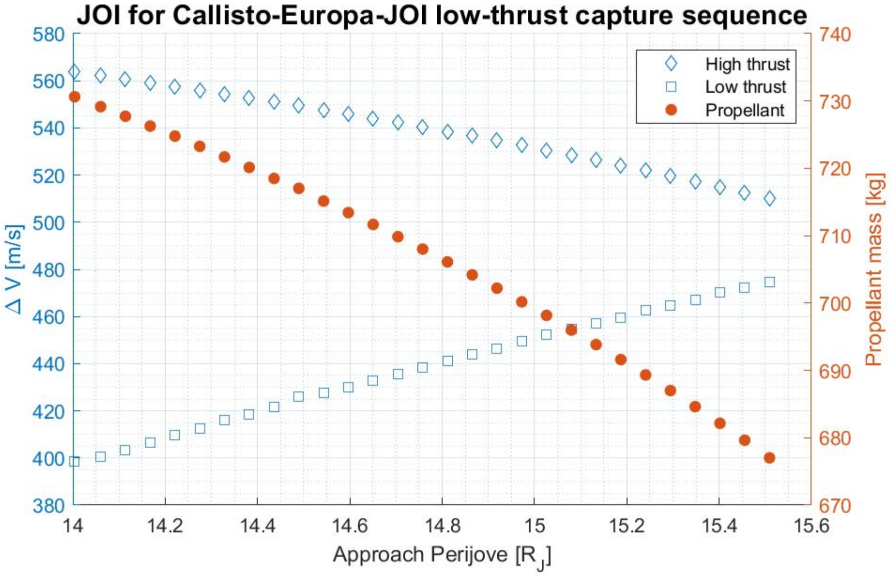

Figure B.17: Required JOI maneuver in terms of ΔV and propellant mass considering a Callisto-Europa-JOI capture sequence.

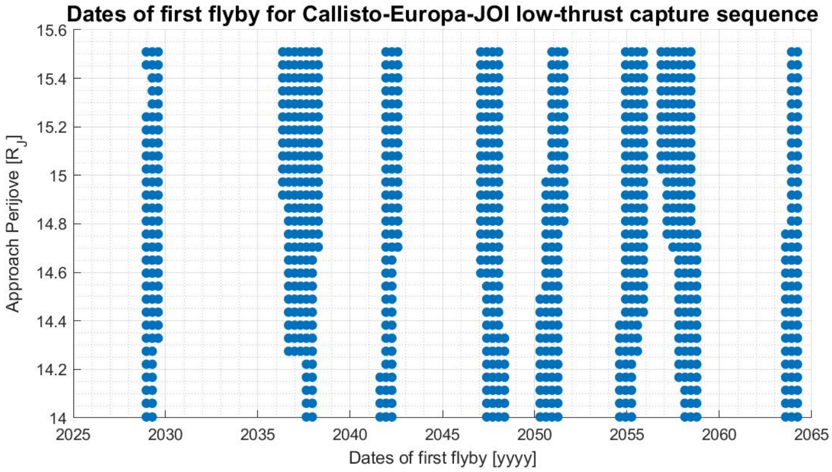

Figure B.18: Ephemerides results within the 2025-2065 time interval for varying perijove considering a Callisto-Europa-JOI low-thrust capture sequence. Short periodic pattern repeats every 12.20 year.

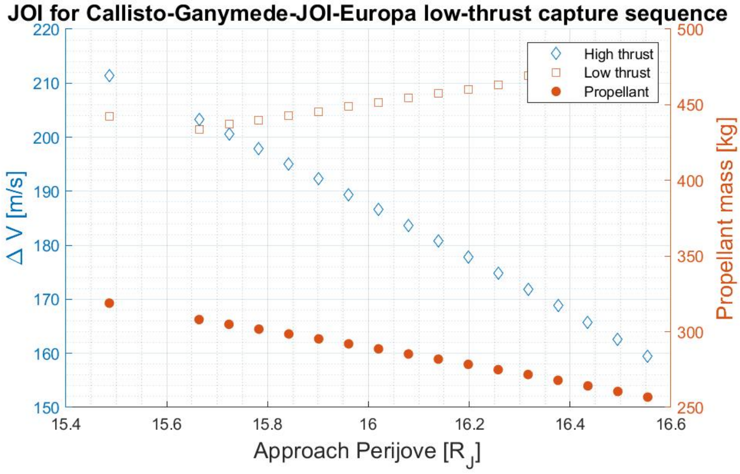

Figure B.19: Required JOI maneuver in terms of ΔV and propellant mass considering a Callisto-Europa-JOI-Ganymede low-thrust capture sequence.

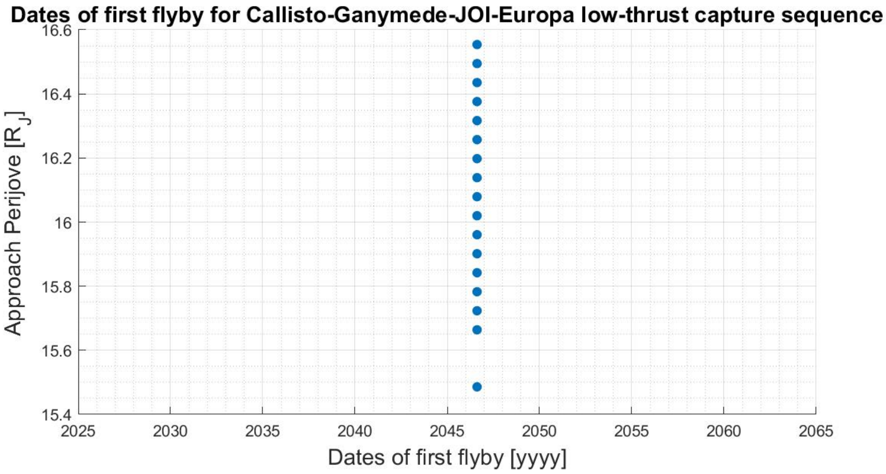

Figure B.20: Ephemerides results within the 2025-2065 time interval for varying perijove considering a Callisto-Europa-JOI-Ganymede low-thrust capture sequence.

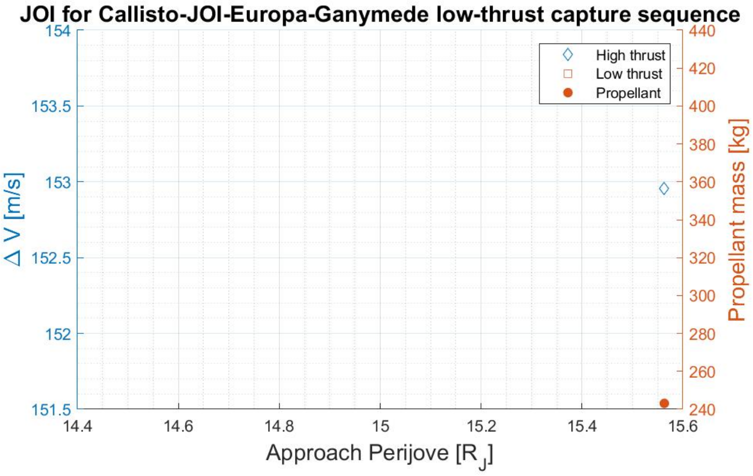

Figure B.21: Required JOI maneuver in terms of ΔV and propellant mass considering a Callisto-JOI-Europa-Ganymede low-thrust capture sequence.

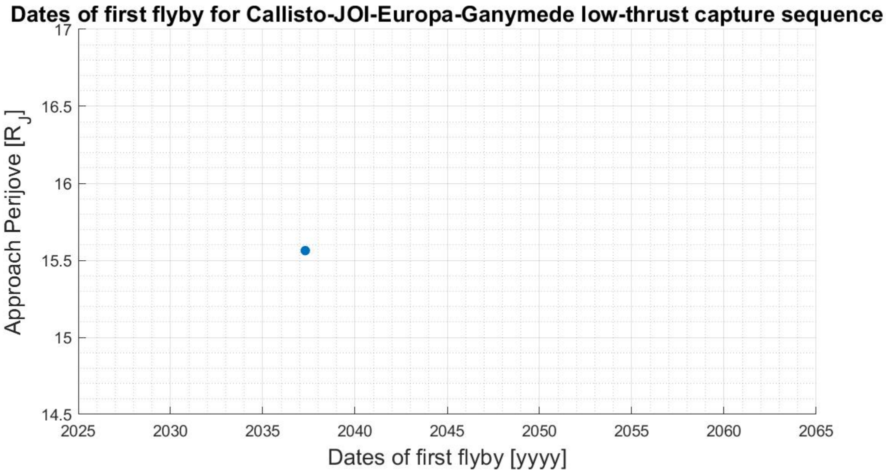

Figure B.22: Ephemerides results within the 2025-2065 time interval for varying perijove considering a Callisto-JOI-Europa-Ganymede low-thrust capture sequence.

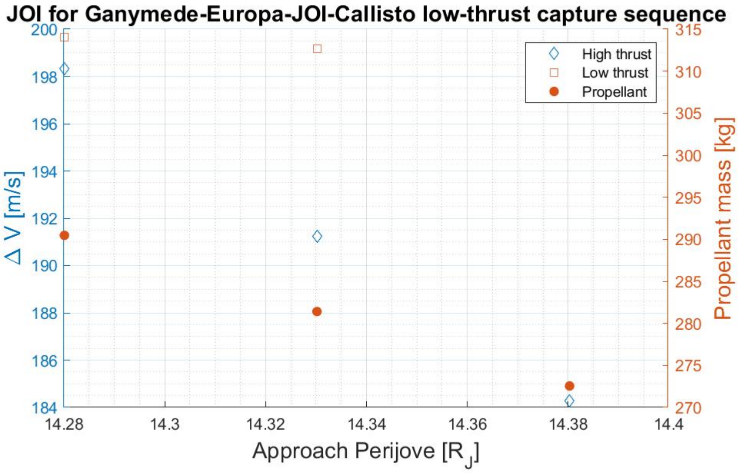

Figure B.23: Required JOI maneuver in terms of ΔV and propellant mass considering a Ganymede-Europa-JOI-Callisto low-thrust capture sequence.

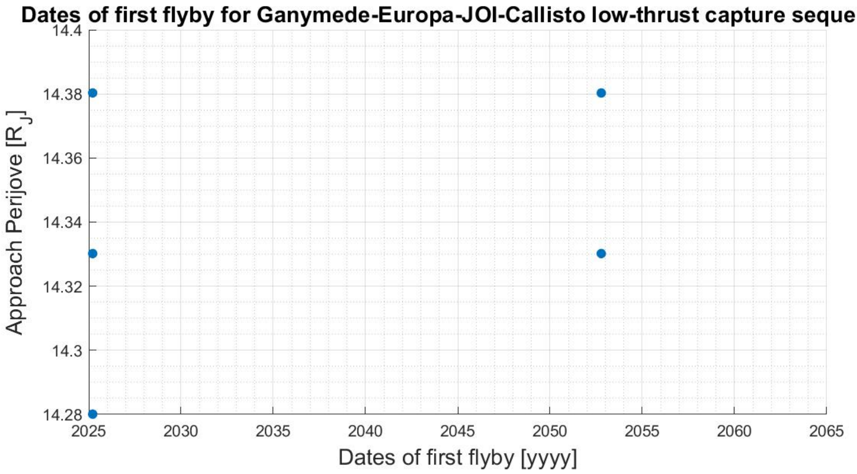

Figure B.24: Ephemerides results within the 2025-2065 time interval for varying perijove considering a Ganymede-Europa-JOI-Callisto low-thrust capture trajectory.

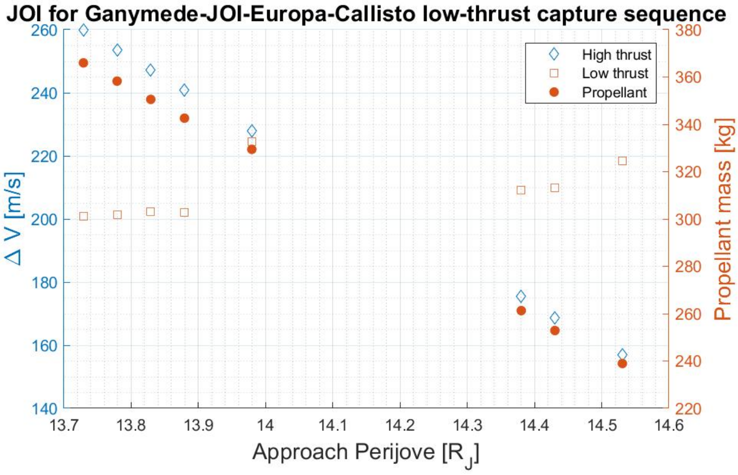

Figure B.25: Required JOI maneuver in terms of ΔV and propellant mass considering a Ganymede-JOI-Europa-Callisto low-thrust capture sequence.

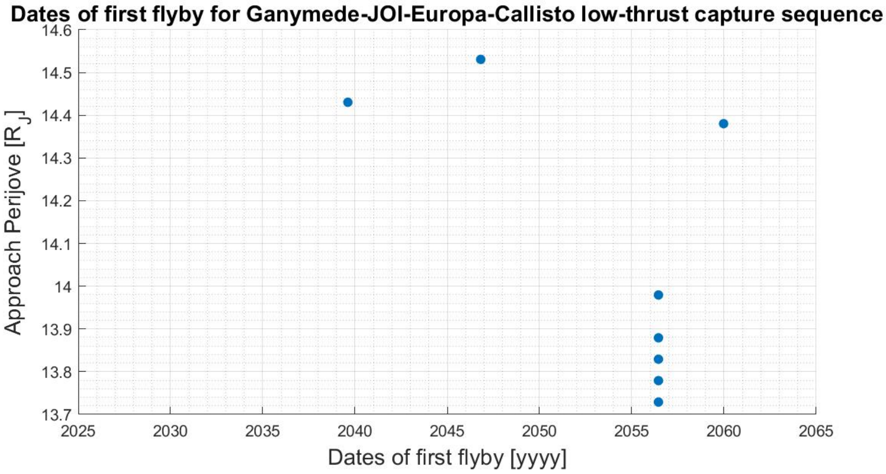

Figure B.26: Ephemerides results within the 2025-2065 time interval for varying perijove considering a Ganymede-JOI-Europa-Callisto low-thrust capture trajectory.

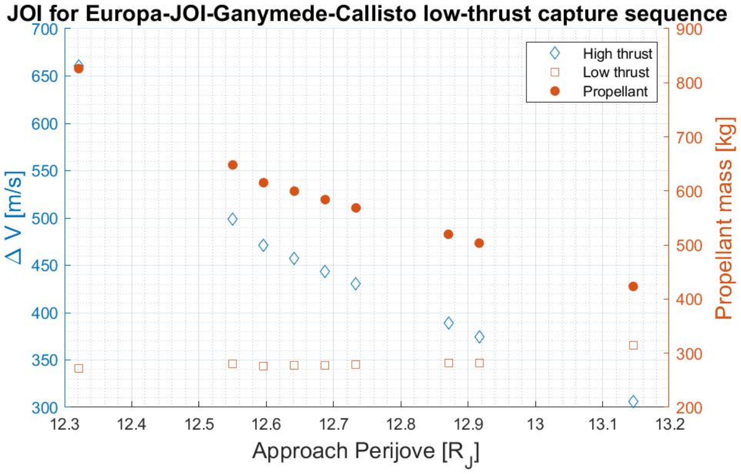

Figure B.27: Required JOI maneuver in terms of ΔV and propellant mass considering a Europa-JOI-Ganymede-Callisto low-thrust capture sequence.

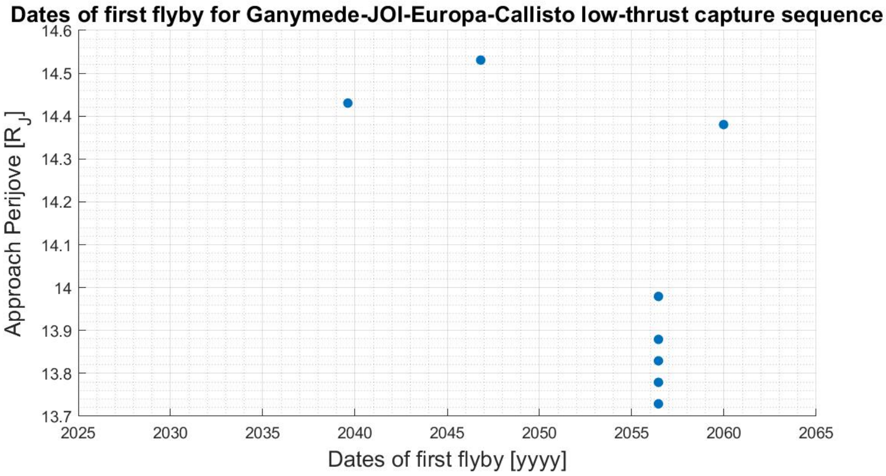

Figure B.28: Ephemerides results within the 2025-2065 time interval for varying perijove considering a Europa-JOI-Ganymede-Callisto low-thrust capture trajectory.

Bibliography

[1] Johannes Benkhoff, Jan van Casteren, Hajime Hayakawa, Masaki Fujimoto, Harri Laakso, Mauro Novara, Paolo Ferri, Helen R. Middleton, and Ruth Ziethe. Bepicolombo—comprehensive exploration of mercury: Mission overview and science goals. *Planetary and Space Science*, 58(1):2 – 20, 2010. ISSN 0032-0633. doi: https://doi.org/10.1016/j.pss.2009.09.020. URL `http://www.sciencedirect.com/science/article/pii/S0032063309002840`. Comprehensive Science Investigations of Mercury: The scientific goals of the joint ESA/JAXA mission BepiColombo.

[2] F. Biscani, F. D. Izzo, W. Jakob, M. Märtens, A. Mereta, C. Kaldemeyer, S. Lyskov, S. Corlay, K. Manani, J. Mabille, T. Misko, A. Huebl, Z. Fu, T. G. Badger, M. Nimier-David, L. ehovin Zajc, J. Adler, J. Travers, J. Lee, J. Jordan, I. Smirnov, H. Nguyen, F. Lema, E. O'Leary, and A. Mambrini. Pagmo and Pygmo documentation. 2019. URL `https://esa.github.io/pagmo2/docs/algorithm_list.html`. accessed on 20 october 2019.

[3] William Burrows. Mission to deep space : Voyager's journey of discovery. *New York : Scientific American Books for Young Readers, c1993.*, 01 1993.

[4] William Burrows. Mission to deep space : Voyager's journey of discovery. *New York : Scientific American Books for Young Readers, c1993.*, 01 1993.

[5] Jerry K. Cline. Satellite aided capture. *Celestial mechanics*, 19(4):405–415, May 1979. ISSN 1572-9478. doi: 10.1007/BF01231017. URL `https://doi.org/10.1007/BF01231017`.

[6] A. Coradini. The cassini mission. *Memorie della Societa Astronomica Italiana Supplementi*, 9:140, 01 2006.

[7] Mark Denny and Alan McFadzean. *Theory: The Rocket Equation and Beyond*. Springer International Publishing, Cham, 2019. ISBN 978-3-030-28080-2. doi: 10.1007/978-3-030-28080-2_3. URL `https://doi.org/10.1007/978-3-030-28080-2_3`.

[8] Franklin O'Donnell Douglas Isbell and Ann Hutchison. Galileo jupiter arrival. pages 1–20, 12 1995. National Aeronautics and Space Administration.

[9] Michael G. Wilson, Christopher L. Potts, Robert A. Mase, Allen Halsell, and Dennis V. Byrnes. Maneuver design for Galileo Jupiter approach and orbital operations. *Space Flight Dynamics, Proceedings of the 12th International Symposium held 2-6 June 1997 in Darmstadt, Germany. Edited by T.-D. Guyenne. ESA SP-403. Paris: Eurpoean Space Agency*, page 341, 09 1997.

[10] Harm-Pieter Gijsens. *The Tisserand Graph with Low Thrust*. Technical University Delft, 05 2014. Master of Science thesis report.

[11] R.A. Jacobson. Planetary satellite ephemeris list. `https://ssd.jpl.nasa.gov/?sat_ephem`, December 2016.

[12] Vanwesenbeeck Jorn. *NaturalSatellite-aided PlanetaryCapture (Literature Study Report)*. Technical University Delft, 01 2019. Part of the MSc thesis.

[13] A. V. Labunsky, O. V. Papkov, and K. G. Sukhanov. *Multiple Gravity Assist Interplanetary Trajectory*. Overseas Publishers Association N.V., Amsterdam, 1998. ISBN 90-5699-090-X.

[14] Chuan Lin, Anyong Qing, and Quanyuan Feng. A comparative study of crossover in differential evolution. *J. Heuristics*, 17:675–703, 12 2011. doi: 10.1007/s10732-010-9151-1.

[15] I.L. Lopez Cruz, L.G. Van Willigenburg, and G. Van Straten. Efficient differential evolution algorithms for multimodal optimal control problems. *Applied Soft Computing*, 3(2):97 – 122, 2003. ISSN 1568-4946. doi: https://doi.org/10.1016/S1568-4946(03)00007-3. URL `http://www.sciencedirect.com/science/article/pii/S1568494603000073`.

[16] Alfred Lynam. Broad-search algorithms for the spacecraft trajectory design of callisto-ganymede-io triple flyby sequences from 2024-2040, part i: Heuristic pruning of the search space. *Acta Astronautica*, 94:246–252, 02 2014. doi: 10.1016/j.actaastro.2013.07.018.

[17] Alfred Lynam. Broad-search algorithms for finding triple-and quadruple-satellite-aided captures at jupiter from 2020 to 2080. *Celestial Mechanics and Dynamical Astronomy*, 121, 02 2015. doi: 10.1007/s10569-015-9602-y.

[18] Alfred Lynam, Kevin Kloster, and James Longuski. Multiple-satellite-aided capture trajectories at jupiter using the laplace resonance. *Celestial Mechanics and Dynamical Astronomy*, 109:59–84, 01 2011. doi: 10.1007/s10569-010-9307-1.

[19] James McAdams, David Dunham, Robert Farquhar, Anthony Taylor, and Bobby Williams. Trajectory design and maneuver strategy for the messenger mission to mercury. *Journal of Spacecraft and Rockets - J SPACECRAFT ROCKET*, 43:1054–1064, 09 2006. doi: 10.2514/1.18178.

[20] James Miller and Connie Weeks. *Application of Tisserand's Criterion to the Design of Gravity Assist Trajectories*. doi: 10.2514/6.2002-4717. URL `https://arc.aiaa.org/doi/abs/10.2514/6.2002-4717`.

[21] O Montenbruck, E Gill, and FH Lutze. Satellite Orbits: Models, Methods, and Applications. *Applied Mechanics Reviews*, 55(2):B27–B28, 04 2002. ISSN 0003-6900. doi: 10.1115/1.1451162. URL `https://doi.org/10.1115/1.1451162`.

[22] P. Musegaas. *Optimization of Space Trajectories Including Multiple Gravity Assists and Deep Space Maneuvers*. Technical University Delft, 01 2013. URL `http://resolver.tudelft.nl/uuid:02468c77-5c64-4df8-9a24-1ed7ad9d1408`. Master of Science thesis report.

[23] John Navagh. Optimizing interplanetary trajectories with deep space maneuvers. September 1993.

[24] Christopher Scott, Martin Ozimek, Amanda Haapala, Fazle Siddique, and Brent Buffington. Dual satellite-aided planetary capture with interplanetary trajectory constraints. *Journal of Guidance, Control, and Dynamics*, 40:548–562, 03 2017. doi: 10.2514/1.G002102.

[25] Rainer Storn and Kenneth Price. Differential evolution - a simple and efficient heuristic for global optimization over continuous spaces. *Journal of Global Optimization*, 11:341–359, 01 1997. doi: 10.1023/A:1008202821328.

[26] Nathan Strange and James Longuski. Graphical method for gravity-assist trajectory design. *Journal of Spacecraft and Rockets - J SPACECRAFT ROCKET*, 39:9–16, 01 2002. doi: 10.2514/2.3800.

[27] Nathan Strange, Damon Landau, Richard Hofer, Steve Snyder, Thomas Randolph, Stefano Campagnola, James Szabo, and Bruce Pote. Solar electric propulsion gravity-assist tours for Jupiter missions. pages 1–9, 08 2012. doi: 10.2514/6.2012-4518.

[28] Nathan Strange, Damon Landau, Richard Hofer, Steve Snyder, Thomas Randolph, Stefano Campagnola, James Szabo, and Bruce Pote. Solar electric propulsion gravity-assist tours for Jupiter missions. pages 1–9, 08 2012. doi: 10.2514/6.2012-4518.

[29] Karel Wakker. *Fundamentals of Astrodynamics*. TU Delft, 01 2015. ISBN 978-94-6186-419-2.